EPFL

Thèse n° 8327

A Fast Ion Loss Detector for the TCV Tokamak

Présentée le 1er octobre 2021

Faculté des sciences de base
SPC - Physique du Tokamak TCV
Programme doctoral en physique

pour l'obtention du grade de Docteur ès Sciences

par

Lorenzo STIPANI

Acceptée sur proposition du jury

Prof. F. Courbin, président du jury
Prof. A. Fasoli, Dr D. Testa, directeurs de thèse
Prof. M. Garcia Munoz, rapporteur
Prof. M. Salewski, rapporteur
Prof. J. Graves, rapporteur

École
polytechnique
fédérale
de Lausanne

2021

C'est dans l'homme, dans sa modeste particularité, dans son droit à cette particularité que réside le seul sens, le sens véritable et éternel de la lutte pour la vie.

Vasily S. Grossman, *Vie et Destin**, 1959.

* The enormous legacy of Andrei D. Sakharov includes, besides conceiving the Tokamak, his collaboration in smuggling the Grossman's masterpiece out of USSR by microfilming one of the two copies rescued from KGB's confiscation. The novel was finally published, for the first time, in Lausanne, by L'Âge d'Homme, in 1980.

Abstract

A Fast Ion Loss Detector (FILD) was designed, assembled, installed and commissioned for TCV. This is a radially positionable, scintillator based detector that provides information on the 2D fast-ion velocity space at the probe's location. The collected particles are collimated inside the probe head and impinge upon a plate coated with a scintillator material that emits light. The photon flux is relayed to two acquisition systems: a sCMOS camera for high spatial resolution measurements of the emission locations in the scintillator, and fast photo-multipliers that allow time-correlation studies of fast-ion losses with high-frequency electromagnetic fluctuations.

From its position with respect to the confined plasma and the fast-ion sources on TCV, FILD probes a small portion of the lost fast-ion phase space with high velocity-space and temporal resolution. Therefore, it naturally complements other available diagnostics such as neutral particle analysers, spectroscopy techniques for light emission from energetic particles following CX reactions, or neutron counters, which feature a broader, but less resolved, spatial coverage of fast-ion dynamics.

The TCV-FILD design introduces some novelties for exploring new ranges of operation that may be adopted in similar systems for other Tokamaks, such as ITER. Two entrance slits can collect particles that circulate in co- and cntr-plasma current directions. This will be particularly useful when the second NBH system, injecting in the opposite toroidal direction, with particle energies that can excite strong Alfvénic modes, will be operated on TCV. A controlled pneumatic linear actuator radially positions the detector to expose the slits to the particle flux up to 9 mm inward of the vessel wall. A plug-in design was conceived to facilitate diagnostic installation.

The diagnostic was installed and commissioned during TCV experiments in 2020. The sensitivity of the detector to the local magnetic field line direction was investigated. The direction of the plasma current was found to select which of the two slits may be traversed by lost particles. The operational limits in discharges with NBH with total delivered energies up to 1 MJ were assessed with the help of sensors monitoring the temperature of the probe head and cameras detecting visible light emissions resulting from the graphite shield heating by particle fluxes.

Using FILD, fast-ion losses were detected for the first time on TCV in plasma discharges exhibiting strong MHD modes. Ejections of energetic ions were found correlated in time with Sawtooth crashes, as a sequence of individual events, and in strong phase coherence, as a continuous loss in time, with magnetic perturbations of a saturated and toroidally rotating magnetic island of a NTM.

These observations, in addition to providing initial results on the relevant physics phenomena, stimulating further experiments and comparisons with theory, demonstrate the ability of TCV-FILD to provide valuable information in plasma discharges of interest for fast-ion studies. These measurements and additional information from other TCV diagnostics may now be combined to reconstruct, with

tomographic inversion techniques, more of the fast-ion phase space. This will be used to identify the conditions for the excitation/suppression of magnetic instabilities, develop methods for their real-time control with heating and/or shaping actuators and investigate their dependencies on plasma parameters.

Keywords: Nuclear fusion, Plasma, Tokamak, Fast ions, Diagnostics, sCMOS, Photo-multiplier, Pneumatic actuator, Plasma instabilities, Neutral Beam Injection.

Sinossi

Un rivelatore di perdite di ioni rapidi (FILD) è stato progettato, costruito, installato e collaudato per il Tokamak TCV. FILD è basato su uno scintillatore posizionabile radialmente, che fornisce informazioni sullo spazio delle velocità 2D di ioni rapidi deconfinati rispetto al nucleo del plasma e che raggiungono la sonda. Le particelle raccolte sono collimate all'interno e colpiscono uno schermo con materiale scintillatore che emette luce. Il flusso di fotoni che ne risulta è convogliato verso due sistemi d'acquisizione: una fotocamera sCMOS per misurare, in alta definizione, le emissioni dello scintillatore, e dei foto-moltiplicatori veloci per studi di correlazioni nel tempo tra le perdite e le fluttuazioni elettromagnetiche.

Per via della sua posizione rispetto al plasma confinato ed alle sorgenti di ioni rapidi, FILD esplora una piccola porzione dello spazio delle fasi degli ioni rapidi con grande risoluzione e rappresenta un naturale complemento ad altre diagnostiche come gli analizzatori di particelle neutre, tecniche di spettroscopia o rivelatori di neutroni.

TCV-FILD introduce alcune novità che permetteranno di esplorare nuovi campi di operabilità e che potrebbero essere adottate in sistemi simili su altri Tokamak, ad esempio ITER. Due aperture possono raccogliere particelle che circolano in senso uguale o contrario alla direzione della corrente di plasma. Questo sarà utile quando un secondo sistema NBH, che inietterà in direzione opposta e con energie delle particelle che potranno eccitare intensi modi Alfvénici, sarà operativo. Un attuatore pneumatico controllato posiziona radialmente il rivelatore in modo da esporre le due aperture al flusso di particelle, per un massimo di 9 mm dal muro del reattore. Una concezione *plug-in* è stata preferita per facilitare l'installazione.

La diagnostica è stata installata e collaudata durante vari esperimenti su TCV nel 2020. È stata valutata la sensibilità dello strumento alla direzione del campo magnetico locale. Si è confermato che la direzione della corrente di plasma seleziona quale delle due fessure può essere attraversata dalle particelle perse. Sono stati quantificati i limiti operazionali in scariche con NBH con energie totali fino a 1MJ. Questo grazie all'ausilio di sensori che monitorano la temperatura della sonda e fotocamere che rivelano emissioni di luce visibile dovute al riscaldamento dello scudo termico in grafite causato dal flusso di particele.

Per la prima volta su TCV, utilizzando il FILD, sono state rivelate perdite di ioni rapidi in scariche caratterizzate da intensi modi MHD. Espulsioni di ioni energetici sono state trovate, come sequenza di eventi individuali, in correlazione con i *sawteeth crash* e, come perdite continue nel tempo, in forte coerenza di fase con le perturbazioni di un'isola magnetica, in rotazione toroidale, di un NTM. Queste osservazioni, oltre a fornire dei primi risultati su alcuni fenomeni rilevanti che hanno stimolato ulteriori esperimenti e confronti con la teoria, dimostrano la capacità di TCV-FILD nel fornire informazioni utili per lo studio degli ioni rapidi. Ulteriori informazioni da altre diagnostiche su TCV potranno essere combinate per ricostruire, con tecniche d'inversione tomografica, sempre più porzioni dello spazio delle fasi. Ciò per identificare le condizioni per l'eccitazione/soppressione delle instabilità magnetiche, sviluppare metodi di controllo in tempo reale ed indagare la loro dipendenza dai parametri di plasma.

Parole chiave: Fusione nucleare, Plasma, Tokamak, Ioni rapidi, Diagnostica, sCMOS, Fotomoltiplicatore, Attuatore pneumatico, Instabilità di plasma, Iniettore di fascio di neutri.

Contents

List of Figures

List of Tables

Chapter 1

Introduction

1.1 Nuclear Fusion

Life requires energy. The simplest biological systems and the most complex human society are both rooted in transforming primary resources into energy to be used at a later time and somewhere else. The story of mankind became a story of outstanding success when new methods of exploitation of natural resources were found to produce energy with increasing power and availability [69, 35, 36]. The energy obtained from burning carbon and oil has been the basis for the Industrial Revolutions that shaped the World as it is today. Evidences for a strong relation between energy consumption and economic growth, shown in Figure 1.1, and improvements to basic living conditions are overwhelming [65].

New means of energy production are necessary to face the increasing global demand for electric energy, whilst reducing the fossil fuel share, widely considered as responsible for Global Warming. Among the alternatives proposed to date, Nuclear Fusion, although as yet not directly exploited, is one of the most promising for our future.

Nuclear fusion is the process of fusing two nuclei together to form heavier nuclei. The most accessible of such reactions is

$$ {}^2_1D +^3_1 T \rightarrow^4_2 He\,(3.5\text{ MeV}) +^1_0 n\,(14.1\text{ MeV})\,, \tag{1.1}$$

where the reactants are Deuterium (D) and Tritium (T) nuclei that produce a nucleus of Helium (also termed an α particle) and a neutron. The mass defect between the two sides of the reaction becomes kinetic energy according to $E = \Delta m\ c^2$. Fusion reactions occur if the nuclei are brought close to distances $\sim 10^{-15}$ m where the Coulomb repulsion is overcome by nucleon attraction (the Strong force). In order to achieve this economically, the thermonuclear approach to nuclear fusion heats the fuel to temperatures of the order of 100 millions of degrees. At these temperatures, the fuel is a *plasma*, a globally-neutral ionized gas that must be confined, i.e. maintained in limited contact with the reactor to keep the required temperature and density to obtain sufficient fusion reactions. Sufficient plasma particle and energy confinement and external heating enable self-sustained reactions in which external heating is, in part, replaced by the collisional transfer of the α particle kinetic energy to the plasma, a mechanism called *slowing-down*. A figure of merit of the success in reaching reactor conditions is the Q factor, the ratio between the density of power produced by the fusion reaction and that provided externally to sustain the plasma. This number can be related to the fraction of α-heating, the ratio

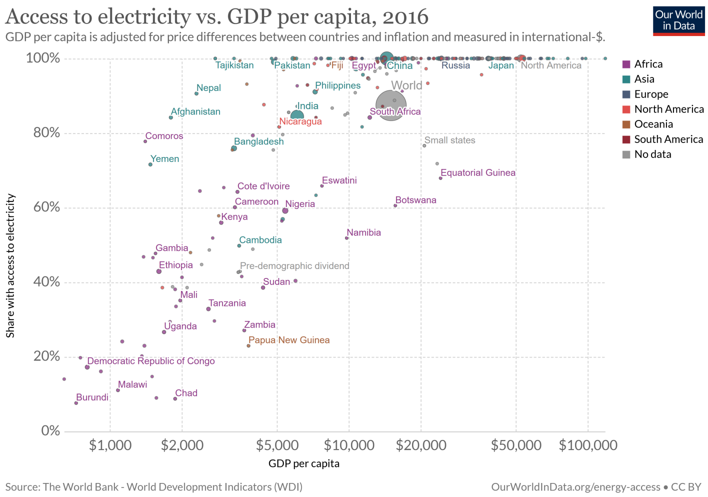

Figure 1.1: Electric energy consumption vs GDP per person, per country, in 2016. Credits: Ourworldindata.org

between the density of power from α particles and the total density of heating power, as

$$f_\alpha \simeq \frac{Q}{Q+5}. \tag{1.2}$$

The $Q \geq 5$ scenario, or equivalently when $f_\alpha \geq 50\%$, is called the *burning plasma* regime.

Plasma confinement can be achieved by different confinement strategies. Among these, the Tokamak, which confines the plasma by constraining the particle motion with magnetic fields, is, to date, the most studied and advanced. For this reason it has been chosen as the model for power plant-scale reactors to be build in the next decades. The International Tokamak Experimental Reactor (ITER), for instance, will be the first-ever reactor that may achieve a plasma discharge in the burning plasma regime up to values of $Q \sim 10$. An introduction to the Tokamak configuration and physics is in Section 2.2.

1.2 Motivation of this thesis

To reach a burning plasma regime, α particles and non-fusion born ions with energies much higher than those in the thermal bulk plasma must also be confined [13]. In addition to resulting from DT fusion reactions, a suprathermal ion population (or *fast ions*) may originate from neutrals externally injected (NBI) that undergo ionization in the plasma bulk, or as particles accelerated within the plasma by electromagnetic forces. Fast ions can also be exploited to generate non-inductive currents that supplement and modify the Tokamak toroidal current that is necessary to confine the plasma and is often only provided inductively (as this approach is, of necessity, limited in time).

While slowing-down, fast ions may follow unconfined orbits and be lost. These *losses* will reduce the effective heating power delivered to the plasma lowering the reactor's performance. They also cause intense heat fluxes on localised parts of the reactor wall, particularly detrimental in Tokamaks such as ITER where the α power is expected to be large (100 MW in ITER $Q = 10$ discharges).

Fast-ion losses are caused by a wide variety of mechanisms. If the fast ions are lost few toroidal turns after birth (as fusion products or ionised following NBI), in this thesis, we will say that they are subject to *early losses*. While circulating inside the Tokamak, fast ions may interact with Magneto-Hydrodynamic (MHD) modes and other electromagnetic fluctuations that provide further loss mechanisms. For instance, a *Sawtooth* (ST) instability, observed in a large number of Tokamaks, causes repetitive fast changes in the magnetic topology that, in turn, produce periodic plasma redistributions, including for fast ions that can be displaced to where they are poorly confined. Another example is the Neoclassical Tearing Mode (NTM) that produces significant, but here continuous, changes of the magnetic field line structure, again affecting certain regions of fast-ion phase space and their confinement.

An interplay between fast ions and high-frequency electromagnetic fluctuations can be observed with reciprocal effects. Modes may exist as solutions of the dispersion equation for the thermal plasma and be driven unstable by wave-particle resonant interactions. When the fast particle pressure is significant, modes may result from the fast-ion contribution not only in term of drive, but also as a result of the modification of the plasma dispersion relation. For instance, in ITER-like-size machines, fusion-born α particles may excite a wide class of Alfvén Eigenmodes (AEs) or Fishbones leading to nonlinear interaction regimes that enhance the fast-ion outward transport with a consequent reduction of the driving mechanism.

The excitation of such electromagnetic fluctuations and their effects on suprathermal ions have been extensively studied in many Tokamaks. For instance, the damping of the AEs is a function of the plasma shape [76], heating and non-inductive current drive [25], and some plasma parameters [29]. These and many other findings are today the basis for a systematic investigation of the effect of the plasma shape and configuration on fast-ion losses, together with the search for possible actuators to maintain control of them, which is still incomplete.

The Tokamak à Configuration Variable (TCV), located at the Swiss Plasma Center, Lausanne, is able to provide confined plasmas with a large variety of shapes. Therefore, it is an ideal device for the investigation of the stability of the modes and, more specifically, of their effects on the fast ion confinement, as a function of plasma shape and configuration. The Neutral Beam Heating (NBH) is a strong source of fast ions with a delivered power of 1.3 MW for a total injected energy presently limited to 1.1 MJ of Deuterium atoms with energies up to 28 keV. Depending on plasma parameters, it may also be used to control MHD instabilities that can alter the plasma configuration's stability. A second 1 MW class NBH system, with neutral energies up to 60 keV injected in the opposite toroidal direction, will be installed in 2021. This will access plasma scenarios optimal in the excitation of several AEs. TCV also features a lower power 50 keV highly collimated diagnostic beam that injects near radially for Charge Exchange Spectroscopy providing a further source of fast ions. 1.4 MW Electron Cyclotron Resonance Heating (ECRH) can provide localized heating and current drive that can play a strong role in the excitation/suppression of certain plasma electromagnetic modes. A large set of diagnostics is available to survey the plasma state and perform measurements of interest for fast-ion studies. A Neutral Particle Analyser and spectroscopy techniques (FIDA) have, to date, been exploited in investigation of the physics of fast ions on TCV.

A unique tool to assess fast-ion losses over the wide range of plasma scenarios accessible on TCV, forms the bulk of this thesis work consisting in designing, assembling, installing and commissioning a new Fast Ion Loss Detector (FILD). This is a radially positionable, scintillator based, diagnostic sensitive to the energy E and pitch $\lambda = v_{\parallel}/v$ (the angle between the particle velocity and the magnetic field line) of lost fast ions. Detected particles are collimated into the probe head and impinge upon a plate coated with a scintillator material that emits light. An optical setup relays the resultant photon flux to two acquisition systems. A high-resolution camera images the entire scintillator plate to infer the 2D ion velocity space from the particle strike positions, and a fast light detection system with an analog bandwidth of 1 MHz is used for time-correlation studies of the fast-ion losses with measured fast electromagnetic fluctuations. From its location at a given position with respect to the confined plasma and fast-ion sources, FILD only probes, although with high velocity-space and temporal resolution, a small portion of the lost fast-ion phase space. It is, therefore, a natural complement to other diagnostics such as NPA, FIDA and neutron counters, that have a less resolved but often broader spatial coverage of fast-ion dynamics.

Similar FILD systems are installed on many existing Tokamaks, such as DIII-D [16], JET [4], NSTX [12], MAST-U [71] and AUG [21, 34, 33].

Examples of FILD observations in AUG include experiments that demonstrated the existence of a convective fast-ion transport due to single AEs, or diffusive loss mechanisms given by the overlapping of the resonant conditions with multiple AEs in the particle phase space [27]. Fast-ion ejections were detected by FILD also caused by ELMs [26], NTMs [24, 19] and other high-frequency instabilities [23]. The FILD system in JET has observed losses of fusion-born particles as a consequence of non-resonant interactions with Fishbones excited by NBI-sourced fast ions [50]. On DIII-D, coherent losses of injected fast ions following resonant interactions with a large variety of AEs were recorded and such measurements validated by numerical simulations [81]. All these observations again highlight a continued need to further study fast-ion behaviour for an α heated fusion reactor.

TCV-FILD introduces some novelties in the detector design to expand its field of operation in view of future applications in similar systems in other Tokamaks, such as ITER. A double slit design permits collecting particles that circulate in co- and cntr-plasma current directions. This will be particularly necessary in discharges with fast ions provided by the second, upcoming, NBH system. Unlike other systems, a feedback-controlled pneumatic linear actuator was employed to position the detector in vessel. This solution avoids problems arising with electric motors in the vicinity of strong magnetic fields. A plug-in design was chosen to facilitate diagnostic installation in the vessel port and access its outside vessel components.

The diagnostic installation was completed and the detector commissioned during TCV experimental campaigns in 2020. FILD first-ever detection of fast-ion losses was performed in plasma discharges, featuring strong MHD activity. Fast-ion losses were found correlated in time with ST crashes as a sequence of intense and individual events. On the other hand, energetic ion losses were observed, continuous loss in time, in strong phase coherence with NTM toroidally rotating magnetic island perturbations. These findings, reported in this thesis, demonstrate the TCV-FILD's ability to detect fast ions ejected by a range of transport mechanisms affecting such particles differently in time and in spatial orbits.

1.3 Thesis outline

- **Chapter 1: Introduction.** Nuclear fusion concepts, motivation of this thesis and its outline.

- **Chapter 2: Fast-ion physics in TCV.** The fundamental concepts of the plasma magnetic confinement are presented with focus on the Tokamak concept. The physics of fast ions in Tokamak plasmas is described in its salient aspects: the effect of collisions in determining the long-run suprathermal ion population, the different orbits in presence of drifts and magnetic mirrors, and the interactions of the particles with electromagnetic fluctuations. The TCV Tokamak, where this work was performed, is presented. Its capabilities and heating schemes mostly relevant to fast-ion studies are highlighted. A review of the available diagnostic systems typically employed in fast-ion dedicated experiments is included.

- **Chapter 3: The FILD diagnostic.** The making of the FILD apparatus is laid out. The design of its components, in particular the novelties introduced in TCV-FILD to explore new ranges of operation, is presented. This work was aided by simulations of the particle trajectories with the numerical codes ASCOT and Engineering-FILDSIM (e-FILDSIM). The optical setup and the two acquisition systems are detailed. These include techniques for the calibration of the camera images of the scintillator plate and the investigation of noise sources affecting the fast light detection. Suggestions for further improvements are given in the conclusions. Finally, the choice of the materials is motivated and the assembly procedure reported.

- **Chapter 4: Commissioning and operational limits.** The diagnostic was installed on TCV and commissioned with dedicated experiments. Early losses of fast ions injected by either NBH or DNBI were detected. The instrumental resolution and accuracy were estimated by interpreting the scintillator emissions captured by the PCO Panda camera with the mapping to the fast-ion velocity space provided by simulations of the particle trajectories inside the probe head with the e-FILDSIM code. The sensitivity of the detector to the equilibrium magnetic field was investigated. The issues in comparing the measured lost fast-ion velocity space to the synthetic one from particle orbit simulations with the ASCOT code are pointed out and discussed. The temperature of the probe components, measured by a set of thermocouples, and the monitoring of the probe head with cameras looking internally and externally helped to identify the pragmatic range of operation in plasma discharges with NBH. The observed visible light emission from the overheated graphite shield was found correlated with the NBH total injected energy.

- **Chapter 5: Fast-ion losses correlated with MHD instabilities.** The first-ever direct detection of fast-ion losses on TCV is described. The losses are shown to be correlated in time with MHD instabilities in plasma discharges with NBH. FILD observed rapid increases of the fast light detection signal occurring at Sawtooth crashes. Sawooth stabilization by ECRH was employed to provide sawteeth with a range of periods and their impact on the fast-ion ejection was investigated. For another MHD instability, magnetic perturbations due to a strong NTM were found in clear phase coherence with the FILD scintillator emissions from the lost impinging particles. These are termed *coherent losses* and may be due to interactions of the fast ions with a saturated and toroidally rotating magnetic island produced by this MHD mode. FILD observations supporting the hypothesis of such transport mechanisms, proposed in literature, are provided.

- **Chapter 6: Conclusions and outlook.** A summary of the status of the diagnostic, its demonstrated capabilities, the novelties introduced with its design, and the measurements performed in fast-ion relevant experiments on TCV is given. Future upgrades of the system are proposed to improve the accuracy of measurements, expand the operational range of the diagnostic for a wider range of TCV experiments, improve the reliability of the positioning actuator and reduce overheating monitoring of the device.

Chapter 2

Fast-ion physics in TCV

2.1 Introduction

The magnetic confinement of the plasma is briefly introduced in Section 2.2 with the main focus on the Tokamak reactor concept.

Given the importance of the fast-ion confinement in achieving a burning plasma, the physics of such particles in a Tokamak is detailed: the collision effects in determining the long-term suprathermal ion distribution, the Neoclassical orbits followed by the particles due to the particular magnetic topology and the possible interactions between these particles and electromagnetic fluctuations that may give fast-ion losses, are shown in Section 2.3.

The work presented in this thesis was carried out at the TCV Tokamak facility. This is presented in Section 2.4, together with the salient features of the available heating systems and the already existing diagnostics more relevant for studying the fast-ion dynamics and the properties of electromagnetic field perturbations.

2.2 The magnetic confinement

Charged particles of species s have a helical motion around the magnetic field line, with the Larmor frequency and radius defined as

$$\Omega_{\mathrm{s}} = \frac{qB}{\gamma m}, \tag{2.1}$$

$$\rho_{\mathrm{s}} = \frac{v_{\perp}}{\Omega_{\mathrm{s}}}, \tag{2.2}$$

where q/m is the charge to mass ratio, γ the relativistic factor, $v_{\perp}$ the perpendicular component of the velocity with respect to the magnetic field direction and B the magnetic field strength. As a result, charges are bound to the field line.

A linear device relying on such simple confining mechanism would be affected by end losses of the particles streaming along the field lines. This is solved by bending the field lines into a torus. Such a

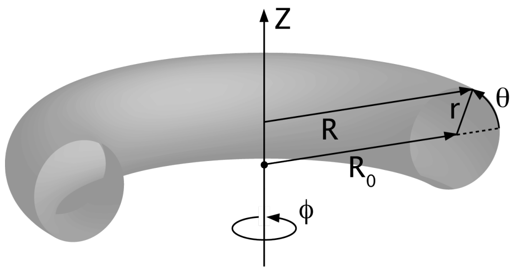

Figure 2.1: Sketch of a torus with the cylindrical co-ordinates (R, Z, ϕ) and the flux co-ordinates (r, θ, ϕ). From fusionwiki.ciemat.es

shape, drawn in Figure 2.1, is described by the following equations

$$x = (R_0 + r\cos\theta)\cos\phi, \tag{2.3}$$
$$y = (R_0 + r\cos\theta)\sin\phi, \tag{2.4}$$
$$z = r\sin\theta. \tag{2.5}$$

An important parameter in this geometry is the *aspect ratio* R_0/r. In the limit of large aspect ratio (or equivalently $\epsilon = r/R_0 \ll 1$) the torus can be approximated as an infinitely long cylinder.

A toroidal magnetic field, that is along the $\hat{e}_\phi$ direction, is generated by coils surrounding the vacuum vessel that contains the plasma. As a consequence, the field scales with the radial co-ordinate as

$$B_\phi \propto \frac{1}{R}. \tag{2.6}$$

Particles in such a non-uniform and curved magnetic field are subjected to vertical drifts

$$\boldsymbol{v}_{\nabla B} = -\frac{mv_\perp^2}{2q}\frac{\nabla B \times \boldsymbol{B}}{B^3}, \tag{2.7}$$
$$\boldsymbol{v}_{\mathrm{c}} = \frac{mv_\parallel^2}{q}\frac{\boldsymbol{R}_{\mathrm{c}} \times \boldsymbol{B}}{R_{\mathrm{c}}B^2}, \tag{2.8}$$

with $\boldsymbol{R}_{\mathrm{c}}$ the curvature radius. These velocities are charge dependent, implying that ions and electrons are displaced in opposite directions giving rise to a vertical electric field that induces the radial drift velocity

$$\boldsymbol{v}_{E\times B} = \frac{\boldsymbol{E} \times \boldsymbol{B}}{B^2}, \tag{2.9}$$

that moves the particle radially outwards.

This effect is overcome by superimposing a poloidal magnetic field, i.e. in the plane of a vertical cross-section of the torus. Hence the particles circulate in this plane averaging out the effects of such drifts. This magnetic configuration is a necessary condition for plasma confinement.

At the present time, between the machines with such a configuration, the best candidate as a basis for a commercial power plant is the Tokamak. This is a russian acronym for *Toroidal Chamber with Magnetic Coils*. In a Tokamak the magnetic field topology is achieved by a set of coils that produce a strong toroidal field, of the order of several Tesla, whereas the main poloidal field is provided by the

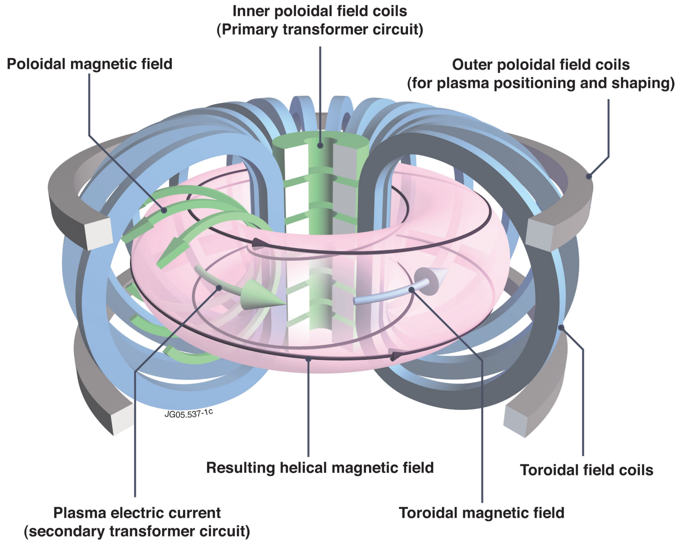

Figure 2.2: Conceptual picture of a Tokamak with the salient features highlighted. From euro-fusion.org

plasma itself. A primary transformer coil is operated with increasing current flow to induce a toroidal electric field which gives rise to a plasma current I_{p}. In effect, the plasma acts a secondary of the transformer. The poloidal field is typically an order of magnitude less intense than the toroidal one. The combined field components are characterised by helical field lines that wrap around the plasma as in Figure 2.2. Toroidal axisymmetry is often assumed to simplify the study of the plasma confinement by reducing the dimensionality of the particle phase space. However, the finite number of coils breaks such a symmetry producing field *ripples* that can have an impact on the confinement. This is briefly discussed in Section 2.3.

At the macroscopic scales of a Tokamak, the interactions between plasma and magnetic fields are described by the Magneto-Hydrodynamics (MHD). The positive and negative charges are modeled as a single fluid and the force balance equations, in the case of a constant-flow plasma, read

$$\nabla p = \boldsymbol{J} \times \boldsymbol{B}, \tag{2.10}$$

where p is the plasma pressure and $\boldsymbol{J}$ the current density.

The equilibrium magnetic field satisfying Equation (2.10) can be written as the sum the toroidal B_ϕ and the poloidal B_{p} components as follows

$$\boldsymbol{B} = RB_\phi \nabla\phi + \underbrace{\nabla\phi \times \nabla\psi}_{B_{\mathrm{p}}}. \tag{2.11}$$

The stream function ψ is related to the poloidal magnetic flux:

$$\psi(R_2) - \psi(R_1) = \int_{\mathrm{S}} B_{\mathrm{p}} \cdot \mathrm{d}\boldsymbol{S}, \tag{2.12}$$

where S is the surface in the toroidal plane bounded by the circumferences of radii R_1 and R_2.

It is useful to use ψ to label the magnetic flux contours in the poloidal plane (termed *flux surfaces*) that magnetic field and current lines lie upon. From Equation (2.10) it is easily shown that $\boldsymbol{B} \cdot \nabla p = 0$ implying that flux surfaces are iso-baric regions. The quantity ψ can be used as a radial co-ordinate, or equivalently the related dimensionless quantity:

$$\rho_\psi = \sqrt{\frac{\psi - \psi_{\text{axis}}}{\psi_{\text{LCFS}} - \psi_{\text{axis}}}}, \tag{2.13}$$

with ψ_{axis} evaluated on the magnetic axis and ψ_{LCFS} at the Last Closed Flux Surface (LCFS). Moreover, since the time scales of energy and particle transport along the field lines are much shorter than those across the nested flux surfaces, the plasma equilibrium quantities such as density and temperature may often be described by a simple 1D model accounting solely for a radial dependence.

The twisting of the field lines on each flux surface is characterised by the *safety factor* defined as

$$q(\psi) = \frac{1}{2\pi} \int_0^{2\pi} \frac{\boldsymbol{B} \cdot \nabla\phi}{\boldsymbol{B} \cdot \nabla\theta} \, \mathrm{d}\theta. \tag{2.14}$$

This represents the number of toroidal loops a field line needs to perform to close one poloidal turn. A closed field line on a flux surface has a length, called *connection length*, given by

$$L_{\mathrm{c}} = 2\pi q R. \tag{2.15}$$

In the cylindrical approximation for large aspect ratio ($\epsilon \ll 1$) one can write the Equation (2.14) in the following fashion

$$q(r) = \frac{r}{R_0} \frac{B_\phi}{B_{\mathrm{p}}}, \tag{2.16}$$

that in a Tokamak is typically of the order of unity, therefore $B_{\mathrm{p}}/B_\phi \sim \epsilon$. The q quantity has an inverse dependence on the plasma current I_{p} and, in turn, is a function of the radial co-ordinate. Its name is related to its important role in plasma stability, as it will be shown in Section 2.3.3.

2.3 Fast-ion dynamics

The motion of a charged particle in an electromagnetic field is described by

$$\boldsymbol{v} = \boldsymbol{v}_{\perp,\text{gyro}} + v_\parallel \frac{\boldsymbol{B}}{B} + \boldsymbol{v}_{\perp,\text{GC}}, \tag{2.17}$$

where "gyro" stands for the rapid Larmor motion around a magnetic field line, $v_\parallel$ is the stream along such a field line and "GC" is the guiding-center of the helical trajectory, which is determined by the slow, compared to the gyromotion, drifts in Equations (2.7), (2.8) and (2.9).

In a Tokamak, the phase space of an energetic particle (EP), generally a $(6 + 1)$ ($+1$ is the time) dimensional space, can be reduced to a $(3+1)$D description. The time an EP takes to travel along the magnetic field lines is much smaller than the collision time so that its energy is conserved. Moreover, the axisymmetry gives the conservation of the toroidal canonical momentum, and slow variations of the magnetic field in the length and time scales of the Larmor motion imply that the magnetic moment is a constant of motion. In brief:

$$L_\mathrm{c}/v_\parallel \ll \tau_\mathrm{coll} \quad \Rightarrow \quad \boxed{E = \frac{mv^2}{2} = \mathrm{const}}, \tag{2.18}$$

$$\frac{\partial}{\partial \phi} = 0 \quad \Rightarrow \quad \boxed{p_\phi = mRv_\phi + Ze\psi = \mathrm{const}}, \tag{2.19}$$

$$\rho_\mathrm{i} \ll \left|\frac{\nabla B}{B}\right|^{-1}, \Omega_\mathrm{i}^{-1} \ll \left|\frac{\mathrm{d}B}{\mathrm{d}t}\frac{1}{B}\right|^{-1} \quad \Rightarrow \quad \boxed{\mu = \frac{mv_\perp^2}{2B} = \mathrm{const}}. \tag{2.20}$$

Therefore the distribution function for suprathermal (or fast) ions can be written as a function of these constants of motion, the sign of the parallel velocity $\sigma = \mathrm{sgn}(v_\parallel)$ and time:

$$f_\mathrm{fast} = f_\mathrm{fast}(E, p_\phi, \mu, \sigma, t). \tag{2.21}$$

This distribution can be modified by Coulomb collisions, sources, loss mechanisms and interactions with electromagnetic perturbations. Sources of fast ions in a Tokamak plasma include:

- fusion products, namely α particles with a birth energy of 3.5 MeV,
- injected fast neutrals undergoing ionization processes that provide energy and momentum to the bulk plasma,
- ions energized via electromagnetic waves, for instance at the cyclotron frequency resonance,
- thermal particles accelerated by fluctuations in the electric field.

On the other hand, fast-ion losses result from the non-perfect confinement. On long time scales, Coulomb collisions (Section 2.3.1) can scatter the fast ions into unconfined orbits (Section 2.3.2), or drifts acting on the guiding-center move all, or part of the particle's orbit, outside the plasma. Additionally, in Tokamak a trapping effect on the particles exists due to toroidal field ripple, that is a breaking of the axisymmetry due to the finite number of toroidal field coils. This reduces the mechanism of averaging out the drifts given by the motion along twisted field lines. Moreover, fast ions can be displaced by resonant and/or non-resonant interactions with electromagnetic fluctuations (Section 2.3.3) into regions of non-confinement, or in regions of higher neutral density where charge-exchange reaction becomes more effective (Section 2.4.2).

2.3.1 Coulomb collisions

On the time scale of τ_coll, fast ions undergo binary Coulomb collisions with the bulk plasma. Collisions among fast ions are usually negligible at very low density. Coulomb interactions with thermal electrons or ions have different effects on the fast-ion energy and pitch-angle Λ or pitch λ, defined as

$$\lambda = \frac{\boldsymbol{v}\cdot\boldsymbol{B}}{vB} = \frac{v_\parallel}{v}, \tag{2.22}$$

$$\Lambda = \mathrm{acos}\left(\lambda\right). \tag{2.23}$$

These effects depend on the energy of the incident fast ion with respect to the *critical energy*

$$E_{\mathrm{crit}} = 14.8 T_{\mathrm{e}} \left(\frac{A^{3/2}}{n_{\mathrm{e}}} \sum_{\mathrm{i}} \frac{n_{\mathrm{i}} Z_{\mathrm{i}}^2}{A_{\mathrm{i}}} \right)^{2/3}, \tag{2.24}$$

with T_{e} measured in energy units, A is the atomic mass of the fast ion and the sum is over the ion species forming the plasma. Since, usually in a Tokamak, $v_{\mathrm{Th,e}} \gg v_{\mathrm{fast}} \gg v_{\mathrm{Th,i}}$, the relative velocities between colliding species are dominated by $v_{\mathrm{Th,e}}$ in one case and v_{fast} in the other. Thus, only the electron temperature enters in Equation (2.24). A fast ion with velocity above $v_{\mathrm{crit}} \propto \sqrt{E_{\mathrm{crit}}}$ will be subject to electron drag, transferring its energy and slowing down primarily on electrons. In contrast, if $v_{\mathrm{fast}} < v_{\mathrm{crit}}$ collisions with ions dominate.

The slowing-down time for the fast ions to deliver their energy to the bulk ions and electrons up to thermalization is

$$\tau_{\mathrm{SD}} = \frac{\tau_{\mathrm{S}}}{3} \log \left(1 + \left(\frac{E}{E_{\mathrm{crit}}} \right)^{3/2} \right), \tag{2.25}$$

where $\tau_{\mathrm{S}} \propto T_{\mathrm{e}}^{3/2} n_{\mathrm{e}}^{-1}$ is the Spitzer [74] slowing-down time of ions upon electrons.

The collisional interactions at play and the fast-ion sources and sinks can be brought together in the following Fokker-Planck equation [39] governing the evolution of the fast-ion distribution function

$$\begin{aligned} \frac{\partial f_{\mathrm{fast}}}{\partial t} = & \underbrace{\frac{1}{v^2 \tau_{\mathrm{S}}} \frac{\partial}{\partial v} \left(\left(v^3 + v_{\mathrm{crit}}^3 \right) f_{\mathrm{fast}} \right)}_{\text{slowing-down}} + \\ & \underbrace{\frac{1}{2 v^2 \tau_{\mathrm{S}}} \frac{\partial}{\partial v} v^2 \left(\frac{v_{\mathrm{e}}^2 m_{\mathrm{e}}}{m_{\mathrm{fast}}} + \frac{v_{\mathrm{crit}}^3 v_{\mathrm{i}}^2 m_{\mathrm{i}}}{v_{\mathrm{e}}^3 m_{\mathrm{fast}}} \right) \frac{\partial f_{\mathrm{fast}}}{\partial v}}_{\text{velocity diffusion}} + \\ & \underbrace{\frac{1}{2 \tau_{\mathrm{S}}} \frac{m_{\mathrm{i}}}{m_{\mathrm{fast}}} \frac{Z_{\mathrm{eff}}}{\langle Z \rangle} \frac{v_{\mathrm{crit}}^3}{v^3} \frac{\partial}{\partial \lambda} \left(\left(1 - \lambda^2 \right) \frac{\partial f_{\mathrm{fast}}}{\partial \lambda} \right)}_{\text{pitch-angle scattering}} + \\ & \underbrace{S_0 \left(\lambda, t \right) \delta \left(v - v_0 \right)}_{\text{source}} - \underbrace{\frac{1}{\tau_{\mathrm{loss}}} f_{\mathrm{fast}}}_{\text{loss}} . \end{aligned} \tag{2.26}$$

The quantity $Z_{\mathrm{eff}} \approx n_{\mathrm{e}}^{-1} \sum n_{\mathrm{j}} Z_{\mathrm{j}}^2$ is the effective charge and $\langle Z \rangle \approx n_{\mathrm{e}}^{-1} \sum n_{\mathrm{j}} Z_{\mathrm{j}}^2 \left(m_{\mathrm{i}} / m_{\mathrm{j}} \right)$ is the average charge, where the sum is over the ion species. The source term is modelled by a simple mono-energetic contribution with rate $S_0 = S_0(\lambda, t)$ and losses are assumed to be exponentially decaying with a characteristic time τ_{loss}.

If we neglect the losses and the terms of diffusion in energy and pitch-angle, we are left with an equation that can be solved analytically in the steady-state case to give the *slowing-down distribution*:

$$f_{\mathrm{SD}} = \frac{S_0 \tau_{\mathrm{S}}}{v^3 + v_{\mathrm{crit}}^3}. \tag{2.27}$$

2.3.2 Passing and trapped orbits

The conservation of E and μ in a magnetic equilibrium configuration with $|\boldsymbol{B}|$ that scales as $\sim 1/R$, see Equation (2.6), is responsible for the *magnetic mirror* reflection of a particle. The particle can therefore be *trapped* in a magnetic well, to contrast with a *passing* orbit that goes around the magnetic axis in the poloidal plane. When trapped, the guiding-center of the particle doesn't close such a poloidal loop, but rather bounces back and forth in toroidal direction and up and down in the poloidal plane. As a consequence, if the GC trajectory projected in the poloidal cross-section typically resembles a banana. Hence these orbits are called *banana orbits*. We will see that the effect of vertical drifts on such orbits eventually give unconfined particles.

We can write the parallel component of the velocity as a function of the poloidal angle and the radial co-ordinate:

$$v_{\parallel}(r,\theta) = v\sqrt{1 - \frac{\mu}{E}B(r,\theta)}. \tag{2.28}$$

The condition for the reflection is $v_{\parallel} = 0$, hence there should exist a $\theta_{\mathrm{b}} \in (0,\pi)$ such that

$$\sqrt{1 - \frac{\mu}{E}B(r,\theta_{\mathrm{b}})} = 0 \;\Rightarrow\; B(r,\theta_{\mathrm{b}}) = \frac{E}{\mu}, \tag{2.29}$$

where the angle θ_{b} corresponds to the tip of the banana orbit.

As a result, a particle is trapped if:

$$\frac{E}{\mu} < B_{\mathrm{max}} \simeq B_0\left(1+\epsilon\right), \tag{2.30}$$

where the magnetic strength is expressed, for $\epsilon \ll 1$, by means of the Equation (2.6) as

$$B \simeq B_{\phi} = \frac{B_0 R_0}{R_0 + r\cos\theta} \simeq B_0\left(1 - \epsilon\cos\theta\right). \tag{2.31}$$

The trapping condition is equivalent to a condition on the pitch-angle, the latter defined in Equation (2.22). In fact, we can write Equation (2.30) also as

$$\lambda < \sqrt{\frac{\epsilon\left(1+\cos\theta\right)}{1+\epsilon}}. \tag{2.32}$$

This means that fast ions with larger perpendicular velocity compared to the total velocity are more likely to be trapped. Particles with velocity mainly aligned with the field direction are, in contrast, mostly passing. Moreover, the fraction of the trapped population increases towards higher r, as highlighted by taking the maximum magnetic field amplitude variation, namely for $\theta = 0$ in the Equation (2.32):

$$\lambda < \sqrt{2\epsilon} \sim \sqrt{r}. \tag{2.33}$$

By solving the equation of motion of a trapped particle, subject to the mirror force $\boldsymbol{F} = -\mu\nabla_{\parallel}B$, one obtains the *bounce frequency* of a banana orbit:

$$\omega_{\mathrm{b}} = \frac{v_{\perp}}{qR_0}\sqrt{\frac{r}{2R_0}}. \tag{2.34}$$

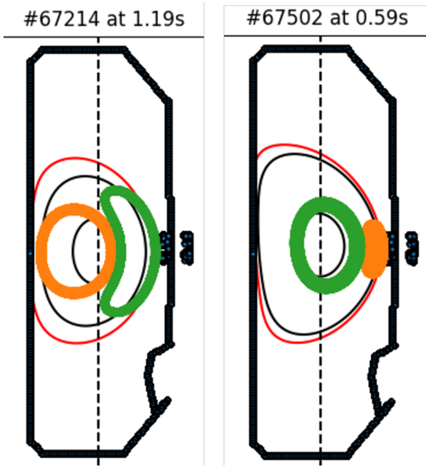

Figure 2.3: (Left) Cntr-I_{p} injected fast ions: passing orbit (orange) is shifted inwards of its initial flux surface (outer solid black), while the banana orbit (green) outwards with respect to the initial flux surface (inner solid black) with the consequence that its outer leg ends up onto the FILD placed in the outer midplane. (Right) Co-I_{p} injected fast ions: passing orbit (green) is outwards shifted from its initial flux surface (inner solid black), while the banana orbit (orange) is inwards shifted with respect to the initial flux surface (outer solid black). In both pictures the LCFS (red) and a vertical line passing through the magnetic axis (black dashed line) are depicted. The showed orbit thickness is due to the gyromotion of the particle as evident in the trapped orbit on the right in which the Larmor radius is comparable with the banana width.

It is important to note that large angle scattering due to Coulomb collisions can change the pitch-angle of such particles that may thus be detrapped. This occurs when $\tau_{\mathrm{coll}} \ll \omega_{\mathrm{b}}^{-1}$.

The conservation of the toroidal canonical momentum p_ϕ in the Equation (2.19) implies that particles drift across flux surfaces along their paths, proportionally to $v_\parallel$. This is due to the curvature drift in the Equation (2.8) and the gradient drift in the Equation (2.7), both in the vertical direction. Such shifts depend on the toroidal field and poloidal field directions, the latter determined by the plasma current direction. In the case of both B_ϕ and I_{p} pointing outwards in the poloidal section with the total drift $\boldsymbol{v}_{\mathrm{d}}$ pointing downwards, the passing particle will slip onto an outer surface when moving in the same current direction (co-I_{p}) or an inner surface when the reverse is true (cntr-I_{p}). A banana orbit, however, will be shifted outwards/inwards in the co-I_{p}/cntr-I_{p} case. These effects are showed in Figure 2.3. The extension of such displacement is also called *banana width* and for large aspect ratio and strongly trapped particles ($\theta \ll 1$) may be written

$$w_{\mathrm{b}} = \frac{v_\parallel}{\Omega_{\mathrm{i}}} \frac{q}{\epsilon}. \tag{2.35}$$

Fast-ion banana orbits can easily achieve $w_{\mathrm{b}} \sim a$, i.e. comparable to the minor radius of the machine, particularly in medium-sized Tokamaks and, if the particle motion is cntr-I_{p}, may eventually be lost.

2.3.3 Interactions with electromagnetic fluctuations

Perturbations of the Tokamak magnetic field are ubiquitous due to the turbulent nature of a confined plasma. These perturbations span large ranges in time and position depending on the underlying mechanism. Besides slow modifications of the axisymmetric equilibrium field, high-frequency fluctuations are routinely detected with frequencies up to several hundreds of kHz, with varying amplitudes and spatial structures. These magnetic fluctuations can be driven unstable by plasma pressure and current profiles, equilibrium shaping or energetic particle distributions, e.g. fast ions.

An important example are MHD modes that are solutions of the Magneto-Hydrodynamic equations. These consider a plasma as a neutral and conductive fluid. Such a fluid description is justified if collisions are taken into account as they lead the electrons and ions to local thermal equilibria. This is a requirement for well defining the fluid quantities such as density and velocity. Therefore a fluid model can be employed for describing phenomena that evolve slowly with respect to the ion Larmor frequency, characterised by length scales larger than the ion Larmor radius, and non-relativistic velocities. If the length scales are large compare to $\lambda_{\mathrm{Debye}} \propto \sqrt{T_{\mathrm{e}}/n_{\mathrm{e}}}$, quasi-neutrality $n_{\mathrm{e}} = n_{\mathrm{i}} = n_0$ ensues (with $Z_{\mathrm{i}} = 1$ for simplicity). The MHD equations become:

$$\frac{\partial \rho_{\mathrm{mass}}}{\partial t} + \nabla \left(\rho_{\mathrm{mass}} \boldsymbol{u}\right) = 0, \tag{2.36}$$

$$\rho_{\mathrm{mass}} \left(\frac{\partial}{\partial t} + \boldsymbol{u} \cdot \nabla\right) \boldsymbol{u} = -\nabla \left(p + \frac{B^2}{2\mu_0}\right) + \frac{\boldsymbol{B} \cdot \nabla \boldsymbol{B}}{\mu_0}, \tag{2.37}$$

$$\frac{\partial \boldsymbol{B}}{\partial t} = \nabla \times (\boldsymbol{u} \times \boldsymbol{B}) + \frac{\eta}{\mu_0} \nabla^2 \boldsymbol{B}. \tag{2.38}$$

Here the quantities mass density $\rho_{\mathrm{mass}} \approx m_{\mathrm{i}} n_0$ and the fluid velocity $\boldsymbol{u} \approx \boldsymbol{u}_{\mathrm{i}}$, for $m_{\mathrm{e}}/m_{\mathrm{i}} \ll 1$, describe the plasma as a single fluid. The set is typically closed by a polytropic relation between the kinetic pressure and the mass density. In Equation (2.38) the diffusive contribution is negligible if the Spitzer collisionality is low to make the plasma an ideal conductor. Here the Frozen-Flux Theorem holds where the plasma always follows magnetic perturbations and no field line reconnection occurs.

In a Tokamak, a MHD mode can be decomposed as a sum of coupled poloidal components labeled by the m-numbers with the toroidal components treated independently as n-numbers are conserved for axisymmetry:

$$\delta \boldsymbol{B}(\psi, \theta; n, \omega) = \sum_{m \in \mathbb{Z}} \delta \hat{B}_{n,\omega}(\psi, \theta)\, e^{+im\theta - in\phi}\, e^{-i\omega t} \quad \text{with} \quad n \in \mathbb{Z},\, \omega \in \mathbb{R}^+. \tag{2.39}$$

By applying the operator $\boldsymbol{B} \cdot \nabla$ to the plasma displacement vector $\boldsymbol{\xi}$ for the study of the MHD stability, one finds that perturbations can be made unstable when $q \approx m/n$. At these, so called *rational*, values of q, corresponding to *resonant* surfaces, the helicity of the magnetic perturbation matches that of the equilibrium configuration. As a consequence, any damping from the magnetic shear $s \propto \mathrm{d}q/\mathrm{d}\psi$ is reduced. The presence of such surfaces in the plasma give rise to instabilities caused by pressure and/or current gradients. Examples are Sawteeth (ST) and Neoclassical Tearing Modes (NTMs). These not only affect the fast ions but the plasma as a whole by causing rapid internal redistribution or as an enhancement of the radial transport.

There also exist resonant interactions between fast ions and magnetic fluctuations. Suprathermal ions drive Alfvén Eigenmodes (AEs) unstable [38]. These modes can also be directly driven by external antennas. AEs are MHD modes with dispersion relation of the form:

$$\omega(R) = k_{\parallel}\, v_{\mathrm{A}}(R), \tag{2.40}$$

$$v_{\mathrm{A}} = \frac{B}{\sqrt{\mu_0 \rho_{\mathrm{mass}}}}. \tag{2.41}$$

The Alfvén speed in Equation (2.41) is proportional to the strength B of the equilibrium field that for $\epsilon \ll 1$ can be taken to be $B \simeq B_{\phi}$. A physical perturbation has a finite spatial extent, therefore, according to continuous spectrum in Equation (2.40), there are different phase velocities so that the wave packet is dispersed. Gaps, however, can be opened in this Alfvén continuum due to the coupling of poloidal harmonics. Modes existing in the gap are only weakly damped. A minimum in the safety factor profile is at the origin of the Reversed Shear AEs (RSAEs), characterised by single toroidal and poloidal mode numbers and frequency inversely proportional to the minimum of q. These typically appear in the ramp-up phase of a discharge, when the plasma current profile evolves strongly, as series of modes sweeping in frequency (Alfvén Cascade) resonating on the rational surface of q_{min}. Gaps stem from a coupling of counter-propagating poloidal components in a periodic poloidally depending magnetic field, as evident in Equation (2.31). For instance, Toroidal AEs (TAEs) grow in the gap produced by the coupling of the m and $m+1$ poloidal components of the mode with the same n-number, an example shown in Figure 2.4, with frequency

$$f_{\mathrm{TAE}} = \frac{v_{\mathrm{A}}}{4\pi q R}, \tag{2.42}$$

where the gap width is proportional to the inverse aspect ratio. Kinetic effects and shaping of the plasma play a role in “breaking” the Alfvén continuum, leading to a wide variety of AEs.

However, the presence of a gap is just a necessary condition for the growth of an instability. For a net energy transfer between the energetic particles and the AE it is required that summed over many orbits:

$$\oint \boldsymbol{v}_{\mathrm{d}} \cdot \boldsymbol{E}_{\perp} \neq 0, \tag{2.43}$$

where $\boldsymbol{E}_{\perp}$ is the perturbation and $\boldsymbol{v}_{\mathrm{d}}$ the slow drift velocity experienced by the particle guiding-center. At the frequencies of the AEs, this is the only relevant term as the fast gyromotion averages out. Together with the frequency matching condition

$$\omega + (m+l)\,\omega_{\theta} - n\omega_{\phi} \simeq 0 \quad \forall\, l \in \mathbb{Z}, \tag{2.44}$$

the effective resonant condition on the velocity of a fast ion for a TAE becomes

$$v_{\parallel} = \frac{v_{\mathrm{A}}}{1+2l} \quad \forall\, l \in \mathbb{Z}. \tag{2.45}$$

Energy exchange occurs through a mechanism similar to the inverse Landau damping. While the typical distribution in velocity, e.g. the slowing-down in Equation (2.27) for injected particles, has a negative slope it extracts energy from the wave, the radial profile is usually peaked towards the plasma core so the gradient in the canonical toroidal momentum, p_{ϕ} in Equation (2.19), is positive. The growth rate of the mode may become positive as it is given by

$$\gamma \propto \omega \frac{\partial f_{\mathrm{fast}}}{\partial E} + n \frac{\partial f_{\mathrm{fast}}}{\partial p_{\phi}}, \tag{2.46}$$

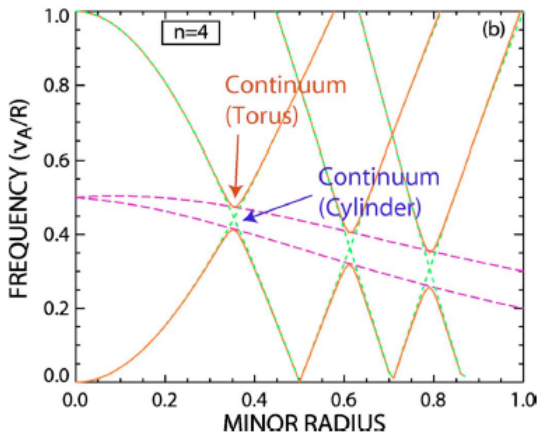

Figure 2.4: The real part of the dispersion relation of the Alfvénic modes as a function of the normalized minor radius, for $n = 4$. The toroidicity effect of coupling the m and the $m+1$ components thus opening a gap (purple dashed), where TAEs may be excited, is shown. Credits: [38]

where $E \propto v^2$ is the energy of the particles. In addition, it should be noted that the radial extension of the AE must, at least in part, coincide with the fast-ion orbits.

Finally, there exist another class of instabilities exists caused by energetic particles. These Energetic Particle Modes (EPMs) are not MHD solutions but result from fast ions in regimes in which their density is not negligible compared to the background plasma. Fast ions determine both the mode frequency, extending also outside the gaps in the Alfvén continuum, and the linear growth rate. Moreover, EPMs exhibit non-linear behaviour with chirping frequencies and bursts typically observed by magnetic diagnostics. A predator-prey model well describes the effects of this instability on the energetic particle population, that moves in phase space thus exciting /damping the waves with subsequent detected bursts/decay of the magnetic fluctuation signals.

In general, such non-linear phenomena may be found in any resonant interaction. Together with AEs and EPMs, another example is the Fishbone instability, named after its outline on magnetic probe signal plots. This is a $m/n = 1/1$ mode that resonates with trapped particles. Across the banana trajectories, ions experience vertical drifts in the poloidal plane and, as a consequence of the twisted field line, a toroidal precession with a frequency

$$\omega_{\mathrm{d},\phi} = \frac{q v_\perp^2}{2\Omega_{\mathrm{i}} r R_0}. \tag{2.47}$$

The instability results from the coupling of the MHD perturbation with the fast-ion toroidal motion that allows a net energy transfer [82, 9, 11] and the following non-linear behaviour. Fishbones have been observed in discharges with perpendicular injection of high energy neutrals [58] where the fast-ion distribution is skewed towards more particles in trapped orbits, although modes with a similar behaviour were found in experiments with tangential injections [42, 41] with a larger passing population that may resonate with a $m/n = 1/1$ mode.

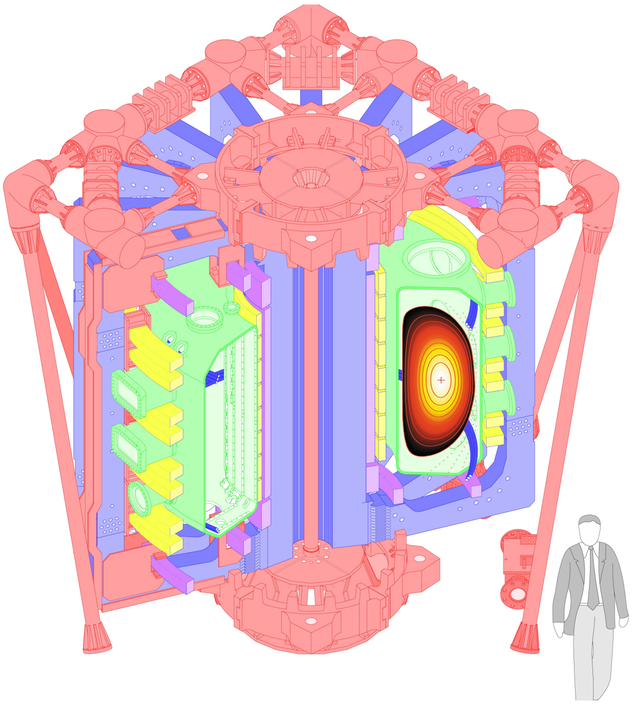

Figure 2.5: Schematic of the TCV Tokamak: the supporting structure and the central column (red), the vacuum vessel (green), the toroidal field coils (blue) and the poloidal field coils (yellow). Credits: SPC

2.4 The TCV facility

The *Tokamak à Configuration Variable* (TCV) [10], in Figure 2.5, is a medium-sized Tokamak located at the Swiss Plasma Center, EPFL, Lausanne. It operates plasma discharges in Hydrogen, Deuterium and Helium. The great variety of shapes that can be produced in the TCV, examples are in Figure 2.6, gives it its name. To accommodate a vast range of plasma shapes the stainless steel vacuum vessel is vertically elongated to 1.4 m with minor radius $a = 0.25$ m and major radius $R_0 = 0.88$ m. TCV houses 16 toroidal field coils that generate field strengths up to ~ 1.5 T and 16 poloidal field coils independently supplied for plasma shaping and positioning, on both the High Field Side (HFS) at $R_0 - a$ and the Low Field Side (LFS) at $R_0 + a$.

The vessel is organized in 16 sectors, 15 of which equipped with three lateral ports on the LFS at different z and other viewports at the top and the bottom. Such ports allow accessing components inside of the Tokamak and housing diagnostics systems and plasma actuators such as NBIs or ECRH launchers.

Together with the radial R_{axis} and the vertical z_{axis} position of the magnetic axis, the flux surface shapes are often described by a local elongation κ and triangularity δ. Their definitions are shown in Figure 2.7. Since the plasma shape is an important factor in MHD stability, the excitation of fluctuations and the particle confinement, TCV represents a valuable asset for the fusion researchers worldwide.

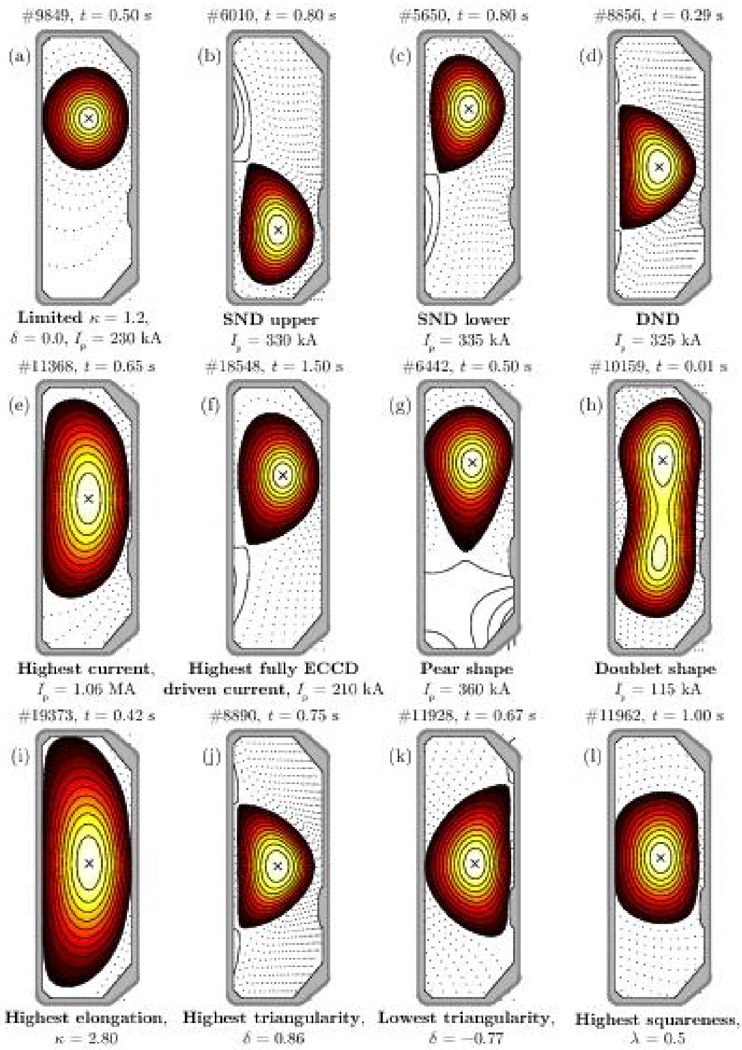

Figure 2.6: Examples of plasma discharge shapes produced in the TCV. From spc.epfl.ch

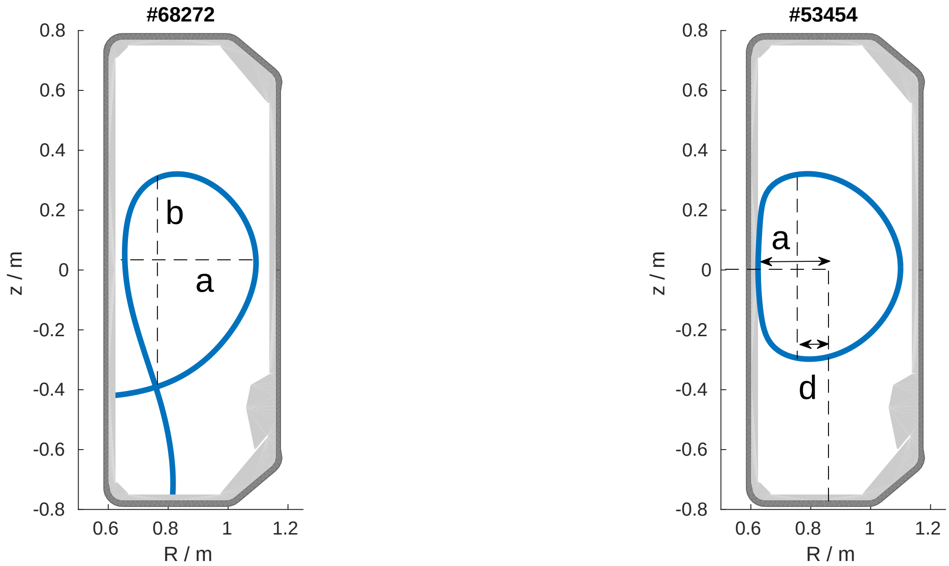

Figure 2.7: (Left) A diverted plasma. The elongation is defined as $\kappa = b/a$, namely ratio between the minor a and major b axes. (Right) A limited plasma. The triangularity is defined as $\delta = d/a$. Credits: SPC

A crucial aspect in any Tokamak is the interaction of the plasma with the vessel walls. A plasma in the TCV can be produced in two configurations : *limited* and *diverted*, see Figure 2.7. In the limited configurations the magnetic field lines outside the LCFS intercept the vessel structure at the limiter, often located at the central column. A diverted configuration features an X-point in the magnetic topology (poloidal magnetic null) which forms flux "legs" at the bottom of the vessel. Intense heat fluxes are here delivered by the particles following magnetic field lines from the separatrix. In larger Tokamaks diverted configurations reduce the plasma dilution by reducing the concentration of high-Z impurities sputtered from the limiter that cool the core plasma and reduce fusion performance. This configuration is affected by the high thermal stress delivered by the plasma to the vessel materials. In TCV the main source of impurity is Carbon because of the graphite tiles employed to cover the metal vessel, see Figure 2.8.

TCV has the ability to set the toroidal field and the plasma current in either direction. In the TCV convention, looking at the machine from above, a positive sign of the toroidal angle increment is in counter-clockwise direction. This is important in the study of the confinement of the fast ions provided by the neutral beam injectors, see Section 2.4.2.

The induced plasma current attains values up to 1 MA. By Joule Effect, the plasma is thus heated to a maximum of ~ 1 keV. Here the resistivity of a fully ionized gas scales with the temperature as $\sim T^{-3/2}$, according to the Spitzer formula. In other words, the hotter the plasma the less collisional, and less resistive, it becomes.

In order to access plasma regimes in which $T_\mathrm{e}/T_\mathrm{i} \sim 1$, additional heating schemes are necessary. Such sources are based on the injection and absorption of electromagnetic waves or neutral particles. TCV is equipped with an Electron Cyclotron Resonance Heating system and two Neutral Beam

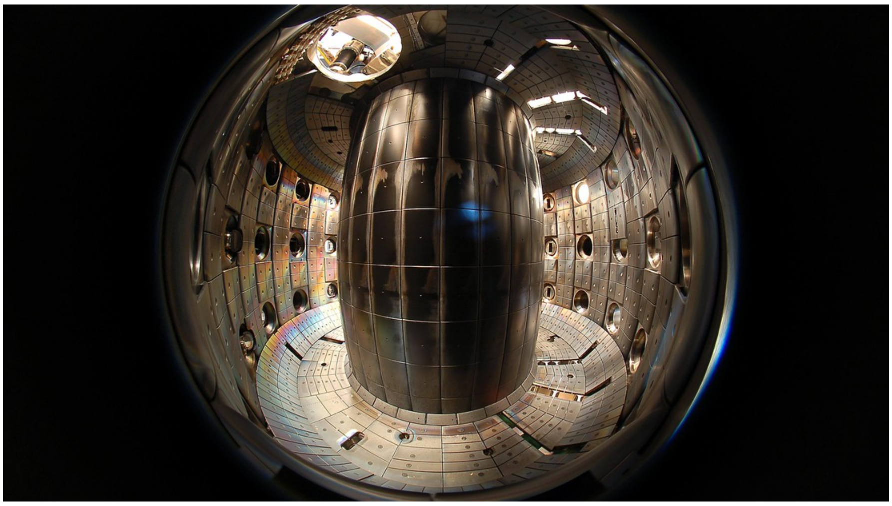

Figure 2.8: Photo of the inside of the TCV. Graphite erosion is clearly visible on the tiles at the central column. Credits: Alain Herzog.

Injectors.

Typical TCV parameters may be found in Table 2.1.

2.4.1 The ECRH system

Electromagnetic waves are used in Tokamaks to provide energy to the plasma. In the Electron Cyclotron Resonance Heating (ECRH) system [1, 2], microwaves heat the electrons at harmonics of the Larmor frequency. With the dependence of Ω_e on the magnetic strength which is, itself, a function of the radial co-ordinate, the ECRH is a tool for extremely localized power delivery to the plasma. This is of great importance for high precision modifications of the plasma pressure and current profiles.

In the TCV, the EM waves are injected polarized in the Extraordinary mode (X-mode) so they may propagate through the plasma from the LFS, where the *launchers* are located: two of them launch in the equatorial plane and two from the vessel top. During the period of this thesis, six Gyrotrons produce EM waves at frequencies of 82.7 GHz that heat at the second harmonic (termed X2) with total power of 750 kW, and three Gyrotrons at 118 GHz (X3) for 450 kW of power.

By steering the launcher, the microwaves are injected with a toroidal component to produce a non-inductive current, a mechanism known as Electron Cyclotron Current Drive (ECCD). This makes it possible to locally tailor the I_p profile and possibly remove instabilities responsible for the degradation of the confinement that can engender plasma disruption.

The injected microwaves can travel if their frequency remains above some cut-off limits that are determined by the plasma density. The largest local density allowed for the X2 is $n_{\mathrm{e,X2,max}} = 4.25 \cdot 10^{19}\ \mathrm{m}^{-3}$ and for the X3 is $n_{\mathrm{e,X3,max}} = 11.5 \cdot 10^{19}\ \mathrm{m}^{-3}$.

Power deposition to the electrons is an efficient way to increase the temperature T_e. As a result, a longer slowing-down time, defined in Equation (2.25), is obtained. This to have a larger suprathermal ion population on the Alfvénic time scales that may excite AEs. Also the ECCD can be employed

Minor radius	$a = 0.25$ m
Major radius	$R_0 = 0.88$ m
Number of toroidal field coils	16
Number of poloidal field coils	16 (+2 internal)
Inverse aspect ratio	$\epsilon = a/R_0 = 0.28$
Maximum magnetic field	$B_0 = 1.54$ T
Maximum plasma current	$I_\mathrm{p} = 1$ MA
Elongation range	$\kappa \in [0, 2.8]$
Triangularity range	$\delta \in [-0.6, +0.9]$
First wall material	graphite R6650 P10
Maximum Ohmic power	$P_\mathrm{OH} = 1.0$ MW
Maximum NBH-1 power	$P_\mathrm{NBH} = 1.3$ MW
Maximum NBH-1 energy for Deuterium	$E_\mathrm{NBH} = 28$ keV
Maximum NBH-2 power (expected in 2021)	$P_\mathrm{NBH} = 1.0$ MW
Maximum NBH-2 energy for Deuterium (expected in 2021)	$E_\mathrm{NBH} = 55$ keV
Maximum DNBI power	$P_\mathrm{DNBI} = 70$ kW
Maximum DNBI energy for Hydrogen	$E_\mathrm{DNBI} = 50$ keV
Maximum ECRH power	$P_\mathrm{ECRH} = 1.45$ MW
Typical pulse duration	2 s
Time between pulses	$12'$
Main species	H, D, He
Electron density	$n_0 \in [1, 20] \times 10^{19}$ m^{-3}
Maximum electron temperature	$T_\mathrm{e} = 15$ keV
Maximum ion temperature	$T_\mathrm{i} = 2.5$ keV
Maximum toroidal rotation	$v_\phi = 200$ km/s

Table 2.1: TCV numbers.

to modify the local q-profile to match the conditions for the excitation of magnetic fluctuations of interest.

2.4.2 Neutral beam injectors

A Neutral Beam Injector (NBI) is a source of energetic neutrals that penetrate the plasma volume until they are ionized and then magnetically confined, or they traverse the plasma (*shine-through*). An NBI can deliver energy and momentum to the plasma for heating and generation of a Neutral Beam Current Drive (NBCD), respectively. Also, it may induce plasma toroidal velocities up to ~ 100 km/s as measured by spectroscopic techniques.

An NBI system comprises different stages: at first an electrical breakdown makes charge separation in a gas of the species to be injected, then the ions are accelerated through a high voltage grid system, also known as Ion Optical System (IOS). The resulting *beamlets* emerging from the grid apertures have spatial divergence that after collimation and traversing the vacuum vessel duct determines the beam size. A stripping gas chamber is located after the IOS, in which the accelerated charged particles are neutralized. Before the beam enters the vacuum vessel, a magnetic field at the end of this chamber acts as a dump deflecting the remaining ions "polluting" the neutral flux. Finally, the neutrals penetrate the plasma where they may be ionized. The ionization processes are due to ion-ion, ion-electron or charge-exchange interactions. The latter, dominant at energies below 50 keV/amu, consist in an exchange of electric charge between the incoming neutral and a plasma ion:

$$A_{\text{beam}} + A^{+}_{\text{neutral}} \quad \rightarrow \quad A^{+}_{\text{beam}} + A_{\text{neutral}}. \tag{2.48}$$

Once ionized, the fast ions, as discussed in Section 2.3, follow passing or trapped orbits depending on the plasma current and the radial position of deposition, that determine the pitch-angle. Those ionized at the very edge of the plasma, mostly in banana orbits, are likely prone to escape the confining field after only a few toroidal turns. These are called beam *early losses*.

TCV currently houses two NB systems: the Neutral Beam Heating (NBH) and the Diagnostic Neutral Beam Injector (DNBI) (Figure 2.9).

The NBH system [48, 80] provides up to 1.3 MW of power by injecting atoms of Deuterium (D), but it is also possible to inject Hydrogen and, in the future, possibly Helium. In order to protect the beam duct, the total energy is presently capped at 1.1 MJ. The maximum particle energy is ≤ 28 keV/amu, determined by the accelerating voltage and, as a consequence, beam optimisation makes this directly related to the neutral power. The presence of molecules at the IOS stage, which are later dissociated in the stripping gas, implies 1/2 and 1/3 energy components in the injected beam of the order of 10% of the total power. The energy-power relation and the molecular components are showed in Figure 2.10.

The beam line is drawn in the equatorial plane ($z = 0$ m) within few millimeters of uncertainty, from a port in sector 9. The beam is elliptically-shaped with 21.6 cm of horizontal width and 9.4 cm vertically.

NBH injection is nearly tangential to the flux surfaces, to maximise beam absorption and provide fast ions mostly in passing orbits. The fast-ion confinement is of the order of, or longer than, the slowing-down time in Equation (2.25), so that their energy is effectively transferred to the bulk plasma. Moreover, beam penetration is optimal to avoid large shine-through power, of non-ionized neutrals eventually sputtering plasma facing materials on the opposing wall. A CNPA diagnostics (Section 2.5.4) is located in front of the beam and monitors the NBH power deposition characteristics.

With TCV's shaping possibilities, on- or off-axis injections are possible by displacing the plasma vertically. This technique is employed to produce fast ions with particular radial distribution required for the excitation of energetic particle-driven instabilities such as AEs, as discussed in Section 2.3.3.

A second NBH system is planned to be installed in 2021, to deliver 1 MW of neutral power with energies up to 60 keV/amu injected in the opposite direction to the present one. A higher neutral energy will make it possible to match the condition of resonance with AEs in TCV, for instance that in Equation (2.45) for the TAEs. Moreover, a system of two NBs makes it possible to reach plasma regimes with external ion heating but zero net torque, that is plasma rotation, for studies on MHD stability.

Limitations to the injection from both NBHs derive from safety concerns on the neutron production. When using such energetic Deuterium beams in Deuterium plasma, the rate of $D(D,n)^3He$ reactions can not be neglected. Several experimental strategies are envisaged to remain below the daily neutron production limit of 4 μSv for biological safety. The neutron emission rate is measured by dedicated diagnostics. If the ion temperature is known, the measured neutron flux is a global monitor of changes in the reaction rate following modifications in the suprathermal ion population that can change on extremely fast time scales and/or be modulated by cyclic plasma activity.

The diagnostics beam (DNBI) is a low power 70 kW actuator providing Hydrogen atoms with energies up to 50 keV/amu. It is used to induce active C^{VI} emission for the CXRS diagnostics (Section 2.5.3) without perturbing the plasma state. The high energy of the neutrals maximises the cross section and the beam penetration. Ions to be accelerated are produced by an arc discharge in order to decrease the molecular content and increase final beam purity. A consequence is that the lower energy fractions are smaller compared to the NBH.

The DNBI is located at the sector 14. Its injection line is in the equatorial plane and features a circular beam cross-section of 12.1 cm. With beam penetration orthogonal to the flux surfaces, the shine-through for the primary energy component can be high. The DNBI is modulated such that beam pulses are produced with periods of several milliseconds.

In the last year of this thesis work, the DNBI was extensively employed for the commissioning of TCV-FILD. The beam purity and the low power, with negligible effects on the plasma state, make this injector a reliable source of fast ions that eased the interpretation of the FILD measurements. Moreover, the radial injection direction produces a suprathermal ion population mainly skewed towards trapped orbits thus allowing the identification of fast-ion losses from unconfined trajectories of different kind.

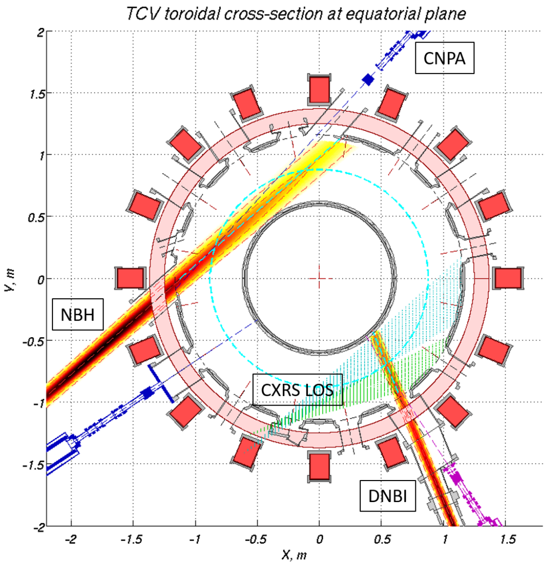

Figure 2.9: Arrangement of the NBH and DNBI and their injection paths in the TCV. Currently the CNPA diagnostics is placed where indicated (top right), but also the previous locations are showed. The CXRS line of sights are plotted (light blue and green). Credits: SPC.

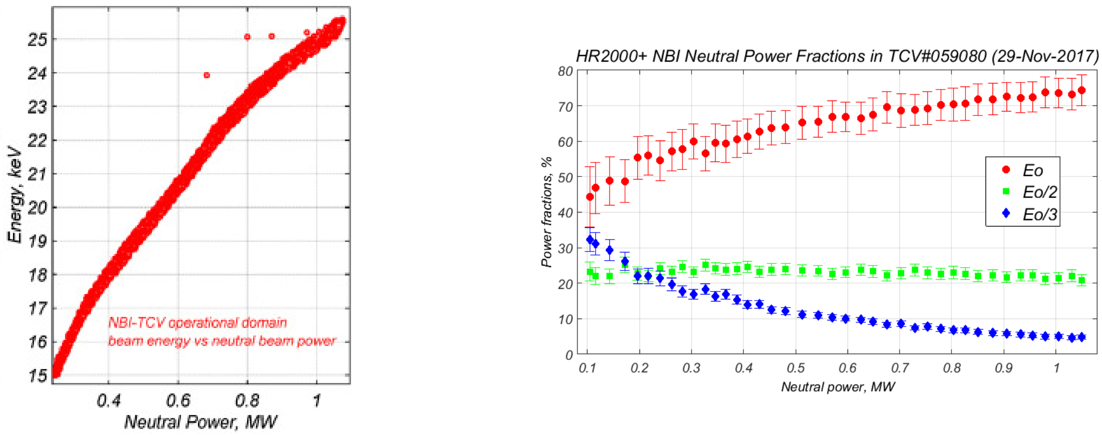

Figure 2.10: (left) The relation between the NBH neutral power and maximum energy of injection. (right) The power fractions of the NBH species components as function of the neutral power. Credits: SPC.

2.5 Available diagnostics on the TCV

The state of the plasma is routinely surveyed during a TCV discharge by a large variety of diagnostic systems. In this section, the mostly relevant ones for the subject of this thesis are presented. Some of them are able to measure global plasma parameters or electromagnetic fluctuations. Other systems are dedicated to the study of fast ions such as the CNPA and the FIDA.

With the contributions of such different diagnostics it could be possible to infer information on the fast ion distribution function by solving the following inversion problem [72]

$$F = W^{-1}M \tag{2.49}$$

where F is the fast ion distribution function (discretized), M the array of measurements and W^{-1} a Moore-Penrose pseudoinverse matrix of weight functions comprising the characteristics of the diagnostic systems. Since F is highly affected by the measurement noise, a method of regularization, such as the Tikhonov method, is employed to solve the problem. This consists in estimating a distribution function $\tilde{F}$ that satisfies

$$\tilde{F} = \mathrm{argmin}_F \left(||WF - M||_2^2 + \lambda^2 ||LF||_2^2 \right) \tag{2.50}$$

where L is a penalty matrix and λ a parameter. These quantities are imposed to the solution as prior-information from, for instance, the non-negativity of the solution, the estimation of the neutral beam deposition and/or numerical predictions of particle orbits. However, it is possible to relax these constraints by combining together the information obtained from the different diagnostics. In particular, the CNPA and the FIDA provide information on a rather large portion of the suprathermal ion phase space though with reduced resolution for the velocity components. FILD, therefore, represents a natural complementing diagnostics by probing a much smaller phase space but with high resolution in time and velocity-space co-ordinates.

2.5.1 Magnetic probes

In order to measure high frequency magnetic perturbations, the TCV is equipped with 203 Mirnov pick-up coils [60] routinely operated at an acquisition sampling frequency of 500 kHz.

The working principle of such detectors relies on the Faraday-Neumann-Lenz equation, with a pick-up voltage given by:

$$V = -\frac{\mathrm{d}}{\mathrm{d}t} \int \delta B_\mathrm{p} \, \mathrm{d}A, \tag{2.51}$$

where the integration domain is the effective area enclosed by coil's wire and the mainly relevant local component of the magnetic field perturbation is the poloidal one, since the toroidal contribution is negligible due to the absence of a radial current at the probe location and the radial component is small for the arrangement of the pick-up coil.

The probes are made from THERMOCOAX© mineral insulated wire wound around a ceramic support. To determine the spatial structure of the magnetic fluctuations, namely the n and the m-numbers in the Equation (2.39), probes are deployed within the vessel in different physical arrangements, attached to supports bolted to the wall and screened by graphite tiles. There are four sets of 38 probes for the poloidal sectors 3, 7, 11 and 15 separated by 90°, and three toroidal arrays at $z = (-230, 0, +230)$ mm of 8 probes on the HFS and 17 probes on the LFS. In the midplane array

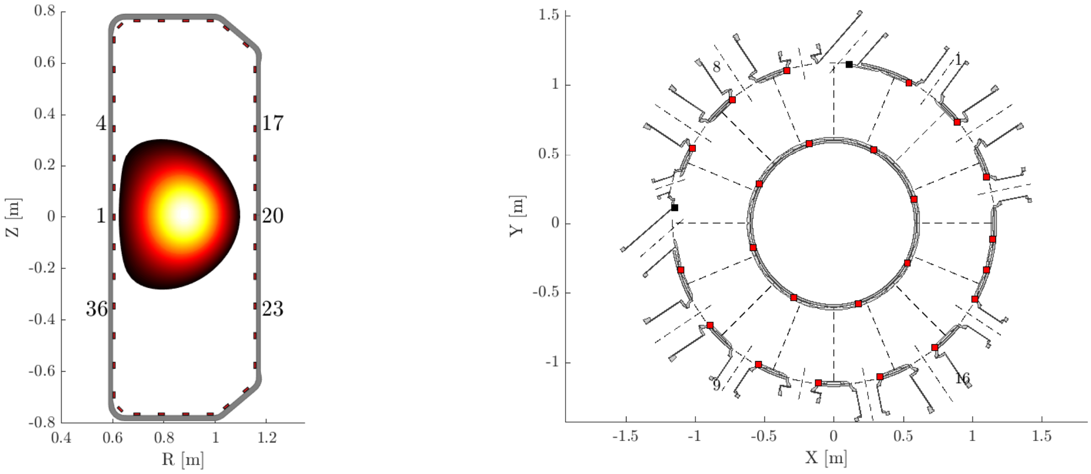

Figure 2.11: Arrangement of the Mirnov probes in the TCV. (left) Poloidal section of the TCV with the positions of the Mirnov probes (red shapes). The probes (36,1,4) on the HFS correspond to the (BOT,MID,TOP) locations respectively. The same applies to the probes (17,20,23) on the LFS. (right) Top view of the TCV sectors with the Mirnov probes (red shapes) on the HFS and the LFS. In the LFS-MID array the two probes (black shapes) are missing because of the presence of the NBH in sectors 4 and 8.

on the LFS two probes were displaced at $z = -115$ mm after the NBH installation. See Figure 2.11. Additionally, a "blind" probe, not comprising the pick-up coil, is used for noise estimation from the electromagnetic fields detected by the in-vessel cabling.

Three LTCC-3D (Low Temperature Co-fired Ceramic) [77] are also mounted within TCV in three sectors at $z = -115$ mm, with a potential bandwidth of 1 MHz for high frequency detection of all three local components of $\mathrm{d}\boldsymbol{B}/\mathrm{d}t$, that were especially useful in plasma discharges exhibiting coherent modes at high frequencies and for monitoring electromagnetic turbulence.

The Mirnov probes are also employed in equilibrium reconstruction together with a set of toroidally arranged Saddle Loops attached to the vessel, where their bandwidth is curtailed by the metallic vessel electromagnetic shielding. Finally, Rogowski coils are employed to measure the local plasma current variation with time.

The acquisition lines of both Mirnov probes and LTCC-3D sensors have been characterized so that an absolute calibration of the measurements is possible. This allows, for instance, a consistent estimation of the phase delay between the acquired signals. This for the identification of the spatial structures of coherent modes, namely the toroidal and the poloidal mode numbers. Moreover, magnetic field variations are measured in T/s, that is required for the accurate numerical modeling of the interaction between energetic particles and MHD modes. The acquisition schematic in Figure 2.12 shows the probe-and-cable in-vessel setup, an input stage filter that filters by a factor of 30 the detrimental high voltages and high frequency components occurring, for instance, during disruptions. This filter is quite well described by a one-zero (100 Hz) together with a one-pole (3.5 kHz) model. The signal is then amplified with programmable gain, and relayed to the adjacent treatment room. After traversing an over-voltage protection stage, the signal is split in two branches: one is directly integrated

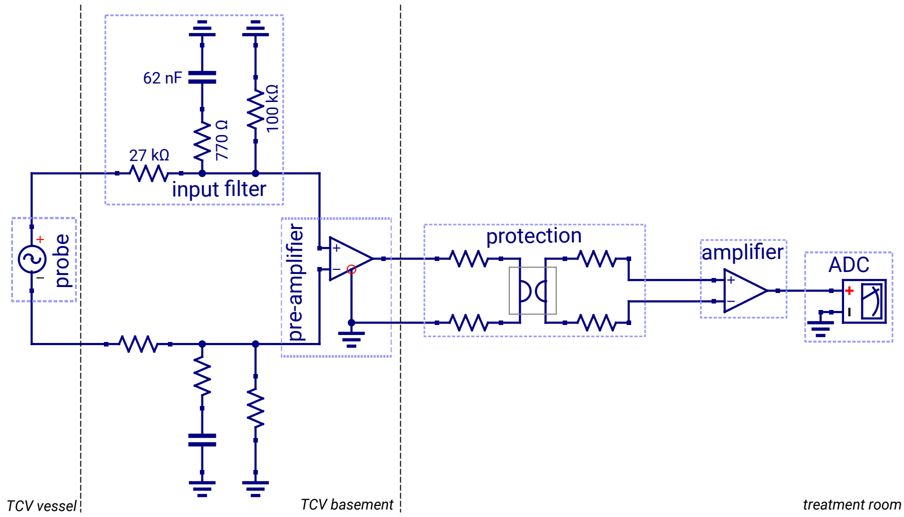

Figure 2.12: Acquisition line for the Mirnov probes.

for equilibrium reconstruction purposes and the other is further amplified and finally acquired.

During this thesis, an end-to-end characterization of this acquisition line has been performed. It is found that the estimated transfer function is better modeled with a second pole around 160 kHz in addition to the input filter stage. This improved the calibration of the Mirnov coil signals in the range of frequencies of magnetic fluctuations on TCV of interest for properly detecting, for instance, Alfvénic modes. An example of the Bode Plots of this result is shown in Figure 2.13 and more details are in Appendix A.

2.5.2 DMPX

The Duplex Multiwire Proportional X-rays counter (DMPX) detects the Soft X-Ray (SXR) emission by the plasma core in the range of energies $1 \div 15$ keV, along 64 vertical lines of sight (LOS) for large coverage of the plasma volume. Variations of such emission can be due to fluctuations of the bulk plasma pressure in case of turbulence or MHD instability, the sawteeth for instance. These are investigated in this thesis by combining the information from the DMPX signals and the FILD measurements. The acquisition runs at 200 kHz thus allowing the identification of electromagnetic perturbations up to 100 kHz.

2.5.3 CXRS

The main impurity element in the TCV is Carbon from the graphite tiles for nearly full wall coverage. Charge-Exchange Radiation Spectroscopy (CXRS) [57] exploits the light emission C^{VI} (529.06 nm) of recombined ions after charge-exchange interactions with neutrals, see Equation (2.48). For TCV's main CXRS system, these are provided by the DNBI. Vertical (poloidal section) and horizontal (toroidal plane) whose lines of sight intercept the beam path, as in Figure 2.9, providing local measurements of the density, temperature and toroidal velocity rotation of the Carbon impurities. On the time scale of the ion-ion collisions, the Carbon temperature can be assumed to be that of the bulk ions, particularly

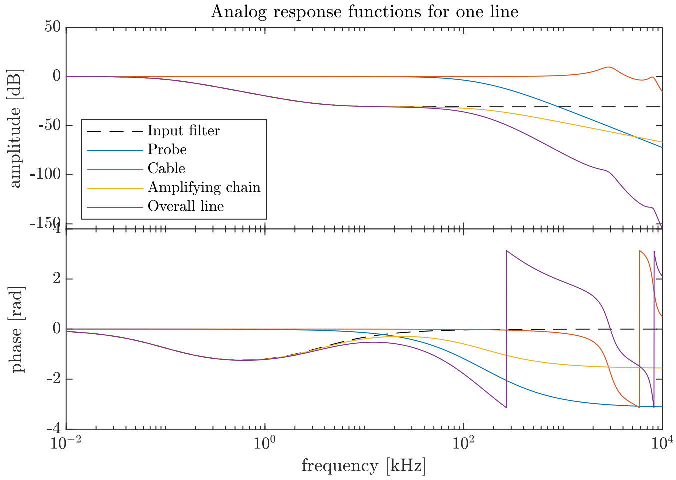

Figure 2.13: Analog response functions of single parts and of the whole line for one Mirnov probe (DBPOL-003-002). Note the wrapping of the phase typically occurring beyond the Nyquist frequency of 250 kHz.

in the plasma core. These information are required, for instance, to accurately compute the NBI ionization profile in codes such ASCOT or TRANSP.

2.5.4 Compact NPA

The Compact Neutral Particle Analyzer (CNPA) [49] measures the energy spectrum of neutral fluxes escaping the plasma, mostly after neutralization by charge-exchange (CX) within the plasma. It is based on a $\boldsymbol{E} \parallel \boldsymbol{B}$ spectrometer, with $B = 1$ T, able to discriminate the energy of ion species with two different q/m values. For Hydrogen the range of energies is $[0.64, 50]$ keV while for Deuterium $[0.56, 33.6]$ keV. To obtain energy dispersion, the neutrals are ionized by passage through a carbon foil 100 Å thick.

The CNPA is mounted on a support to change the Line of Sight (LOS), in the equatorial plane, for each shot. The LOS ranges from radial to quasi-tangential to the flux surfaces. Given its *compact* size, it is placed just outside the vessel. This improves the S/N ratio because the interactions with ambient neutrals outside the plasma volume before reaching the detector are strongly reduced. Also its low etendue (cone angle of acceptance) makes it possible to have precise measurements.

Sources of neutrals in Tokamaks are: cold edge particles, neutral beam injection, the halo surrounding the beam and ions undergoing neutralizing processes. When collecting across the DNBI injection, active CX measurements are possibile.

Upon such an interaction, fast ions are neutralised and are no longer confined. The flux of neutrals as a function of the energy, integrated over a LOS, may be written

$$J(E) = \Omega S \int_{\lambda-\text{range}} \int_{\text{LOS}} n_{\text{a}}(l) n_{\text{i}}(l) \gamma_{\text{att}}(E, l) \langle \sigma_{\text{cx}} v_{\text{ia}} \rangle f_{\text{i}}(E, p, l) \, \text{d}l \, \text{d}\lambda \tag{2.52}$$

where ΩS is the detector étendue (or acceptance), the λ-range is the set of pitch values detectable as

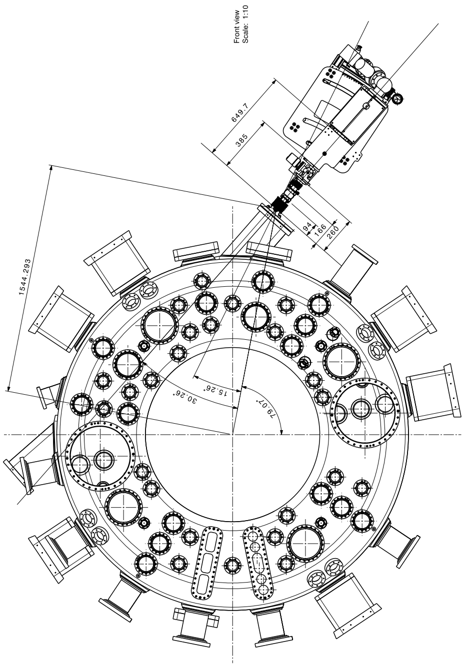

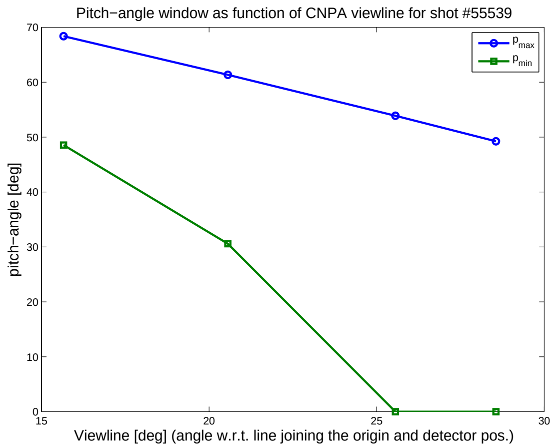

Figure 2.14: (left) The CNPA installed on the TCV. View from above with the north pointing upwards. Credits: SPC. (right) Pitch-angle Λ range as a function of the LOS. The viewline definition is such that the higher angle the more tangential the LOS is.

function of the LOS, see Figure 2.14. The CX rate $\langle\sigma_{\rm cx}v_{\rm ia}\rangle$ depends on the relative velocity $v_{\rm ia}$ between the neutral and the ion. The probability for an atom to not be re-ionized along its further path to the CNPA is

$$\gamma_{\rm att}(E,l)=\exp\left[-\int_{l_0}^{l}\mu(z)\,{\rm d}z\right], \tag{2.53}$$

where the ionization rate is given by

$$\mu(z)=\frac{1}{v_{\rm a}}\left[\langle\sigma_{\rm ei}v_{\rm ea}\rangle\,n_{\rm e}+\langle\sigma_{\rm ii}v_{\rm ia}\rangle\,n_{\rm i}+\langle\sigma_{\rm cx}v_{\rm ia}\rangle\,n_{\rm i}\right] \tag{2.54}$$

By measuring the energy spectrum of such neutrals it is possible to infer the fast-ion distribution at source i.e. within the plasma, as well as the ion temperature $T_{\rm i}$ following NBH deposition. The measured flux of neutrals may be written as

$$J(E)=\frac{N(E)}{\alpha_{\rm det}(E)\tau_{\rm s}\Delta E}, \tag{2.55}$$

where $N(E)$ is the number of the detector counts per energy channel, $\tau_{\rm s}\in[1,2.5]$ ms the sampling time, $\alpha_{\rm det}(E)$ an efficiency parameter that depends on the diaphragm used to avoid saturations, and ΔE the channel resolution. Since the stripping carbon foil has higher efficiency for energetic particles, the energy relative uncertainty is $\Delta E/E\sim 10\%$ for fast ions and $\Delta E/E\sim 70\%$ for thermal ions.

We divide the fast-ion distribution function into a sum of a thermal and a suprathermal component,

$$f_{\rm i}=2\sqrt{\frac{E}{\pi}}T_{\rm i}^{-3/2}{\rm e}^{-\frac{E}{T_{\rm i}}}+f_{\rm fast}. \tag{2.56}$$

By assuming a Maxwellian population for the bulk ions, only one ion species and $\gamma_{\mathrm{att}} = 1$, the CX-spectrum is approximated for $E \gg T_{\mathrm{i}}$ as

$$-\log F_{\mathrm{dc}} = -\log \frac{J(E)}{\sigma_{\mathrm{cx}}(E)E} = \frac{E}{T_{\mathrm{i}}(E)} + \frac{3}{2}\log T_{\mathrm{i}}(E), \tag{2.57}$$

where a simple dependence on the ion temperature is elucidated. The CNPA provides measurements of the fast-ion temperature for two ion species, thus complementing the CXRS measurement of the bulk ion temperature and the rate of change of fast-ion fluxes.

2.5.5 FIDA

The Fast-Ion D-Alpha (FIDA) [28] is a case of CXRS for the D_α radiation, that is the Balmer-Alpha line ($3 \to 2$) emission for Deuterium at $\lambda_0 = 656.1\,\mathrm{nm}$. CX collisions occur between fast ions and neutrals of the background neutral density (passive signal) or donors from a neutral beam injector (active), here from NBH. Since the emitting particle moves in the Tokamak reference frame, the light is Doppler shifted by a change in wavelength of

$$\Delta\lambda = \lambda_0 \frac{\boldsymbol{v}_{\mathrm{n}} \cdot \hat{\boldsymbol{e}}_{\mathrm{LOS}}}{c}, \tag{2.58}$$

with $\boldsymbol{v}_{\mathrm{n}}$ the velocity of the neutralized particle and $\hat{\boldsymbol{e}}_{\mathrm{LOS}}$ the unitary vector along the LOS direction. The FIDA intensity measurements are spatially resolved at the intersection of the LOS and the NB injection line, arranged in the poloidal and in the toroidal planes.

Resolved measurements of energy and pitch-angle are not possible, since the same shift $\Delta\lambda$ may be obtained for different combinations of energy and pitch-angle. Put otherwise, passing and trapped particles can yield similar values of the Doppler shift. Moreover, the CX cross-section depends on energy so that it becomes difficult to account for all the different contributions to the Balmer line. Modelling the underlying process for a given NBH deposition profile is performed with the TRANSP/NUBEAM [63] code with the FIDA emission simulated by the FIDASIM code [40]. Differences between the synthetic spectrum thus obtained and that measured are due to mechanisms beyond the Neoclassical effects such as acceleration by electromagnetic fluctuations and/or turbulence.

2.5.6 ECE

Measurements of fast variations in the Electron Cyclotron Emission (ECE) due to MHD modes or turbulence are possible with radiometry techniques. If the regions in which the plasma can be taken as optically thick, a condition for which the plasma behaves like a black body, the measured frequencies and intensities can be related to the local electron temperature.

TCV's main ECE consists of 24 channels acquired at 200 kHz with antenna LOS orthogonal to the flux surfaces in order to reduce the Doppler broadening due to the energy distribution of the electrons in the emitting volume. In addition, 6 channels acquired at 1.75 MHz are used for the Correlation-ECE [17]. This is a fluctuation diagnostics that, by means of temporal correlation, provides measurements of the temperature variations of $\delta T_{\mathrm{e}}/T_{\mathrm{e}} \sim 1\%$.

As already seen for the ECRH system in Section 2.4.1, the spatial dependence of Ω_{e} allows this diagnostic to probe different radial position within the plasma thus becoming a valuable tool for inferring the internal shape of the MHD modes by cross-correlating the EC signals with those from the magnetics at the wall. This technique is employed in Section 5.2.1 for the case of the magnetic precursor appearing at the Sawtooth crashes.

2.6 Conclusions

The TCV high versatility in producing different plasma scenarios is suitable for studying the impact of plasma shaping on the excitation/suppression of magnetic instabilities interacting with energetic particles. The available heating actuators allows accessing plasma regimes of interest for such investigations. For instance, off-axis injection of energetic neutrals with high $\lambda = v_{\parallel}/v$ by the NBH generates a suprathermal ion population with a radial density distribution that can eventually drive EP-driven fluctuations, e.g. TAEs, unstable. Off-axis injection is easily obtained in TCV by displacing the plasma volume center above the midplane. The ECRH, also, plays an important role in such kinds of discharges. The extremely localized heating, a salient feature of this system, may be used to increase the electron temperature and, in turn, to increase the slowing-down time so as to have a larger fast-ion energy content during the shot. In addition, ECCD techniques are usually exploited to tailor the plasma current profile, important for the MHD stability and/or the excitation of EP-driven modes.

Moreover, NBH and ECRH are usually employed for Sawtooth stabilization and excitation/suppression of NTMs. The impact of these modes on the fast-ion population in TCV was studied during the work for this thesis. In Chapter 5, fast-ion losses as detected by the FILD are shown to be potentially caused by such instabilities.

The DNBI was employed as a reliable source of fast ions, mostly performing trapped orbits, in the FILD commissioning. To characterise the FILD sensitivity to the local magnetic field, the TCV possibility of producing plasmas with both directions of I_{p} was exploited. The results of these studies are reported in Chapter 4.

In fast-ion dedicated experiments, the FILD was complemented by the measurements performed by a large set of diagnostic systems presented in this chapter. Also, the possibility of combining these data to infer, with the help of regularization techniques, the 2D fast-ion distribution function was briefly discussed. In view of this, additional LOS for the FIDA system may be useful. Moreover, the installation in the next future of the Imaging Neutral Particle Analyzer (INPA) would make richer the set of fast-ion dedicated diagnostics in TCV. This novel concept is based on a scintillator, as the FILD case, that “converts” the collected escaping neutrals, then ionized, into photons that are insensitive to the electromagnetic noise in the vicinity of the Tokamak thus ensuring more accurate measurements. Therefore, the FILD development, that will presented in the next chapter, was also an occasion to acquire the know-how for the development of new diagnostics for TCV.

Chapter 3

The FILD diagnostic

3.1 Introduction

The Fast Ion Loss Detector (FILD) is a radially positionable scintillator probe, able to provide information about the velocity components of the collected fast ions exiting the confined plasma region.

The detector is protected by a graphite thermal shield with two *slits* through which particles enter, traverse a collimator and strike a plate where a deposited luminescent material, the *scintillator*, emits light as shown in Figure 3.1. Depending upon the strike position, the velocity-space components can be inferred from the measured light emission in terms of Larmor radius ρ_i and pitch $\lambda = v_\parallel/v$. The 2D distribution function of the lost fast ions can be inferred from the following equations

$$v_\perp(\rho_\mathrm{i}) = \rho_\mathrm{i}\Omega_\mathrm{i}, \tag{3.1}$$

$$v_\parallel(\rho_\mathrm{i}, \lambda) = v_\perp(\rho_\mathrm{i})\left(\frac{\lambda}{\sqrt{1-\lambda^2}}\right). \tag{3.2}$$

Alternatively, the co-ordinates of the velocity space can be expressed in terms of the particle energy and pitch:

$$E(\rho_\mathrm{i}, \lambda) = \frac{m}{2}\Omega_\mathrm{i}^2\rho_\mathrm{i}^2\frac{1}{1-\lambda^2}. \tag{3.3}$$

The FILD reduces the 3D velocity space of the impinging particles into a two-dimensional image by acting as a selector of gyrophases.

In order to perform measurements with high temporal and velocity space resolution, the scintillator's photons are relayed to two acquisition systems: a set of Photo-Multiplier Tubes (PMTs) and a sCMOS camera. Accurate measurements are ensured by the insensitivity of photons to electromagnetic noise, ground loops etc.

The probe is installed in the equatorial port of TCV sector 13, on the low field side, where higher losses are expected, in a toroidal position that minimises the shine-through flux from the NBH. The diagnostic is shown in Figure 3.2. Although observed in high resolution, as only particles reaching this position are collected, the FILD probes aims at a rather small region of the lost fast-ion phase space, populated by either beam-injected first orbit losses or those ejected from the effect of MHD fluctuations.

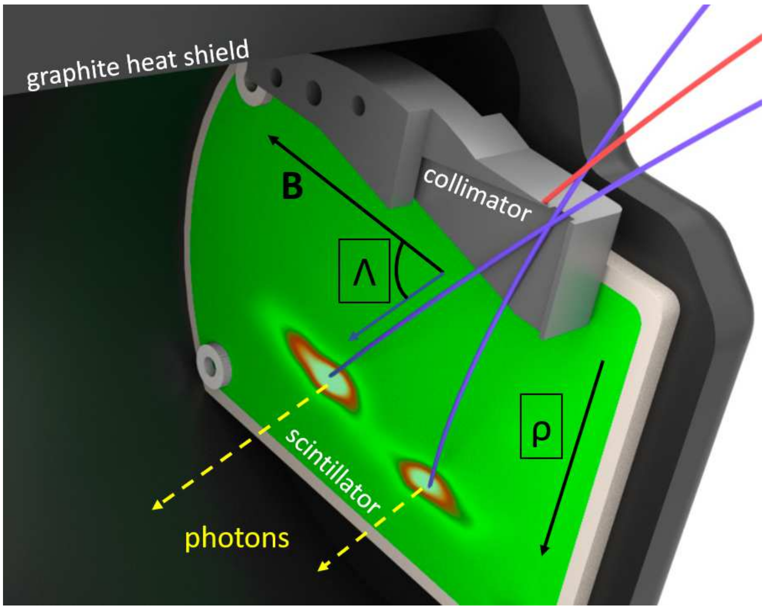

Figure 3.1: Conceptual design of the FILD working principle. Lost fast ions are accepted (blue line) or rejected (red line) by the collimator. The vertical and horizontal co-ordinates in the scintillator plate are respectively proportional to the Larmor radius ρ and the pitch-angle Λ. Modified from [20] with author's permission.

The TCV-FILD apparatus comprises three main elements. The development of each of these necessitated specific scientific and technical domains. The probe head is where the working principle of the loss detection resides. This is determined by the fast-ion trajectories in the vicinity of the vacuum vessel port from which the detector is exposed to the particle flux. The unique design of a double slit makes it possible to detect fast-ion losses in different plasma scenarios with injection of energetic particles in co- or cntr-I_p direction. Moreover, the probe head is equipped with further sensors: two thermocouples for monitoring the temperature, and a Faraday Cup to measure the total current to the target from energetic ions. The probe head components are detailed in Section 3.2, and the code used for simulating the fast-ion orbits inside the probe is presented in Section 3.5. The probe is moved radially by a pneumatic actuator that is controlled by a closed-loop system. This is a novelty for FILD systems on Tokamaks and allows a compact design to reduce the space usage and the ease of installation of the diagnostic. The setup and the tests carried out in vacuum and in a magnetised environment are reported in Section 3.3. The optical setup and the two different systems for the scintillator-emitted photon acquisition are detailed in Section 3.4, together with the solutions adopted for reducing the ambient light and electrical noise. Lastly, the choice of the materials employed in the manufacturing of the probe and the assembly of all components are detailed in Section 3.6 and Section 3.7, respectively.

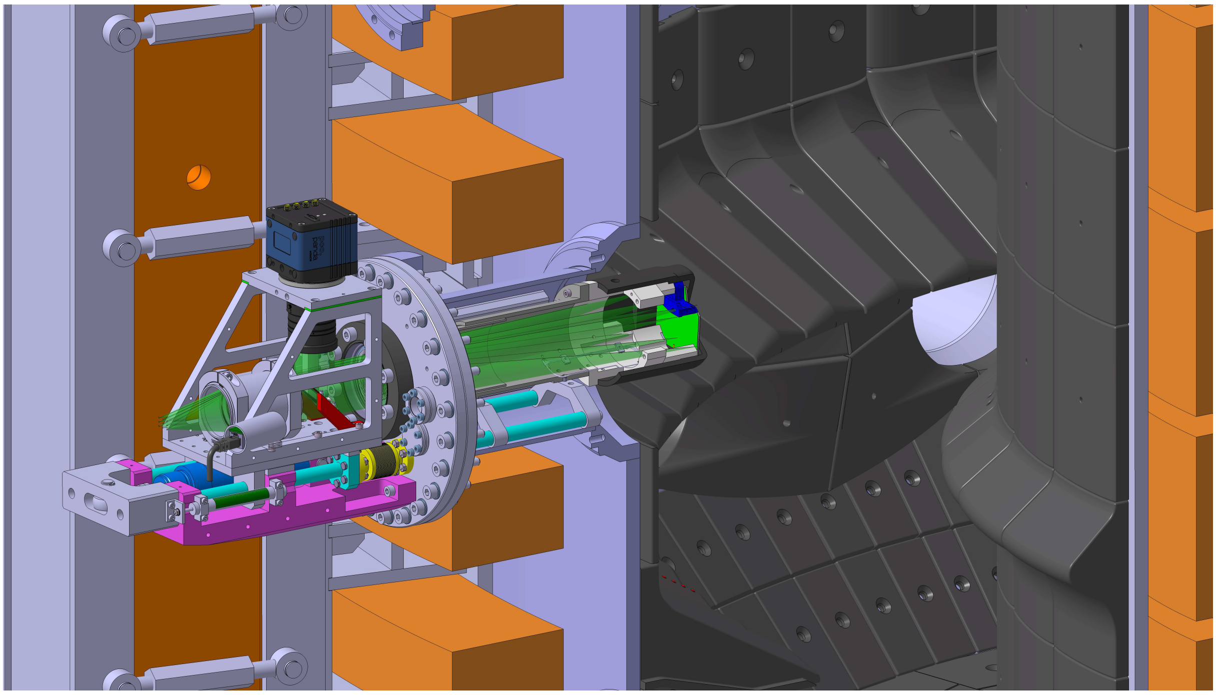

Figure 3.2: The FILD in the equatorial port of sector 13. TCV parts: vacuum vessel (light blue), toroidal and poloidal field coils (orange) and protecting tiles in graphite (black). At the end of the in-vacuum section of the diagnostics, inward of the CF-200 flange (light grey with bolts), there is the probe head: SHAPAL$^{\mathrm{TM}}$supporting components (white), scintillator screen (green), collimator (blue) and graphite heatshield (black). The in-air section comprises the main support (magenta) to accommodate the positioning system: piston (blue), feedback potentiometer (dark green), bellows (yellow) and the two shafts (cyan). The optics: viewport (frame in dark grey), supports of the beamsplitter (red), at the top the PCO Panda 4.2 camera, and on the side a cylinder (light grey) to hold the fiber bundle. The light rays (green) emitted by the scintillator are showed to go through the whole optical arrangement.

3.2 The probe head

The core of the diagnostic comprises a graphite shield (or *heatshield*) enclosing a collimator and a scintillator plate. The trajectories of the collected lost fast ions are selected by the combination of shielding and collimator, depending on their $\rho_{\rm i}$, λ and gyrophase.

At the probe location, for the discharges of interest, the local magnetic field amplitude is typically 1.1 T. This implies, for the nearly tangentially injected particles from the NBH, a maximum Larmor radius of 20 mm and 30 mm, respectively, for the present and the future injectors. TCV-FILD was designed to measure values of the Larmor radius all the way down to those corresponding to the third energy component of the primary beam voltage ($\approx$ 8 keV). The magnitude of the magnetic field doesn't vary substantially over the range of the probe's radial displacement.

To approximately align the slits to the local magnetic field, the probe head is installed with an inclination of 4° with respect to the vertical axis. This is an average estimation corresponding to the plasma scenarios of interest, which typically have $q_{95} \approx 5$.

The probe temperature and integrity are monitored by a set of thermocouples and a Raspberry Pi camera observing the heatshield through a top viewport of the vacuum vessel.

3.2.1 Scintillator

The scintillator is a 68 mm $\times$ 50 mm stainless steel plate coated ($\sim$ 1 μm) with a scintillating material that "converts" the collected fast ions into photons. This ionoluminescence process consists in the de-excitation of the electronic levels of atoms excited by collisions with energetic particles. The coating was deposited at the University of Sevilla. The chosen material for the TCV-FILD is the TG-Green that emits green light at wavelength of 540 nm. This has been adopted in other FILD systems (AUG, MAST) because of its optimal properties [46, 22], namely:

- high levels of saturation,
- decay time of 500 ns thus allowing the detection of photon emission due to losses from interaction with fast MHD activities at frequencies $\leq$ 1 MHz,
- longer life-time under intense ion fluxes compared with other commercial materials (P46, P43 and P56),
- no optical quenching up to temperatures of 700° C,
- insensitivity to neutrons, X- and Gamma rays.

At Deuterium energies below 60 keV (the maximum available on TCV with the second NBH) the yield per unit length of the TG-Green is given by the Birk formula [5]:

$$\frac{dY}{dx} = \frac{\epsilon \frac{dE}{dx}}{1 + k \frac{dE}{dx}}, \tag{3.4}$$

where dE/dx is the stopping power, that is the energy released to the phosphor along the penetration of the "bullet" particle, k measures the quenching of the material, and ϵ is the efficiency per unit of

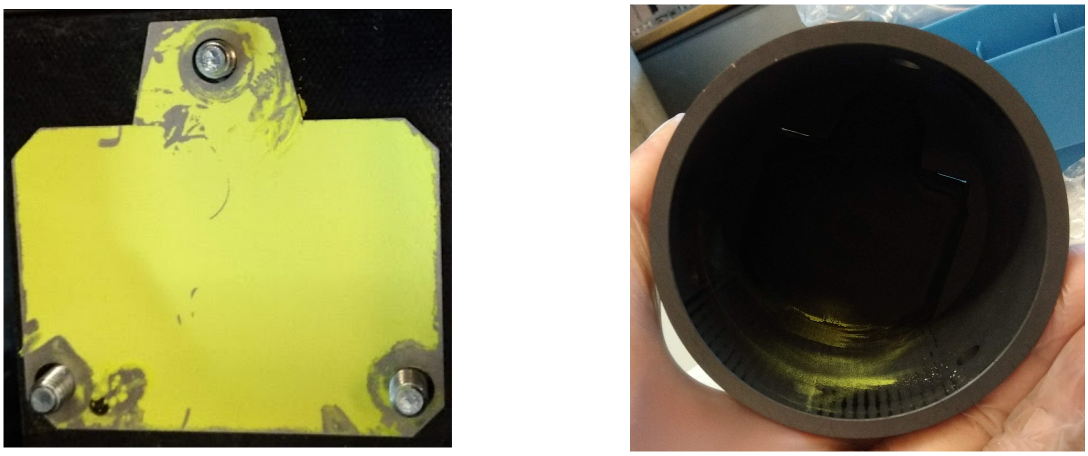

Figure 3.3: (left) The scintillator plate with TG-Green coating. Scratches and losses especially at the edges are evident. (right) Traces of the TG-Green powder inside the heatshield. The picture was taken after the first version of the FILD, installed in October 2019, was uninstalled from the TCV in January 2020.

energy. If the quantity $k\, dE/dx$ is small, the whole energy is assumed to be transferred to the phosphor and the above relation becomes linear. For instance, a 25 keV Deuterium ion gives ≈ 3000 photons.

The scintillator deposited onto the plate proved to be fragile. Some powder was found inside the probe mounting as showed in Figure 3.3. This was probably the result of particularly abrupt radial movements of the detector over several weeks of operation. However, such losses don't reduce the responsiveness of the phosphor. The scratches on the scintillator, that can be seen in the left photo in Figure 3.3, indicate more substantial removals of the phosphor that accidentally occurred during the assembly. Yet, these do not lower the quality of the measurements since the traces generated by the striking particles are wider.

3.2.2 Collimator

The double slit collimator of the TCV-FILD is one of the novelties introduced in the design of the TCV-FILD probe. The slit designed for the present NBH flux of particles is termed "slit 1". These particles are co-I_{p} propagating when $I_{\mathrm{p}} < 0$ (counterclock-wise from above) that is the most usual case on TCV. On the other side of the probe head, "slit 2" collects cntr-I_{p} propagating lost fast ions.

The collimator consists of two trapezoid-shaped slits carved out by electro-erosion in a sheet of stainless steel. This fine machining technique was chosen to guarantee manufacturing precision necessary for such a component directly interacting with the fast-ion gyrating trajectories. The upper part comprises two rectangular apertures (1 mm $\times$ 2 mm) on top, and two, larger, slits (12.6 mm $\times$ 2 mm) on the bottom side. The inner part of the collimator, that selecting the orbits, is showed in Figure 3.4. The top of the collimator is completed by a trapezoid shape that accommodates the fixing screw, on the left in Figure 3.4, and an L-shaped extension that blocks direct light entering through apertures accidentally left when mounting the heatshield, see Figure 3.10.

The design was supported by numerical simulations of the particle trajectories inside the probe head

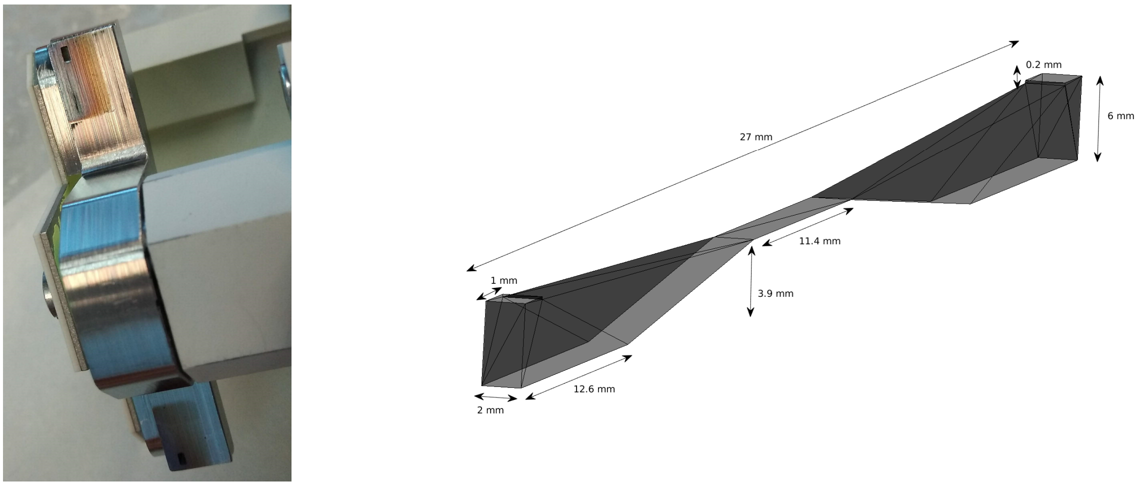

Figure 3.4: (left) Photo of the collimator seen from above and fixed to the ceramic support. The plasma erosion is evident in the rectangles around the slits, the only parts not shielded by the graphite. (right) Triangular mesh of the collimator. The 0.2 mm step of the pinholes is required by the manufacturing precision of the electro-erosion technique. The two sides of the collimator are symmetric.

performed by a dedicated code, called "e-FILDSIM" [20], that models the orbit as helixes with uniformly distributed random gyrophase, see Section 3.5 for more details. From the synthetic spectrum in ρ_{i} (or equivalently energy) and λ of the collimated markers, the instrumental resolution was estimated. The simulations can be run for both slits for ions streaming in opposite directions along the same magnetic field line. Examples of the collimator gyrophase acceptance are shown in Figure 3.5.

Using the simulated orbits, the collimator position with respect to the scintillator plate was determined. The larger their distance the higher the resolution for high energy particles. This distance remains, however, constrained by the size of the heatshield which, in turn, is limited by the exposition of the probe to plasma flux. As a result, the slits are located 16 mm away from the innermost plasma facing side of the shield and 8 mm from the scintillator plate. The vertical distance between the collimator slit plane and the top side of the scintillator rectangle is 6.3 mm.

3.2.3 Heatshield

The heatshield protects the probe head components against impinging plasma flows and tightly encloses it with two rectangular holes allowing the particle flux to reach the two slits. It is a cylinder 100 mm long with radius of 50 mm, manufactured in graphite R6650 P10, the same material used for the TCV tiles [66]. The plasma facing side features a rather complex geometry to accommodate the two apertures, avoid sharp edges and reduce the thermal stresses. The lateral edges are D-shaped to reduce collisions with fast ions with large $v_\perp$ component. Such collisions were simulated by following the orbits backwards from the scintillator plate for one complete gyromotion, an example of which is shown in Figure 3.6.

The heatload this shield has to withstand is mainly due to the bulk plasma convection and the

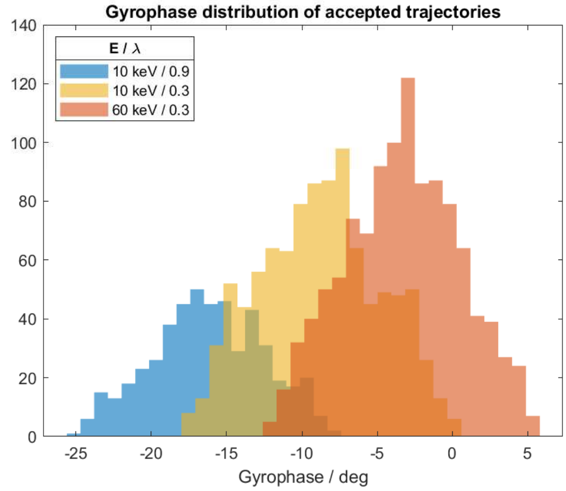

Figure 3.5: Gyrophase distributions for three cases of particle energy and pitch. Evaluated from the simulated orbits striking the scintillator plate.

additional flux of lost fast ions during NBH injection. These contributions were estimated, respectively, with a simplified model of plasma convection and ASCOT [43] simulations of the fast-ion trajectories. Scenarios with NBH and ECRH up to 2 MW of total power were studied, for discharges demonstrating the interaction between fast ions and magnetic fluctuations.

The plasma heat flux deposited on a surface is given by

$$q_{\text{dep}} = q_{\parallel} \sin\alpha + q_{\perp} \cos\alpha, \tag{3.5}$$

where α is the angle between the magnetic field line and the target surface, and the cross-field transport is typically $q_{\perp} \sim 0.02 q_{\parallel}$ [44]. In the discharges of interest, $\alpha \approx 5°$ for the heatshield face towards the plasma core so that the delivered heat flux is of the order of $0.1 q_{\parallel}$. The lateral sides of the graphite shield, instead, are exposed to a heat load $\approx q_{\parallel}$, as shown in Figure 3.7. A simplified and conservative model for the plasma Scrape-Off-Layer (SOL) can be assumed to estimate the parallel heat flux in regions with $R \geq R_{\text{LCFS}}$,

$$q_{\parallel}(0) = \gamma n_{\text{e}} T_{\text{e}} c_{\text{s}}, \tag{3.6}$$

$$q_{\parallel}(r_{\text{u}}) = q_{\parallel}(0)\, e^{-r_{\text{u}}/\lambda_{\text{q}}}, \tag{3.7}$$

where $\gamma \sim 5$ [78], the ion-acoustic speed is $c_{\text{s}} \simeq \sqrt{T_{\text{e}}/m_{\text{i}}}$, the *upstream* radial position is defined as $r_{\text{u}} = R - R_{\text{LCFS}}$, and the scaling factor for the TCV in L-mode is typically $\lambda_{\text{q}} = 20 \div 40$ mm. The L-mode scenario is the case of highest flux as it displays lower confinement. This model, however, overestimates the heat flux by several orders of magnitude at the typical distances between the LCFS and the probe head (≈ 30 mm), since it lacks a "near" SOL description of a rapid decay of power within few millimeters, as seen on TCV by [61]. An empirical estimation of the SOL heat flux decay is provided on TCV by the Reciprocating Langmuir Probe (RPTCV) [78]. In a discharge similar to those of interest, the measured value was $q_{\parallel} \approx 300$ kW/m^2, at the FILD location. Assuming a similar

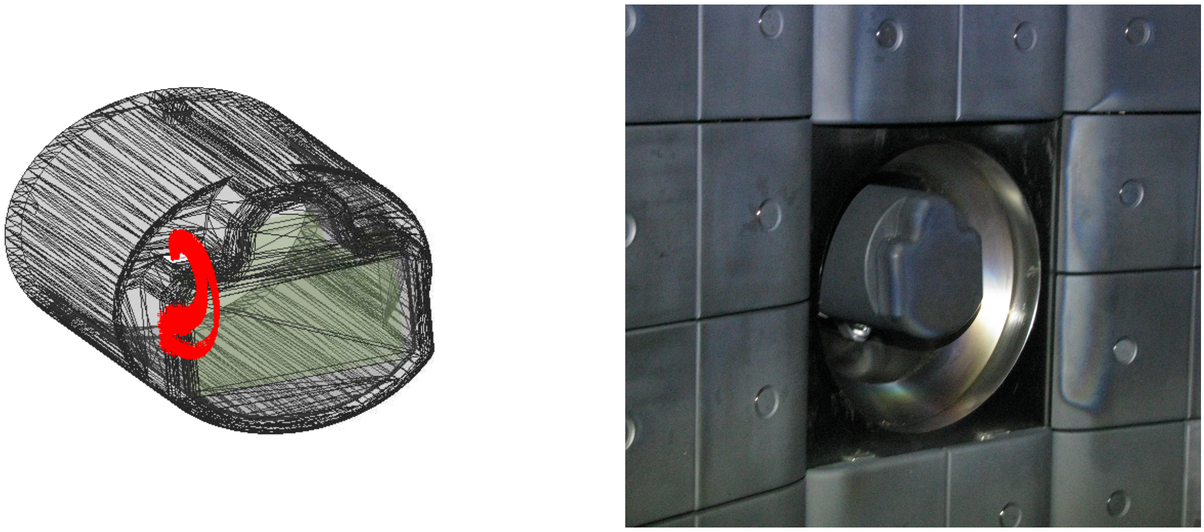

Figure 3.6: (left) Simulation of the particle trajectories backward in time from the slit up to collisions with the heatshield edge. (right) The FILD installed in the TCV midplane port of sector 13, seen from inside the vacuum vessel. Credits: F. Dolizy. (SPC)

decay for discharges with ECRH the heat load on the probe head reaches values of the order of several MW/m^2.

The heat load from fast ions is estimated using ASCOT simulations of the trajectories reaching the heatshield 3D mesh. Each marker represents a bunch of ionized particles with energy E_i. The rate of the beam deposition is measured by the weight quantity w_i. By collecting the markers ending on each single mesh triangle of surface A, the heatload per triangle is

$$\text{heatload} = \frac{1}{A} \sum_{i\,\in\,\text{markers}} E_i \times w_i. \tag{3.8}$$

As can be seen in Figure 3.8, the heatload attains values of the order of several MW/m^2 on the sharp edges facing the fast-ion flux. Given the small size of such parts, the total delivered power is below 100 W. In these shots the FILD was not over exposed due to the small clearance between the wall and the LCFS; a condition that is usual in discharges of interest for fast-ion studies.

3.2.4 Sensors

The probe head is equipped with two thermocouples to measure the temperature on the inside of the heatshield and the rear side of the scintillator plate. The tips of these sensors are kept in thermal contact with the components by mechanical springs.

A thermocouple consists of an electric junction of two materials with different resistivities. A gradient of temperature produces a voltage difference between the tip of the sensor and the cable shielding, an effect termed TIEMF. The FILD employs k-type thermocouples, of the kind extensively

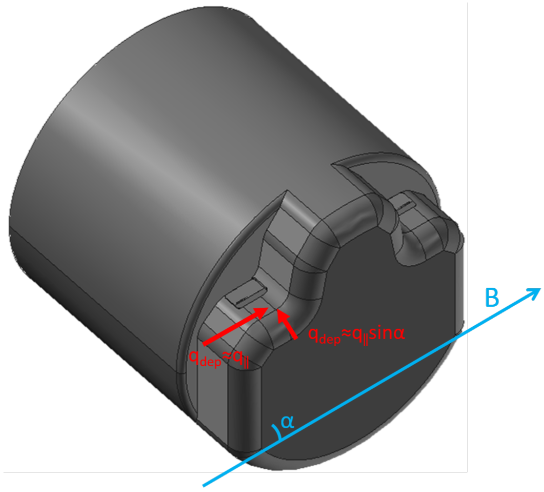

Figure 3.7: Sketch of the graphite shield and the deposited heat fluxes. The angle α is between the magnetic field line (cyan) and the plane of the heatshield innermost face.

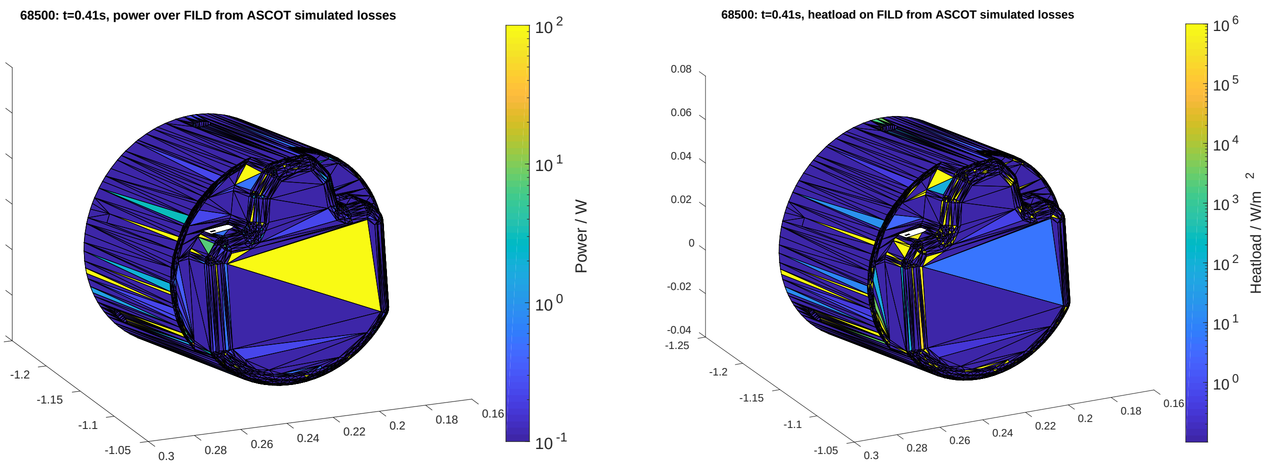

Figure 3.8: ASCOT simulated losses of fast ions injected by NBH (1 MW and maximum energy 28 keV), in shot 68500 at $t = 0.41$ s. (left) Power. (right) Heatload.

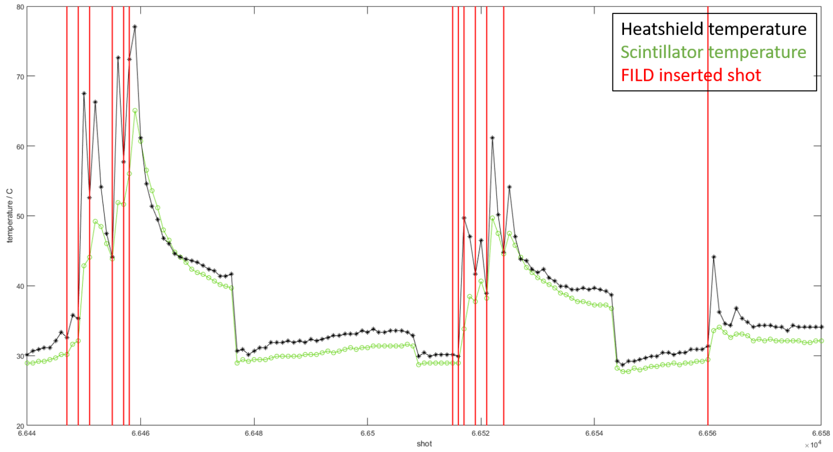

Figure 3.9: The heatshield (black) and scintillator (green) temperatures varying across the shots, in three days of operations. The FILD insertions for measurements are highlighted (red). The sudden drop of temperature corresponds to the night between the last shot and the first one of the following day. When the FILD is left in parking position the temperature is that of the vacuum vessel. It takes around ten shots in parking position to cool down the probe head after being inserted for measurements.

used in the TCV to monitor the graphite tiles protecting the vessel. The k-type consists in a Chromel-Alumel junction suitable to operate at temperatures up to 2000° C with a characteristic response given by the relation

$$\Delta T = \frac{\Delta V}{20\mu\text{V}/^\circ\ \text{C}} \pm 10\ ^\circ\ \text{C}. \tag{3.9}$$

The time resolution of these measurements is of order of seconds, so that this information cannot be used to stop the plasma discharge. Nonetheless, these sensors provide a reliable way to track the temperature as a function of the wall time so as to monitor the integrity of the probe across experiments during the day, see Figure 3.9.

Additionally, a Faraday cup can support the FILD measurements with the absolute flux of the impinging charged particles. This monitors the total ion signal independently of the scintillator luminosity. The sensor comprises the scintillator plate and a back stainless steel plate that are electrically insulated by an interlayer 0.5 mm thick and bushings in ceramics.

Four THERMOCOAX cables are routed from the probe head to the main flange feedthroughs and protected from eventual plasma exposure or parasitic microwaves by a stainless steel shroud. These components are grounded to TCV through the main CF-200 FILD mounting flange.

A close-up view of the sensors arrangement inside the probe head is in Figure 3.10. In Section 3.7 the assembling procedure is presented with further details.

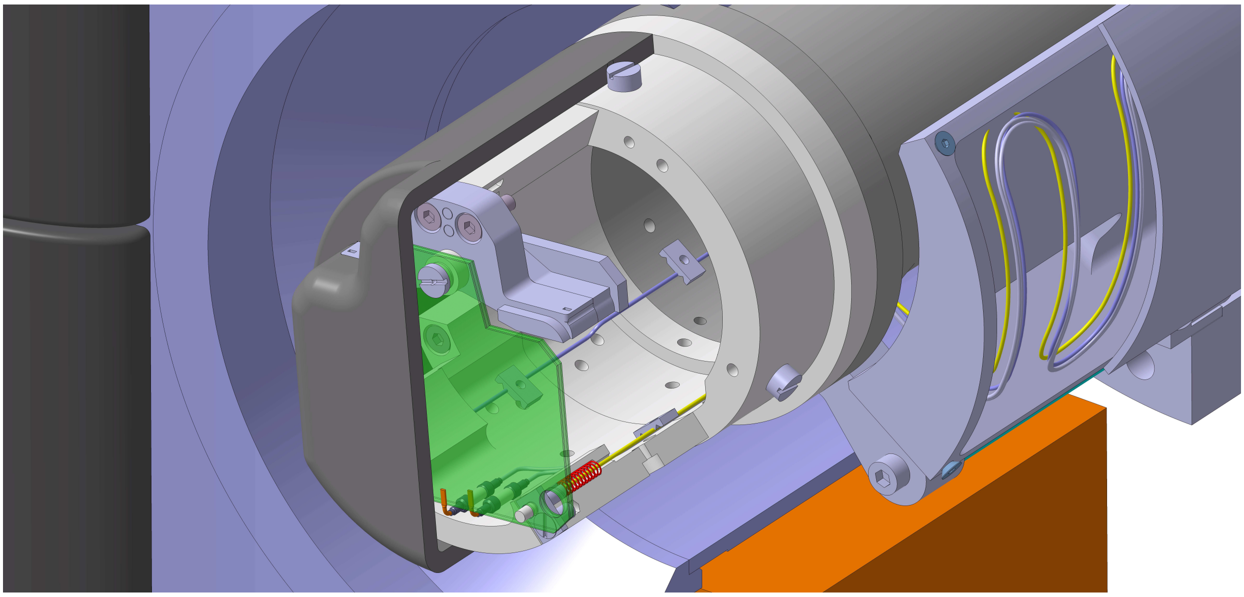

Figure 3.10: Close-up of the FILD probe head. The graphite thermal shield (black) has two lateral apertures (or slits) to accommodate the pinholes of the collimator (light grey). The particular geometry of the latter hampers the direct radiation from the plasma to pollute the signal thus improving the signal to noise ratio. The scintillator plate (green) is made of three parts: the outward stainless steel plate coated with the TG-Green posphorus, a ceramic layer and the inward blank stainless steel plate. Two cables are brazed on the two plates (orange pins at the bottom) which made up the Faraday Cup. Two k-type thermocouples measure the temperature of the scintillator plate (blue wire) and the thermal shield (yellow wire). Springs (red) are employed to keep the thermocouple tips in direct contact with these parts. One of the tips is equipped with a thermal conductive ceramic bushing to ensure electrical insulation. The cables, S-shaped to compensate the axial movement, are routed from the probe head to the feedthroughs in a stainless steel case (light blue).

3.3 Positioning system

When the FILD is idle, it is “parked” in the port duct to avoid exposure to the plasma. The detector can be moved up to 25 mm inward of the first wall by means of a pneumatic positioning system. This kind of system is employed on a FILD diagnostics for the first time in a Tokamak. It made the device more compact and easy to install on the machine.

The probe head is mounted on a cantilever comprising two 500 mm long shafts that transfer the radial motion provided by a pneumatic piston to the probe head. This actuator, manufactured by FESTO, has a diameter of 32 mm and a stroke of 60 mm. The two rods, made from non-magnetic stainless steel hardened by QPQ-process, are guided by a set of four bush rings with graphite rollers to reduce friction.

The in- and out-flow to the piston of the 6 bar-pressurised air, via 2 mm internal diameter pipes, is piloted by an S2 controller from Enfield Technologies. This is a PD controller that regulates the electro-valves depending on the feedback measurements of the piston’s position provided by a potentiometer.

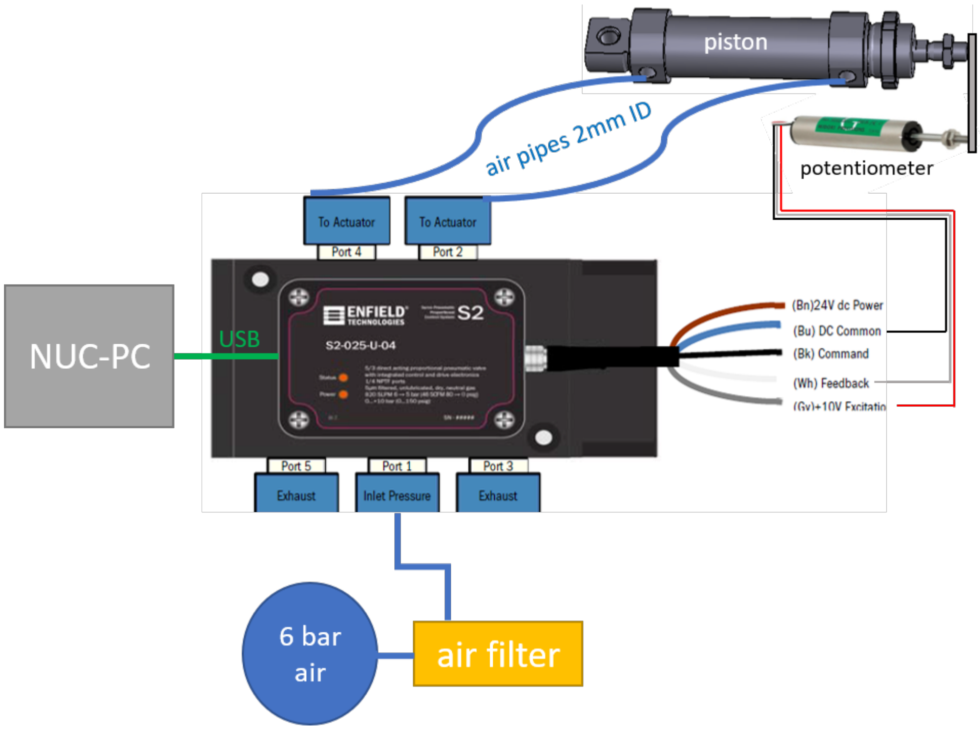

Figure 3.11: Schematics of the controlled pneumatic positioning system. The "command" input (black) is left open since the PD controller is piloted by the PC via USB connection. Also the 24 V supply (red) is provided by the PC itself.

This was provided by Midori Precision and features a linear resistance in the range 20 Ω ÷ 5.8 kΩ, see left plot in Figure 3.12. The S2 comes with a Windows application that runs on an Intel® NUC-PC to remotely control the position. The complete setup is shown in Figure 3.11.

The controller was tested in a static magnetic field provided by the RAID facility [18] at the SPC. By varying the field amplitude up to 600 G, the S2 system was shown to work nominally as shown in the right plot in Figure 3.12. This field strength is typical of that found outside the TCV vessel at the location of the installed FILD position. During a plasma discharge, time-varying magnetic fields are generated that can magnetise the piston rod. Nevertheless, the S2 controller was able to overcome the resultant force keeping the detector at the position set before the magnetic field ramp-up at the start of a TCV discharge cycle.

The mapping between the piston stroke and the potentiometer value was measured before installation. The closed-loop feedback optimisation was performed in the TCV-vacuum after installation of the diagnostic. The optimal values of proportional gain $P = 15\%$, derivative gain $D = 6\%$, impulse offset $= 12\%$, damping factor $= 3\%$, and ramp-up/down velocities $= 80\%$ were determined by parameter scans and acquiring the measurements of the potentiometer performed with a simple setup using Arduino® UNO controller.

The radial accuracy of the system is better than 2 mm, which is of the same order of the uncertainty of the equilibrium reconstruction. The detector is carefully positioned step-by-step to reside not more

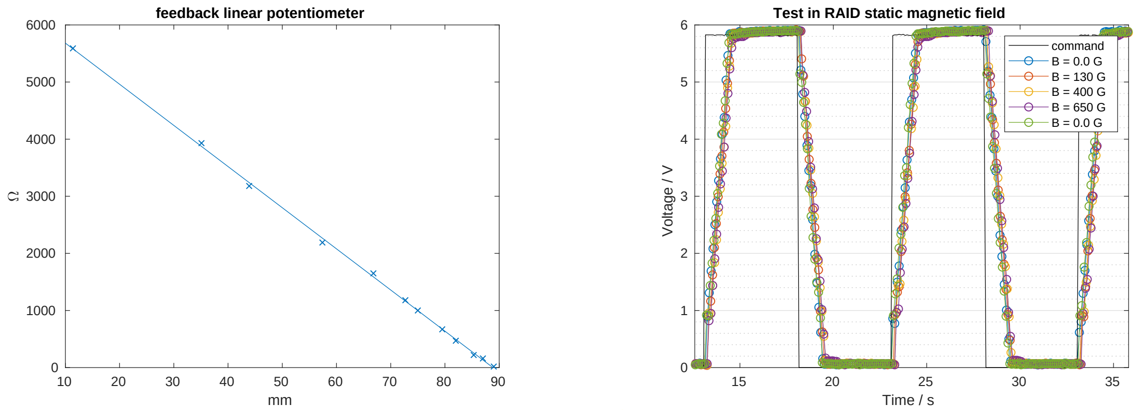

Figure 3.12: (left) Linear response of the potentiometer employed to measure the stroke extension and provide a feedback to the S2 valve controller. (right) Response in time of the positioning system to the *command*, measured in voltage at different values of the static magnetic field provided by the RAID facility.

than the largest Larmor radius away from the LCFS.

By moving inwards and outwards the piston in the TCV vacuum system position reproducibility was measured. This is strongly affected by the strong friction and the asymmetry of the forces in the axial direction, but remained acceptable. See Figure 3.13 for a report of these estimations.

A pneumatic closed-loop system was preferred to an electromagnetic stepper motor coupled to a worm-gear actuator because of the reduced space usage outside the TCV vessel and the system reliability when operating within a magnetised environment. An electromagnetic motor would have required shielding against the magnetic fields and its rather convoluted setup would have been in conflict with the external structures of TCV. Furthermore, a piston is insensitive to radiation and thermal stresses whereas a piezoelectric linear actuator, although a more compact and elegant solution, may have not withstood the bake-out temperature of the TCV vessel.

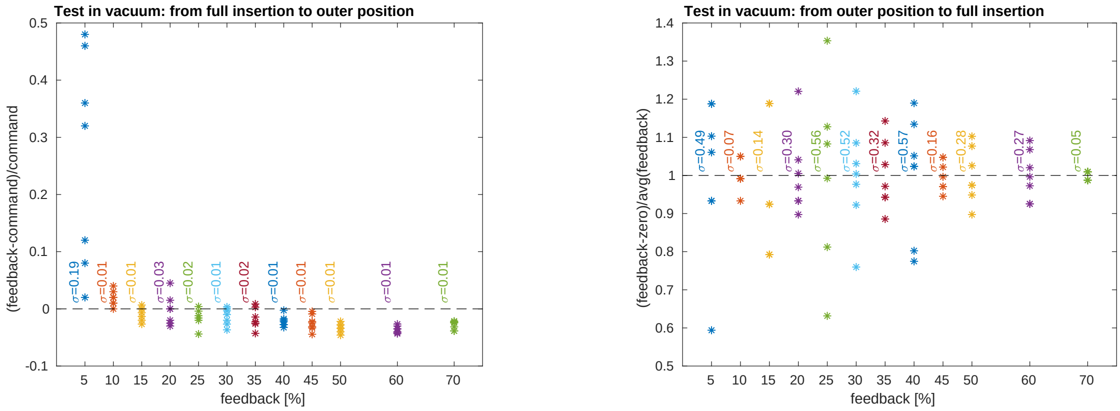

Figure 3.13: In-vacuum test of the positioning system. The sigma estimates the dispersion of the measured positions, i.e. it is a measure of the repeatability. (left) From the full insertion of the detector, that is the zero position of the piston stroke to the outer positions measured in % of the feedback response. On the y-axis the distance from the requested position (*command*) and the reached one normalized to the former. (right) From the outer position of the detector to the full insertion measured in % of the feedback response. On the y-axis the distance from the zero normalized to the average position reached.

3.4 The light detection systems

The photons emitted by the scintillator exit the vacuum-side of the diagnostic through a window, and are relayed by a beamsplitter to two different acquisition systems. Instead of a pierced mirror, a beamsplitter was preferred as, according to numerical simulations, it allows more light to be collected by the fiber bundle for fast detection. The entire optical setup with the dedicated electronics for acquisition and control is showed in Figure 3.14.

The optical components can be either movable together with the detectors during the positioning, thus keeping the optical paths unchanged, or held to the support platform for better stability. This arrangement can be easily changed without reinstalling the FILD from TCV. However, measurements showed no detrimental vibrations of the system in the former configuration, that was retained.

The viewport is a CF-63 (Conflat standard of 63 mm diameter) housing a Sapphire vacuum-tight window from Hositrad Holland. This material features high transmission at green wavelengths and excellent resistance to the vessel bake-out temperature of 250°C.

Velocity-space measurements

Highly resolved measurements in the velocity space are performed with a PCO Panda 4.2 camera. This is a 2048×2048 pixels camera, with pixels 6.5 μm square, by a monochromatic sCMOS sensor. The quantum efficiency is above 70% in the range $400 \div 700$ nm with a peak of 80% at green wavelengths.

The sensitive area exposure is in *rolling-shutter* mode, that is each horizontal line is independently exposed and read out after 12.136 μs of the previous one as showed in Figure 3.15. As a consequence, at full resolution, the first and the last lines are separated by 2048×12.136 $\mu\text{s} = 24.85$ ms. This limits

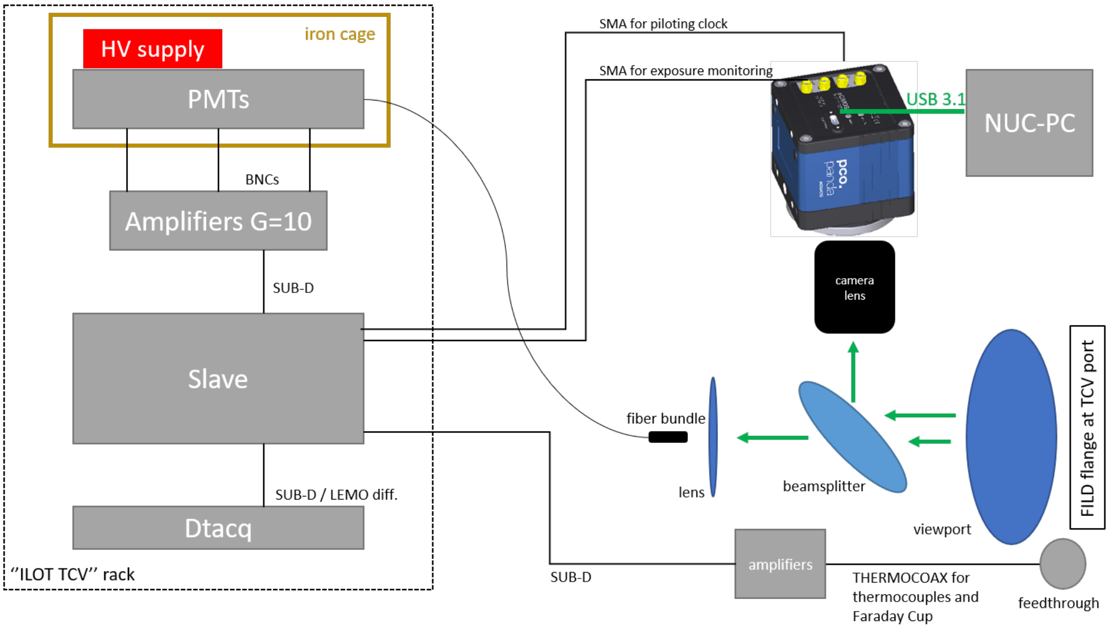

Figure 3.14: The acquisition setup of light detectors (sCMOS camera and fast PMTs) and sensors. The rack is located some meters away from the Tokamak. All the devices are grounded to the vacuum vessel.

the maximum frame-rate to 40 fps. However, by binning along the vertical dimension or reducing the region of interest (ROI), the acquisition rate can be increased.

The exposure and acquisition of each frame is triggered by a TTL square wave (50% duty cycle) with a period of 30 ms, synchronised to the TCV clock, while the camera exposure set to 29 ms to avoid overlapping of the external piloting clock and the camera's internal clock. The PCO Panda provides signals for diagnostic purposes such as the exposure status and the timing of acquisition of the lines. This information was routinely acquired during the experiments for time-base reconstruction. It was found that one frame was missed at the beginning of every acquisition.

A photographic lens with focal length of 75 mm and aperture spanning f/16 to f/1.8, images the scintillator plate onto the sensor. Depending on the fast-ion source, either the NBH or the DNBI, different light intensities are generated therefore the lens aperture was, respectively, reduced or increased.

The camera frames are calibrated by converting each pixel, or for better statistics a group of pixels, into the 2D velocity space components using the strikemap; see Section 3.5 on how this is computed. It is necessary to identify at least two edges of the probe head parts, such as the scintillator plate corners, in one frame. See an example in Figure 3.16. This can be achieved by lighting from outside, thanks to the ease of access the diagnostics, or by inspecting a frame particularly well illuminated during a discharge. Once the reference points are measured in camera pixels, the factor of conversion M between pixels and meters is evaluated as follows

$$M[\mathrm{mm/px}] \simeq \frac{d[\mathrm{mm}]}{d[\mathrm{px}]} \cos\theta, \tag{3.10}$$

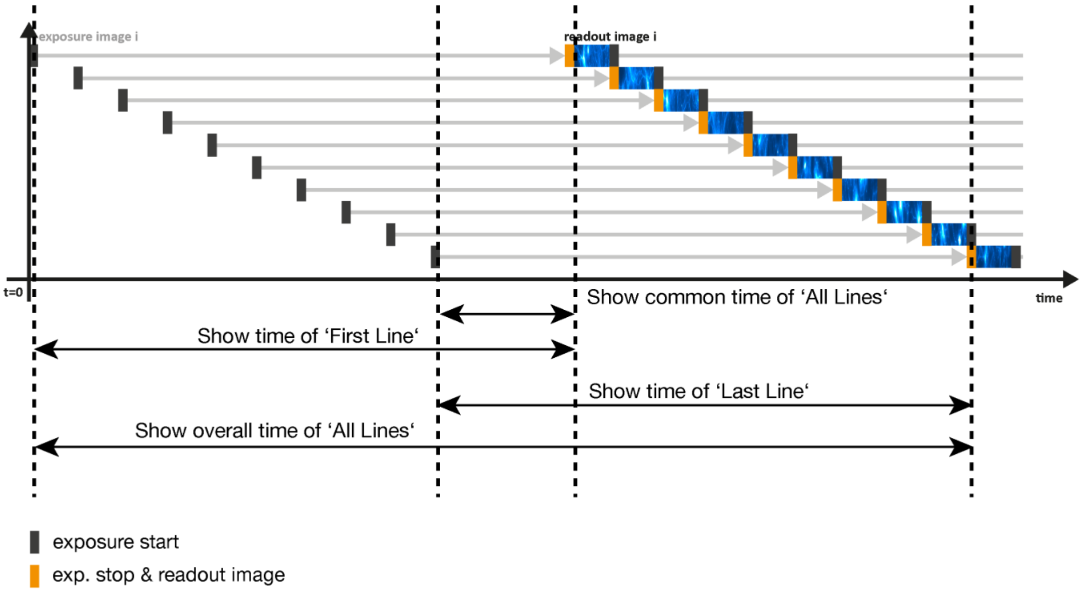

Figure 3.15: The rolling shutter mechanism: each line is independently exposed and read out. Credits: pco.panda user manual® , PCO AG.

where d[mm] is the distance between two points in the real scintillator plate and d[px] the same distance in the camera frame. The formula holds for small values of the angle of inclination of the probe head with respect to the equatorial plane, that for the TCV-FILD is $\theta = 4°$ C.

Pollution by ambient light is reduced by covering the diagnostics with a black cloth. Spurious light reflected by the metallic parts and the beamsplitter before the camera lens resulted in a spurious signal level lower than the emission due to fast ions. The extremely large dynamic range of the camera (16 bit A/D converter) guarantees high system dynamic range. The constant background across the pixels is effectively removed by subtracting a no plasma frame, obtained at the beginning of each discharge, from the other frames. No harmful effects on the camera by the varying in time magnetic fields were found.

The camera is controlled via an Intel®NUC-PC, located close to the diagnostics, and the acquisition launched via MATLAB® routines developed in-house. The data are stored as *.mat* files containing a three-dimensional array with disk usage of $\approx$ 300 MB per shot at full resolution, and continuously backed-up to a remote server.

Fast light detection

The photons emitted by the scintillator go through the beamsplitter and are collected by a lens coupled to a fiber bundle which feeds a set of Photo-Multiplier Tubes (PMTs).

A PMT is an opto-electronic device able to transform light into an enhanced electric signal with a large S/N ratio. When light comes in through an input window, see Figure 3.17, it strikes a photocatode. This emits electrons by external Photoelectric Effect inside the vacuum tube. These electrons

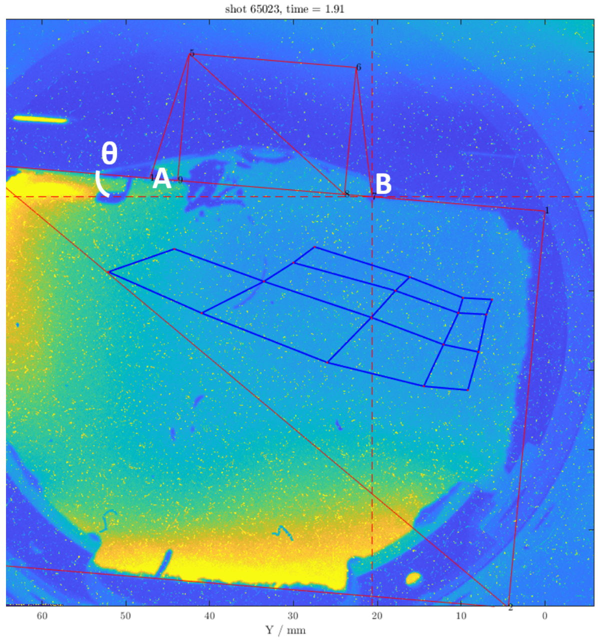

Figure 3.16: Example of acquired frame used to calibrate the strikemap (blue solid lines). The scintillator plate (red solid line) is superposed once the reference points identified on the imaged plate. The corner B is the zero of a local co-ordinate set (red dashed line) and, together with the corner A, is used to evaluate the conversion between pixel and meters. In this case 1 px = 0.0359 mm.

are then accelerated to impinge a chain of dynodes where secondary electron emission occurs so that the number of charges is increased at each stage. A high-voltage supply module coupled to a voltage-divider provides the voltage difference 1 kV between the photocatode, the dynodes and the anode at the end of the tube. Here the resulting current is extracted. This cascade mechanism allows the detection of very weak light signals. The device response is intrinsically linear. The whole process lasts ~ 10 ns, thus making such device apt for highly resolved temporal measurements of photon fluxes.

The output high-impedance current is converted into a low-impedance voltage after the shortest possible path to stave off the additive ambient noise due to the TCV power supplies, in particular those of the NBH. This is performed using amplifiers with gain of 10, decoupled from the rest of the acquisition electronics. Moreover, more robust grounding of all the components to the Tokamak vessel in the “Ilot TCV” rack was implemented using braided copper cables. The improved S/N ratio is showed in Figure 3.19. The signals are finally acquired by a 16-bit A/D card from D-TACQ Solutions at a sampling frequency of 2 MHz for 2.5 s. Such a large bandwidth allows time-correlation studies of the FILD signals with magnetic fluctuations in the Alfvénic range of frequencies. Due to a wrong setup of the A/D card, a delay of 6 μs between the signals from the fast light detection and the LTCC-3D sensors of magnetic fluctuations was found. The FILD signals are, therefore, corrected at a pre-processing stage.

The PMTs need to be shielded against the magnetic field generated by the TCV coil array in the longitudinal direction of the tube to not interfere with the electron path through the tube and, thus,

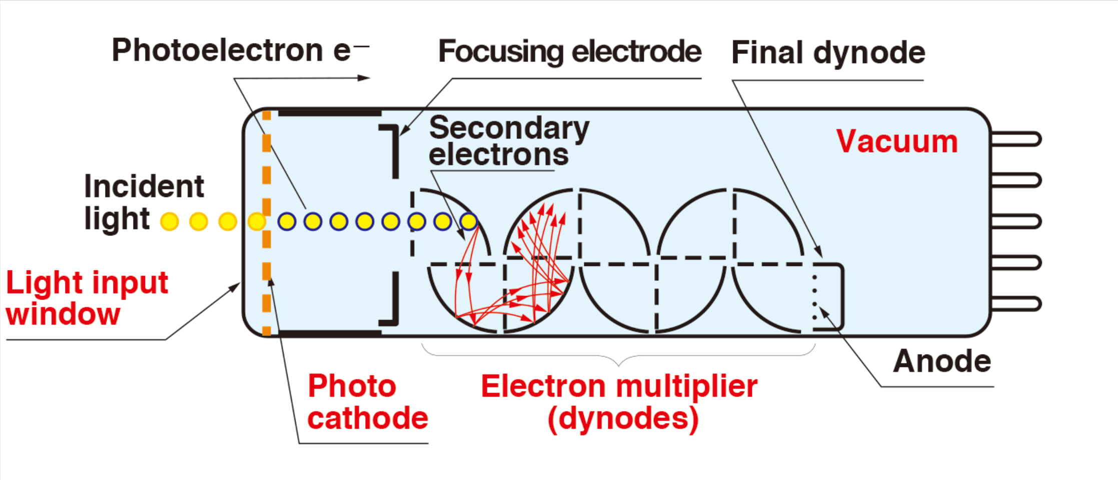

Figure 3.17: Schematic of the working principle of a Photo-Multiplier Tube. Credits: Hamamatsu Photonics.

its gain. This was performed by housing the PMTs inside a cage made of large and thick plates in a steel with magnetic permeability. PMTs are also strongly affected by penetrating X-rays, as reported in Figure 3.18 for the case of TCV experiments on electron runaway. It is clear that the flux of X-rays as measured by several diagnostics including the CNPA (Section 2.5.4) is correlated with the promptly saturated signals from the PMTs during these discharges. Blocks of Lead were inserted between the PMTs and TCV to reduce this effect.

Depending on the fast-ion population that originates the light emission, different values of amplification gain G for the PMTs were set by varying the supplied voltage V, owing to the PMT gain equation

$$G = V^{kn}, \tag{3.11}$$

where $k = 0.8$, a factor depending on the dynode structure, and $n = 10$ is the number of dynodes for the device employed on the FILD, provided by Hamamatsu Photonics. In case of signals from NBH losses, the gains are set to values about ten times lower than for the DNBI losses.

Different arrangements for the fibers were tested to independently cover the most relevant parts of the scintillator thus discriminating between different pitch-angle emissions. However, a unique fiber and one PMT detecting light from the whole scintillator were often employed in the experiments reported in this thesis. Although a simpler setup, it provided valuable measurements of fast-ion losses correlated with high-frequency magnetic fluctuations.

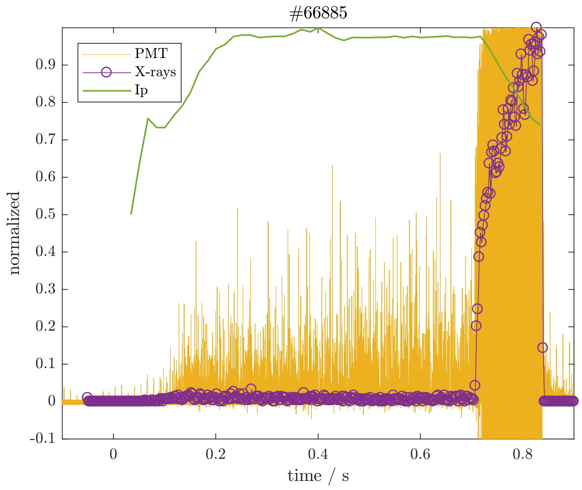

Figure 3.18: Saturation of one of the FILD PMTs following X-ray emission, detected by the CNPA diagnostics. It is also possible to see that during a plasma discharge other sources of electric noise reduce the FILD fast acquisition S/N ratio.

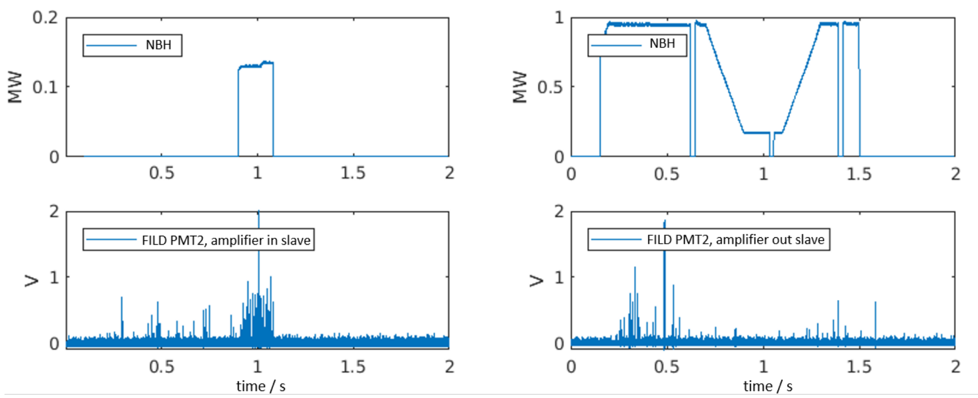

Figure 3.19: Signals of FILD PMT2 before (right) moving out (left) the amplifiers of the slave. In these tests the FILD probe was not exposed to the plasma flux, therefore the showed signals are due to spurious electric or light noise. It is clear that during the NBH power supplies strongly affected the FILD signal before the modification of the electronics.

3.5 Orbit prediction

Simulations of the fast-ion orbits inside the probe head, from the slits up to the scintillator, are performed with the "e-FILDSIM" code [20]. The gyromotion of a particle around the local magnetic field at the slit is modeled as a helix with given Larmor radius, or equivalent energy according to Equation (3.3), and pitch-angle. This approximation holds for the TCV-FILD where the field only varies of the order of 1% inside the probe head. A bunch of independent helixes are simulated for each pair of ρ and λ, with random gyrophases and starting positions at the slit.

The initial flux of helixes at the slit Γ_{slit} $\left[\text{ions}/m^2 s\right]$ is related to the flux reaching the scintillator Γ_{scinti} by the instrument function ω as

$$\Gamma_{\text{scinti}}(\rho,\lambda) = \int_0^{\infty} \mathrm{d}\rho' \int_{-1}^{+1} \mathrm{d}\lambda'\, \omega(\rho,\rho',\lambda,\lambda')\Gamma_{\text{slit}}(\rho',\lambda'). \tag{3.12}$$

The helix is discretized as a set of locally tangential segments and the possible intersection with the triangular mesh of the probe head components computed by means of the Moller-Trumbore algorithm [59], Figure 3.20. The helixes that go through the collimator without being blocked, thus *collimated*, may intersect the scintillator plate mesh. Thus, the strike position is determined. A "centroid" is evaluated as the average position of the striking points of the collimated helixes of same pair of Larmor radius and pitch values. The centroids are the knots of a map, termed *strikemap*, that is employed to transform the scintillator emission into a measurement of the impinging fast-ion 2D velocity space. As already showed in the left picture in Figure 3.6, using a backward trajectory simulation it is possible to assess the potential collisions with the shielding. Those helixes that intercept the probe head structures are, therefore, rejected because such trajectories cannot traverse the slit. Finally, a distribution of the gyrophase range accepted by the collimator is obtained for each pair of energy and pitch, see Figure 3.5. The collimator factor f_{col}, that is the ratio of the number of collimated helixes to the total number, is typically $\approx 10\%$ and is higher for higher energies. An example of strikemap and collimator factor from a simulation is shown in Figure 3.21.

From a mathematical viewpoint, the code initializes the following slit flux of N helixes for each pair of ρ_0 and λ_0:

$$\Gamma_{\text{slit}} = N\,\delta\left(\rho-\rho_0\right)\delta\left(\lambda-\lambda_0\right) \tag{3.13}$$

The analytical form of the ω function is the solution of the Green's problem,

$$\omega(\rho,\rho_0,\lambda,\lambda_0) = \frac{\Gamma_{\text{scinti}}(\rho,\lambda)}{N}, \tag{3.14}$$

where the flux at the scintillator is found by fitting to the results of the simulation a skewed Gaussian model:

$$\omega = \frac{f_{\text{col}}(\rho_0,\lambda_0)}{2\pi\sigma_\rho\sigma_\lambda}\exp\left[-\frac{(\rho-\rho_0)^2}{2\sigma_\rho^2}-\frac{(\lambda-\lambda_0)^2}{2\sigma_\lambda^2}\right]\left(1+\operatorname{erf}\left[\alpha_\rho\frac{(\rho-\rho_0)}{\sqrt{2}\sigma_\rho}\right]\right), \tag{3.15}$$

where $\alpha_\rho(\rho_0,\lambda_0)$ measures the asymmetry towards larger Larmor radii, and $\sigma_\rho(\rho_0,\lambda_0)$ and $\sigma_\lambda(\rho_0,\lambda_0)$ are the standard deviations in Larmor radius and pitch, respectively. In this way, the instrument function of the FILD is determined, as showed in Figure 3.22. The energy distribution shows a long tail at high values. This is consistent with the poor collimator resolution on the nearly-straight

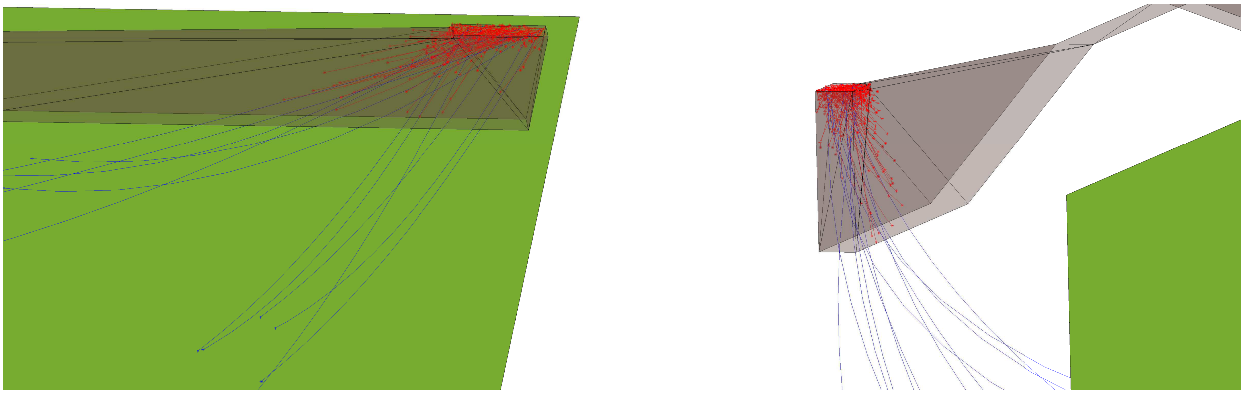

Figure 3.20: Two views of the simulated orbits starting from the collimator slit. Some are accepted (blue) and strike the scintillator (green), others are blocked (red) because colliding with the collimator (grey).

trajectories of high energy particles. On contrast, the pitch distribution is well fitted by a symmetric Gaussian around λ_0.

The weight functions can be used to find the lost fast-ion flux at the slit, starting from the measurements of the scintillator emissions once the transfer function of the optics and the scintillator dependence on the impinging particle energy, see Equation 3.4, are taken into account. Further details are in [20]. In this work, the mapping between the scintillator plane as imaged by the PCO Panda camera and the velocity space of the Γ_{scinti} ions is carried out by means of the strikemap computed for each camera frame. No inversion techniques are employed using the weight functions to retrieve the Γ_{slit}, i.e. the flux of lost fast-ion at the slit.

Details on the implementation of the algorithm are in Appendix B.

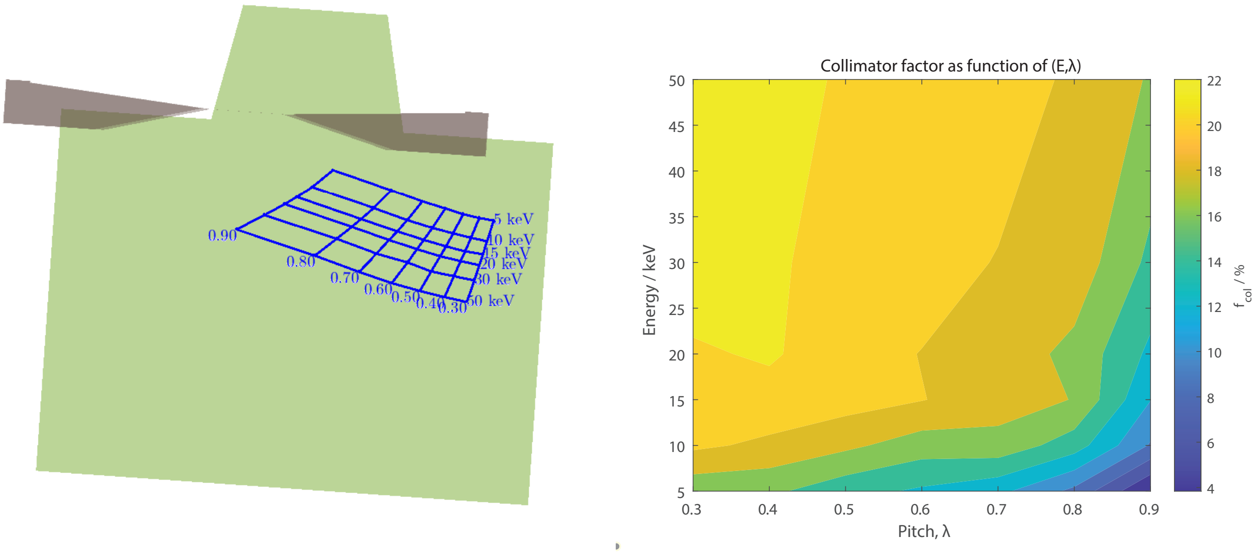

Figure 3.21: (left) A strikemap from simulated orbits for energies in the range $5 \div 50$ keV and pitch in $0.3 \div 0.9$. (right) The collimator factor f_{col} in percent as a function of the energy and pitch of the helixes. It is clear that the higher the energy the more the helixes are accepted by the collimator.

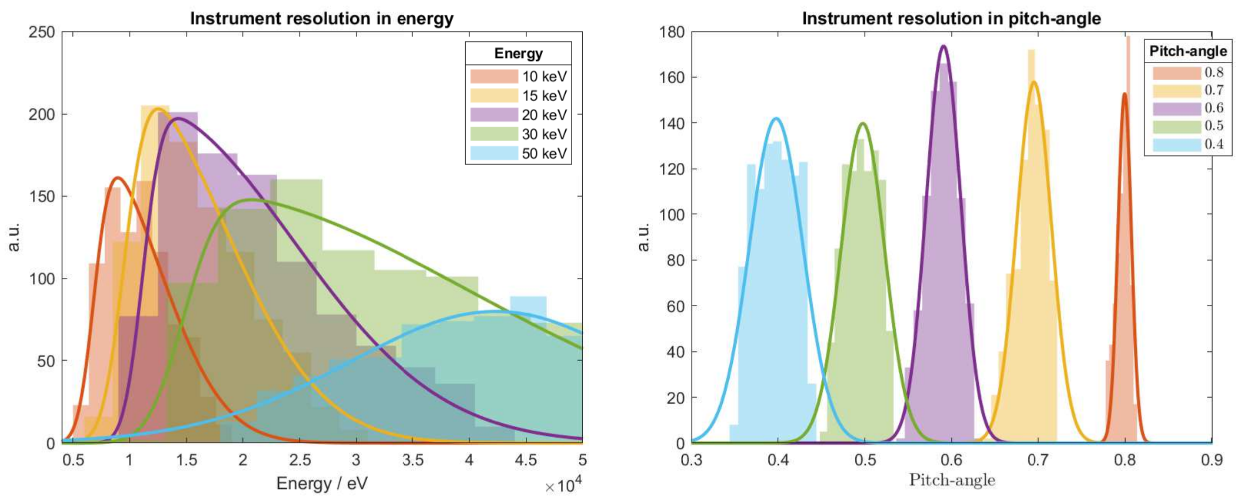

Figure 3.22: Instrument resolutions from simulations of the particle orbits inside the probe head. (left) Resolution in energy for fixed value of pitch $\lambda = 0.7$. (right) Resolution in pitch for fixed value of the energy $E = 10$ keV.

3.6 Materials

Since the FILD is located inside the vacuum vessel where both strong static and time-varying magnetic fields are present, its metallic components are made of non-magnetic materials. This prevents parasitic magnetization and potentially detrimental motion of the diagnostic's movable parts. Therefore, in the vacuum-side, where Aluminium is forbidden, austenitic stainless steels grade EN 1.4435 (AISI 316L) and EN 1.4429 (AISI 316LN), featuring a relative magnetic permeability $\mu_{\rm r} < 1.02$, were used.

On the air-side at the midplane port of sector 13, Aluminium was mostly used to reduce the weight of the device.

Because of potentially intense flows of plasma over the probe head, high electrical currents may be expected to flow along the diagnostic so electrical isolation is required to protect the electronics. Furthemore, some components are fabricated from ceramic materials. The heatshield is mounted on a support made of SHAPAL$^{\rm TM}$(Aluminium Nitride), a highly thermal conductive material ensuring heat dispersion with low electrical conductivity. This material is also used for isolating the thermocouple tip touching the graphite shielding. Other components are made of MACOR® , which features lower heat conduction compare to the Aluminium Nitride but it's cheaper and easier to machine. Finally, Alumina Oxide is the material chosen for the insulating interlayer between the two plates making up the Faraday Cup.

3.7 Assembly

All the in-vacuum metallic parts are cleaned thoroughly in ultrasonic baths of water and soap, then dried overnight in an oven. The graphite heatshield, however, is cleaned in an alcohol solution.

The two translation shafts are first mounted together with the edge-welded CF-16 60 mm long bellows on the CF-200 (Conflat standard with diameter of 200 mm) main flange. Bellows and annealed copper gaskets are employed at the air-vacuum interface. Stoppers are used to avoid detrimental compression or traction of the bellows during the FILD positioning.

The support platform and the piston are then fixed to the flange, see Figure 3.23. The two shafts are kept together at the outermost ending by a rectangular block. This is connected to the piston rod with a ball joint to relax the constraints in the direction orthogonal to the piston stroke.

Once the viewport and the feedthroughs are mounted, proper sealing of these air-vacuum interfaces is verified. The tests are conducted in an ad-hoc box in which a TCV-like vacuum is produced, by applying a flow of Helium in region around the interfaces, as showed in Figure 3.24, and measuring the rate of change of He pressure inside the test box.

The in-vacuum side components are assembled. The support cylinder is fixed to the flange, while a sliding cylinder enclosing the former is held by two D-shaped supports mounted on the shafts. At the innermost ending of this tube, three SHAPAL$^{\rm TM}$ parts are screwed gently, because of the fragility of this material. Owing to required tolerances ≈ 0.1 mm, pins are employed to correctly place the parts and to compensate for the misalignments following tightening of the assembly screws.

The THERMOCOAX cables for the thermocouples and the Faraday Cup are routed from the probe head to the feedthroughs at the flange. These are kept attached to the SHAPAL$^{\rm TM}$ parts by small holders and exit the probe head through an aperture in the moving tube, bent in S-shapes to compensate for the radial movement, and protected by a stainless steel case next to the support

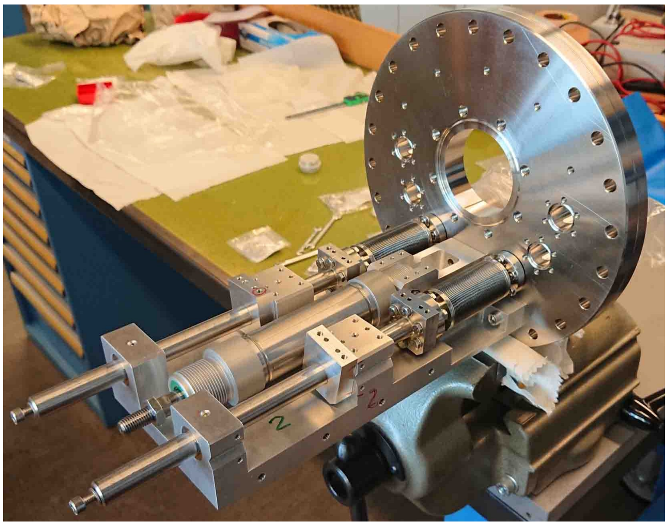

Figure 3.23: The bottom platform fixed to the main flange is the support for the two shafts and bellows and the piston placed in the middle.

cylinder. See Figure 3.25.

The probe head components are installed in multiple steps. First, the collimator and the scintillator plate are mounted on the ceramic supports. The graphite heatshield is inserted to verify whether the tolerances allow such insertion in a safe manner. Once the ability to fully tighten the screws of the heatshield is confirmed, this is again removed. The scintillator plate is unmounted for brazing of the Faraday Cup endings as showed in the left photo in Figure 3.26. These are at the bottom side of the scintillator plate and of the rear plate not coated. For the purposes of electric insulation, the plates are kept together at the top and at the bottom through screws and bushings in isolating MACOR®. In mounting these parts, the tips of the two thermocouples have to be correctly placed and insulated with SHAPAL^{TM} covers.

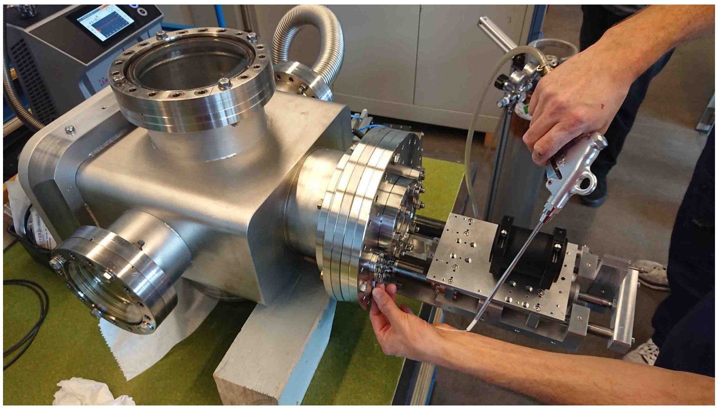

Figure 3.24: The vacuum-test carried out by Mr. S. Barberis (SPC).

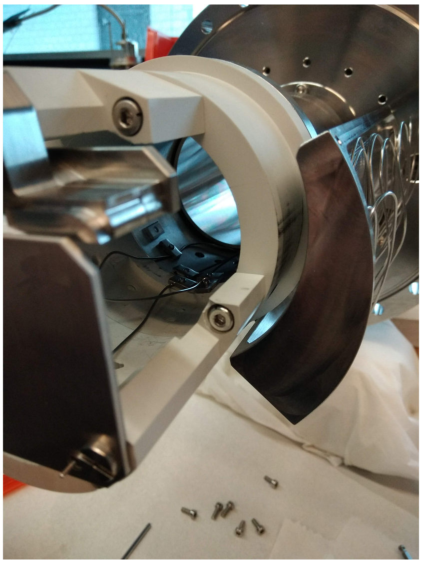

Figure 3.25: The THERMOCOAX cables are routed from the probe head to the feedthroughs on the right (point of view of the photo) inside the lateral case. In the picture the cover is missing. Such cables are clung on the ceramics parts by small rectangular holders screwed from the bottom.

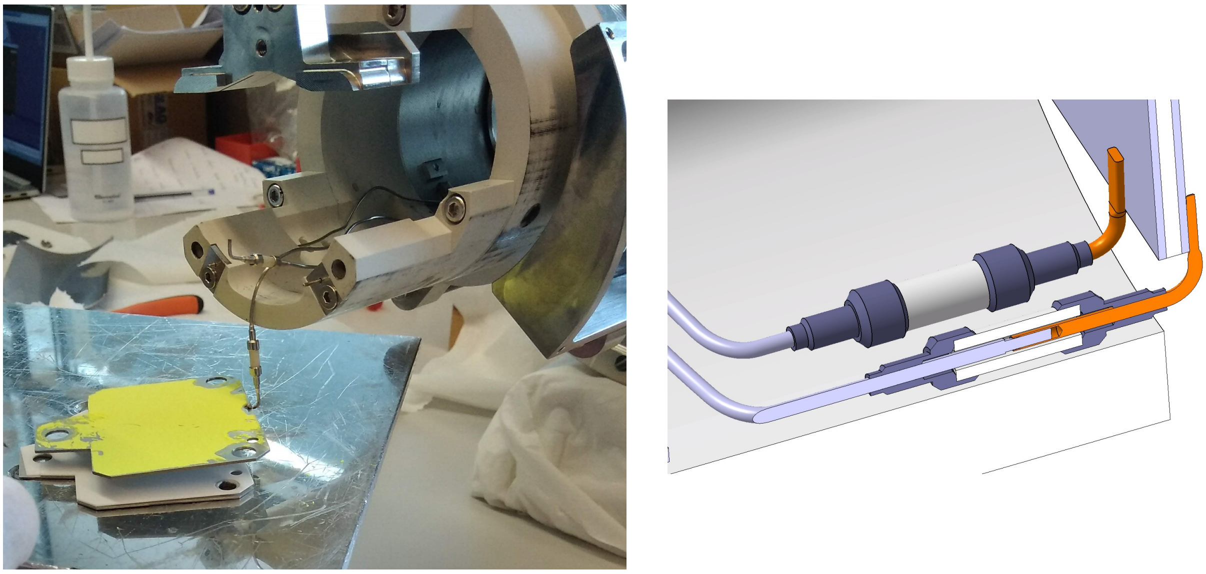

Figure 3.26: (left) The Faraday Cup is made by brazing the THERMOCOAX cable ending to the bottom side of the scintillator plate and the blank reference plate. In between an Alumina Oxide plate is placed to isolate the two sides of the sensor. This operation was conducted once the cables were routed. (right) Detail of the interface between the THERMOCOAX cable shield (grey) and the core (orange). This guarantees the vacuum-tight condition when removing the shield to perform the brazing of the cable endings onto the plates for making the Faraday Cup.

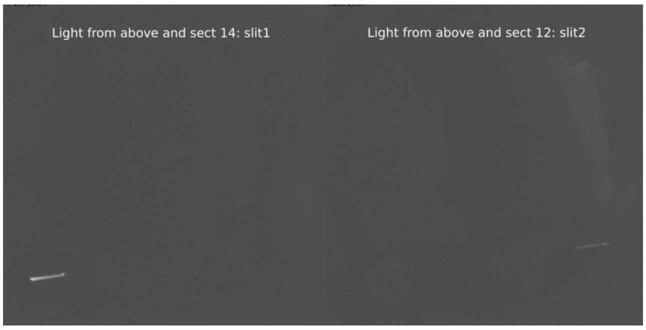

Figure 3.27: (left) The heatshield is carefully inserted by Mr. O. Bartolomeoli (SPC) as last stage of the assembling process. (right) Pictures taken with the PCO Panda camera while a pocket lamp is used inside the TCV vacuum vessel to shed light at different angles onto the FILD heatshield. The misalignment of the heatshield and the collimator caused light to traverse the probe head and appearing as a bright segment. Note that the pictures are upside down, whereas the *above* in the description means the actual orientation of the probe head, that is the bottom of the photo.

The heatshield is eventually inserted and re-attached, as in the photo on the left in Figure 3.27. The unavoidable misalignment between the holes of the heatshield and the collimator leaves some apertures where direct light from the plasma may enter during the discharge. Apart from the collimator pinholes for the fast ions, no other apertures should be present to avoid extraneous light saturating the sensitive fast light acquisition. These sources of spurious light are removed by inserting an L-shaped piece to the collimator. Indeed, no other light transmitting apertures were found once the diagnostic was installed in the TCV port, as showed on the right in Figure 3.27.

3.8 Conclusions

The TCV-FILD design was presented along with the choice of the materials and the assembly of the components. The design of the components was supported by numerical simulations of the fast-ion trajectories in the vicinity of the probe by the e-FILDSIM code. This is used for interpreting the sCMOS camera acquisitions of the scintillator emissions, caused by the impinging fast ions, by means of a strikemap (see Section 3.5) that converts the scintillator plane co-ordinates into the fast-ion velocity space in terms of Larmor radius and pitch-angle. With the help of this tool, the instrument resolution, the detector sensitivity to the local magnetic field and the conditions for the two slits to collect lost particles are investigated in Chapter 4.

The pneumatic positioning system adopted to deploy the probe in vessel, for performing measurements at different radial locations, was described in Section 3.3. This proved to be reliable in safely achieving the required position with sufficient accuracy. Therefore, TCV-FILD may be a prototype for investigating the possibility of installing similar actuators in other FILDs for future installations in Tokamaks where electric motors could be unfit due to the time-varying magnetic fields generated in plasma discharges.

The thermocouples installed inside the probe head can be used to monitor the thermal stresses on the graphite shield. Also the sCMOS camera for the scintillator emission detection and an additional 90 Hz Raspberry Pi camera looking at the heatshield from a top vessel viewport are employed for this purpose. This is detailed in Chapter 4 where full-power NBH injection is shown to be the dominant source of intense heat loads.

The scintillator-emitted light is detected by a set of PMTs for fast light detection. These, with bandwidth of 1 MHz, allow studying the fast-ion losses in correlation with high-frequency magnetic fluctuations. A setup comprising only one PMT to detect the photons from the entire scintillator plate was extensively exploited in the discharges analysed in this thesis work, and presented in Chapter 5. Such kind of experiments will benefit from a partition of the scintillator into regions of emission independently acquired, to measure losses of fast ions with different energy and pitch-angle values correlated in time with high-frequency magnetic fluctuations. Furthermore, the fast light detection system was found to be largely affected by ambient noise, mainly due to spurious X-rays emitted during plasma discharges, magnetic fields produced by the TCV coils and the pick-up of electric power supplies, in particular those of the NBH. To achieve a S/N ratio low enough to guarantee the identification of ejections of fast ions due to a wide variety of plasma instabilities, great effort was devoted to the setup of the acquisition electronics and the shielding of the PMTs. A further improvement of the signal would be obtained by moving the entire setup away from the Tokamak, e.g. in a separated room as currently done for the spectroscopy diagnostics. Alternatively other optical devices insensitive to the magnetic noise, such as the Avalanche Photo-diode (APD) or the Silicon Photo-multiplier (SiPM), can be used to transmute the emitted photons in electric signals.

The full characterisation of both detection systems is presently missing so that no absolute calibration could be performed. While the transmission factor of the optical paths and the efficiency of the PCO Panda camera and the Hamamtsu PMTs can be relatively easily evaluated, the major difficulty consist in using a known source of energetic ions in a stable magnetic field. Moreover, the scintillator coating uniformity has to be measured.

The Faraday Cup was found to be very fragile and the interpretation of the measurements not straightforward. Its improvement is, also, left as a future upgrade.

Chapter 4

Commissioning and operational limits

4.1 Introduction

A first version of the FILD, which we call *FILD-lite*, was installed on TCV in October 2019. This was characterized by a simplified design to serve as a test device. In particular, compared to the full design this version lacked the thermocouples used to monitor the temperature of the probe head, the Faraday Cup and a fast light detection system. After being employed in the MST1 - Topic 11 experimental campaign on the TCV, the FILD-lite was retired in January 2020. In March 2020 the installation of the current version of the FILD was completed and a campaign of experiments for commissioning purposes followed.

In this chapter the FILD is shown to function according to its specifications, namely as a detector of lost fast ions performing a gyromotion around the magnetic field at the entrance slit. These are typically early losses, i.e. particles lost a few toroidal turns after injection, or caused by the particle interactions with magnetic fluctuations on time scales of microseconds. In Section 4.2, the detection of early losses from the NBH are shown to have energy spectra consistent with the beam primary component energy within the instrumental uncertainty. The issue of validating the observations with numerical simulations of the fast-ion losses with a dedicated code is discussed.

The sensitivity of the detector to the field line direction was studied in discharges with DNBI-sourced fast ions and in different plasma scenarios where the I_p current was modified in amplitude and direction. How the double-slit FILD detects losses from either entrance slit is described in Section 4.3 as an effect of the plasma current direction. Furthermore, in Section 4.4 the impact of changing the local magnetic field direction by varying the I_p amplitude is assessed. These experiments show that the presence of magnetic fluctuations may populate/depopulate the lost fast-ion phase-space differently than that expected from only NB early losses in an axisymmetric equilibrium.

Finally, the wide range of plasma scenarios with the available NBH and ECRH systems gave us the possibility to identify the operational limits of the diagnostic, as supported by measurements of the detector's temperature by the thermocouples and observations of the component heating with internal and external cameras. This is reported in Section 4.5.

4.2 NBH early losses

Fast-ion losses are usually detected in discharges with NBH as a source of energetic ions, on TCV. For instance, in shot 68574 the NBH provided Deuterium atoms with energies up to 28 keV for a total injected energy of 1.1 MJ during ~ 1 s. The beam line, in the same direction of the plasma current, was nearly tangential to the flux surfaces at ionization so that the 70% of the particles were ionized on the HFS with pitch values above $\lambda = v_{\|}/v = 0.8$. Since the trapping condition requires $\lambda \leq 0.65$, fast ions were born mostly followed co-I_{p} passing orbits.

A frame from the PCO Panda camera captured at $t = 0.18$ s, when the NBH was turned on and the primary injection energy was 25 keV, shows a wide spot of scintillator emission in a region corresponding to energies slightly above those of injection and pitch values around $\lambda = 0.85$. Other weaker traces were found with similar values of energies and pitch below $\lambda = 0.7$. The mapping into the Deuterium velocity space, from the e-FILDSIM code, is shown in Figure 4.1. No weighting was employed to invert such measurements from the scintillator flux of impinging ions to the flux of lost particles at the slit. In what follows, information on the fast-ion velocity space at the slit will be inferred by comparing the the weight functions to the measurement distributions in the scintillator velocity space. One could have chosen to compute these distributions in terms of spatial distances of the measured strikes to the strikemap knots. However, it was preferred to show the scintillator velocity space to highlight the effect of the collimator on the lost particle trajectories. Neither the scintillator efficiency nor the collimator factor are included in this mapping. The energy and pitch distributions of the measurements are defined as the integrals of the camera pixel counts along one of the velocity-space co-ordinates:

$$h_{\lambda}(E) = \int_{\lambda_1}^{\lambda_2} \left[\omega(E, E', \lambda, \lambda') \star \Gamma_{\mathrm{slit}}(E', \lambda')\right] \epsilon(E) T_{\mathrm{optics}}\, \mathrm{d}\lambda \qquad \forall\, \lambda_1, \lambda_2 \in \mathbb{R}, \tag{4.1}$$

$$h_{E}(\lambda) = \int_{E_1}^{E_2} \left[\omega(E, E', \lambda, \lambda') \star \Gamma_{\mathrm{slit}}(E', \lambda')\right] \epsilon(E) T_{\mathrm{optics}}\, \mathrm{d}E \qquad \forall\, E_1, E_2 \in \mathbb{R}, \tag{4.2}$$

where (E, λ) are the fast-ion velocity-space co-ordinates in the scintillator plate, (E', λ') at the slit, ω is the instrument function presented in Section 3.5, ϵ the scintillator efficiency and T_{optics} includes the optical transmission coefficient and the efficiency of the camera in converting the photon flux to pixel counts. The T_{optics} parameter is currently unknown, so no absolute calibration is possible. For the measurements here reported, these distributions are shown in Figure 4.2, together with the weight functions used to evaluate the collimator effect on the particle trajectories.

To validate these measurements, a synthetic velocity space of the lost particles may be computed from simulations of the unconfined trajectories in an axisymmetric equilibrium performed with the ASCOT code [43]. A caveat is that FILD losses in ASCOT are considered through those markers, with each one representing a bunch of actual particles, whose orbits intercept the structure of the graphite shield (the slits themselves are reached by very few markers). This makes the comparison difficult unless sophisticated simulation strategies are employed to populate the phase space of the losses at the slit in a statistically significant manner.

The lost-ion velocity space and the initial phase space of these particles are reported in Figure 4.3. The energies of the simulated losses are those of the beam components. In the latter plot, two regions of origin of such losses are found with pitch-angle values corresponding to those of the lost particles:

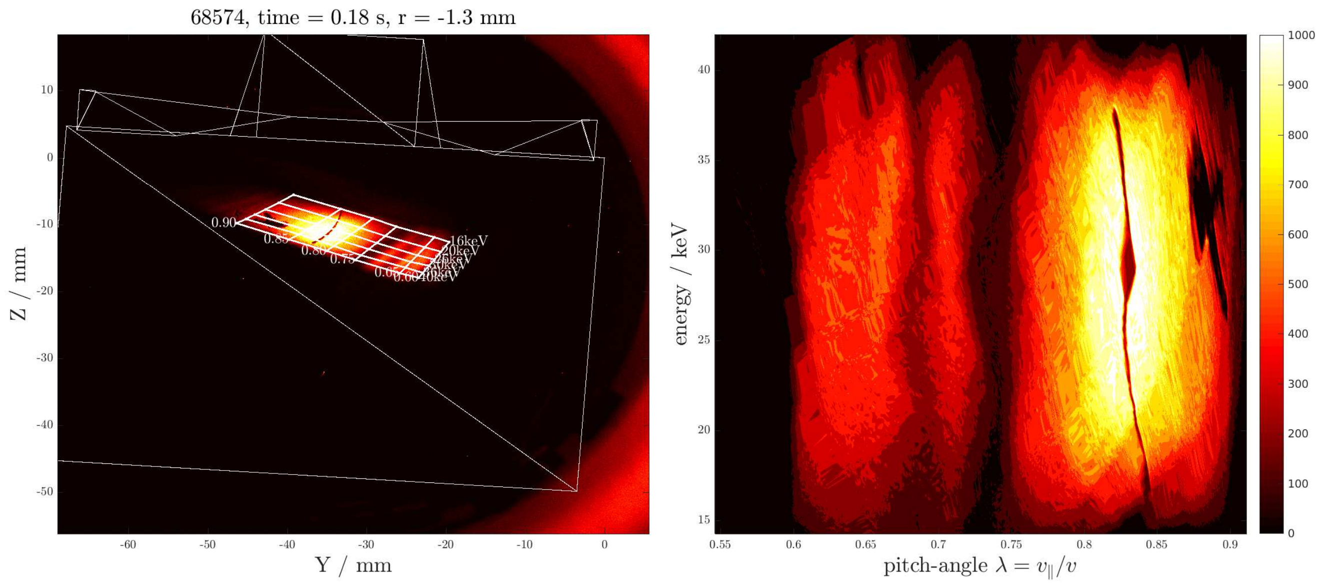

Figure 4.1: Shot 68574 at $t = 0.18$ s. (left) PCO Panda camera measurements. (right) Mapping from the scintillator plane (Y, Z) to the Deuterium velocity space in the scintillator, in (E, λ) co-ordinates. The scratch crossing the brightest spot is due to partial removal of scintillator powder occurred during the assembly.

one region at $(R = 0.8 \text{ m}, \lambda \geq 0.9)$ and another, less populated, at $(R = 1.1 \text{ m}, \lambda = 0.7)$.

No particularly intense MHD activity, that may give a transport contribution, was present at this stage of the discharge. Therefore, the detected lost particles can be interpreted primarily as *early* losses, i.e. these are from co-passing orbits (defined in Section 2.3.2) that after few toroidal turns, following ionization, are lost because of an outward shift of the guiding-center trajectory and their large Larmor radius that may extend outside of the confined plasma region. The sum of the two effects can, indeed, lead the particles to intercept the probe head. Particle acceleration by electric field perturbations are excluded as there are no rapid changes in the equilibrium configuration. Moreover, the confinement time of these particles is not long enough for an effective slowing-down by collisions on the bulk plasma (responsible for plasma heating). In fact, the energy distribution exhibits a peak of emission with broad extent in energy around 30 keV for $\lambda \in [0.76, 0.88]$ whereas the primary injection energy was 25 keV. The curve of camera pixel counts as a function of the energy, see lhs plot in Figure 4.2, well matches the low-energy tail of the 30 keV instrument function sitting between the high-energy tails of the 25 keV and 35 keV functions. As a result the uncertainty in energy is estimated of the order of 20%. The main source of errors, that yields such a degree of accuracy, is the imperfect mapping (performed by applying the strikemap from e-FILDSIM) due to an insufficiently accurate calibration of the camera frames and differences between the CAD design and the assembled detector and their tolerances. As an example, a difference of few millimeters in the distance, in TCV radial direction, between the scintillator plate and the collimator gives, as shown in Figure 4.4, largely separated strikemaps and, therefore, changed mapping to the particle velocity space. No other beam components appear resolved at the scintillator.

The pitch distribution features two main peaks, as shown on the right of Figure 4.2. One peak is around $\lambda = 0.65$, close to the ASCOT predictions. The other at $\lambda = 0.85$ doesn't display the same agreement. Parameter scans for e-FILDSIM simulations are usually performed when analysing scintillator emissions during the shot ramp-up, as in this case. At this stage, typically, the impact on the lost particle trajectories inside the probe head of the strongly changing in time equilibrium magnetic field are averaged during the long camera acquisition and are not resolved. To account for such modifications, the values of the elevation angle θ (between the magnetic field line and the midplane) and the azimuthal angle ϕ (between the field line and the scintillator plate) can be varied so as to perform a fine-tuning of the strikemap. In Figure 4.5, the pitch distributions from FILD and ASCOT are compared, for a range of mappings computed for different values of the angle $\phi \in [-10°, 0°]$, according to the measured variations of the local equilibrium field. This shows slightly improved velocity-space reconstruction although still not enough to reach agreement. Equilibrium reconstruction errors are usually of the order of $\leq 5\%$ in limited plasmas. Therefore the observed disagreement is likely due to the inherent differences between the FILD measured velocity space and the synthetic diagnostic at the slit from ASCOT simulations. It should be noted that the pitch distributions from ASCOT simulations of the particles at the slit and the distributions from the scintillator emissions can be safely compared in qualitative terms because the collimator effect on the pitch-angle is generally small and symmetric around a mean value.

To properly compare the synthetic velocity space to that measured in the scintillator plate, the transfer function of the global system has to be taken into account. Yet, as described above, a characterization of the optics is missing. Here, a simple estimation is performed: the pitch distributions of the camera pixel counts h^{px} and the ASCOT markers $h^{\mathrm{syn}} \propto \Gamma_{\mathrm{slit}}$ are integrated in the pitch ranges of the two peaks λ_1 and λ_2 for similar energies, these are shown in Figure 4.5, separately. If one assumes delta functions for the instrument function in Equation (4.2) the ratios of the integrated distributions becomes

$$\frac{\int h^{\mathrm{px}}(\lambda_1, E)}{\int h^{\mathrm{px}}(\lambda_2, E)} \approx \frac{\omega(\lambda_1, \lambda_1', E, E')}{\omega(\lambda_2, \lambda_2', E, E')} \frac{\int h^{\mathrm{syn}}(\lambda_1', E')}{\int h^{\mathrm{syn}}(\lambda_2', E')}, \tag{4.3}$$

By including the collimator factors, a factor of 4 is required to satisfy the inequality. This discrepancy may be due to an imperfect mapping and the strict assumptions made. However, once more, an incorrect estimation of the lost fast-ion velocity space at the slit by the ASCOT code is likely to be the main culprit.

In summary, the energy measurements can be significantly affected by small disagreements, of few millimeters, between the detector modeled in the e-FILDSIM code and the real assembly, and inaccurate calibration of the camera. The present system accuracy was found to be limited by a relative error of $\sim 20\%$. The observed mismatch between the measured pitch distributions and those simulated may come from multiple causes. Errors in the positioning of the probe (probably not bigger than few millimeters) and in the equilibrium reconstruction at the slit cannot be sufficient since the q-profile slowly changes in such far regions from the Tokamak plasma. An imperfect numerical mapping via the e-FILDSIM code from numerical limitations and the aforementioned sources of errors can play a role. However, the major issue is the difficulty in estimating the fast-ion velocity space at the detector slit by means of codes like ASCOT without employing sophisticated simulation strategies. In conclusion, it is clear that a detailed comparison between FILD measurements and ASCOT simulations requires more accurate modeling of the particle trajectories at the probe head that would require much calculation and interpretation that was not possible during this thesis.

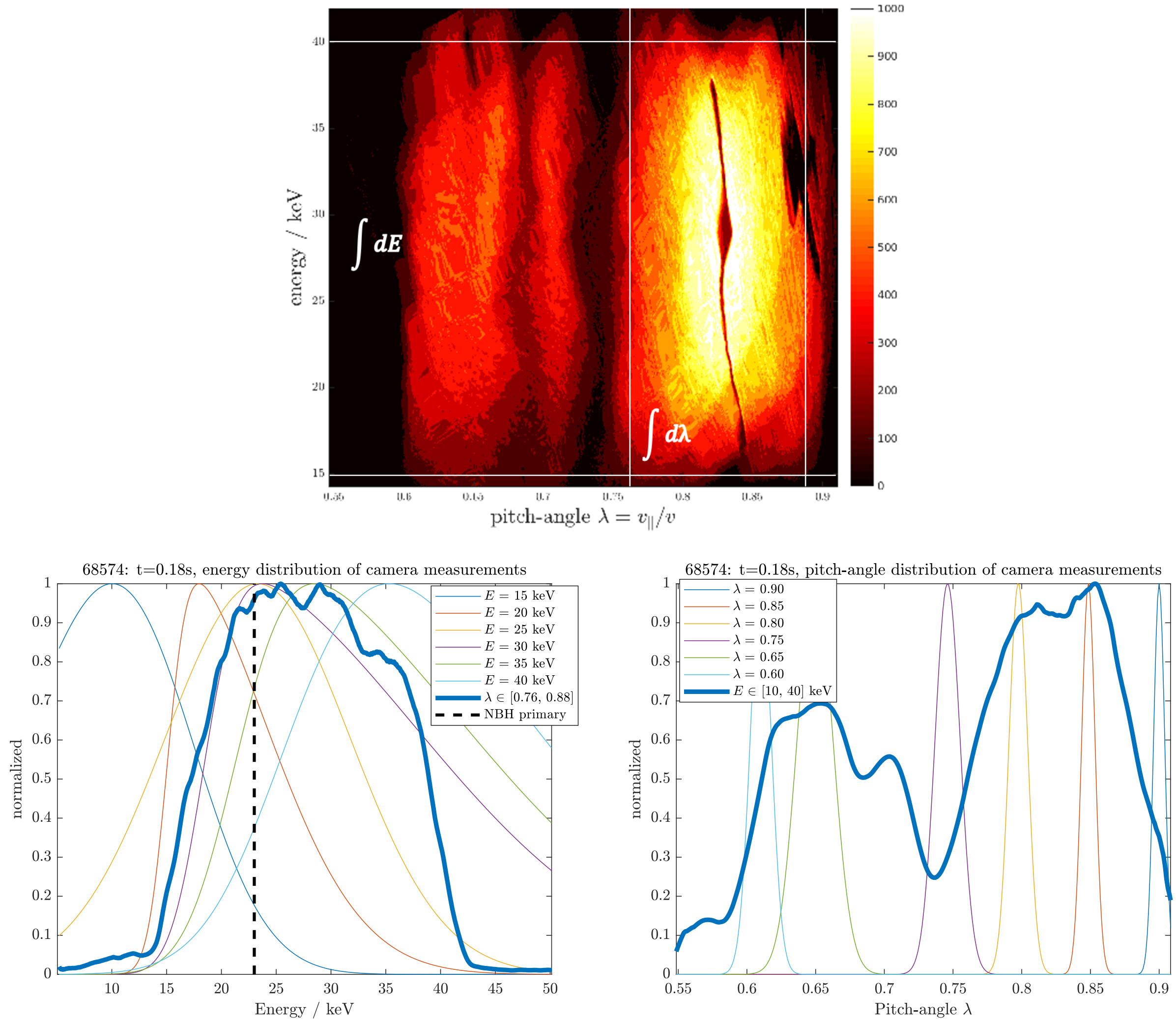

Figure 4.2: Shot 68574 at $t = 0.18$ s. (top) The scintillator velocity space with the integration ranges for computing the distributions below. (bottom) In both pictures the instrument functions for the mean value of the integration interval are superimposed in different colors. (left) Energy distribution of the PCO camera measurements integrated in the pitch range $[0.76, 0.88]$. The NBH primary energy is reported (dashed black). (right) Pitch distribution of the same camera frame integrated in the energy range $[10, 40]$ keV.

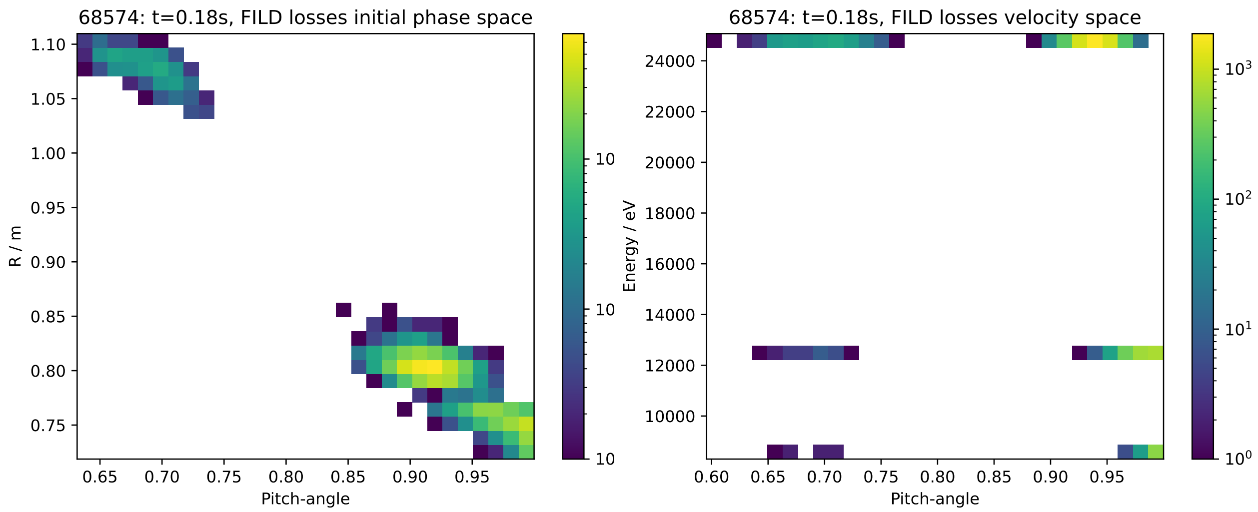

Figure 4.3: Shot 68574 at $t = 0.18$ s. ASCOT simulated losses, i.e. those trajectories that intercept the heatshield, for shot 68574 at $t = 0.18$ s. (left) Initial phase space of the FILD losses upon NBH deposition. (right) Velocity space of the losses at the FILD.

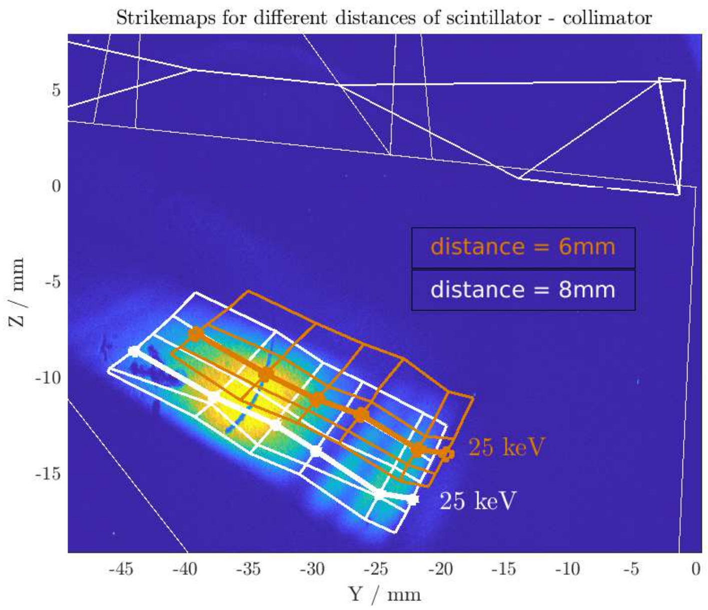

Figure 4.4: Two strikemaps from e-FILDSIM simulations with different scintillator-collimator distances (in the TCV radial direction) are superimposed to the scintillator emission, for shot 68574 at $t = 0.18$ s. The correct map (white) is for a distance equals to 8 mm, the other example (orange) is for 6 mm. The 25 keV line is highlighted with markers.

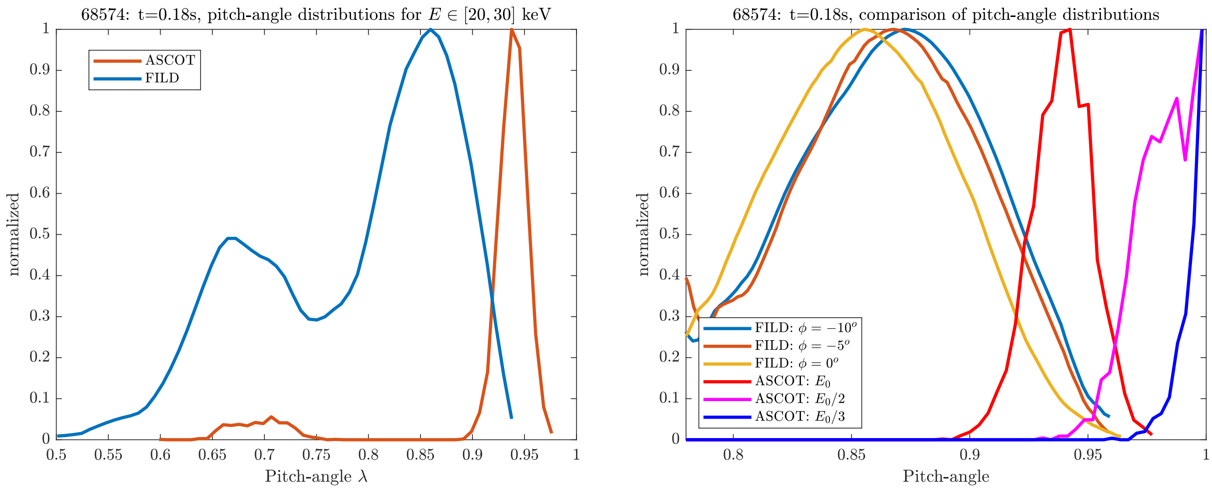

Figure 4.5: Shot 68574 at $t = 0.18$ s. Comparison of the pitch distributions from FILD and ASCOT. Higher order smoothing was used for these distributions compared to the one shown in Figure 4.2. (left) The distributions integrated in the energy range of the primary beam component. (right) FILD mappings for different values of the angle ϕ between the magnetic field line at the slit and the scintillator plane. The distributions from the ASCOT loss simulations are for each energy component of the beam.

4.3 Two slits for co- and counter-current propagating fast ions

In the previous section, FILD measurements of early losses from co-passing orbits were presented. Losses can also be due unconfined orbits as determined by the plasma current direction. For instance, a particle on the LFS following a cntr-I_p banana orbit will bounce back on the outer side in the poloidal plane. If this banana orbit side (or *leg*) is far enough from the starting flux surface inside the LCFS, the particle may become unconfined and eventually collected by the FILD through one of the two slits.

In the two cases of opposite I_p directions, the FILD only detected lost fast ions from one slit or the other, exclusively, although both slits were open. When the plasma current direction is reversed, the vertical magnetic component direction at the slit reverses. Equivalently, the sign of the elevation angle θ between the field line and the plane of the slits changes.

This section addresses the impact of the plasma current direction in determining the magnetic field line inclination at the slits, hence which slit can be traversed by the losses, and the displacement of the particles following different orbits. In other words, the convolution of the collimator+heatshield acceptance with the phase space of the particles that may reach the FILD "selects" the collecting slit. To obtain a fast-ion population of mainly trapped orbits, the DNBI was employed due to a nearly radial line injection, providing particles with small pitch values. It should be noted that discharges with different values and/or directions of the plasma current may feature different beam depositions, or in other words, fast-ion phase space at birth. For this reason, the FILD measurements presented in this section were compared to ASCOT simulations of particle trajectories in an axisymmetric equilibrium field. As already pointed out in Section 4.2, a direct comparison is affected by many issues. However, in the cases here reported, it can help to identify the fast-ion population that may reach the probe head, although not accurately resolving the particle velocity space at the slits, and being collected by the FILD.

In this thesis the following convention is used: looking at the probe from outside the vessel, namely radially towards the Tokamak, "Slit 1" is on the right, "Slit 2" on the left.

The helix acceptance was evaluated for each slit by means of the e-FILDSIM code. Helixes for a wide range of energies and pitch-angles were drawn for both directions of I_{p} and $v_{\|}$. It was found that there are no values of (E, λ) such that the corresponding helixes starting from Slit 1 are collimated in the case $\left(I_{\mathrm{p}} > 0, v_{\|} > 0\right)$. In the remaining three cases, instead, some trajectories are accepted. An example is shown in Figure 4.7. For the Slit 2 there are not accepted helixes in the case $\left(I_{\mathrm{p}} < 0, v_{\|} < 0\right)$.

Since the fast-ion losses are determined by the injection direction with respect to the I_{p} direction, not all four possible combinations of $\operatorname{sgn}(I_{\mathrm{p}})$ and $\operatorname{sgn}\left(v_{\|}\right)$ may correspond to scenarios with fast-ion losses that enter the FILD. The DNBI injection line is slightly in counter-clockwise direction (11^{o} on TCV seen from above), see the left plot in Figure 4.6, therefore the $I_{\mathrm{p}} < 0$ case corresponds to a counter-current injection. In this scenario, the $v_{\|} < 0$ ions are traveling along the outer leg of a banana orbit, so that these particles may be easily lost and pass through this slit. On the contrary, ions with $v_{\|} > 0$ are on either cntr-passing or inner legs of banana orbits, and are well confined. In the $I_{\mathrm{p}} > 0$ scenario corresponding to co-injection, instead, particles with $v_{\|} > 0$ travel along either co-passing or the outer leg of banana orbits that can be unconfined, while particles in inner banana legs ($v_{\|} < 0$) are not lost.

ASCOT simulations of fast ions in both scenarios confirm that some orbits would be lost, leading to particles potentially detectable by the FILD. The poloidal section of these orbits are on the right in Figure 4.6. Although the Slit 1 is sensitive to fast ions with positive parallel velocities, these are not likely to be lost. Outer co-I_{p} banana legs, instead, can be unconfined orbits but not collimated as showed above. A similar reasoning can be applied for the Slit 2 as well as to the case of NBH, that currently injects particles with $v_{\|} < 0$. A recap of all possible losses and the detector's acceptance is given in Table 4.2.

To probe the phase space of the fast ions originated from the DNBI with the CNPA and detect the subsequent early losses with the FILD, experiments were conducted varying the CNPA line of sight (LOS) in three shots for each plasma current direction, as reported in Table 4.1. The scan of the CNPA LOS intended to probe the pitch-angle distribution of those fast ions undergoing CX reactions, therefore traveling in the outer regions of the plasma. The orientation of the LOS crossing the flux surfaces determines the range of pitch-angle values of the escaped neutral particles. The DNBI-originated fast ions with a large population of trapped particles are more likely to intercept the probe head with both signs of parallel velocity. Moreover, DNBI injected Hydrogen atoms in pulses of 30 ms with 90 ms of pause between, a duration close to the value of the slowing-down time so as to mainly detect direct losses, on time scales of several microseconds, where collisions play no role.

The CNPA findings confirmed that the lost fast-ion velocity space is greatly skewed towards large perpendicular energies and that the population of losses mainly comprised cntr-I_{p} circulating particles. The CX spectrum as function of the Hydrogen energy, reported on the left of Figure 4.8 for the $I_{\mathrm{p}} < 0$ case and the three LOS, shows that the neutral particle flux from low pitch ions ($v_{\perp} \gg v_{\|}$) was 100 times larger than the flux from higher pitch values. In the right plot in Figure 4.8 the two cases of plasma current direction are compared for a given LOS: the flux from neutralized fast ions, with energies close to the third beam component, is much larger for the $I_{\mathrm{p}} < 0$ discharge.

In these experiments, the FILD detected losses uniquely from the Slit 1/Slit 2 for $I_{\mathrm{p}} < 0/ > 0$. In the case of co-injection ($I_{\mathrm{p}} > 0$) the Slit 1 would only accept particles streaming along the magnetic field line with $v_{\|} < 0$. Nevertheless, these ions are following the inner leg of co-current banana orbits so are well confined. Experimentally, no ions were detected entering this slit.

In the $I_{\mathrm{p}} > 0$ scenario, Slit 2 collected lost particles mainly with nominal energies below the maximum injection energy (50 keV) and around two values of pitch. The comparison between the measured and the ASCOT synthetic fast-ion velocity space at the slit is shown in Figure 4.10. The two emission spots have energy distributions fairly consistent with the instrument function for $E = 40$ keV (such instrument functions in energy for the two ranges of pitch are similar in this case), although the brightest spot has a low-energy bump that corresponds to the energy of the third beam component. The measurements are, therefore, within the uncertainty of 20% discussed in Section 4.2. The pitch distributions are well identified but there is a significant discrepancy in λ values and amplitude with respect to the ASCOT model. These distributions are shown in Figure 4.11. ASCOT simulations were used to track the particle trajectories inside the plasma volume. It was found that the losses at $\lambda = -0.7$ correspond to co-passing particles, and those with $\lambda = -0.35$ to fast ions along the outer banana legs. The pitch-angle sign is, therefore, consistent with the direction of B_{ϕ}: $\mathrm{sgn}(\lambda) = -\mathrm{sgn}(v_{\|})$. Although these orbits can be confined, ions have Larmor radii large enough to leave the confined region, since their guiding-centers sit on inner magnetic surfaces nearby the LCFS. Examples of such orbits are shown in Figure 4.6.

When the plasma current direction is reversed ($I_{\mathrm{p}} < 0$), Slit 1 can accept particles with either sign of $v_{\|}$ and, in effect, losses were detected from particles travelling along the outer leg of cntr-I_{p} banana orbits. The FILD measurements are reported in Figure 4.12 together with the ASCOT synthetic velocity space. A positive pitch-angle value is consistent with these trajectories, see right plot in Figure 4.6. Slit 2, instead, was not accessible by any losses. In this case the only accepted trajectories belong to particles with $v_{\|} > 0$, corresponding to the well confined inner leg of a banana orbit. The observed losses have energies around $E = 50$ keV and pitch values around $\lambda = +0.3$, with fainter traces at $\lambda = 0.4$ and $\lambda = 0.6$, as shown in Figure 4.13. The energy distributions of the two main spots are close to the instrument function for 50 keV corresponding to the DNBI primary component. The comparison between the measured and the synthetic pitch-angle distributions underlines, yet again, of the need for tailored simulations. In fact, the simplified modeling of the ASCOT losses at the probe head gives a distribution of the markers in λ that is large enough to cover the two peaks observed by the FILD, so the discrepancy may not, in fact, be real.

No losses at energies of the secondary beam components were found in the $I_{\mathrm{p}} < 0$ case, in contradiction with the ASCOT predictions. On the contrary, in the discharge with $I_{\mathrm{p}} > 0$ a spot of emission in regions corresponding in energy to the third beam component was observed. Further investigations are necessary to characterise the sensitivity of FILD to the different beam components and plasma scenarios. In a future work, the combination of several injection energies and directions may be used, following significant modelling, to provide an 'in-situ' energy calibration.

Shots with $\mathrm{sgn}\,(I_\mathrm{p})$	LOS	$\lambda = v_\parallel / v$
68067 (+), 68068 (−)	30°	$0.6 \div 1.0$
68065 (+), 68070 (−)	23°	$0.5 \div 0.9$
68066 (+), 68071 (−)	16°	$0.3 \div 0.6$

Table 4.1: CNPA lines of sights and the pitch ranges of the neutralized fast ions detected.

$\mathrm{sgn}\,(I_\mathrm{p})$	$\mathrm{sgn}\,(v_\parallel)$	Orbit type (likely lost y/n)	e-FILDSIM	FILD
+ (co-injection)	+	outer banana leg (y), passing (y)	Slit 2	Slit 2
− (cntr-injection)	+	inner banana leg (n), passing (n)	Slit 1,2	-
+ (co-injection)	−	inner banana leg (n)	Slit 1,2	-
− (cntr-injection)	−	outer banana leg (y)	Slit 1	Slit 1

Table 4.2: A table to summarize the experimental findings (FILD) and the simulated (e-FILDSIM) acceptance of the detector for each combination of plasma current and parallel velocity signs. The orbit type is reported for each case with the possibility of resulting unconfined.

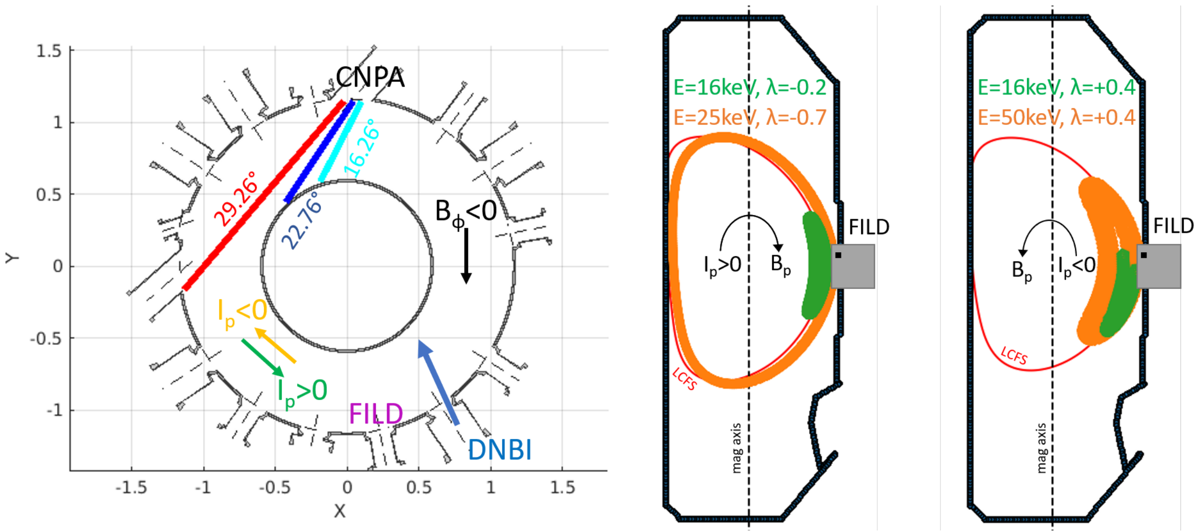

Figure 4.6: (left) TCV seen from above, the CNPA lines of sight, and the I_p and the B_ϕ sings in the TCV convention. (right) Poloidal section with lost orbits of DNBI injected fast-ions for both signs of the plasma current. Banana orbits with different extent and width as function of the particle energy are shown.

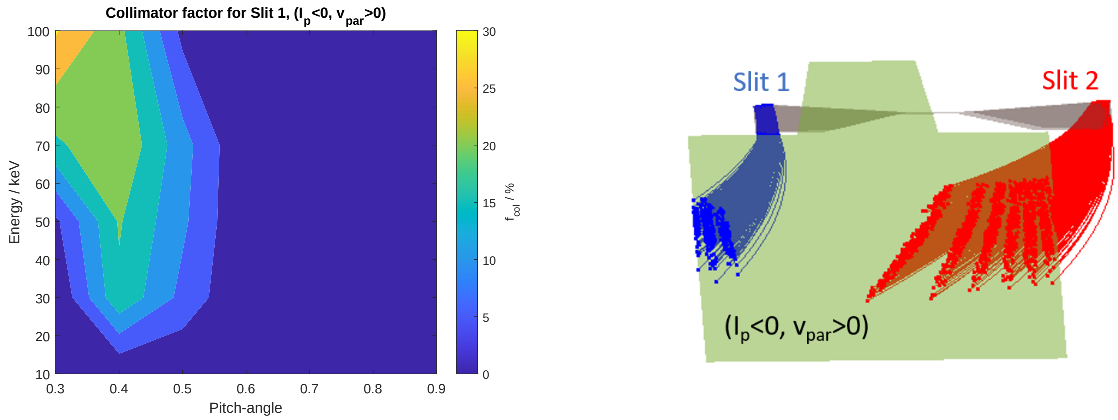

Figure 4.7: (left) Collimator factor for the Slit 1 as evaluated from the simulation of the lost trajectories. (right) Simulated helixes at both slits for the optimal range of gyrophase values.

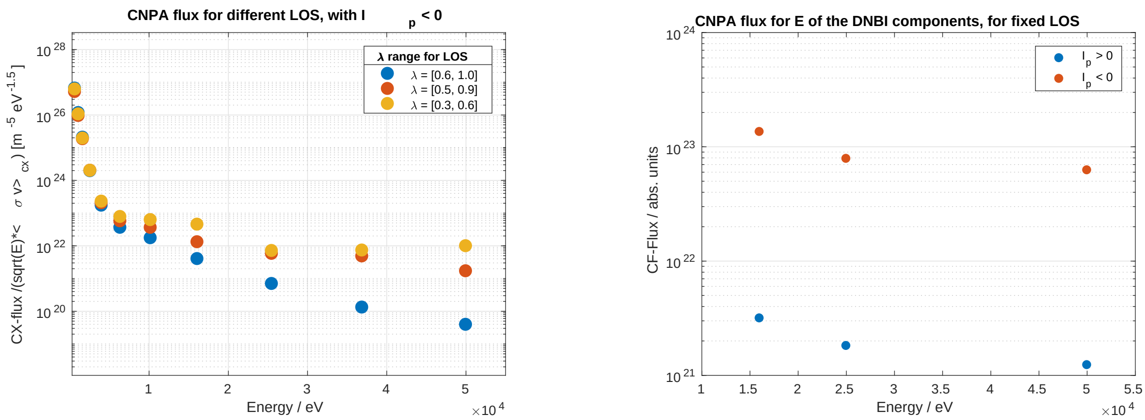

Figure 4.8: CNPA flux. (left) For $I_\mathrm{p} < 0$, comparison between the three LOS corresponding to different pitch ranges. Higher counts are found for Hydrogen particles with energy of maximum DNBI injection and larger perpendicular component of the velocity. (right) For the CNPA LOS corresponding to $\lambda \in [0.3, 0.6]$, larger fluxes are found for the plasma scenario with $I_\mathrm{p} < 0$ at the energies of the three DNBI molecular components.

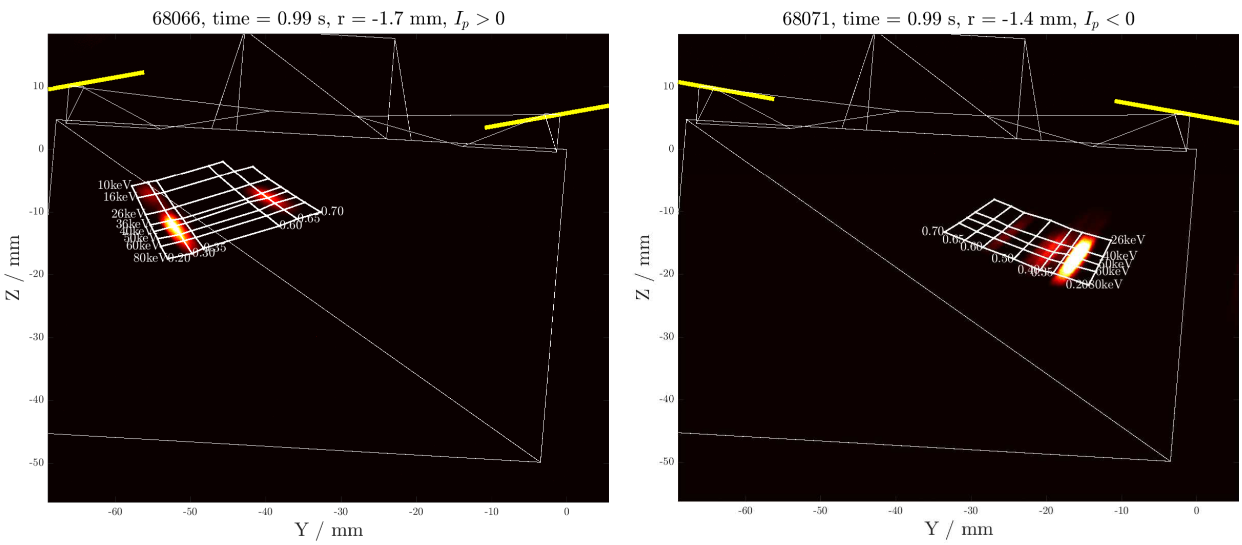

Figure 4.9: The scintillator emissions in both cases. The magnetic field line at the slits is in yellow. The scintillator plate and collimator edges are in white. The strikemap with the pitch and energy values of the knots are also shown. (left) Shot 68066: $I_{\mathrm{p}} > 0$. (right) Shot 68071: $I_{\mathrm{p}} < 0$.

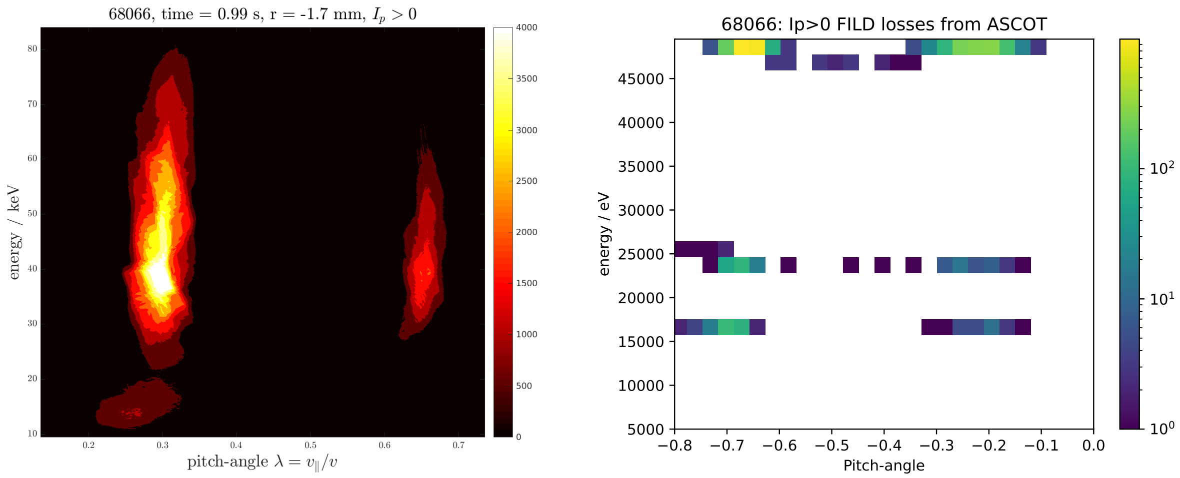

Figure 4.10: Shot 68066, FILD relative radial position $r = -1.7$ mm, scenario with $I_{\mathrm{p}} > 0$. (left) FILD scintillator mapped into Hydrogen velocity space at $t = 0.99$ s. The pixel count scale is not optimized to reduce saturations to show fainter traces. (right) ASCOT simulated velocity space of the FILD losses. For $B_\phi < 0$, a negative pitch-angle stands for particles with positive parallel velocity.

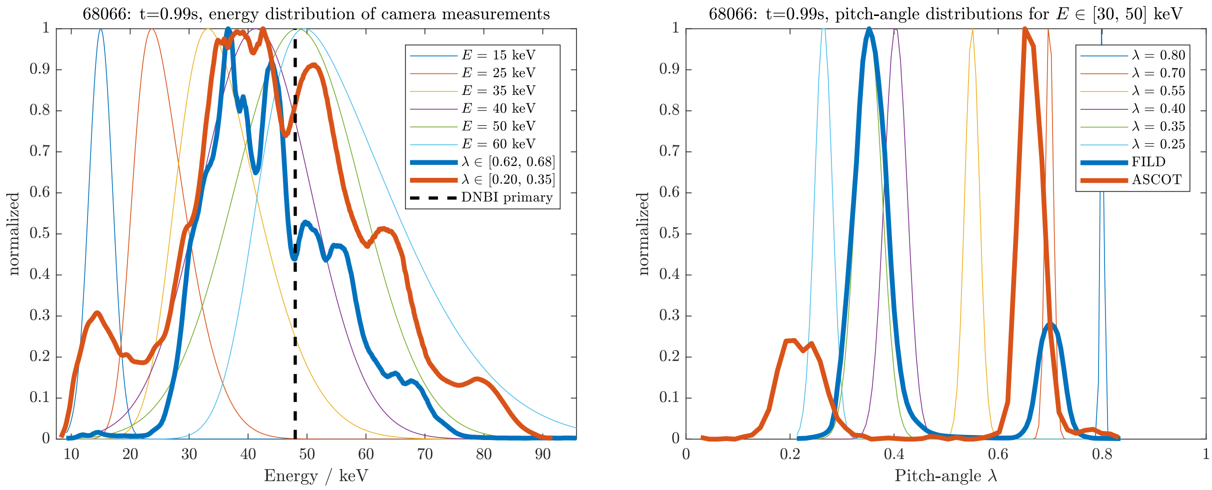

Figure 4.11: Shot 68066, scenario with $I_{\mathrm{p}} > 0$. The weight functions are superimposed in different colors. (left) FILD energy distributions of the spots of emission for two different ranges of pitch values. (right) Pitch distributions from FILD and ASCOT predicted losses for energies in the range $[30, 50]$ keV. The pitch-angles are in absolute value.

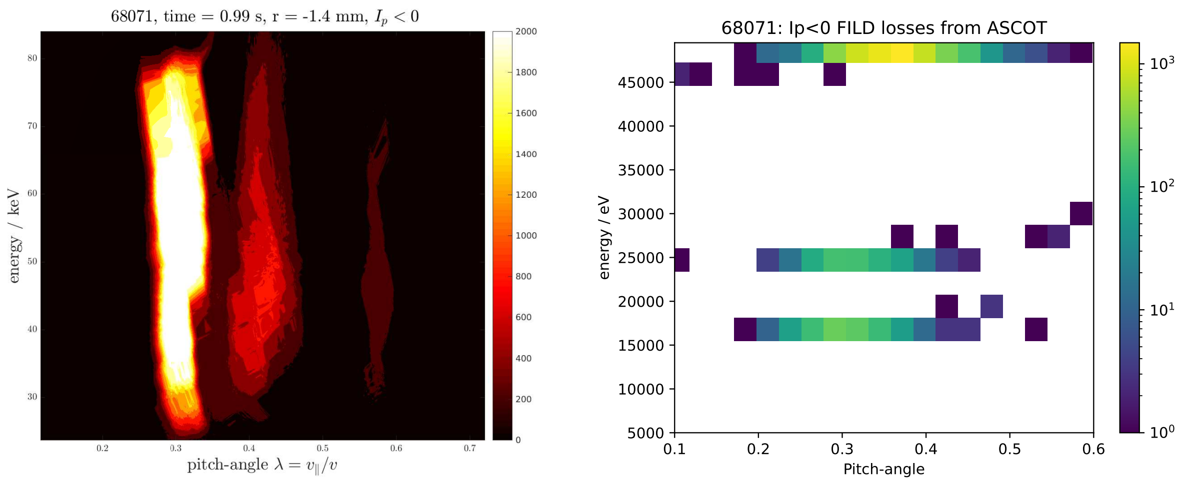

Figure 4.12: Shot 68071, FILD relative radial position $r = -1.4$ mm, scenario with $I_{\mathrm{p}} < 0$. (left) FILD scintillator mapped into Hydrogen velocity space at $t = 0.99$ s. The pixel count scale is not optimized to reduce saturations to show fainter traces. (right) ASCOT simulated velocity space of the FILD losses.

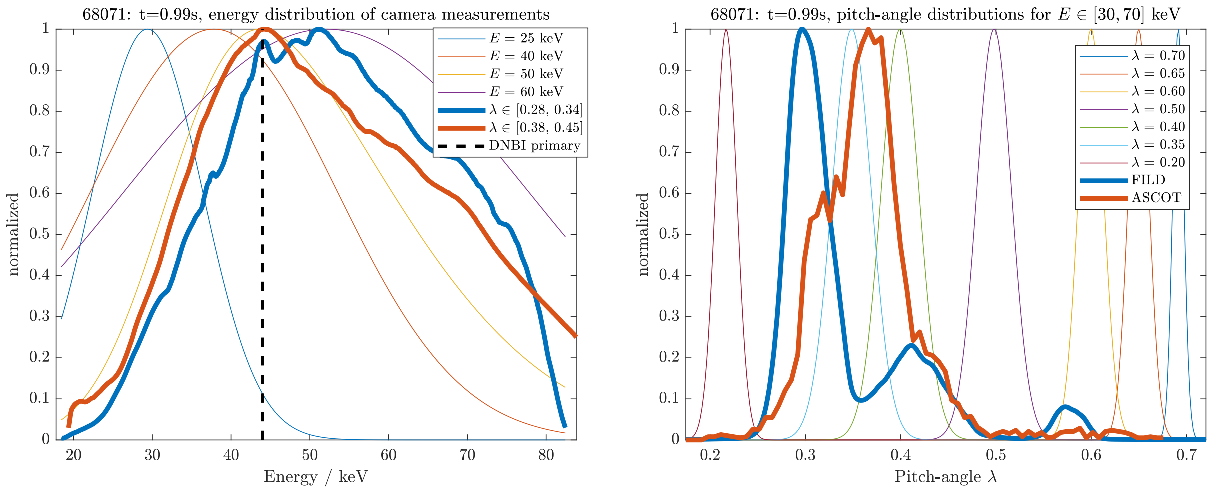

Figure 4.13: Shot 68071, scenario with $I_{\mathrm{p}} < 0$. The weight functions are superimposed in different colors. (left) FILD energy distributions. The dashed black line indicates the peak of the weight function relative to the DNBI primary component energy. (right) Pitch distributions from FILD and ASCOT predicted losses for energies in the range $[30, 70]$ keV.

4.4 FILD sensitivity to the local magnetic field line direction

The FILD detects energetic ions whose trajectories are outside the confined plasma region. The probe was built to detect positively charged particles performing a left-handed gyromotion around the magnetic field line. For this reason, provided that the standard configuration of a TCV discharge has B_ϕ in counter-clockwise direction (TCV viewed from above), the slits were placed at the upper side of the probe head. Particles with opposite gyromotion can not be collected, as it can be demonstrated by reversing the B_ϕ direction. This was performed for shot 67504, where the plasma shape and the relevant parameters were similar to those of discharges typically characterized by fast-ion losses. In this experiment, the CNPA detected energetic neutral particles, although without resolution of the gyromotion of these particles, correlated in time with the DNBI pulses, an effect of fast-ion early losses following the injection. ASCOT simulations predicted orbits colliding with the probe head. Nonetheless, as expected, no scintillator emissions were found during the discharge. A comparison between similar discharges but opposite toroidal field directions is in Figure 4.14. In both shots CNPA counts of Hydrogen atoms are significant while the FILD PMT detected scintillator emissions time-correlated with the beam pulses only in the $B_\phi < 0$ case.

In Section 4.3, it was shown how the plasma current direction selects the FILD slit collecting the particles as a result of the convolution between the unconfined orbits and the probe's acceptance aperture. This is determined by the direction of the local magnetic field line at the slit that points upwards or downwards, depending on the sign of I_{p}. The particle trajectories, indeed, are not only given by the field strength that determines the Larmor radius, but also on the inclination of the field line with respect to the equatorial plane (the elevation angle θ) and the scintillator plate (the azimuthal angle ϕ).

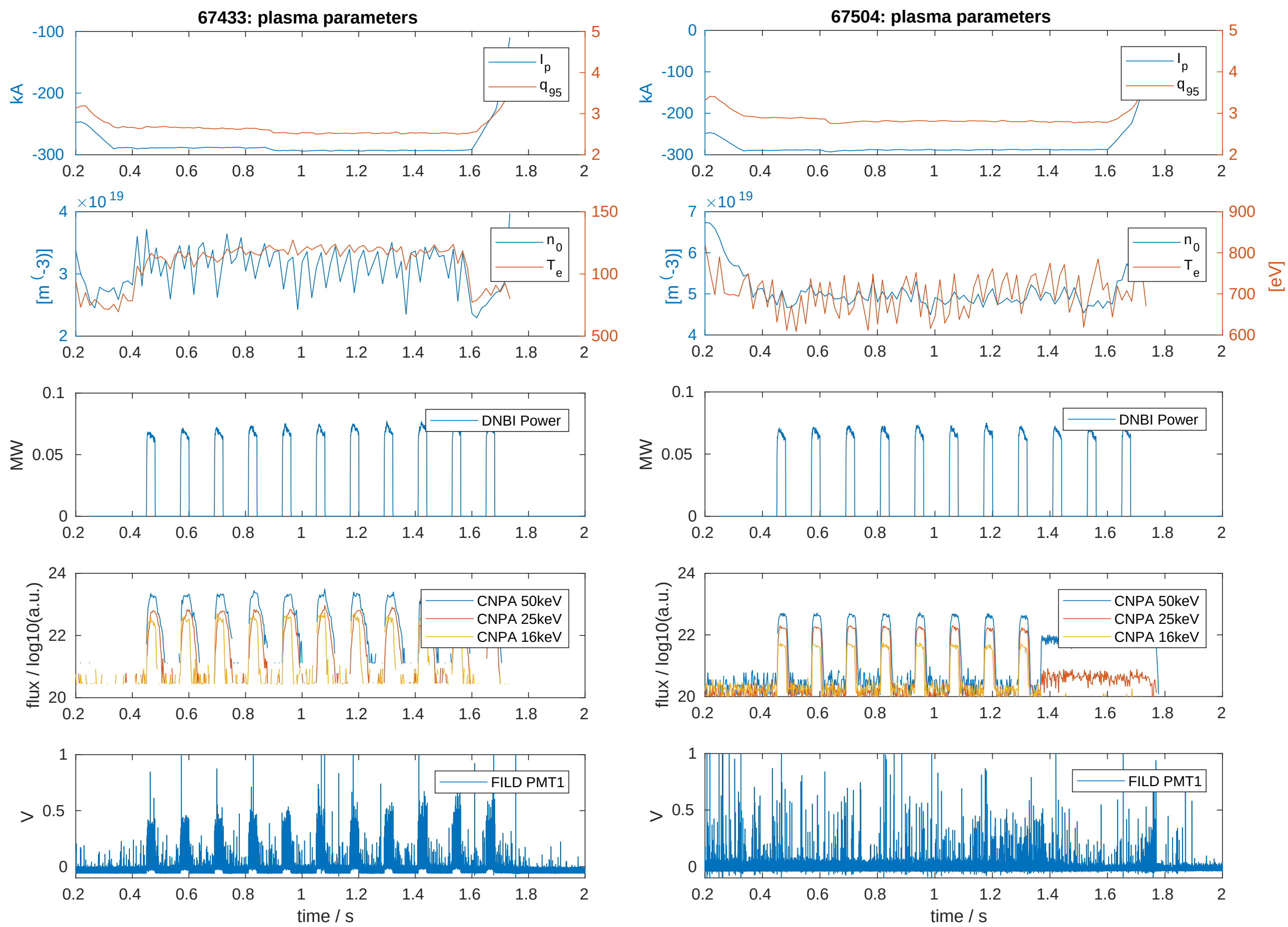

Figure 4.14: Relevant plasma parameters in time. The CNPA fluxes take into account the detector response. (left) Shot 67433 with $B_\phi < 0$. (right) Shot 67504 with $B_\phi > 0$.

Here, the sensitivity of the detector to small variations in θ are examined by varying, in time, the plasma current. In shot 67214 the $I_{\rm p}$ amplitude was lowered from -230 kA to -80 kA starting after the ramp-up phase, while the magnitude of the toroidal magnetic field was constant. In the TCV convention, when $B_\phi < 0$, the field line on the LFS points upwards or downwards for $I_{\rm p} < 0$ or $I_{\rm p} > 0$, respectively. As a consequence, the angle θ at the slit decreases and the helical trajectories move rightwards in the scintillator plate, as shown in Figure 4.15. The strikemap is shifted accordingly. In other words the FILD instrument function changes as a function of the plasma current amplitude (or more correctly, the field pitch angle).

Also in this study, ASCOT simulations of the lost fast-ion velocity space at the probe head are provided. The comparison of FILD velocity-space measurements with this predictions is in this case further complicated by the presence of a significant MHD mode, sweeping in frequency during the discharge from 7 kHz to 14 kHz. Its amplitude detected at the wall by the Mirnov probes is around 100 mG with a dominant $m = 3$ poloidal component and $n = 1$ toroidal mode number. The $q = 3$ flux surface of such mode follows the evolution in time of the q-profile, as a consequence of the $I_{\rm p}$ amplitude scan. Therefore, the resonant surface moves inwards from $\rho_\psi \approx 0.9$ at the beginning of the discharge to $\rho_\psi \approx 0.3$ at the end and may cross, at multiple places, the fast-ion orbits. As a consequence, particles may encounter additional transport from such wave-particle interactions that are not accounted for by ASCOT. In addition, the temporal variation of the plasma current amplitude changes the equilibrium magnetic configuration and the DNBI deposition of the energetic particles. As a consequence, the lost fast-ion velocity space will change with the time in the discharge. These is mirrored by the ASCOT velocity space of the markers colliding with the FILD in Figure 4.20 and the phase space of the same markers at the ionization time in terms of (λ, R).

To elucidate the FILD sensitivity to the magnetic field line inclination, two strategies are employed, as in [70]. The pitch distributions of the scintillator emissions at different times were computed with a "fixed" mapping (e.g. the strikemap for $t_0 = 0.49$ s) and a "moving" mapping, that is the proper strikemap at each time. In Figure 4.18, the pitch distributions evaluated with both strategies are reported for the emissions in the interval of time $t = [0.49, 0.94]$ s. With the moving mappings, the pitch values corresponding to the high-λ peaks of the camera pixel count distributions appear better superposed than those from the fixed mapping approach. In the latter, the variations of the pitch values at the peaks are larger than 5%. This suggest that the impact of the magnetic field orientation is significant. Moreover, the evolution of the equilibrium magnetic field implies that some fine-tuning of the strikemaps is required, as already stressed in Section 4.2.

The camera recorded emissions from the scintillator appear changing in time. As expected, the frames shown in Figure 4.17 feature spots with amplitudes increasing and positions moving from top left to bottom right. This can also be seen in Figure 4.16 in the last plot, where the pixel counts of different scintillator regions vary in time: the top left zone decreases while the other regions towards the right edge have values of pixel counts consistent with the scintillator images. This pattern can be clearly found in the detected emissions from $t = 0.94$ s. At first, the pitch distribution features two clear peaks. Then the low-pitch peak vanishes and the other moves to increasingly smaller values. This behaviour is observed regardless of the mapping strategy employed. A comparison with the distributions as evaluated from ASCOT simulated losses, reported in Figure 4.19, shows large discrepancies that, once more, prove the need for more accurate modeling of losses in the vicinity of the probe.

Different confinement regimes are found. For instance, at $t = 1.12$ s small losses with energies

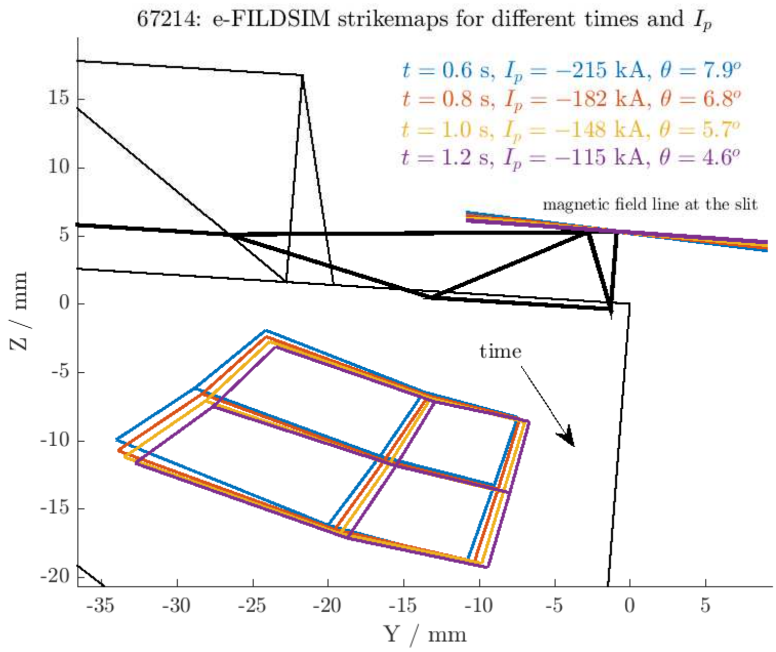

Figure 4.15: Shot 67214. Strikemaps from e-FILDSIM for different times and, therefore, plasma current amplitudes and elevation angles.

at the primary beam component are predicted by ASCOT. This is in part consistent with the CNPA signals. These measurements, although less sensitive to pitch-angle variations, support this hypothesis: from $t = 1.03$ s the full energy counts decrease as the third component becomes dominant, as shown in Figure 4.16. Nevertheless, contrary to the synthetic velocity space at the slit and the CNPA findings, the FILD detected 50 keV losses at these stages of the discharge. However, the two detectors are placed at different positions with respect to the beam direction, and probe different fast-ion phase-space regions making such a comparison non-trivial. Tomographic inversion techniques [72] may be employed to facilitate such comparisons.

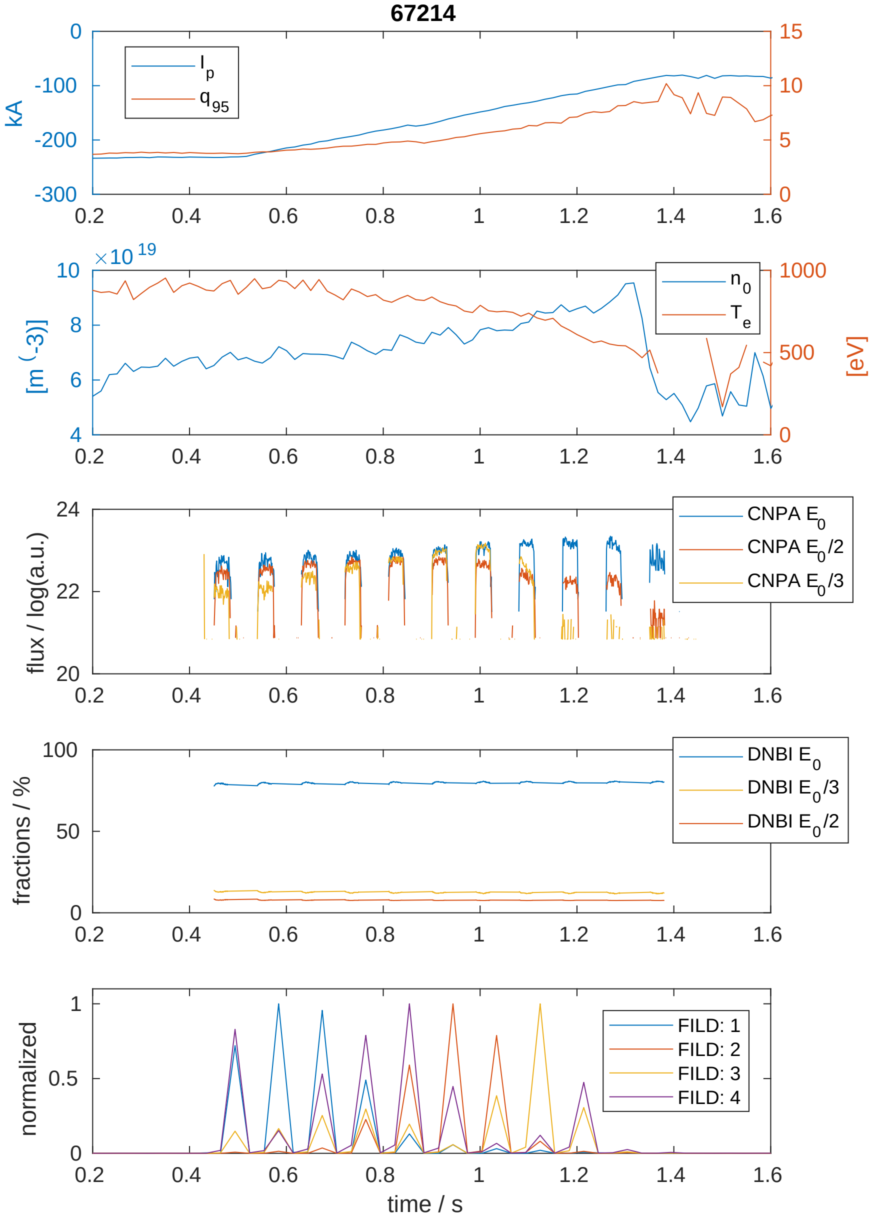

Figure 4.16: Shot 67214. Time evolution of plasma parameters: the plasma current and the q_{95}; the electron density and temperature for their impact on the DNBI deposition; the CNPA fluxes take into account the detector response, and clearly show the pulsed DNBI; the DNBI molecular components are reported as fractions of the total injected power; the FILD signals are the sum of the camera pixels belonging to four regions of the scintillator (1:top left to 4:bottom right) where emissions here studied where found.

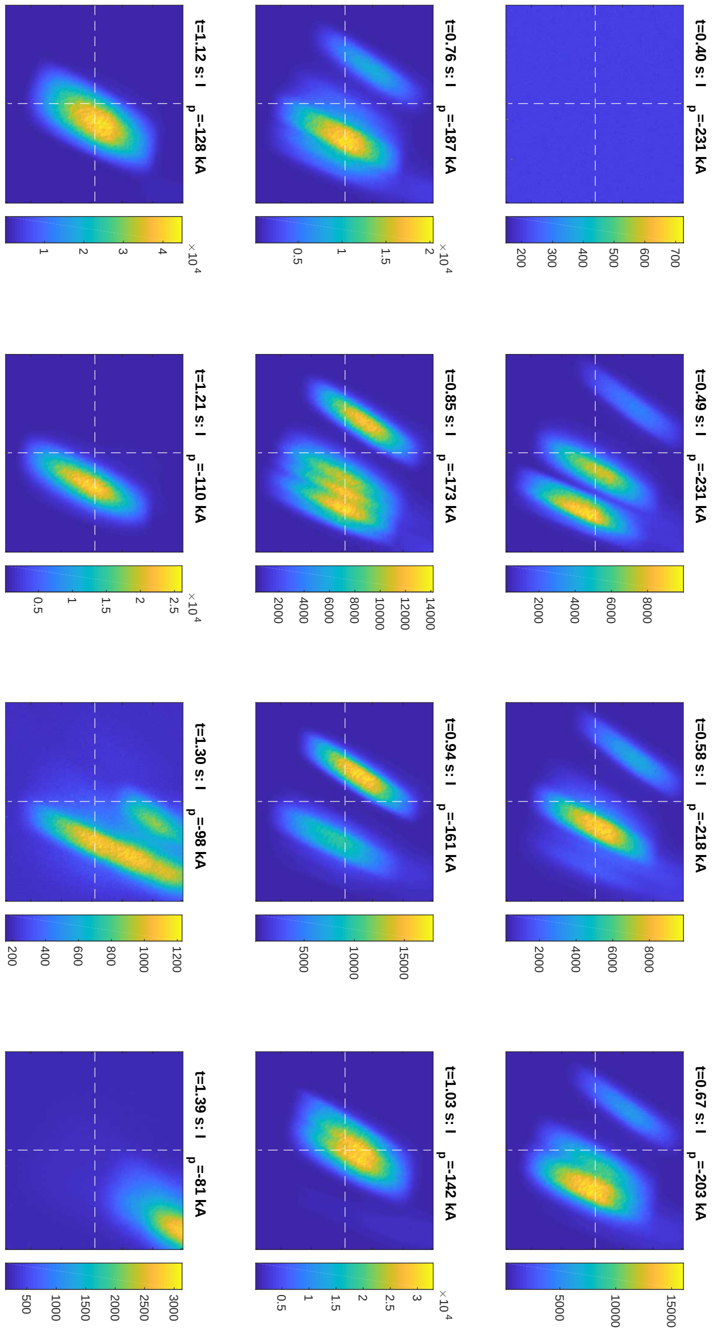

Figure 4.17: A sequence of PCO Panda frames at the times after the DNBI pulses such that the frame exposure was entirely within the beam pulse. A cross (dashed white) is depicted for reference. The units are the pixel counts.

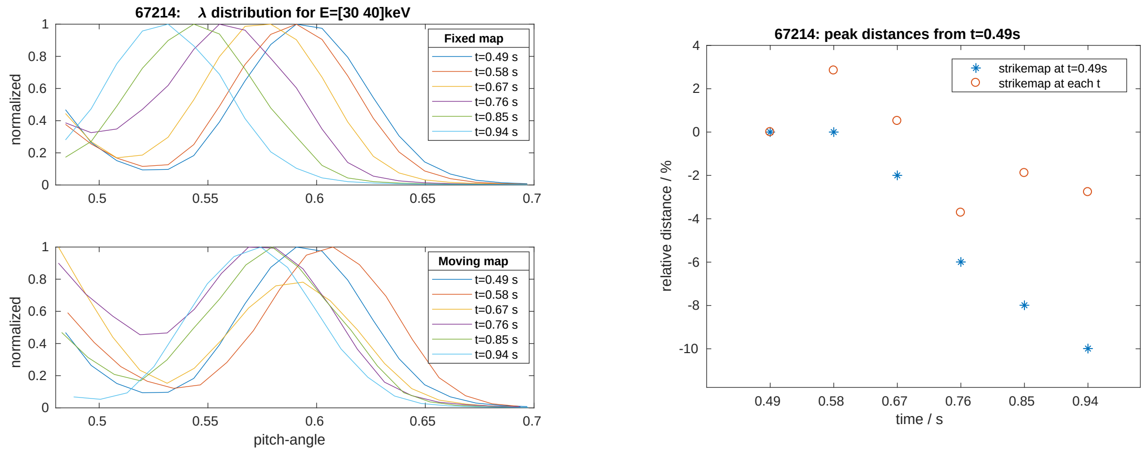

Figure 4.18: Shot 67214. (left) Pitch distributions after integration in energies $[30, 40]$ keV for each time. Comparison between "fixed" mapping, i.e. strikemap for $t_0 = 0.49$ s, and "moving" strikemaps for each time. (right) Comparison between the two mapping methods, as the relative distance of the distribution peaks from the one of $t_0 = 0.49$ s.

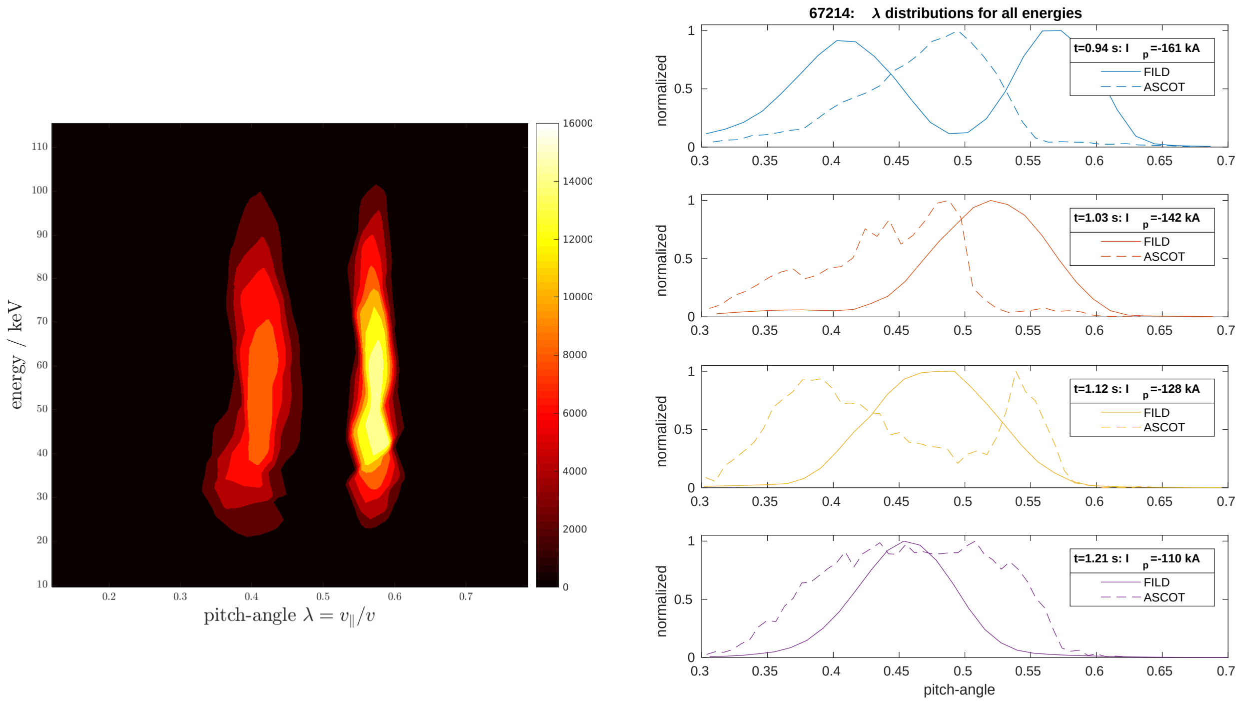

Figure 4.19: Shot 67214. (left) Mapped camera frame at $t = 0.94$ s. (right) Pitch distributions from the FILD measurements once mapped (solid) and the ASCOT simulations (dashed), integrated for all energies. The first plot (blue) corresponds to the measured velocity space shown on the left.

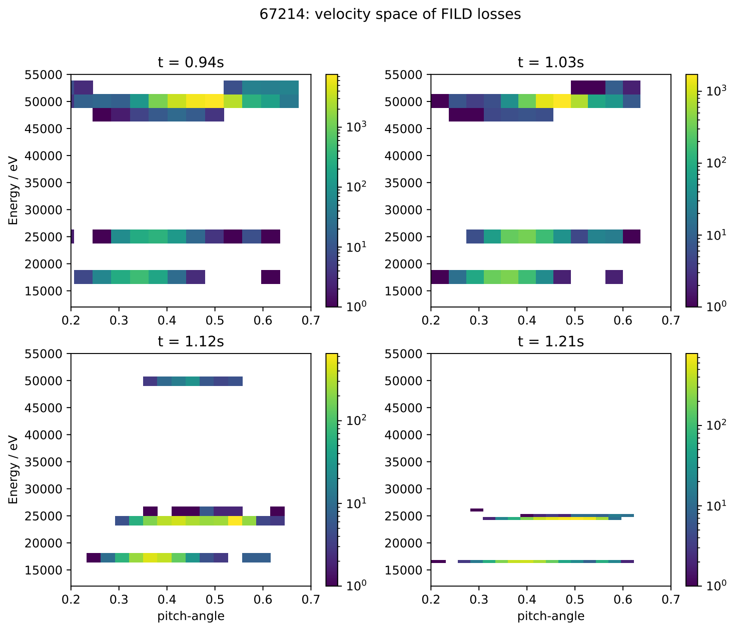

Figure 4.20: Shot 67214. The velocity space (E, λ) of the lost particles collected by the FILD, as simulated by the ASCOT code.

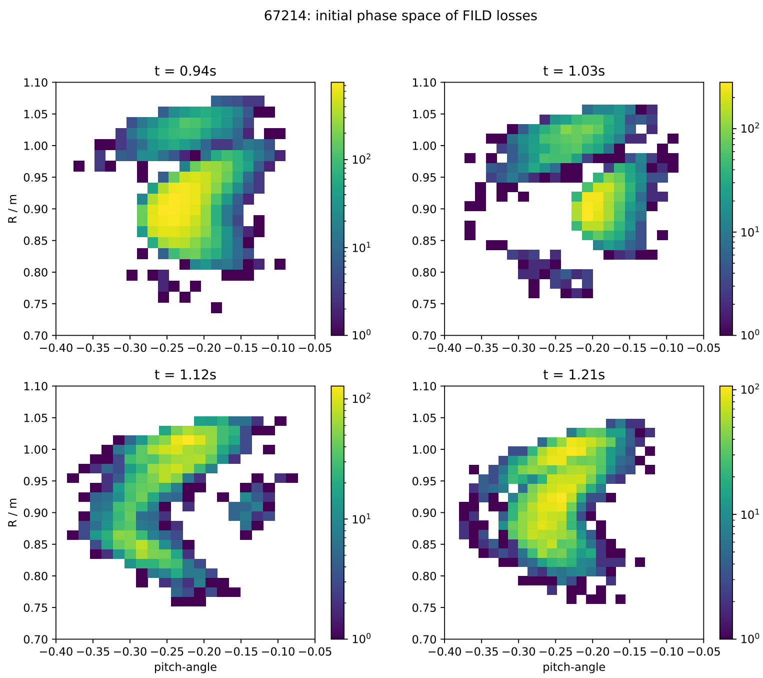

Figure 4.21: Shot 67214. The initial phase space (R, λ) of the ionized particles injected by the DNBI that result into FILD losses as simulated by the ASCOT code.

4.5 Operational limits

The positioning system radially deploys the probe head inside the vacuum vessel up to 25 mm from the first wall. This is defined as the circumference tangent to the graphite tiles of radius $R_{\mathrm{fw}} = 1136.7$ mm, which is taken as the "zero" position. Due to the particular geometry of the vessel port, however, the FILD slits are exposed to the particle flux even if placed farther than this limit of maximum 2 mm. Since the slits are 16 mm away from the innermost face of the heatshield, the maximum insertion of the slits is $r_{\mathrm{slit}} = -9.6$ mm.

As discussed in Section 3.2.3, there are two contributions to the heat load the graphite shield has to withstand: the bulk plasma and the additional NBH fluxes. When inserting the detector the minimum distance allowed between the plasma LCFS and the innermost surface of the graphite shield is equal to the largest Larmor radius. This is an arbitrary threshold that proved to be valid in avoiding excessive heating by the plasma.

The heat load delivered onto the probe head can be estimated by measuring the temperature of the graphite shield at its bottom side with the installed thermocouple. In discharges in which the NBH delivered approximately 1 MJ of total energy, temperatures up to 200° C have been recorded. Since the sampling time is limited to 2 s, that is of the order of the shot duration, the thermocouple signals feature sudden rises of the temperature at the shot time and the subsequent decay as the graphite cools on a time scale of several tens of minutes. This interval is often larger than that between successive shots. As a result, during a day of operations, the average temperature will increase. The thermocouple at the scintillator plate, instead, yields a signal that is lower in amplitude and smoother in time, as shown in Figure 4.22. This is due to much lower heating of this component through heat diffusion in the graphite and to the supports made of SHAPAL$^{\mathrm{TM}}$, a ceramic with good thermal conductivity that is suitable to evacuate the heat through the cantilever structure located in the port duct.

The increase of the probe head temperature, evaluated as the difference from the temperature before and after the shot, displays a robust linearity with the total energy delivered to the plasma by the NBH. In contrast, no dependencies were found with the total energy injected by the ECRH and the plasma Ohmic power integrated as a function of time, as shown in Figure 4.24. No correlation was found between the distance of the probe from the LCFS and the increase in temperature for the discharges with NBH, whereas a quite convincing relation was seen for the shots with fast ions from the DNBI, in which the detector was deployed below the safety limit of one largest Larmor radius. This may suggest that a dependence of the heat load on the LCFS-to-probe distance exists only for the smaller separations.

Although the thermocouples provide valuable data to monitor the thermal stress on the heatshield on the time scales of an experimental session ($\approx$ 1 working day), the temporal resolution and the location of the sensor to the other side of the shield face hampers any characterization of the overheating of the probe components. The combined information from the PCO Panda camera, looking at the scintillator plate and the surrounding inside the probe head, and a 90 Hz Raspberry Pi camera, looking at the probe head through a top vessel TCV port, turned out to be useful due to their higher resolutions.

When heated by radiation and particles, the graphite ablates. A plasma cloud, rich in Carbon, forms around the object. This strongly radiates and absorbs much of the incoming heat thus cooling and simultaneously shielding the heated surface. This is optimal for protecting the FILD probe head

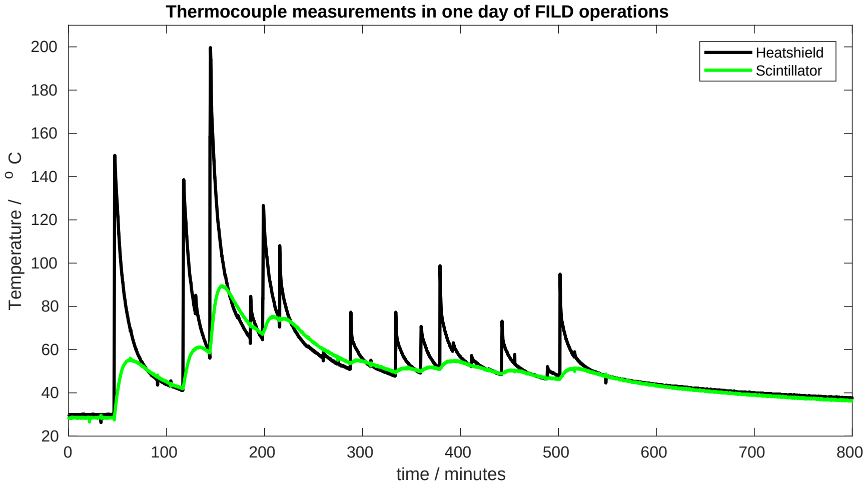

Figure 4.22: The heatshield (black) and scintillator (green) temperatures measured by the thermocouples across a day of FILD operations. A different behaviour in time is evident between the temperatures of the graphite shield and the scintillator plate, the latter appearing much more smoothed due to the heat conduction and dissipation inside the probe head. In the first 200 minutes an increase of the mean temperature is visible for both components following FILD insertions during plasma discharges with high power delivered by the NBH. From 200 minutes the probe slowly cools as a consequence of shots with reduced energy content. However, from the end of the daily operations, it takes approximately a night to restore the room temperature.

Figure 4.23: Two frames from the RasPi camera during the shot 68570 for the MST1 - Topic 11 experiments in TCV. (left) At $t = 0.45$ s the NBH injects 0.85 MW of power. The right side of the heatshield, seen from above, it is more illuminated by the circulating ions than the other side. (right) The heatshield glowing hundreds of milliseconds after the end of the discharge.

components. In effect, bright spots were found when viewing inside the probe head by the PCO Panda acquisitions, with pixel counts increasing seemingly exponentially with a characteristic time of $\approx$ 100 ms until a maximal emission is reached below the saturation level of the camera. A decay in the emission intensity follows on a timescale on the order of seconds at the end of the plasma-FILD interaction. These intense spots correspond to the sharpest edges in the outside of the heatshield where heat flux likely accumulates. The RasPi Camera also detected light emitted by these two spots, although it saturates. In the recorded frames these are found glowing from the end of the NBH pulse to $\approx$ 200 ms later. The time evolution of such emissions detected by both cameras is shown in Figure 4.25. A delay between the two curves of $\approx$ 200 ms is found. This may be ascribed to the thermal conductivity and thermal pulse transit time across the graphite. The characteristic decay times of the spot emissions from the two systems are very similar.

These hot spots were found in FILD measurements with maximum temperatures from 120° C, in plasma discharges in which NBH delivered a total energy above 800 kJ. In some of these cases, but not necessarily those with largest maximum temperatures, the graphite shield was seen to glow in visible light for several hundreds of milliseconds after the end of the discharge. An example is shown in Figure 4.23.

In conclusion, these findings suggest that long and intense NBH injection may, at some point, become detrimental to the integrity of the detector. The two cameras provide useful information to assess the degree of thermal stress the graphite shield underwent during the discharge, though a precise threshold was not encountered.

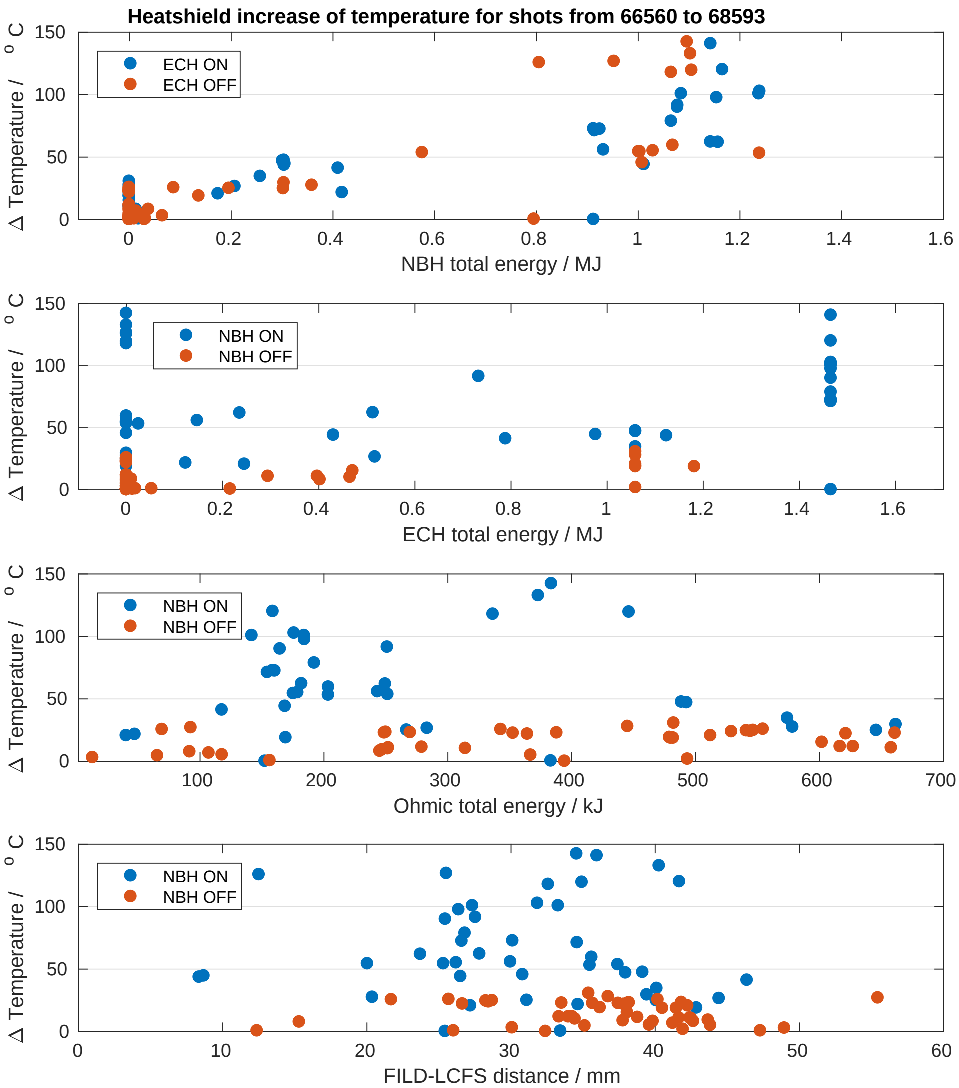

Figure 4.24: The heatshield increase of temperature measured by the thermocouple as the difference between the peak value and that before the shot. Discharges from July to November 2020 only are shown, since no data exist before. The total energy is equal to the time integral of the delivered power. The ECH (aka ECRH) power is the overall power from the X2 and X3 systems. NBH "off" means that the total energy is less than 100 kJ, while ECH "off" is for values less than 50 kJ.

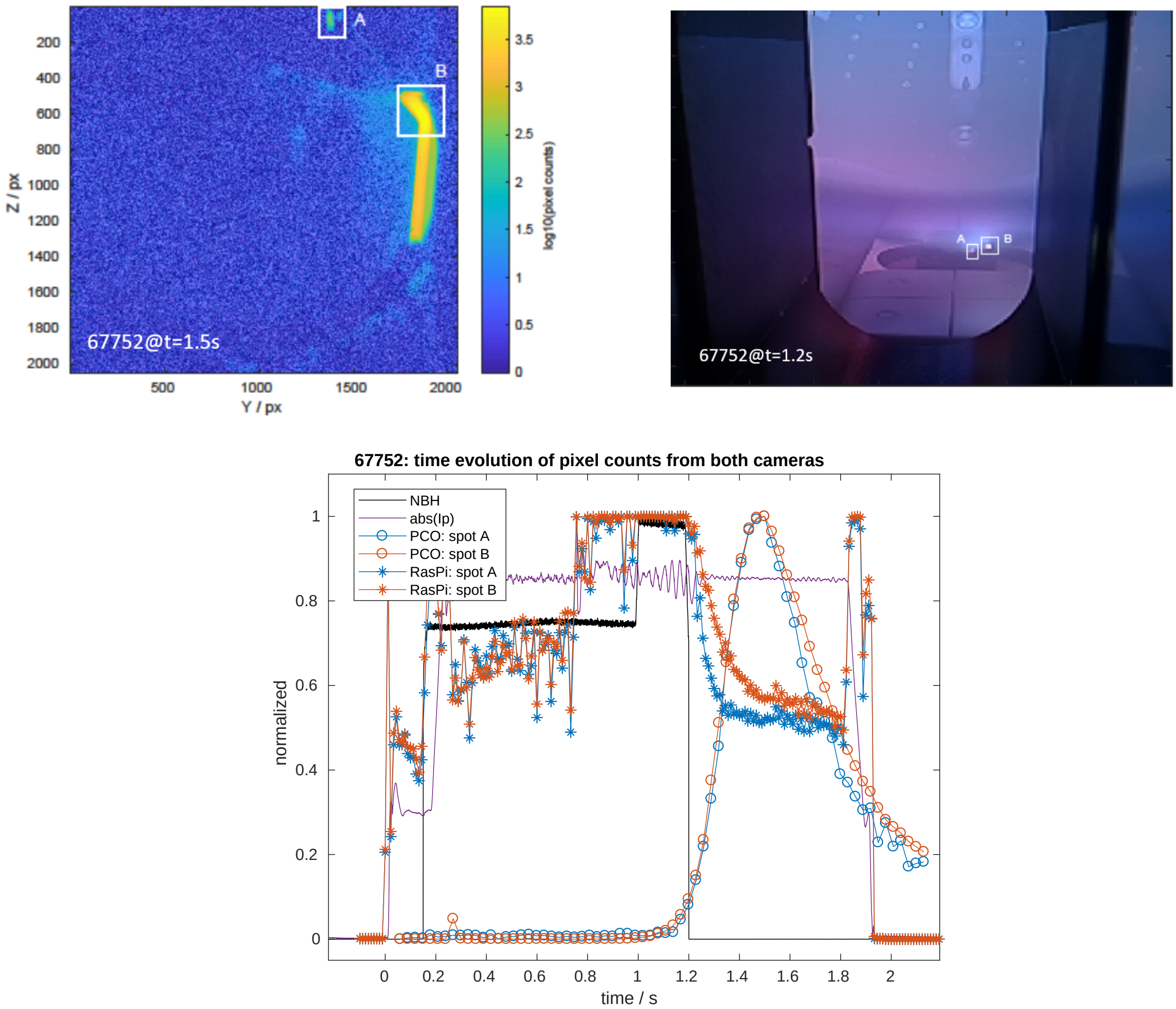

Figure 4.25: (top left) The PCO Panda frame at $t = 1.5$ s with pixel counts in logarithmic scale. The edges of the scintillator and the supports are visibile. The neat shape of the bright spot on the right makes clear that the emission comes from the graphite shield and the scintillator plate in foreground obstructs the light. (top right) The PCO Panda frame at $t = 1.2$ s where the two spots are seen glowing for some tens of milliseconds. The heatshield is seen from above. (bottom) Time evolution of the sum of counts of a of pixels from the region A and B. The PCO camera signals are well within the dynamic range of the camera while the saturated pixel counts of the RasPi camera for $t = [0.7, 1.2]$ s don't allow the characterization of the rise and decay of the light emission. The peak in the RasPi camera counts at the very end of the discharge at $t = 1.9$ s is due to the intense radiation emission at the disruption.

4.6 Conclusions

TCV-FILD was commissioned. It was demonstrated that the probe detects early fast-ion losses following injection from the NBI systems (NBH and DNBI) currently available on the TCV, in different plasma scenarios. These were designed with plasma current and toroidal field in both directions, to investigate the impact of these quantities on the fast-ion dynamics in a Tokamak plasma.

In particular, the plasma current direction “selects“ the FILD slit that may accept the lost particles. This proves the success of the unique double-slit design of TCV-FILD in experiments with co- and cntr-current energetic particle injections. Therefore, the detector will also provide valuable information for fast-ion studies once TCV is equipped with the second NBH system, injecting counter-clockwise with energies up to 60 keV, likely starting in 2021. This will access new scenarios for the excitation of magnetic fluctuations such as the AEs or other EP-driven modes (see Section 2.3.3).

In view of detecting early losses, in the absence of significant magnetic activities that can modify the Neoclassical transport displacing the fast ions into unconfined orbits, the instrument resolution and accuracy were assessed in terms of the velocity-space co-ordinates. The possibility of errors in computing the strikemap with the e-FILDSIM code due to inaccurate camera calibration and differences between the modeled and the assembled detector may cause discrepancies between the measured and the expected distributions in particle energy and pitch values. Also, the sensitivity of the detector to the magnetic field line direction was shown to affect the interpretation of these observations. A fine-tuning of the mapping by means of the elevation and azimuthal angles may help to reduce such inconsistencies. These techniques are employed in the analysis of fast-ion ejections by large events occurring in the plasma correlated with MHD instabilities, reported in Chapter 5.

The direct comparison of the FILD measurements with a synthetic fast-ion velocity space at the probe, as computed by codes such as ASCOT, revealed itself to be problematic. Even though the FILD weight functions are employed to account for the collimator effect on the particle trajectories inside the probe head and map the velocity space from the scintillator plate to the slit, large discrepancies remain. This may be caused by a too coarse-grained simulation of the fast-ion orbits in the vicinity of the detector. A more sophisticated strategy could employ multi-step simulations to firstly assess the phase-space regions of the particles potentially lost at the FILD and then massive refined runs of the code to achieve a statistically significant population of markers at the slit alone. Finally, a better estimation of the plasma parameters in the SOL regions where beam deposition is important, especially in nearly radial injection, may be helpful. Such a calculation heavy approach to experimental and modelling comparison was outside the scope of this thesis project.

The employment of the detector in plasma discharges with a range of fast-ion energy content, namely the 1 MW NBH or the low-power DNBI, requires the identification of a safe range of operations and radial positioning of the detector. A dependence of the heatshield temperature on the total energy injected by the NBH was found. The radial position seems to play a role only in cases of shorter LCFS-to-probe distances. However, in a precautionary approach, the detector was not deployed in the most advanced positions for the discharges with the NBH, therefore no clear prescriptions for the deploying of the probe in such discharges are currently available. The limits imposed by the NBH total energy may be problematic in future TCV plasma scenarios with simultaneous injection of both NBH systems. A strategy of increasing power injections, or equivalently duration of the beam pulses, shot-by-shot, is advised.

Chapter 5

Fast-ion losses correlated with MHD instabilities

5.1 Introduction

In the previous chapter TCV-FILD was shown to be able to detect fast-ion losses in a wide range of TCV plasma scenarios including different values and directions of the plasma current. These losses were mainly of injected particles, either from the DNBI or the NBH, deposited in the plasma in phase-space regions where they can escape from the confined region, on time scales of the order of several microseconds (early losses), when following unconfined trapped orbits or passing orbits with large radial outward shifts.

In this chapter the possible impact on the confinement of the suprathermal ion population of perturbations from the magnetic equilibrium is explored. For the first time in TCV, direct detection of fast-ion losses was performed in discharges experiencing large magnetic fluctuations. Following magnetic field reconnection, the crashes of the Sawtooth instability (ST) typically cause spatial internal redistribution of a sizeable portion of the plasma. Fast ions can be displaced onto unconfined orbits and some of these collected by FILD, giving fast light detected bursts ~ 10 μs long, starting some micro-seconds after the beginning of the crash. These are analysed in Section 5.2.

Fast-ion losses associated with Neoclassical Tearing Modes (NTMs) were also measured in TCV. The NTM instability manifests itself as a magnetic island that rotates in the toroidal direction, enhancing the outward transport of particles including energetic ions. NTMs are routinely found in TCV discharges. The FILD fast light detection displayed fast-ion ejections correlated in time and with strong phase coherence with the magnetic signals monitoring the NTM evolution. The measured lost particles are therefore termed *coherent losses*, and are investigated in Section 5.3 together with the possible impact of this instability on the velocity space of such particles.

5.2 Plasma redistribution by sawteeth

5.2.1 The sawtooth instability

Soft X-Ray (SXR) emissions with sawtooth-shaped signals in time were first observed on ST-Tokamak discharges in 1974 [32]. These are due to the increase of the plasma pressure in the core on time ranges of $1 \div 10$ ms, followed by a fast (~ 100 μs) drop in emissivity, or *crash*, causing a flattening of the temperature around and inside the $q = 1$ flux surface. It is possible to identify this position, termed *inversion radius*, comparing LOS of the SXR diagnostics (e.g. DMPX on the TCV) crossing different flux surfaces where the ST oscillation traces are opposite in sign.

These repetitive modifications of the plasma pressure profile and q-profile were described by the Kadomtsev model of magnetic reconnection [47]. A resistive $m/n = 1/1$ kink mode is driven unstable when the $q = 1$ resonant surface appears in the plasma. Field line reconnection produces a cooler island that moves outwards until it collapses eventually reducing the observed SXR emission, namely the crash. More recent descriptions employ more sophisticated modelings of the evolution of the MHD kink mode as it interacts with trapped thermal and/or energetic ions [8].

The ST crashes may exhibit a magnetic precursor that is detected by pick-up coils at the wall. In some TCV discharges with quasi-tangential NBH injection, such magnetic activities appear as fishbone-like signals, as shown in the rhs plot of Figure 5.3. Unlike the classical Fishbone instability that may be found many times during a single ST cycle and is the result of a resonant interaction between a $m/n = 1/1$ mode and trapped fast ions (see Section 2.3.3), the observed fluctuations can be due to passing particles resonating with a mode of the same helicity at frequencies of the order of tens of kHz, in the vacuum vessel reference frame [42, 41]. This unstable mode was observed in TCV plasma discharges with NBH injection of Deuterium with maximum energy of 25 keV. An example is the shot 53454 that exhibits sawtooth oscillations with varying periods: from some milliseconds, when the ECRH is on, to tens of milliseconds after the ECRH is turned off with NBH is still on. At each ST crash a magnetic burst is found with a frequency peak at $f_1 = 26$ kHz. A second harmonic may be present at $f_2 = 53$ kHz. The spectral composition of a Mirnov coil's signal was found by computing the Power Spectral Density (PSD) estimated with the Modified Covariance method (MATLAB built-in). This consists in fitting the signal with an Auto-Regressive $AR(p)$ model of order p and the PSD evaluated analytically. The order of the model is chosen by eye.

By performing the FFT (Fast Fourier Transform) of the magnetic signals, the n and the m mode numbers can be identified from the evolution of the phase of the dominant components (f_1 and f_2) across the probes at different ϕ angles (toroidal array) and θ angles (poloidal array), respectively. Robust evidence is found for a toroidal mode number $n = 1$ for the first harmonic and $n = 2$ for the second. The FFT of the poloidal array's signals show a much more complex structure. This can be due to the distance of the probes to the plasma volume and the strong ballooning character of this mode. By taking only the probes attached to the LFS wall, which are the most significant due to a higher S/N ratio, the phase analysis indicates $m < 4$. This value is larger than the expected $m = 1$ (for the first harmonic), which ideally characterizes the mode resonating with the passing particles in the plasma core. Such a discrepancy is usually due to the presence of several components with different poloidal mode numbers and radial extents, that can be enhanced at the resonant surfaces where damping by magnetic shear is reduced. As a result, a combination of these components can be detected by the Mirnov coils located outside the plasma volume thus giving a non-integer number close to the last

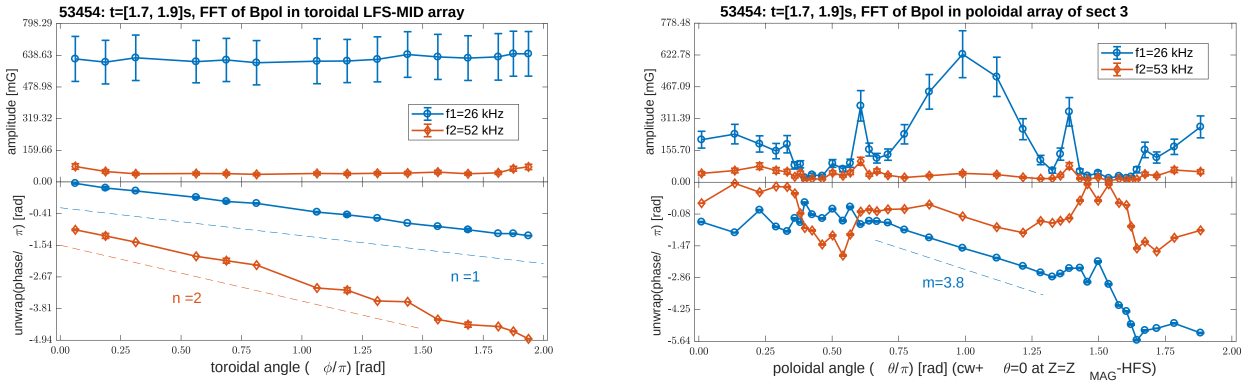

Figure 5.1: Shot 53454, analysis of the phases for the main spectral components as found in the magnetic signals from the Mirnov probes. (left) Toroidal array in the outer midplane (LFS-MID). (right) Poloidal array in sector 3.

resonant surface present in the plasma.

The radial shape of the mode can be inferred from the cross-correlation between the Mirnov coil signals and the C-ECE diagnostic able to detect fluctuations of the Electron Cyclotron Emissions at six radial locations, as described in Section 2.5.6. The underlying assumption is that these fluctuations are, in part, produced by the MHD mode here investigated. This mode is found to peak at $\rho_\psi \approx 0.2$. This corresponds to the position at which the $q = 1$ surface appears in the plasma before the ST crash. The q-profile was estimated from the evaluation of the plasma pressure as modified by the NBH injection and by the presence of ST oscillations with the ASTRA code [64]. Such a technique is an example of MHD spectroscopy in which the location of a resonant surface $q = m/n$ may be identified by the analysis of a (m,n) coherent magnetic perturbation and validation from numerical tools.

Finally, the amplitude of the mode in the plasma core can be estimated by assuming a relation of proportionality between the perturbation amplitude and the cross-correlation power as the integral of the cross-PSD over the mode peak of frequency f_1. This is fitted with a Gaussian shape and matched at the LCFS to the value estimated in the vacuum-approximation $\delta B_\theta \propto r^{-|m|-1} = r^{-4}$ with the Mirnov coils measurements at the wall $\delta B_\theta \approx 640$ mG as boundary conditions. This method, however, does not include the jump at the plasma-vacuum interface of the poloidal component of the magnetic perturbation. An improved modeling may be assumed to numerically compute the radial extent of the mode inside the plasma so as to be later compared to the C-ECE measurements, although this is out of the scope of this study. It is found a peak value at the $q = 1$ surface of $\delta B_\theta \approx 20$ G, on the left of Figure 5.2, that is $\sim 10^{-3}$ times weaker than the equilibrium field.

Correlated in time with the sawtooth crashes, CNPA increased counts of $\approx 30\%$ are found in Deuterium energy channels spanning some keV up to the NBH maximum energy of injection (channel 23 keV), see Figure 5.2. This suggests that cycles of long period sawteeth may affect the ion distribution function by displacing it outwards where the neutralization efficiency is higher so that more neutrals are seen by the CNPA.

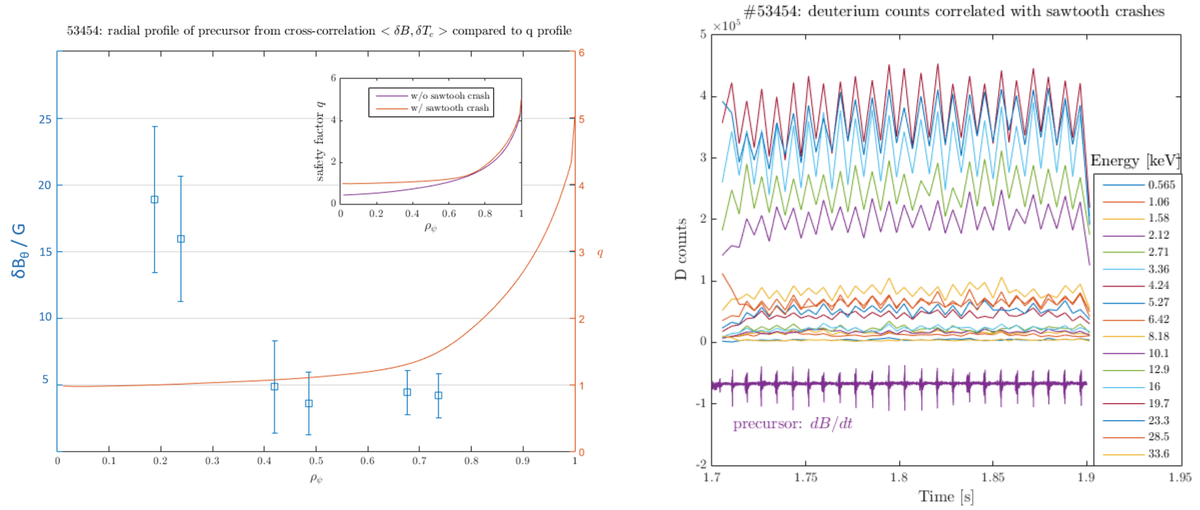

Figure 5.2: Shot 53454. (left) Radial profile of the magnetic perturbation, here referred to as ST precursor, from cross-correlating the magnetic probe and C-ECE signals at 6 radial positions. In the nested plot, a comparison between the ASTRA simulations with and without accounting for plasma pressure modifications at the onset of the ST crash are shown. (right) Averaged counts of escaping neutrals as detected by the CNPA (with sampling time of 1 ms) are shown to be correlated in time with the magnetic precursor, several Deuterium energy channels from ≈ 4 keV.

5.2.2 Sawtooth stabilization

ST instability is usually found in Ohmic discharges with sufficient plasma current. However external sources of plasma heating have an impact on the duration of the sawtooth cycle. The lengthening of the sawtooth period is termed ST stabilization.

Power deposition by ECRH in the nearby of the $q = 1$ surface alters the local current profile by increasing T_e, so reducing the plasma resistivity, increasing the plasma current and decreasing the q value. If such deposition occurs inside the resonant surface then the safety factor profile becomes steeper and the magnetic shear increases such that the island collapse occurs earlier (ST destabilisation). The same happens if co-I_p ECCD is applied. This was found, for instance, in shot 53454 (investigated in Section 5.2.1 for characterising the magnetic precursor at the ST crash). Different heating schemes were applied in this discharge: ECRH, ECRH+NBH and NBH alone. While the first two regimes featured ST periods of the order of some milliseconds, in the phase with only NBH the period was measured to extend up to 20 ms, as shown in Figure 5.3. Injection by the NBH of co-I_p passing energetic ions can result in ST stabilization [8]. However a co-I_p ECCD of the order of 0.1% of the total plasma current was found to be able to cancel this stabilizing fast-ion effect and reduce the ST period an effect that could also be achieved with small amounts of non-induced currents [54].

Longer ST periods may be achieved also with cntr-I_p ECCD or by delivering ECRH power slightly outside the ST inversion radius. As a result, the island grows larger and the collapse leads to a more intense plasma redistribution and possibly to secondary instabilities. This may incur a larger effect on the fast-ion confinement thus leading to an increase of detected losses by the FILD compared to cases

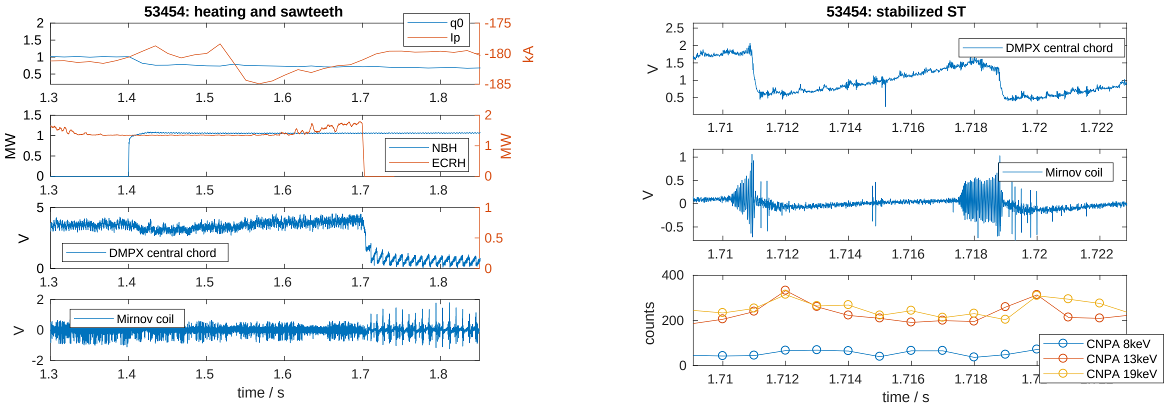

Figure 5.3: Shot 53454. (left) Different heating schemes applied during the shot and their effect upon the sawtooth SXR emission. (right) Close-up with NBH alone of long ST accompanied by fishbone-like magnetic bursts and increase of CNPA counts in the high energy channels.

with shorter ST periods.

5.2.3 ST-induced fast-ion losses in discharges with NBH

Sawtooth stabilization by ECRH was employed by analyzing the impact of a range of ST periods on the fast-ion ejection measured by FILD fast light detection system. Shot 68593 includes a scan of the B_ϕ amplitude in time, while keeping the X2 launcher parameters and the plasma current constant, so as to displace the power deposition position (that occurs at a fixed and resonant magnetic field) to inside the inversion radius. Figure 5.4 shows that sawteeth with periods up to 20 ms, hereafter termed "long ST", for $t \in [0.4, 0.72]$ s. Conversely, toroidal fields below -1.42 T shortened the ST periods to ~ 10 ms ("short ST"). No ST were seen with the NBH off.

Neutral Deuterium atoms were injected by the NBH with 0.35 MW of power to avoid vertical instabilities potentially leading to plasma disruptions. At this power level, according to the relation in Figure 2.10, the energy of the primary beam component is equal to 17 keV. Very few particle losses at the FILD were predicted by the ASCOT code in an axisymmetric equilibrium. This is consistent with the initial phase space of the injected particles, shown in Figure 5.5, which are mostly in well confined passing orbits.

Bursts in magnetic pickup are found in the Mirnov coil signals at the ST crashes. However, these are not characterized by a fishbone-like shape, such as the case discussed in the previous section and shown in Figure 5.3.

FILD scintillator emissions were detected during the phase of the discharge with sawteeth. Such emissions don't move in time on the scintillator plate, and feature a non-periodic time-varying intensity, increasing on average, as it is visible in Figure 5.6. From the fast signal, this is ascribed to the cumulative effect of several crash-caused fast-ion ejections that are averaged by the camera's sampling time, that is longer than the ST period.

Figure 5.7 shows a camera frame mapped to the local (in the scintillator plate) fast-ion velocity space. The energy and pitch distributions for the two brightest spots around $\lambda_1 = 0.6$ and $\lambda_2 = 0.65$

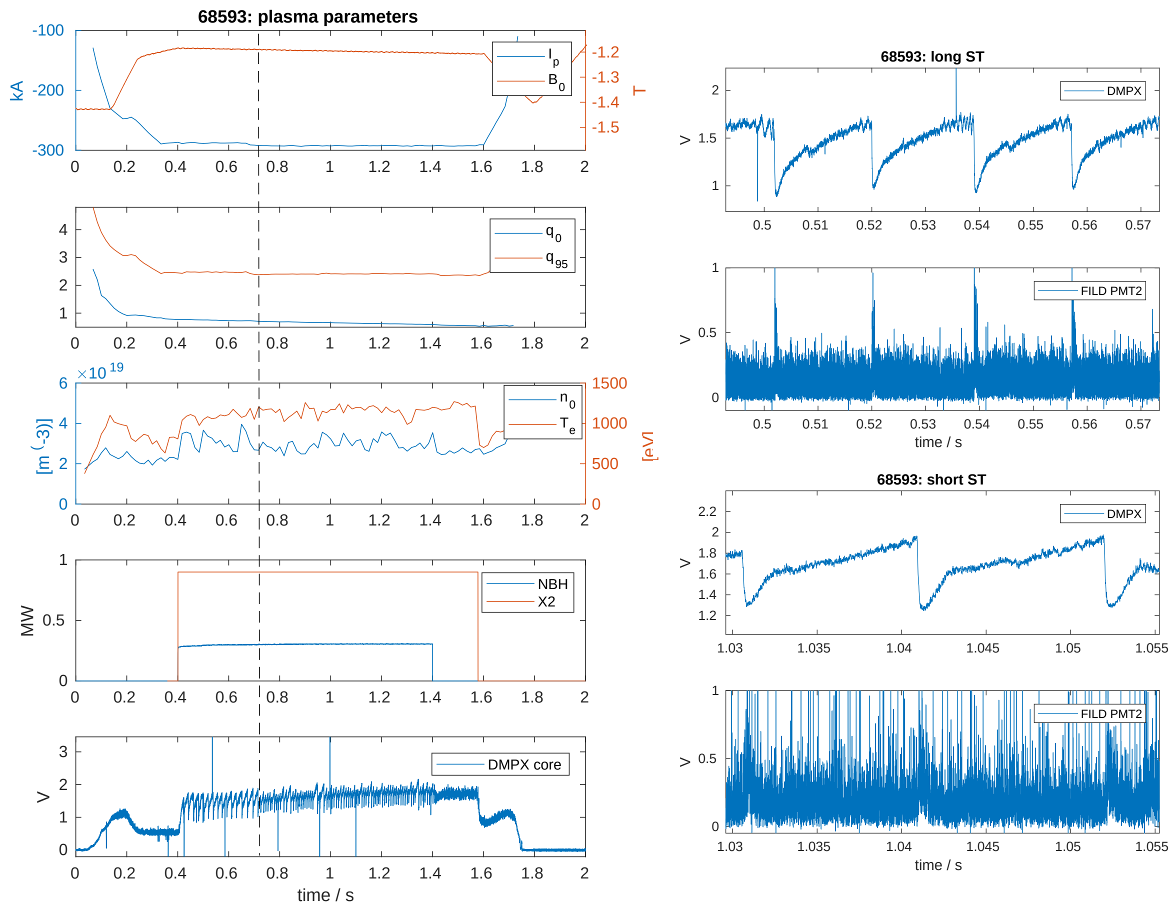

Figure 5.4: Shot 68593. (left) Plasma parameters in time during the discharge. The dashed black line crosses the B_ϕ threshold for the optimal ST stabilization by ECRH during the toroidal field scan. (right) Signals from the DMPX central chord and the FILD PMT2 at a ST crash during the "Long ST" (top) and "Short ST" period (bottom), where the S/N ratio is much higher.

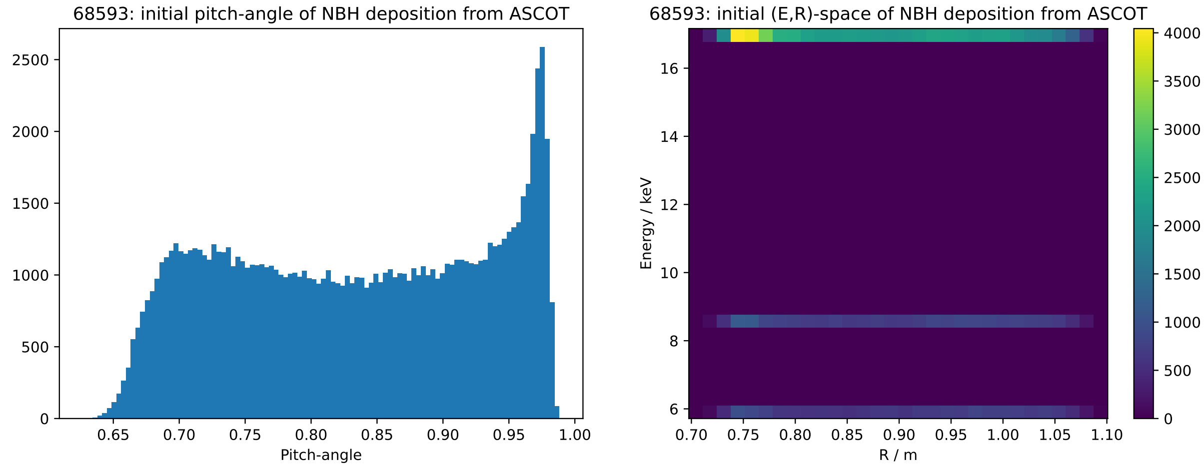

Figure 5.5: Shot 68593, ASCOT/BBNBI evaluation of the NBH deposition at $t = 0.90$ s. (left) Pitch distribution. (right) (Energy,R)-space of the fast-ion distribution.

are indicated. As discussed in Chapter 4 some fine-tuning of the e-FILDSIM simulation parameters is usually necessary to match the expected loss energies with the measurements. In this case, however, small changes of the value of the elevation angle θ (between the magnetic field line and the equatorial plane) didn't produce significant changes. It was found that the measured energy distribution of the pixel count for the λ_1 spot is close to the 20 keV-weight function, thus slightly above the maximum energy available from the NBH, although well within the estimated uncertainty of the detector's calibration (but not resolution). The emission at λ_2, instead, appears peaked at the same values as the 17 keV-weight function. In addition, an emission spot, nearly 5 times weaker than the others, appeared, in a similar range of energy values, for pitch values around $\lambda = 0.3$. This scintillator excitation is likely caused by impinging particles following trapped orbits, a small fast-ion population, although not negligible, in case of NB tangential injection.

The PMT2 of the fast light detection system displays short-lived signals occurring at most of the ST crashes, regardless of the regime of ST stabilization. An example is shown in the plot on the left of Figure 5.8. A strong peak is typically found followed by a lower amplitude tail, that remains above the noise level few milliseconds, at the beginning of the next ST cycle. By normalizing the ST period and averaging the FILD signals among all the crashes, a technique called *conditional averaging*, small but significant differences are found between the signals acquired for Long and Short sawteeth, as shown in Figure 5.9.

A roboust linear proportionality was revealed between the relative change of the SXR intensity from DMPX and the subsequent increase of scintillator light emission for all the analysed ST crashes.

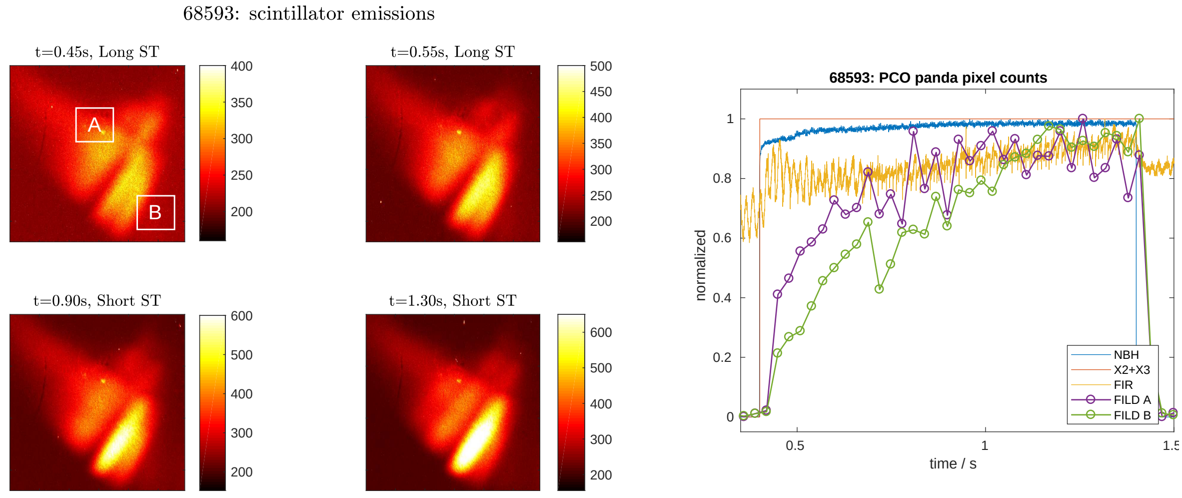

Figure 5.6: Shot 68593, PCO Panda camera pixel counts. (left) Scintillator emissions at different times. (right) Normalized camera pixel counts in time of the two spots A and B of the plot on the left. Also the plasma current, heating power and the line integrated density (FIR) that show the ST oscillations, are drawn.

This is reported in Figure 5.10. The DMPX and FILD changes in amplitude are defined as

$$\Delta(DMPX) = \left| \frac{V_{\text{before}} - V_{\text{crash}}}{V_{\text{before}}} \right|, \tag{5.1}$$

$$\Delta(FILD) = \frac{\int V(t)\mathrm{d}t_{\text{all}} - \int V(t)\mathrm{d}t_{\text{before}}}{\int V(t)\mathrm{d}t_{\text{before}}}, \tag{5.2}$$

where "before" means several hundreds of microseconds before the ST crash, i.e. during the ramp of the sawtooth oscillation.

Longer sawteeth periods are correlated with stronger DMPX signal jumps. In the case of Long ST, the FILD signal jumps are more scattered and a linear regressor only becomes statistically significant if the 3σ outliers are excluded.

These findings support the hypothesis of a relation between the observed global impact on the plasma of a ST crash and a fast-ion phase-space redistribution causing additional losses. By assuming flux surfaces frozen in the plasma (except for the reconnection region) and neglecting collisions since the slowing-down time ($\sim$ 10 ms) is much longer than the ST crash timescale ($\sim$ 100 μs), the fast-ion motion can be described as affected by a radial $E \times B$ drift arising from an electric perturbation linked to the $m/n = 1/1$ kink instability of the sawtooth [51]. This outward drift can displace the fast ion trajectories into unconfined orbits. Alternatively, the ideal magnetic perturbation may move those fast ions at the edge of the plasma volume so as to produce losses. The measured energy distributions of the impinging losses not perfectly match the NBH maximum injection energy, although such discrepancy is within the detector errors. CNPA measurements, reported in the rhs plot of Figure 5.8, show no

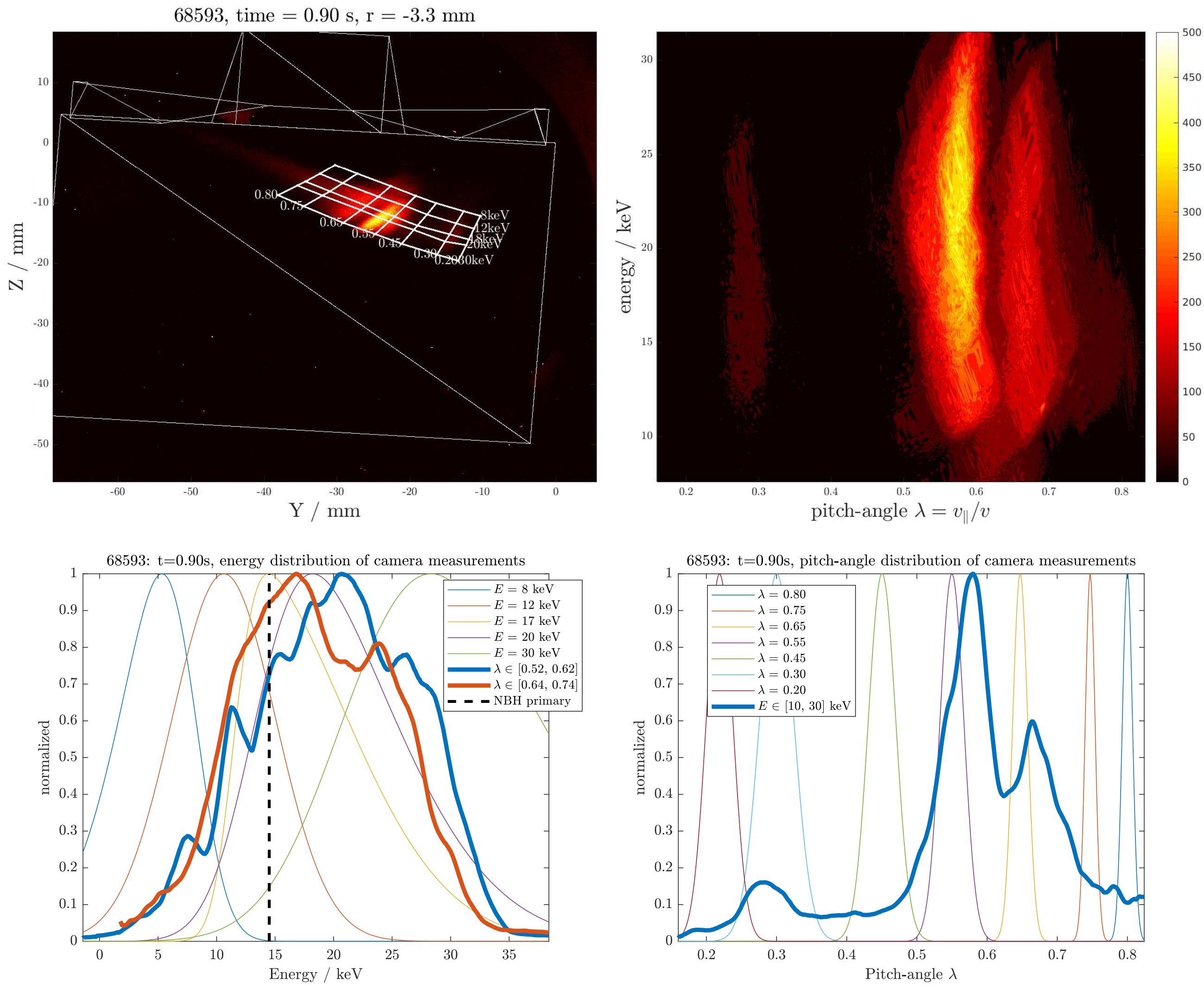

Figure 5.7: Shot 68593 at $t = 0.9$ s. (top) Scintillator emissions mapped to the local velocity space. Note that the strikemap is not smooth due to an insufficient number of markers for some (E, λ) value pairs. This, however, does not unduly affect the mapping to velocity space. (bottom left) Energy distributions of camera pixel counts for two ranges of pitch values corresponding to the brightest spots. The weight functions are similar for the mean values of the two λ ranges considered. The x-axis is the particle energy at the scintillator plate. The dashed black line points to the peak of the weight function for the maximum beam energy at the slit. (bottom right) Pitch distributions of camera pixel counts for the energy range $[10, 30]$ keV. The x-axis is the particle pitch value at the scintillator plate.

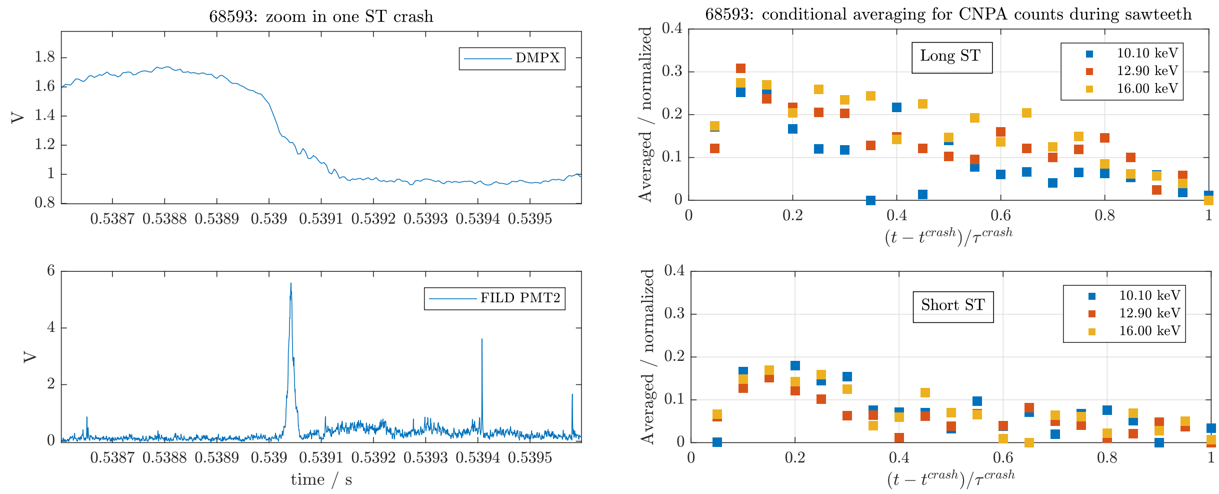

Figure 5.8: Shot 68593. (left) Zoom over a ST crash from the DMPX central chord and the signal from the FILD PMT2. The spikes after $t = 0.5394$ s are due to spurious ambient photons. (right) Conditional averaging at ST crash for the CNPA Deuterium counts.

significant increase of counts of neutrals with energies well above 17 keV. This can be used as proof that the mapping of the scintillator emission shown in Figure 5.7 is partly incorrect. An important caveat is that the two diagnostics probe different regions of the fast-ion phase space, such that a comparison is imprecise without a numerical estimation of the 5D distribution of the energetic ions as they interact with strong sawteeth. For this reason, although not supported by the reported measurements, ion acceleration due to electric field perturbations at ST crashes cannot be excluded. Numerical modeling by the TRANSP code to calculate the evolution of the fast-ion distribution in discharges with sawteeth on NSTX-U Tokamak is reported in [56].

The displacement of the energetic ions in the outer regions of the plasma volume, where the trapping condition becomes stronger, may result in trapped orbits eventually lost to the FILD. This can explain the observed weak spot of emission around $\lambda = 0.3$, since no such values of pitch were initially deposited by the NBH in the plasma.

In conclusion, it was shown that the ST stabilization can play an important role in controlling the extent of such ejections that are detrimental for sustaining a burning plasma (in large devices such as ITER) with the α particle heating, or reducing the negative impact of similar instabilities on the plasma stability and confinement.

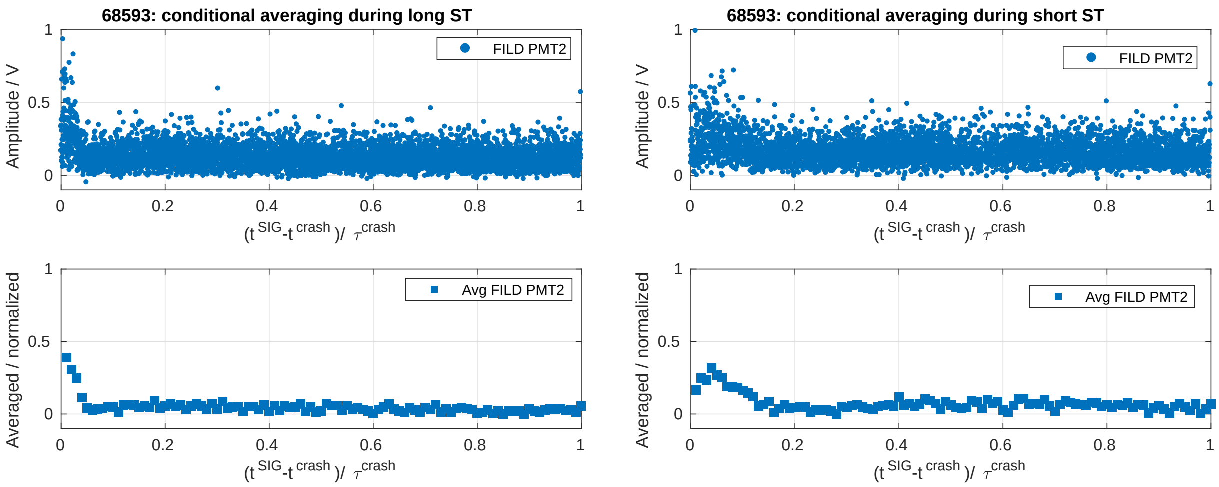

Figure 5.9: Shot 68593, conditional averaging of the FILD PMT2 signals across many ST crashes (left) For the long period ST in $t = [0.4, 0.72]$ s. (right) For the short period ST in $t = [1.05, 1.3]$ s.

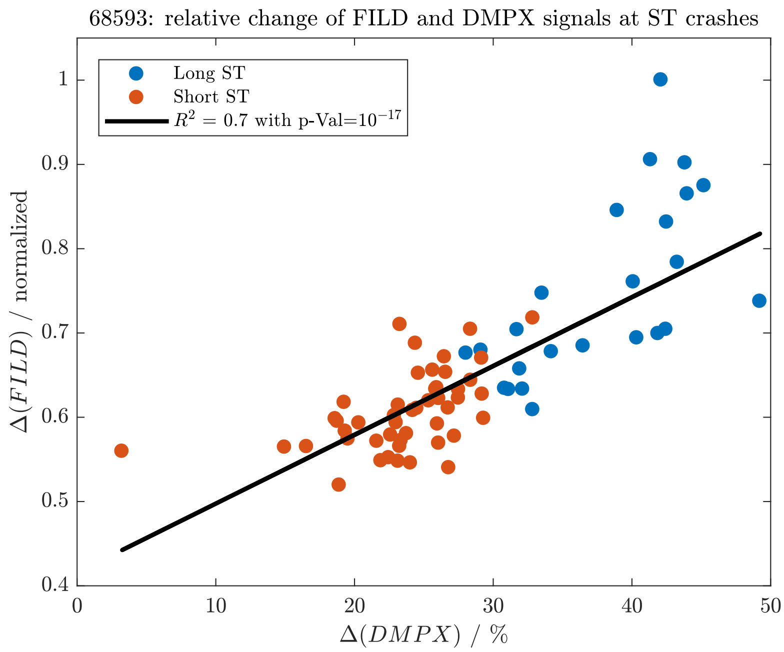

Figure 5.10: Shot 68593. A linear regression between the relative changes of the DMPX central chord and FILD PMT2 signals at each ST crash. Some data, outside 3σ, were excluded from the regression.

5.3 Fast-ion coherent losses associated with NTMs

5.3.1 Neoclassical Tearing Modes

In Section 5.2 the ST crashes were described as a consequence of magnetic reconnection occurring in the vicinity of a resonant surface. The appearance of a magnetic island generally causes a flattening of the plasma pressure profile across the island width due to the high parallel heat conductivity. As a consequence, this lowers the toroidal *bootstrap current*, determined by the trapped bulk particles that are dependent on the radial gradient of the plasma pressure. A negative perturbation of such current can reinforce the initial magnetic perturbation, with dominant mode components typically characterised by $m/n = 2/1$ or $3/2$, thus making the island grow larger. However, a *seed* island of minimal width is required to drive this mode unstable. This is called a Neoclassical Tearing Mode (NTM) [6]. A seed island can be provided, for instance, by a ST instability [73]. The NTM propagates in the plasma rest frame with electron diamagnetic drift frequency, in TCV of the order of a kHz. Moreover, since the vacuum vessel is a conducting shell, induced currents may produce a force on the plasma such that the island may slow down and *lock* [53]. NTM locking is responsible for the lowering of the maximum achievable β (the ratio between kinetic and magnetic pressure) and causing reduction in energy of the confinement [73]. Following growth, an NTM may saturate so as to not cause plasma disruption and have several cycles of oscillations for a significant portion of the discharge duration.

5.3.2 Measurements of fast-ion losses

NTMs were identified in TCV in discharges with heating provided by NBH and ECRH [62]. For instance, in shot 68506 an NTM was found with a frequency evolving in time in the range $2 \div 8$ kHz during few hundreds of milliseconds from $t = 0.39$ s. This behaviour is shown in the spectrograms of Figure 5.11 of the signals from the Mirnov coil closest to the FILD and the PMT2 employed for fast light detection of the FILD scintillator emissions collected across the entire plate.

The spatial structure of the observed NTM is characterised by an $n = 1$ toroidal mode number and, as usual for such perturbations, a superposition of more poloidal mode numbers that gives a total $m < 3$. In other words, a dominant $m = 2$ mode will be "polluted" by other m-components. The identification of the m number was conducted by taking into account only the Mirnov probe signals on the LFS with a sufficient S/N ratio, as discussed in Section 5.2.1. The amplitude of the perturbation measured at the wall is around 800 mG, i.e. $\sim 0.1\% B_\theta$. In Figure 5.12, also a weaker second harmonic was also observed, though with a difficult to ascertain poloidal mode number. In the plot on the left of Figure 5.14, the NTM can be seen rotating toroidally in a counter-clockwise direction (TCV seen from above) from the phase of the magnetic oscillations as detected by a set of Mirnov coils, namely the LFS-MID array (8 probes with good S/N ratio, in non equispaced toroidal positions, in the outer midplane). The rotation direction is consistent with the positive sign of the n toroidal mode numbers of the mode harmonics, according to the TCV co-ordinate convention.

As mentioned above, spectra of the magnetic and the FILD signals exhibit similar features that suggest the existence of a direct relation between the observed magnetic perturbations, as sinusoidal oscillations, and the increases of scintillator emissions caused in the FILD. In effect, the FILD signal was found to be strongly time-correlated with the perturbations of the magnetic poloidal component, see lhs plot in Figure 5.13. This *phase coherence* is further demonstrated by plotting the FILD PMT2

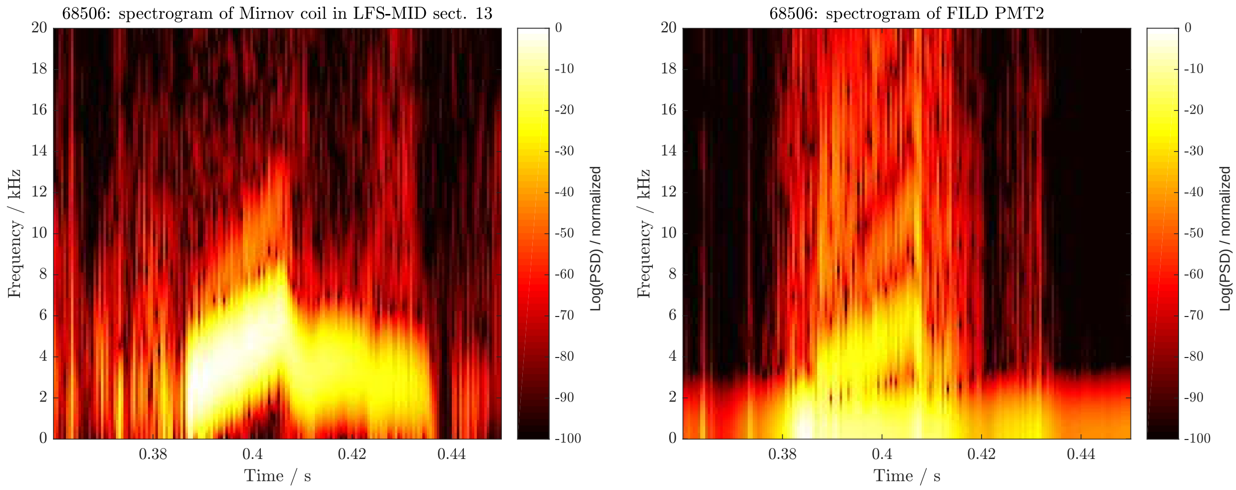

Figure 5.11: Shot 68506, time interval with NTM detected activity. Spectrograms of the Mirnov coil signal in the LFS-MID array sect. 13 (left) and the FILD PMT2 signal (right), computed by the Welch method for the PSD, number of FFT points = 1024.

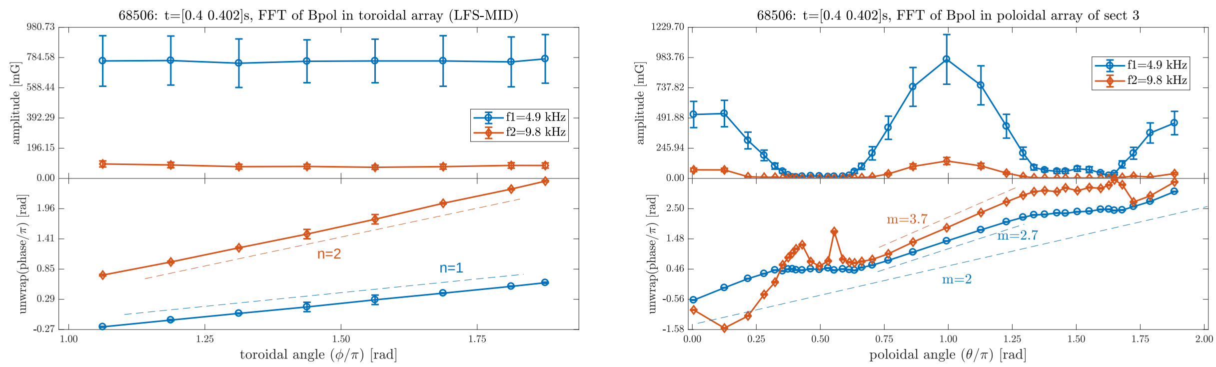

Figure 5.12: Shot 68506, in the interval $t = [0.4, 0.402]$ s featuring NTM oscillations in the Mirnov coils' signals. FFT analysis of amplitude and phase of the components at the frequencies of two harmonics. (left) Identification of the n-numbers from selected probes of the toroidal array in the midplane (LFS-MID). (right) The same analysis for the poloidal array in sector 3. The S/N ratios of such probes clearly vary so only those facing the plasma on the LFS nearby the midplane ($\theta/\pi \approx 1$ in the x-axis) are meaningful in extracting the m-index.

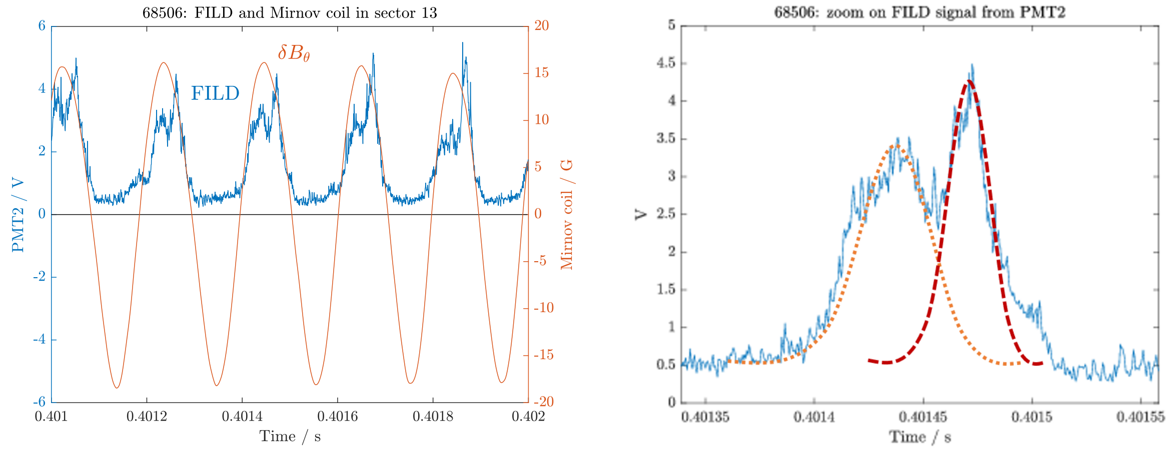

Figure 5.13: Shot 68506. (left) FILD PMT2 and the poloidal component of the magnetic perturbed field from the closest Mirnov coil to the FILD. (right) A zoom of a single strong scintillator emission during the phase with NTM. Bell-shaped curves are superimposed to the double-peaked signal to guide the eye.

amplitude in Volts against the integrated in time and calibrated (measured in Teslas) signal from the Mirnov coil closest to the FILD location (outer midplane, sect. 13). In the plot on the lhs in Figure 5.15, magnetic perturbations in the positive poloidal direction are shown correlated with the increase in scintillator emissions. The peaked traces that can be seen in this plot to the right of "zero" line (dashed black) are due to the specific shape of the FILD trace. The measured photon flux doesn't display a sinusoidal shape but appears, at least often, as the superposition of two peaks with different amplitudes and widths. Steep rising and falling edges of such signals are evident in the rhs plot of Figure 5.13, where two arbitrary bell-shaped curves are drawn to describe the double-peak feature that tracks each NTM cycle. This can be due to a loss mechanism acting differently and in delayed times on the fast ions. A hypothesis for the underlying interaction is provided below.

As shown in the rhs plot of Figure 5.14, the periodic pulses of fast-ion losses disappear as soon the NTM slows down in its toroidal rotation and, most likely, becomes locked. This is further proof that the measured fast-ion losses are caused by the NTM. In addition, the time-modulation suggests that the fast-ion loss detection by the FILD is determined by the toroidal position of the rotating magnetic island with respect to the probe. To shed light on the underlying loss mechanism, the amplitude of the FILD and magnetic signals are plotted against each other for further, similar, discharges in rhs plot of Figure 5.15. These amplitudes are computed by integrating the PSD, see Section 5.2, of the signals in the frequency range of the mode spectral peak, at different times in the NTM interval. A robust linearity is found between the amplitude of the NTM perturbation and the fast-ion losses indicated by the R^2 statistical term and the p-Value for the t-Statistics.

In shot 68506, NBH was used as a source of suprathermal ion population. Energetic Deuterium atoms with primary beam energy of 28 keV were injected on the opposite toroidal port of TCV in a quasi-tangential direction. The resulting fast ions had pitch values above $\lambda = 0.65$ at birth that correspond to mostly passing orbits as calculate by the ASCOT/BBNBI code. Since the toroidal

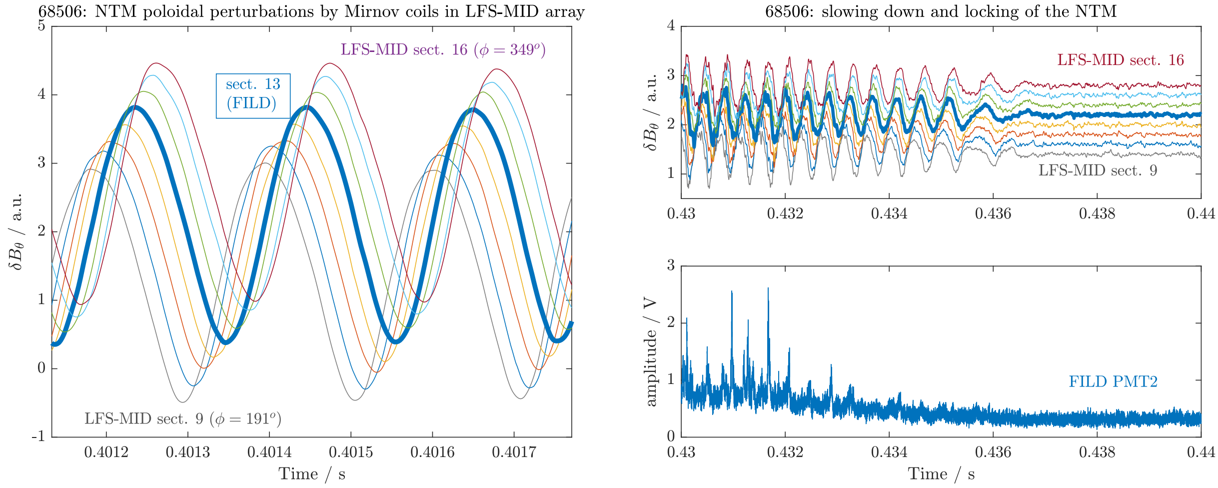

Figure 5.14: Shot 68506. (left) Signals from several probes of the LFS-MID toroidal array. The amplitude values are displaced vertically for clarity. (right) The same probes at the end of the interval of time with the NTM found rotating. Also the FILD PMT2 signal is drawn showing the FILD signal decreasing as the mode appears to damp in the magnetic signals.

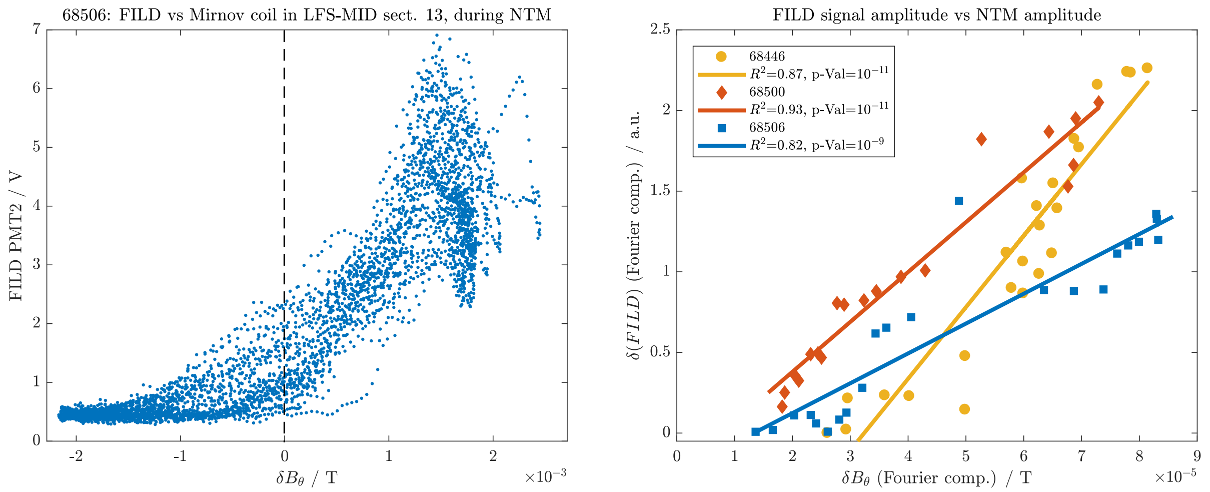

Figure 5.15: (left) Shot 68506. (right) Scatter plot and linear regressions for shots {68446,68500,68506} with NTMs. For each shot the time interval is split into shorter intervals with few oscillations of the magnetic perturbation. "Fourier component" means that the amplitude is estimated as the integral of the PSD of the signal in the frequencies of the PSD peak corresponding to the mode. The R^2 and the p-value for the t-Statistics of the linear coefficients are reported in the legend.

velocity of such particles is an order of magnitude larger than the NTM rotation, fast ions may be considered to see the magnetic island as if at rest. At each toroidal turn the particles in phase with the magnetic island will follow the line of the ideal magnetic perturbation, with helicity $m/n = 2/1$, accompanying the island. Furthermore, the particle guiding centers are displaced by the curvature and gradient drifts in poloidal and radial directions, a modification of the orbits of the kind $(m = 1, n = 0)$ as shown on the lhs of Figure 5.16. The coupling of such perturbations generates a series of drift-islands in fast-ion phase space [31]. This may enhance the fast-ion outwards transport and, therefore, the observed FILD signal. Such behaviour also detected in [24]. Although the NBH injection breaks the axisymmetry in the fast-ion dynamics, losses may be expected in any toroidal position. Therefore, the FILD probes just a small portion of the lost fast-ion phase space. The double-peaked FILD signal indicates that such a mechanism is at play on particles in different regions of the phase space at different times, delayed by few micro-seconds, and different extents. As the island comes closer to the FILD and the related ideal magnetic perturbation displaces the fast ions at the edge, these are affected differently, however in the same way at each toroidal turn of the island, thus giving two light emission peaks in short time that appear as superposed. This possibility is further investigated with the FILD measurements of the fast-ion velocity space, reported below.

In addition, the overlapping of these islands and/or the growth of the NTM can generate a stochastic magnetic region that causes even stronger particle ejections. One could thus expect a non-linear dependence between the amplitudes of the FILD signal and the magnetic perturbation as the footprint of a diffusive transport. For this reason, the linearity shown in Figure 5.15 may suggest such a regime of stochasticity was not achieved in these discharges and the losses are due to a purely parallel transport transport mechanism, in literature also termed “convective”. Interestingly, the FILD amplitude vanishes even for non-null amplitudes of the magnetic perturbation, unlike that found in [27] for fast-ion losses correlated with TAEs. This could imply the existence of a threshold for the onset of the loss mechanism, but further investigations are needed. These may be initiated by establishing plasma scenarios with a long-lasting NTM feedback-controlled by varying the NBH and ECRH power and/or direction.

To evaluate the impact of the NTM on the fast-ion velocity space, two PCO Panda camera frames, and their mapping to the (E, λ) space in the scintillator plane are shown in Figure 5.18. The frame at $t = 0.42$ s (bottom picture) is the acquisition of the emission during the interval of time in which the NTM is seen. The frame at $t = 0.39$ s (top picture) shows the scintillator emissions integrated in 30 ms before the mode’s onset. As shown in the rhs plot of Figure 5.17, strong decreases in the DMPX (an SXR diagnostic) signals for most of the available LOS are found in the “before NTM” interval of time. This may be co-incident with fast-ion losses and also, possibly, ion acceleration. Therefore, a comparison of the velocity spaces measured between these frames may help elucidate the effect of an NTM on the fast-ion population. An increase of the FILD’s light emissions by one order of magnitude is observed with losses during the NTM.

Two main emission spots are identified at $\lambda = 0.5$ and $\lambda \geq 0.6$ during the NTM. The energy distributions of the camera pixel counts for the first case, see Figure 5.20, fits well the instrument function of 30 keV i.e. a value close to the initial injection energy. The second is shifted towards higher values of energy and pitch, centered at 35 keV with a large right tail as also evident in the scintillator picture. Superficially, impinging ions with energies higher than at their birth were detected. The interaction between the magnetic island and the fast ions discussed above doesn’t include any electric field perturbation that may accelerate these particles. Other mechanisms may be at play, e.g. an

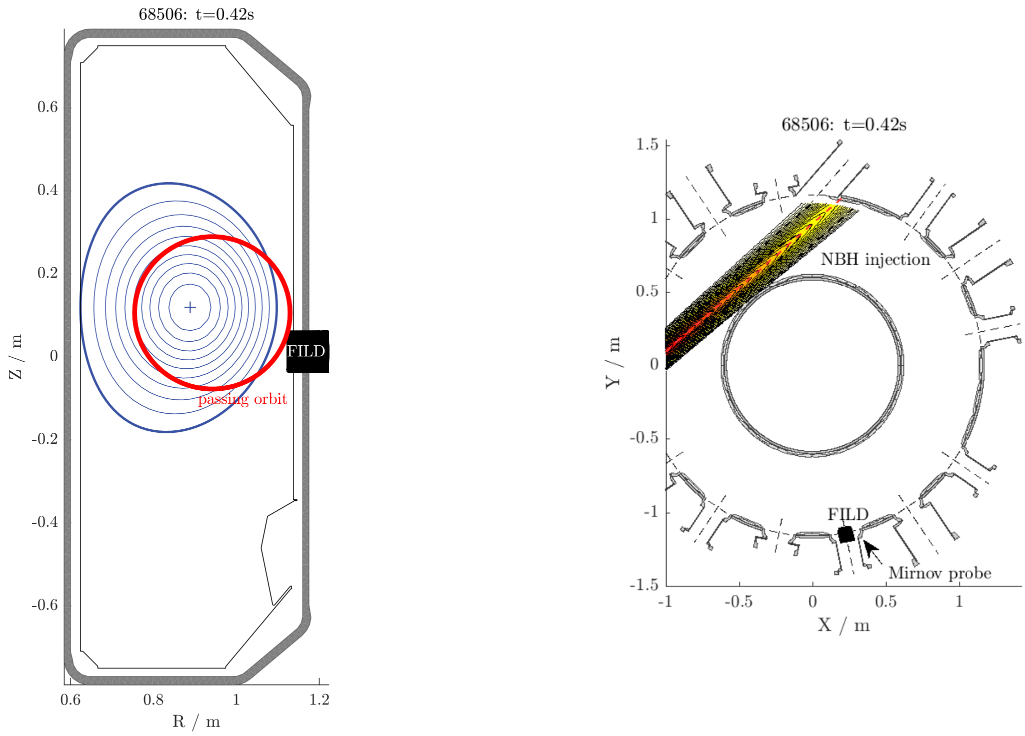

Figure 5.16: Shot 68506, $t = 0.42$ s. (left) Poloidal section of TCV with flux contours (blue) of the axisymmetric equilibrium and a passing orbit (red) colliding with FILD heatshield as displaced by the radial drifts. (right) Toroidal view of TCV from above with the NBH injection, the FILD and the Mirnov probe in sector 13.

electromagnetic fluctuation causing the DMPX signal drop around $t = 0.407$ s seen in Figure 5.17, that could act as a source for the observed increase of energy. A similar mechanism could produce the large deviations from the nominal injection energy of the distribution shown in Figure 5.19 for the frame at $t = 0.39$ s. One order of magnitude in the scintillator emission intensity is found between the two frames that supports the hypothesis of fast-ion losses caused by the NTM perturbation. A much weaker emission was also found for values of pitch at $\lambda = 0.3$. Particles with such trajectories are not present in the plasma from the NBH deposition. These are also observed, with similar magnitudes of light scintillator emission, in the frame acquired at $t = 0.39$ s, as also evident in the pitch distributions of the two time intervals shown in Figure 5.21. This suggests that such fast-ion losses are not due to the NTM. Other transport mechanisms should be invoked since ASCOT simulations in an axisymmetric equilbrium showed no NBH early losses in this range of pitch values. Lastly, a low-energy emission spot can be clearly seen in the frame at $t = 0.39$ s. This may be due to lost particles with the nominal energy of the third beam component if the instrument uncertainty is taken into account.

The observed brightest spots during the NTM correspond to values of pitch that, according to ASCOT, have the potential to become early losses. A clear effect of the NTM is to significantly populate this region of the lost fast-ion velocity space. The increase of scintillator emissions from both spots may be the cause of the observed double-peaked signals in the fast light detection and can be linked to time-delayed mode-particle interactions determined by the particular orbit, although the camera frame rate impedes its resolution. In addition to the difficulties in comparing the FILD measurements with the ASCOT synthetic velocity space, as discussed in Chapter 4, the presence of a large magnetic island strongly perturbs the particle motion in magnetic equilibrium configuration. A numerical simulation of these fast-ion trajectories should take into account such perturbations. An example of such an approach is reported in [30] for experiments on AUG.

Even though at these time intervals the DNBI was also used to inject Hydrogen atoms, the observed losses are not consistent with the pulsed-in-time diagnostic beam injection periods.

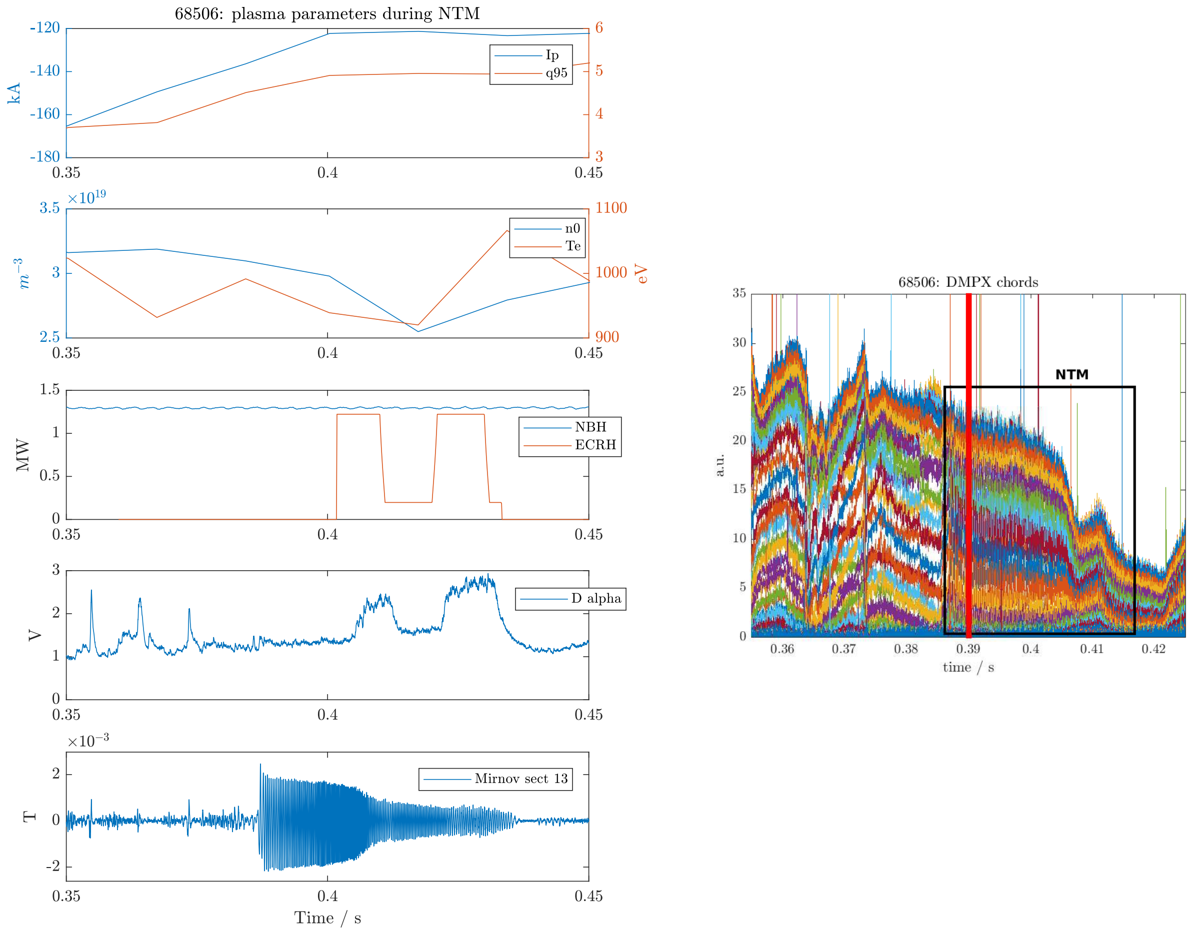

Figure 5.17: Shot 68506. (left) Plasma parameters with time before and during the detected NTM. (right) DMPX signals for all chords. The period of SXR emission during the NTM is enclosed in the black rectangle. The thick red line separates the two interval of times of analysis of the scintillator emission from the camera frame acquisitions.

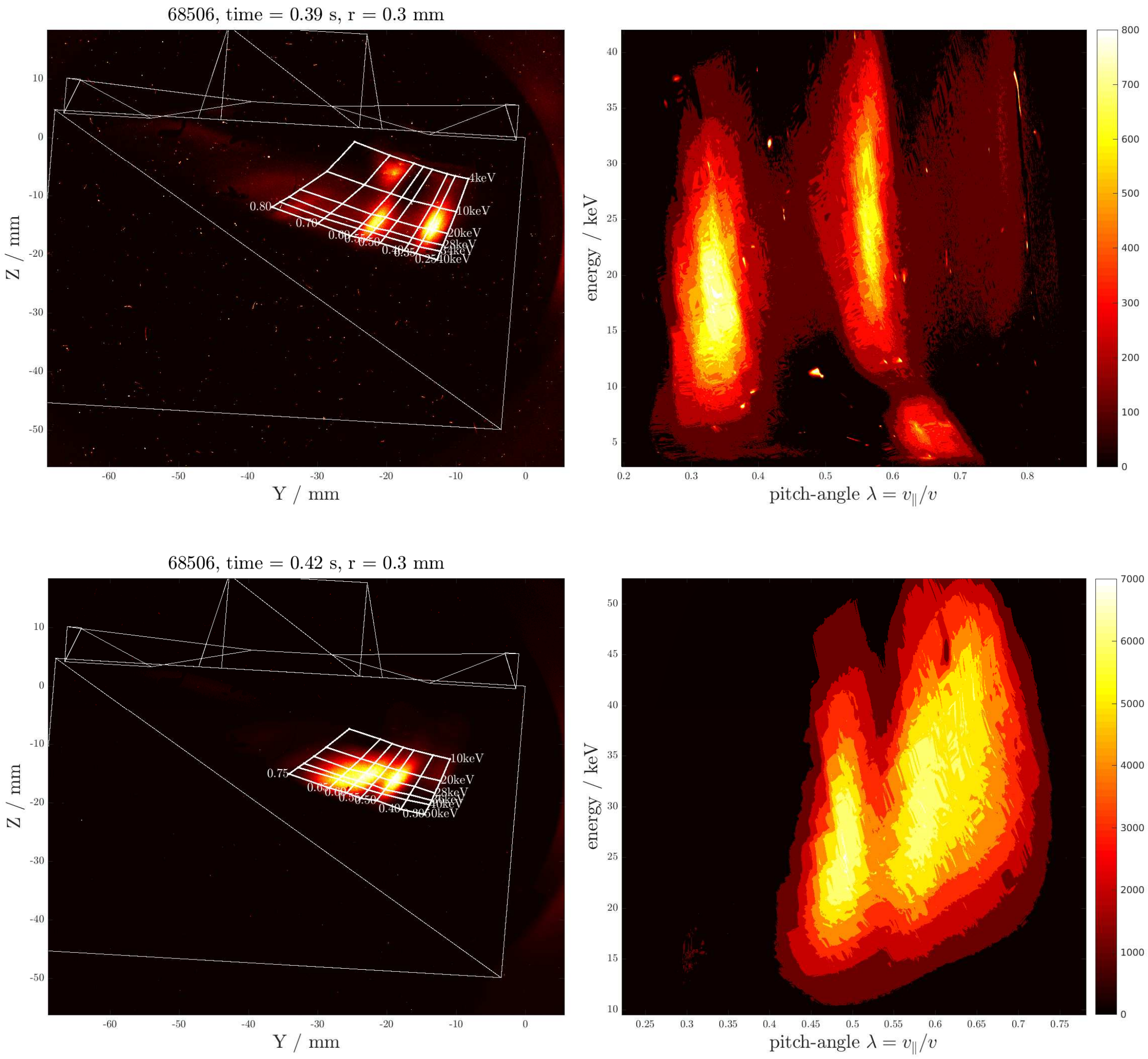

Figure 5.18: Shot 68506. The FILD location is 0.3 mm from the very first wall. Velocity-space mapping of the PCO Panda camera frames at different times. (top) Before the NTM appearing, $t = 0.39$ s. (bottom) During the NTM, $t = 0.42$ s.

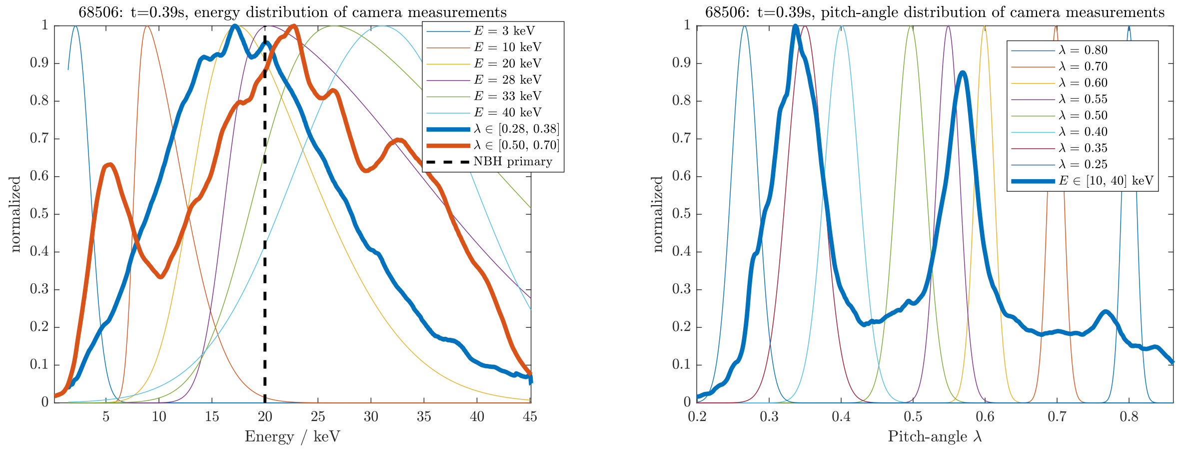

Figure 5.19: Shot 68506. Distributions of the camera pixel counts before the NTM. The instrument functions are included. (left) Energy distributions of the two brightest spots at $\lambda \in [0.32, 0.34]$ and $\lambda \in [0.58, 0.60]$. The weight functions of the mean values of both ranges of pitch are similar. (right) Pitch distribution for $E \in [10, 35]$ keV.

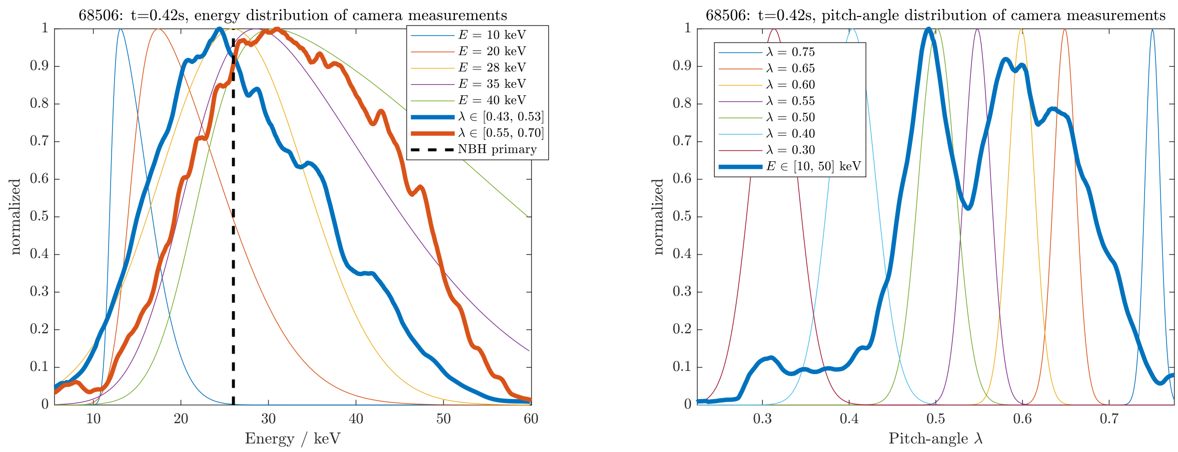

Figure 5.20: Shot 68506. Distributions of the camera pixel counts during the NTM. The instrument functions are included. (left) Energy distributions of the two brightest spots at $\lambda \in [0.55, 0.57]$ and $\lambda \in [0.66, 0.72]$. The weight functions of the mean values of both ranges of pitch are similar. (right) Pitch distribution for $E \in [20, 35]$ keV.

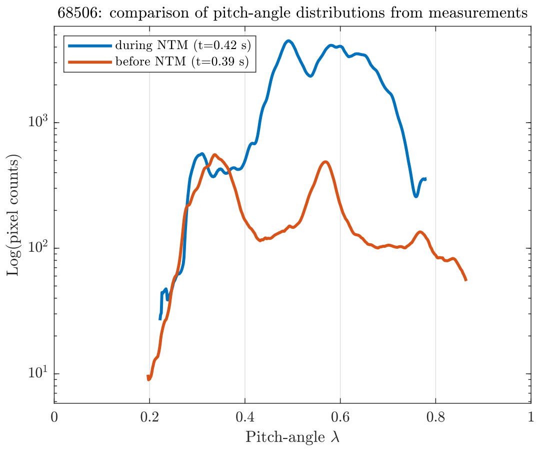

Figure 5.21: Shot 68506. FILD pitch distributions before and during the NTM of the camera pixel counts, from the plots in Figures 5.19 and 5.20.

5.4 Conclusions

Fast-ion losses detected by the FILD were shown to be caused by MHD instabilities such as the Sawtooth and the NTM. These two represented good case studies for assessing the capabilities of TCV-FILD, due to inherent differences in their perturbation mechanisms.

Extreme increases of scintillator emission on timescales of microseconds were detected by the fast light detection occurring at ST crashes. TCV-FILD was, therefore, able to probe the fast-ion phase space as perturbed by plasma reconnection/redistribution events. Also the effect on the suprathermal ion population of such ST crashes of different periods was investigated. This can probe the impact on fast-ion confinement by ST stabilization, a technique that is hoped will improve fusion reactor stability.

In contrast to these events that can be treated as separate from each other, NTMs were shown to cause *coherent* fast-ion losses. Similar observations were already obtained on other Tokamaks [7, 24, 34]. TCV's observations support the hypothesis of an additional convective outward transport of the fast ions, determined by the interactions between passing particles and the magnetic island perturbations. However, further analyses are required to identify the effect of such modes on the particle velocity space to which the FILD, in its current location, is sensitive. Numerical simulations of the fast-ion orbits in the perturbed magnetic field may become necessary to interpret the observations.

The double-peak signals from the scintillator emissions during an NTM may be due to the different effect of the transport mechanism on fast ions performing different orbits along the perturbed magnetic field lines, at different toroidal locations, and/or different times. These lost particles would impinge the scintillator in regions corresponding to different values of energy and pitch-angle. In effect, two spots of dominant emission were identified in the same camera frame, although they may occur at different times. Therefore, a fast light detection looking at more regions of the scintillator, with minimal overlap, would allow the characterization of loss mechanisms that affect different portions of the fast-ion phase space in time depending on the resonant or non-resonant interaction conditions.

The PCO Panda camera employed in the scintillator acquisition features an extremely high spatial resolution. An increase in frame rate, even at the cost of a reduced quality of the images, would be helpful to discriminate between the interval of times where MHD perturbations evolve and cause changes in the fast-ion losses. This is the case reported in Section 5.3 where magnetic activities correlated with significant DMPX (SXR) signal drops may have “polluted” the measurements of the velocity space of coherent losses caused by the NTM, thus impeding a more direct analysis. A frame rate of 1 kHz is high enough to track the loss evolution in time following the NTM.

These measurements highlighted TCV-FILD’s importance in the study of fast-ion dynamics in TCV plasma discharges. For instance, coherent losses may be expected from the fishbone-like magnetic signals observed at ST crashes with quasi-tangential beam injection, as were described in Section 5.2.1. The observed intensity of scintillator emissions resulting from the lost particles opens up to the possibility that FILD would now also generate pertinent measurements of fast-ion losses in experiments characterized by other high-frequency fluctuations, as already reported from other Tokamaks, such as Fishbones [50] and AEs [23, 27]. Moreover, the unique capability of TCV in plasma shaping may now be exploited to relate the FILD measured losses to plasma shaping parameters, e.g. triangularity and elongation. Recently, experimental evidence of Energetic Particle-driven modes (EPM) was seen in TCV discharges and, here again, FILD will help investigate any inherent interplay between fast ions and such instabilities.

Chapter 6

Conclusions and outlook

A new Fast-Ion Loss Detector (FILD) was designed, installed and commissioned for the TCV Tokamak. This is a radially positionable, scintillator based probe that provides direct detection of fast-ion losses during plasma discharges of interest in the study of fast-ion dynamics in a Tokamak. Energetic ions, generated in TCV from NBH and DNBI systems, are detected at the probe's location mostly as early beam losses and/or following interactions with magnetic perturbations. The lost particles are collimated inside the probe head and impinge upon a plate coated with a scintillator material that emits light. The resultant flux of photons is relayed to two acquisition systems: a sCMOS camera for high spatial resolution measurements of the scintillator emission locations, which are related to the size of the particle Larmor radius and the pitch (defined as $v_{\parallel}/v$), and a fast light detection photo-multiplier with bandwidth of 1 MHz, used for time-correlation studies of such losses with fast magnetic fluctuations. From its location with respect to the confined plasma and the fast-ion sources, FILD probes, with high resolution, a small region of the particle phase space. It can therefore complement other diagnostics that have a broader, but lower resolved, coverage of this phase space.

The design of TCV-FILD was partially based on existing similar diagnostics [21, 16]. The probe component design was aided by the e-FILDSIM code [20] that simulates the fast-ion trajectories inside the probe head. This code was developed during this thesis work to cover a wide range of physical and engineering parameters, and different probe component meshes.

TCV-FILD presents some novelties for exploring new ranges of operation. These, detailed in Chapter 3, may be adopted in a future for similar systems for the ITER Tokamak, or possibly other diagnostic devices dedicated to the investigation of the fast-ion interplay with, for instance, AEs or NTMs, where their behaviour is of paramount importance in achieving and maintaining the conditions for a burning plasma where effective α heating is fundamental.

Several mechanical parts of the apparatus, fabricated from either ceramics or stainless steel, were manufactured in-house. Other components were outsourced to external companies located in the Canton Vaud, Switzerland, or to other workshops at the EPFL. Several devices used for the optical setup and the positioning system were procured commercially and sometimes modified for operations, during this thesis.

Two configurations are available for easily installing the out-vessel optical apparatus: one with optics moving radially together with the probe head, thus keeping the optical paths fixed; another attached to the TCV vessel for higher rigidity of the light acquisition devices. The former was preferred since the system was found to not be unduly affected by vessel vibrations in terms of component integrity, measurement accuracy and S/N ratio.

TCV's FILD features two entrance slits, a unique feature for such a diagnostic, that enhance the range for fast-ion loss detection in more plasma scenarios. It was found, in fact, that the direction of the plasma current selects which of the two collimator slits may be traversed by lost particles. The double-slit design expands the range of measurements to different fast-ion trajectories, either co- or counter-plasma current directed. This will make TCV-FILD particularly valuable for fast-ion studies following the installation of the second NBH system on TCV that will operate concurrently with the present system, but with an injection in the opposite direction.

The radial positioning of the detector is performed with a feedback-controlled pneumatic actuator, for the first time for such a diagnostic. TCV-FILD may be considered a prototype for assessing the possibility of employing similar actuators in other FILDs, for installations in Tokamaks where electro-motors would be unfit due to the time-varying magnetic fields generated during plasma discharge sequences.

The probe head deployment into the Tokamak vessel has to be performed with care to avoid detrimental heat fluxes, especially, when the discharge includes high-power NBH injection with a total delivered energy of ~ 1 MJ. To date, although the positioning system remained poorly automated, the limited responsiveness of the pneumatic actuator doesn't permit a fast retraction of the probe during the shot that could, when programmed, be triggered by camera based alerts in case of detrimental plasma heating. A different positioning system is presented in [33], as a novel concept of electric-driven actuator for a FILD system on AUG. The deployment speed, therein estimated of 10 mm/100 ms, may be sufficient to displace the TCV's detector to a safe position, if not excessively exposed at the beginning of the discharge, since the visible light emitted by the overheated parts appears to grow on the time scale of ~ 100 ms.

Numerical thermal analysis of the graphite structure undergoing the observed heat loads would provide useful information on the fatigue over the probe components on the time scales of a single or multiple discharges throughout daily operations and over the diagnostic's life cycle. Such study requires highly time-resolved tracking of the temperature in several regions of the heatshield. A larger set of temperature sensors, with faster sampling compared to the long time-scale of the thermocouples, and an acquisition of such measurements during and after the discharge would be a major upgrade of the diagnostic in terms of operational safety and long-term management.

The diagnostic still strongly relies on the physical presence of an operator. The recent SARS-CoV-2 pandemic has shown the compelling need for deeper automation that would allow the diagnostic to be reliably operated remotely. Although the pneumatic actuator is able to keep the detector at its parked position during many cycles of shots without FILD operation, in case of accidents and subsequent loss of position control, the probe head could be exposed to detrimental heat loads. The position can be monitored by routinely reading the feedback value out. In case of uncontrolled piston motion, this could trigger a mechanical block with, for instance, an electric latch to impede any further displacement. Another aspect to reduce the in-situ presence is to setup the fast light detection gains by remote, an easy task if a modern HV supply with an ethernet port connection is employed. Also the photographic lens requires, at present, manual aperture adjustment depending on the expected flux of emitted photons, namely in experiments with NBH or DNBI. Many devices, provided that are reliable in a strong magnetic environment, are available on the market that would automate this task.

The first observations with the FILD probe on TCV provided the first-ever detection of direct ejections of energetic ions. In discharges exhibiting Sawtooth (ST) oscillations, intense jumps in scintillator emission were found that were correlated in time with the ST crashes. This may be explained when the large plasma redistribution caused by this instability gives an additional outward transport of fast ions. In these experiments, ST stabilization was performed with power deposition by ECRH to obtain a wide range of ST periods that were observed to be correlated with the ST crash intensity. The extent of plasma redistribution, measured by the relative change in the soft X-ray emission at the ST crash, was found to be proportional to the flux of fast ions impinging on the scintillator. Prior to FILD installation, a magnetic instability occurring at the ST crash was observed in the form of fishbone-like signals in the magnetic pickups. CNPA measurements clearly showed an effect of outward transport of the fast ions by this instability. Investigations to assess the likely presence of direct fast-ion losses are now possible with FILD.

NTM instabilities were shown to likely cause coherent losses, with a strong phase coherence between the signals from the magnetic probes, symptomatic of the NTM's saturated magnetic island rotating toroidally around TCV, and the FILD fast light detection. This signal coherence seems to result from the interaction between passing fast ions and magnetic helical perturbations of the magnetic island. FILD fast light detection provided double-peaked signals from such coherent losses. These can be the footprint of a fast-ion transport mechanism involving different kinds of wave-particle interactions. Strong linearity between the measured flux of scintillator emissions and the amplitude of the magnetic mode was found. This proves, in the range of amplitudes accessible in the analysed discharges, the parallel transport mechanism.

The calibration of the camera used for acquiring the scintillator emissions and its mapping to the particle velocity space via the e-FILDSIM code require improvements due to their determinant effect on the interpretation of the energy spectra of the detected losses. The e-FILDSIM tool may also be helpful to design experiments in which the probe is deployed at different radial positions. Collisionless orbit simulations from the probe head back to the plasma LCFS of the markers initialised with different energy and pitch-angle values give an estimation of the lost velocity space as a function of the radial position of the detector. Such particle tracking can be performed by solving the Lorentz equation with Runge-Kutta methods as in [3] or by coupling the e-FILDSIM to the ASCOT code.

The investigation of MHD modes with frequencies of the order of some kHz would be carried out with a more powerful tool if a CMOS or CCD camera, with shorter integration time, and higher frame rate, were employed. The observed high efficiency of the collimator and the high optical transmission of the system allow a reduction of the camera resolution without a significant loss of image quality with an increased frame rate. For instance, acquisitions at 1000 fps would make it possible to start temporally resolving fast-ion ejection mechanisms caused by a NTM as it evolves in time, or by other instabilities with rapidly varying frequencies. Such cameras are available commercially, although their ability to work in the strongly magnetic and highly electromagnetic environment around a Tokamak still needs to be tested.

The experiments reported in this thesis suggest that different regions of the fast-ion phase space may be affected differently by resonant (e.g. Fishbones, AEs) and/or non-resonant (e.g. NTMs) wave-particle interactions. As a consequence, FILD measurements of the fast-ion velocity space were found to cover large ranges of energy and pitch-angle values. For this reason, the fast light detection system will largely benefit from an array of independent detectors covering the scintillator plate, divided in several detection areas, corresponding to different energies and pitch-angles, with minimum overlap. This requires a bundle of fibers each focused onto its portion of scintillator, requiring a more complex optic setup than presently available. Instead of big PMTs, a set of Avalanche Photo-diodes (APDs) or Silicon Photo-multipliers (SiPMs) would be a more compact solution. Their insensitivity to the strong magnetic fields from the nearby of a Tokamak and the supply voltage of the order of some Volts, rather than several kVs, should retain, or possibly improve, the S/N ratio of the measurements presented therein. However X-rays may have a detrimental effect on such devices and Lead shielding may be necessary. The displacement of the fast light detection system to a distant area, as currently employed for the spectroscopy diagnostics, would ensure further improvements due to a strong reduction of spurious X-rays and electromagnetic interference. The use of optical fibers from the FILD apparatus to the detection devices allows nearly loss-less transfer of the emitted photons, even over distances of several tens of meters.

A better characterisation of the detection of magnetic fluctuations in the vicinity of the probe will be necessary to relate the fast-ion losses to the particular temporal and spatial structure of observed perturbations. The probe head could be specifically designed to accommodate an adapted LTCC-3D magnetic sensor, a compact device suitable for measuring time-varying magnetic perturbations in up to three local spatial directions.

The fast-ion loss measurements correlated with ST instabilities and NTMs demonstrate the TCV-FILD's ability to detect fast ions ejected by a range of transport mechanisms affecting these particles differently in time and in their spatial orbits. The observed intense photon flux resulting from the lost particles promises high S/N ratio signals of fast-ion losses on TCV correlated with, for instance, ELMs or high-frequency modes, often less intense with respect to NTMs, such as Fishbones, EPMs and AEs, that are likely to exhibit a coherent-loss character.

The excitation of such electromagnetic fluctuations have been extensively studied in several Tokamaks. For instance, the damping of the AEs is a function of the plasma shape [76], heating and non-inductive current drive [25], and some plasma parameters [29]. However a systematic understanding of the impact of these factors on the electromagnetic fluctuations is, to date, missing.

The TCV facility offers a unique environment for fast-ion studies due to the wide variety of plasma scenarios it can operate. Different plasma shapes and positions, heating actuators and dedicated diagnostics are available. A real time (RT) control system is present that is used, for instance, for the excitation/suppression of MHD instabilities with ECRH/ECCD [52, 15]. A 1 MW NBH produces, by injecting Deuterium with maximum energy of 28 keV, high power density plasma discharges that can excite EPMs. In 2021, a second NBH will provide fast ions with energies up to 60 keV, injected in the opposite toroidal direction to the present one, that will satisfy the resonance conditions for a wide spectrum of AEs that occur at frequencies of several 100 kHz. Evidence for such modes in TCV discharges is reported in [29], but not further information on these modes were obtained during this thesis. The second injector, the TCV's high plasma shape flexibility and the possibility of active control with the ECRH system will be essential in establishing reliable scenarios for such studies. FILD will provide measurements necessary in the success of such experiments.

As an example of such studies on TCV, plasma discharges are currently performed to assess the dependence of MHD instabilities on the plasma shape [79]. In discharges with negative triangularity, FILD has yet to be used for safety reasons, due to the small remaining clearance between the probe head and the plasma volume, typical of such shapes. This may be solved by moving the FILD below the midplane of TCV in a bottom vessel port ($z = -23$ cm) on the LFS, in a non-baffled vessel.

Further investigations of energetic ion ejections correlated with NTMs, starting from the findings reported in this thesis, will help provide a deeper understanding of the NTM-originated fast-ion transport. In high power Tokamaks, such as ITER, this effect may be important and may also engender α particle losses with subsequent lowered reactor performance. Employing and further developing TCV's long duration NTM scenarios will be essential to perform further FILD measurements. A study of the dependence between the observed fast-ion losses and the radial position of the probe was outside the scope of this thesis. A scan of this position in discharges with NTMs may give valuable insights on the underlying mechanism of interaction particularly when combined with numerical codes that model the particle trajectories along the perturbed magnetic field lines in 3D geometries. A comparison between the FILD measured fast-ion phase space with a synthetic diagnostic, computed from particle tracking in an axisymmetric equilibrium field, is an increasingly applied approach when comparing complex models to complex diagnostics. Simulations, e.g. with the ASCOT code, would have to be carefully designed to efficiently populate such a large phase space with a statistically significant number of markers that attain and pass through the FILD slit. Such a task is likely to be computing intensive.

The addition of FILD to the TCV diagnostic set also opens further avenues toward the demonstration of real time control methods, in particular in view of burning plasma regimes in larger Tokamaks. TCV has, in fact, already gained expertise in the RT analysis of camera images, with dedicated algorithms, to extract particular features of interest for control [67]. From the FILD camera image footprint, it will be possible to identify needs for real time interventions to steer the evolution of the plasma discharge in possible dangerous situations. Real-time interpretation of FILD measurements was shown possible by upgrading the e-FILDSIM code to allow fast computation of scintillator mappings as done in [70]. From the FILD fast signal, further information as to effect of Sawteeth, NTMs or AEs can be detected and correlated to signals from magnetic pick-up or other fast-ion dedicated diagnostics. By combining FILD information with such diagnostics, complex observational, and/or plasma state tracking RT algorithms [14] can be provided additional information with which to control the plasma discharge evolution, and demonstrate the possibility of optimizing the plasma burn.

With the contributions of several diagnostics it could be also possible to infer information on the fast-ion distribution function by solving tomographic inversion problems as described in [72, 20]. Combining data obtained from measurements of different portion of the fast-ion phase space with the CNPA, FIDA, Neutron counters, a future INPA and FILD will provide and increasingly detailed and complete picture of the fast-ion dynamics on TCV in fusion relevant plasma conditions.

Appendix A

Magnetic probe acquisition characterization

In Section 2.5.1 the results of the end-to-end characterization of the Mirnov coils' acquisition lines were presented. Here this work is detailed. It includes the identification of: the frequency dependence of the coil effective area, the probe+cable system once installed in the vessel and the amplifying chain from the vessel to the A/D card. The numerical implementation of the calibration based on the estimated transfer function is presented.

A.1 Probe characterization

To determine the Mirnov coil effective area as a function of the magnetic perturbation frequency, a highly uniform oscillating magnetic field was generated by means of a Helmholtz Coils at the spot where the probe was placed. The induced voltage was measured with a 1 GHz oscilloscope. It was found that a second order low-pass filter is quite adequate to describe this dependence, in Laplace space it can be written as

$$H_{\mathrm{probe}}(s) = \frac{A}{(1+s\tau_1)(1+s\tau_2)}, \tag{A.1}$$

where, on average, $A = 0.0091\,\mathrm{m}^2$ and the cut-off frequencies are $1/(2\pi\tau_1) = 95\,\mathrm{kHz}$ and $1/(2\pi\tau_2) = 245\,\mathrm{kHz}$.

Once installed on TCV, a probe is connected to the THERMOCOAX cables inside the vessel and standard coaxial cables after the feedthrough. Such probe+cable system can not be characterized in-situ. However the impedance measurement may be used to infer a transfer function for the system. The measurements were performed over a broad range of frequencies, from 10 Hz to 13 MHz. As shown in Figure A.1, two resonances are found at frequencies higher than 1 MHz. Rather than solving the equations for a transmission line, one can model the system as a sum of elementary circuits provided that the end of the series is connected to a high impedance ($\geq 10\,\mathrm{k}\Omega$) load and the wavelength of the signal is much higher than the physical length of the line. If these requirements are met the measured impedance is best determined as a rational function and the transfer function may be analytically obtained as the inverse of the denominator polynomial, as described in [37].

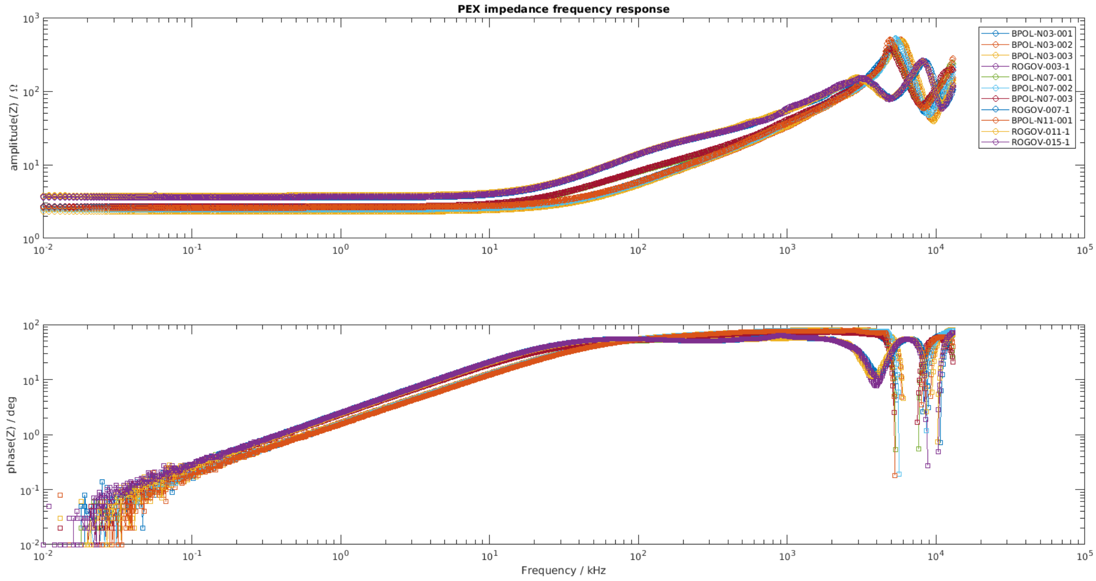

Figure A.1: Bode Plot of the frequency dependent impedances of the Mirnov and Rogowski coils in the baffles.

A.1.1 Characterization of Rogowski Coils

In addition, a set of Rogowski coils for the in-baffle setup [68] was characterized out-vessel. A setup in which an oscillating current flows in a conductor placed on the axis of the probe and the induced voltage is detected, was used. The results, shown in Figure A.1, are in agreement with what was expected from geometrical considerations given the shape and size of the two sets of probes. At frequencies below 1 kHz, the capacitive response of the Helmholtz Coils and the Rogowski lead to a transfer function far from the theoretical one. Nevertheless, this presents no problems for the measurements of interest on TCV.

A.2 Amplifying chain frequency response

The probe's wire endings exit the vacuum vessel via a feedthrough. The signals are then relayed to an amplifying chain. This is located partly in the torus basement. Here an input filter damps by a factor of 30 the detrimental high-voltage and high-frequency components occurring, for instance, during plasma disruptions. The signal is amplified by the *pre-amplis* module that features programmable gain, and it is relayed to the adjacent *treatment room*. After a protection component, the signal is split in two branches: one is integrated to provide the B_θ for equilibrium reconstruction and the other is further amplified and finally digitised by the ADC. This thesis is mostly concerned by these signals that provide measurements of $\mathrm{d}B_\theta/\mathrm{d}t$, relevant to fast MHD studies.

In the past, the amplifying chain in Figure A.2 was characterized piece-wise. The results, limited to a spectral range up to 125 kHz, showed no deviations from the input stage modeled as a one-zero (3.5 kHz) and one-pole (100 Hz) filter. When the sampling frequency was recently raised to 500 kHz to include the possibility of detecting AEs or other high-frequency EP-driven modes, an investigation of the end-to-end amplifying chain response in this range became necessary.

The measurements were performed by feeding to the system a known signal and acquiring it with PCS (Plant Control System) shots. A function generator provided a sinusoidal waveform with log-sweeped frequencies from 5 kHz to 250 kHz over 1 s. The value of the voltage supplied was set to 10 V peak-to-peak to avoid saturations at the reset of the generator sweep. As a reference, an equivalent signal was sent directly to the acquisition card via a 30 m long coaxial cable equipped with BNC connectors. The schematic of the setup is in Figure A.4.

In Laplace space, the acquired signals of one line and their reference are:

$$V_{\text{out}}(s) = V_{\text{in}}(s) H_{\text{amp}}(s) H_{\text{ADC}}(s) \tag{A.2}$$

$$V_{\text{ref}}(s) = V_{\text{in}}(s) H_{\text{BNC}}(s) H_{\text{ADC}}(s), \tag{A.3}$$

where H_{amp} is the transfer function of the amplifying chain from the input filter to the patch panels before the ADC with frequency response H_{ADC}. The quantity H_{BNC} describes the attenuation and delay due to the coaxial BNC cable. It was measured by means of a 1 GHz high-resolution oscilloscope and using a 1 m long cable of the same kind as reference. See the Bode plot in Figure A.3.

Therefore we can write the end-to-end amplifying chain's response function in terms of the measured quantities as

$$H_{\text{amp}}(s) = H_{\text{BNC}}(s) \frac{V_{\text{out}}(s)}{V_{\text{ref}}(s)} = H_{\text{BNC}}(s) H_{\text{meas}}(s). \tag{A.4}$$

With respect to the H_{meas} function, the $V_{\text{out}}(t)$ and $V_{\text{ref}}(t)$ time series have been divided into several narrow intervals of time, corresponding to the frequencies of the swept input signal. Within each interval a Gaussian fit of the amplitude and a linear fit of the phase were performed to infer the $V_{\text{out}}/V_{\text{ref}}$ response at each frequency in the complex plane. The amplitude has been taken as the mean value of the Gaussian model along with the standard deviation as estimate of the uncertainty. However, the measured phase is meaningless because of the low resolution of the ADC system with sampling time of 2 µs. By modeling the system from the solely amplitude response of the $H_{\text{BNC}} H_{\text{meas}}$ function as a two-poles (-3 dB decay at 100 kHz and the 1 MHz cutoff of the cable) filter, only the phase shift at the very beginning of the spectral range of interest could be resolved by such an acquisition. Therefore, the phase response has been assumed to be that of this estimated second-order filter.

From the measured amplitude response and the modeled phase response of H_{amp} in the frequency range [5 kHz; 250 kHz], it is now possible to estimate the overall analog transfer function in the entire spectrum including the known input filter, namely

$$H_{\text{filter}}(s) = \frac{1 + s\tau_{\text{z}}}{1 + s\tau_{\text{p}}}, \tag{A.5}$$

with $\tau_{\text{z}} = 1/\left(2\pi\, 3.5\text{kHz}\right)$ and $\tau_{\text{p}} = 1/\left(2\pi\, 100\text{Hz}\right)$.

In order to obtain a fitting model H_{fit} in the form of rational polynomial, a functional must be

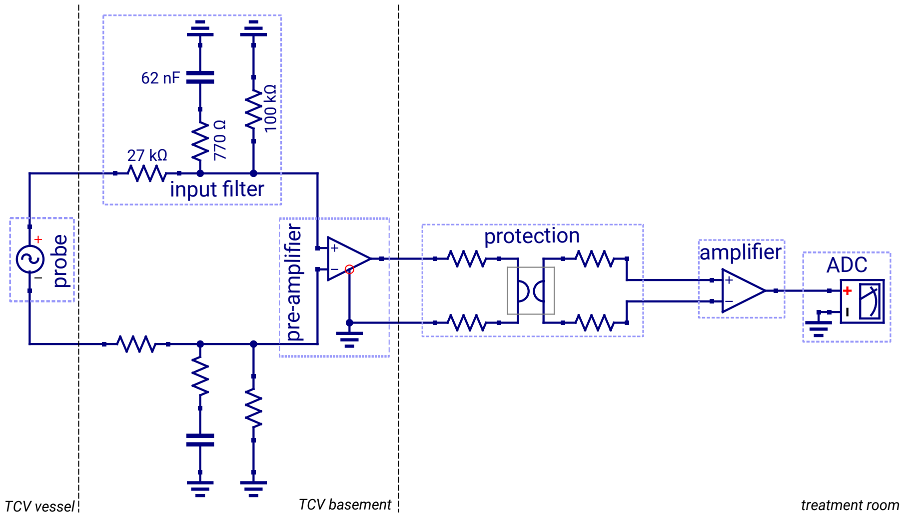

Figure A.2: Amplifying chain for MHD acquisition.

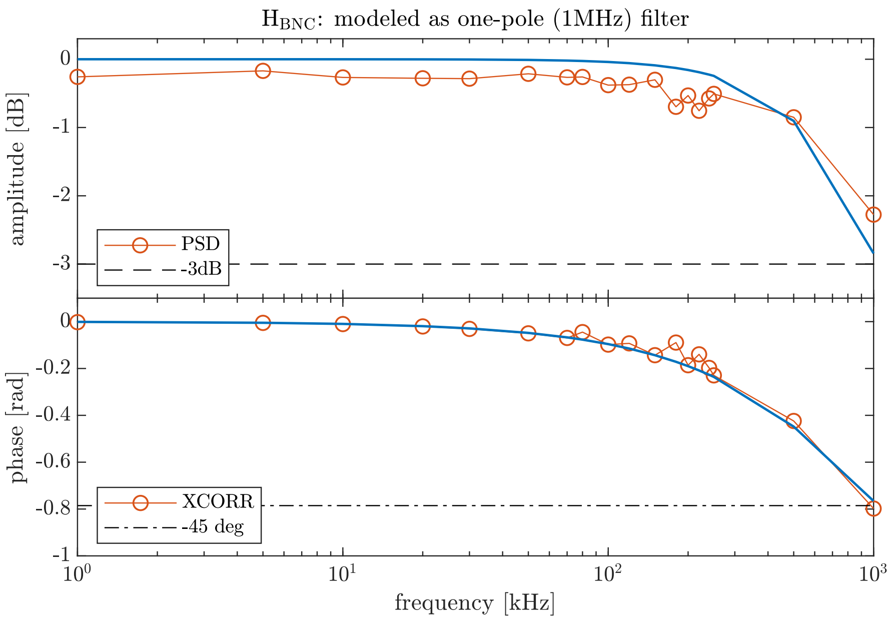

Figure A.3: Bode plot of the 30 m long coaxial BNC cable employed in the acquisition of the reference signal. The amplitude is estimated as the power spectral density peak value for each frequency, and the phase as proportional to the time lag of the maximum cross-correlation between the studied cable and a 1 m long reference cable.

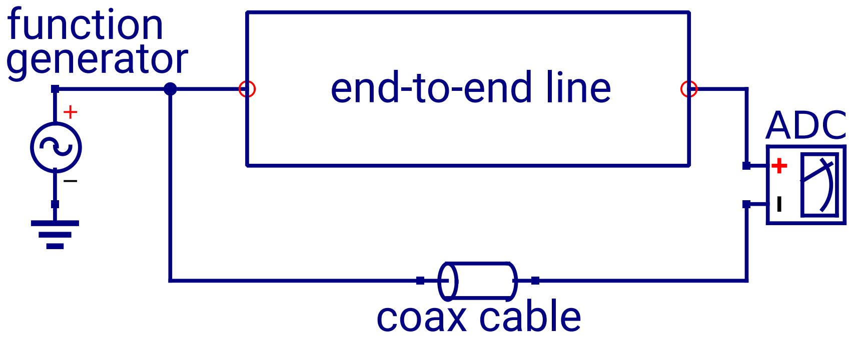

Figure A.4: Schematic of the end-to-end acquisition line characterization setup employing a reference signal sent to the acquisition through a coaxial cable.

minimised with respect to the polynomial coefficients:

$$\min_{\boldsymbol{a},\boldsymbol{b}} \sum_{k}^{N} w_k \left| H_{\text{fit}} - H_{\text{meas}}(s_k) \right|^2 , \tag{A.6}$$

$$H_{\text{fit}}(s) = \frac{b_n s^n + b_{n-1} s^{n-1} + \ldots + 1}{a_m s^m + a_{m-1} s^{m-1} + \ldots + 1}, \tag{A.7}$$

where N is the length of the measured H_{meas}, that is a complex succession with each value corresponding to a frequency $\text{Im}\{s_k/(2\pi)\}$ and $\{w_k\}_{k=1,\ldots N}$ are the weights equal to the squared inverse of the amplitude uncertainties. An order 1 for the numerator and 3 for the denominator of the fitting model were chosen. Except the faulty lines, all lines exhibit an excellent agreement with the zero and the pole of the input filter while a larger standard deviation of $\sim 5\%$ is found for the second pole around 160 kHz.

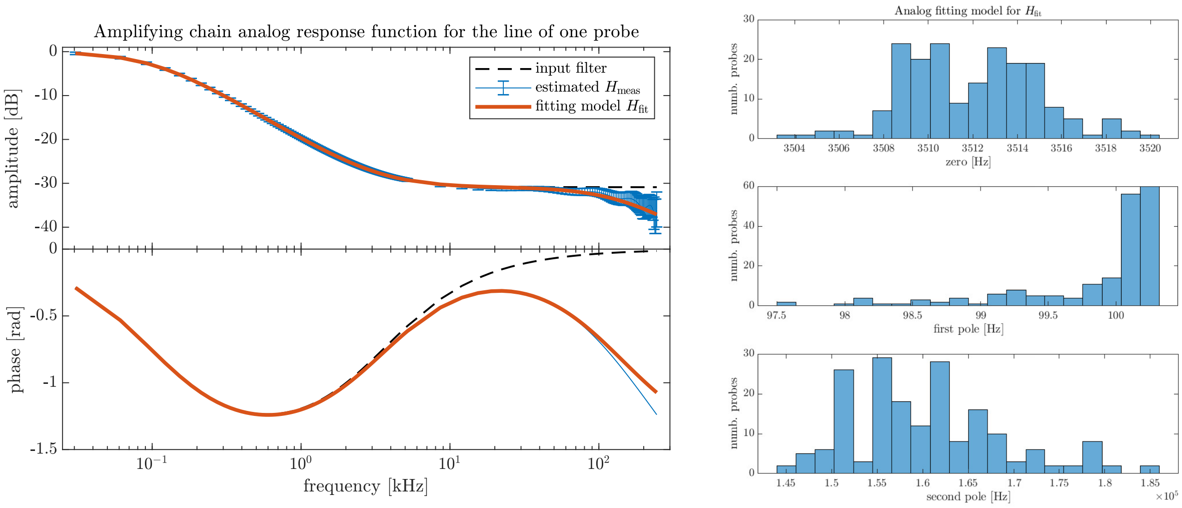

Figure A.5: (left) Analog response function estimated from measurements, blue line with error bars, and fitting model, red line, for the acquisition line of the probe DBPOL-003-002. (right) Zero and poles obtained from the coefficients of the fitting rational polynomials.

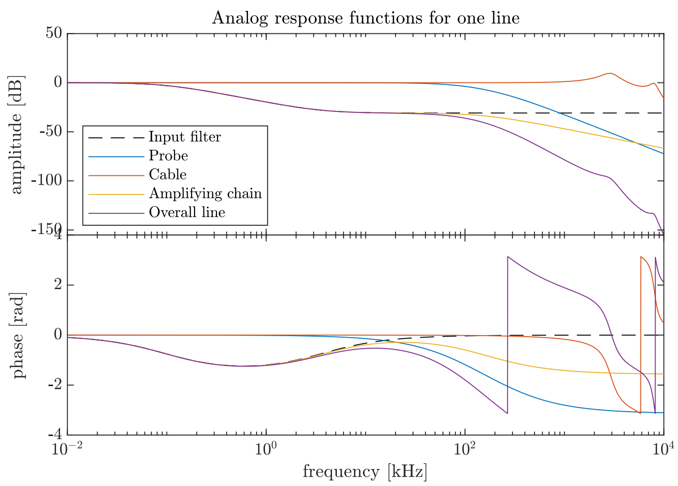

Figure A.6: Analog response functions of each piece and the whole line including the in-vessel and acquisition components, relative to the probe DBPOL-003-002. Note the wrapping of the phase typically occurring beyond the Nyquist frequency (250 kHz).

A.3 Numerical calibration

The post-processing calibration of the probes consists in applying the inverse overall response function in the digital domain, given the finite sampling time τ_s, to the output signals. From the Faraday-Neumann-Lenz equation we can write the acquired signals in time as

$$V_{out}(t) = H_{probe} * (G_{pre}G_{amp}H_{amp}) * V_{in}(t), \tag{A.8}$$

$$= A_{probe}G_{pre}G_{amp}\,(H_{probe} * H_{amp}) * \dot{B}_\theta, \tag{A.9}$$

where $G_{pre,amp}$ are the constant gains of the pre-amplifier and the main amplifier respectively, and the analog response functions H_{probe} and H_{amp} are normalised on the DC gain.

As stressed above, we seek a way to transform the transfer function from the analog (a continuous defined function) to the digital domain. That is, the input $\dot{B}_\theta$ and the output V_{out} signals as time series, i.e. successions in $\mathbb{R}$ as follows

$$\dot{B}_\theta[n] \equiv \dot{B}_\theta(n\tau_s) = \dot{B}_\theta(t), \tag{A.10}$$

$$V_{out}[n] \equiv V_{out}(n\tau_s) = V_{out}(t), \tag{A.11}$$

are related by the digital inverse response function. Hence the calibration process is

$$\dot{B}_\theta[n] = \frac{1}{A_{probe}G_{pre}G_{amp}}\,(H_{probe} * H_{amp})^{-1}\,[n] * V_{out}[n]. \tag{A.12}$$

The digital transfer function can be transformed into a continuous function, still representing a digital response, by the Z-transform:

$$X(z) = \mathcal{Z}\,(x[n]) = \sum_n x[n]z^{-n} \quad \text{with} \quad z \in \mathbb{C}. \tag{A.13}$$

Where Equation (A.12) becomes

$$\dot{B}_\theta(z) = \frac{1}{A_{probe}G_{pre}G_{amp}}\,(H_{probe} * H_{amp})^{-1}\,(z)V_{out}(z). \tag{A.14}$$

Hence we are interested in applying methods able to map a function from the Laplace space to the Z space. The Bilinear transform [75] is a conformal mapping from the $\Re(s) < 0$ plane in the Laplace space to the unitary circle in the Z space which preserves the stability. Starting from $z = \exp(s\tau_s)$, we write, to the first order in $s\tau_s$, the following

$$z = \frac{e^{s\tau_s/2}}{e^{-s\tau_{s/2}}} \simeq \frac{1 + s\tau_s/2}{1 - s\tau_{s/2}} \tag{A.15}$$

By inverting the above expression we find the conversion rule:

$$H_{digital}(z) = H_{analog}\left(s = \frac{2}{\tau_s}\frac{z-1}{z+1}\right). \tag{A.16}$$

It's clear that such mapping is reliable provided that $s\tau_{\mathrm{s}}$ remains sufficiently small. Since in our case $\tau_{\mathrm{s}} = 2\,\mu\mathrm{s}$, the validity range ends around 50 kHz. This strongly affects the applicability of the method for our purposes.

Alternatively an LDS approach can be employed [55]. This look for an algebraic expression in form of rational polynomials that fits the measured frequency response. A curve fitting is performed in the complex Z space by minimising the functional with respect to the polynomials coefficients as already described for the analog case in Equation (A.6). We have the problem

$$\min \sum_{k}^{N} w_k \left| H_{\mathrm{fit}} - H_{\mathrm{meas}}(f_k) \right|^2 , \tag{A.17}$$

for a response function of the form:

$$H_{\mathrm{fit}}(z) = \frac{b_n z^{-n} + b_{n-1} z^{-(n-1)} + \ldots + 1}{a_m z^{-m} + a_{m-1} z^{-(m-1)} + \ldots + 1}. \tag{A.18}$$

Finally, impulse invariant discretization techniques are used when dealing with inputs in the form of finite impulse, such as signals occurring at sawtooth crashes or ELMs. In this case the analog response function should be converted into the digital domain such that the impulse-invariance is ensured as advised by [45].

Appendix B

e-FILDSIM

The code presented in [20] is used for the interpretation of the FILD measurements, by mapping the scintillator pictures into the 2D fast-ion velocity space on the scintillator and inverting these measurements into the velocity space at the slit. The code models the impinging particle trajectories as helixes, i.e. assuming a uniform magnetic field inside the probe head. Due to the $1/R$ scaling of the equilibrium magnetic field, the field varies slowly at the probe's location and the above assumptions is valid. In fact, the results are in good agreement with those by more sophisticated numerical tools such as ASCOT [70].

In the work presented in this thesis, an *alpha* of the MATLAB version of the algorithm was improved to become the engineering "e-FILDSIM" code. This is intended to support the design of the FILD components, as described in Chapter 3. A major upgrade was the conversion into an object-oriented code. This approach, together with the high-level language of MATLAB, is suitable for quickly scanning the parameters of the simulations. Importing geometrical meshes, that model the probe parts, in different file extensions (e.g. .mat, .stl) is possible. A class-based coding, moreover, allows an easy development of further methods, with a range of attributes, to expand the scopes of the code.

A typical call of the code to produce the strikemap for a given shot, time and FILD radial position is, in a MATLAB session:

```
fs=fildsim('foo/input'); % specify the input folder path
fs.makeGeometry;
fs.simulateHelixes;
fs.makeStrikemap;
```

The input folder should compulsory contain the file named as: `equilibrium`, `geometry` and `slit#`, where the `#` stands for the number of the slit. The convention adopted is: looking at the probe from above, in opposite direction to the R co-ordinates, Slit 1 is on the right and Slit 2 on the left.

The class instance `fs` is a struct-like variable with fields containing the input parameters on the geometry of the probe and its position in the Tokamak vessel, the physical quantities to simulate the particle trajectories and the information to retrieve the axysimmetric equilibrium reconstruction in the `eqdsk` format. It is possible to provide the marker energy E (useful for the interpretation of the measurements) or the Larmor radius $\rho_E = v_{\text{tot}}/\Omega_{\text{i}}$ (suitable for designing the probe); and the pitch as $\lambda = v_{\|}/v$ or the pitch-angle as $\Lambda = \text{acos}(\lambda)$.

The method makeGeometry imports the triangular meshes and place them in the Tokamak (X,Y,Z) co-ordinates set. It also computes the magnetic field line orientation at the slit, namely the elevation angle θ between the field line and the equatorial plane (positive upwards), and the azimuthal angle ϕ with respect to the scintillator plate (positive moving away from Slit 1). These quantities, for example, can also be provided when instantiating the fildsim object to arbitrarily set the value, as

```
fs=fildsim('foo/input','slit1.velocity_space.eq_theta',5*pi/180);
```

The meshes are stored in the geometry field of the class instance in the same vertex co-ordinates format employed by the ASCOT code.

The method simulateHelixes performs the actual modeling of the particle trajectories as helixes drawn from the collimator slit to the scintillator plate. The strike point is computed by the Moller-Trumbore algorithm [59]. Also the backward simulation can be performed, when selected, with an input option. The results are stored in the strikes field of the class instance in the built-in table format, for the “forward”, “blocked”, “backward” and “good” (= forward-backward) helixes.

The forward and the good strikemaps are generated by the makeStrikemap method. These can convert the velocity space co-ordinates, e.g. from E to ρ_E.

These results can be visualized by the plot method. It can produce a figure of the detector as deployed with respect to the Tokamak vessel and with the plasma LCFS. Strikemaps, strike points and helixes can be drawn. See Figure B.1.

Other available methods are: evalGyrophase, evalCollimatorFactor and evalResolution. The latter computes the weight functions by fitting the distribution of the strikes with the analytical expression in Equation (3.15).

The interpretation of the scintillator emissions is carried out by the mapCamera method. The camera frame is calibrated in space: the strikemap is moved to a local 2D space, the optics magnification and the inclination of the probe head taken into account to convert the pixel co-ordinates into the real scintillator plate. Then the mapping between this plane and the 2D fast-ion velocity space is performed. The obtained data are stored in the mapped field of the class instance, to be used to evaluate the distributions in, for instance, energy and pitch-angle of the camera pixel counts. This is done by the evalInstrument method for a given range of integration of one of the two velocity-space co-ordinates. Also, the weight functions are drawn to be compared to the evaluated distribution.

Each of these methods has several options. These are parsed by the built-in inputParser, as the MATLAB standard comma-separated parameter names and values. Type in help to read the options available and the default values.

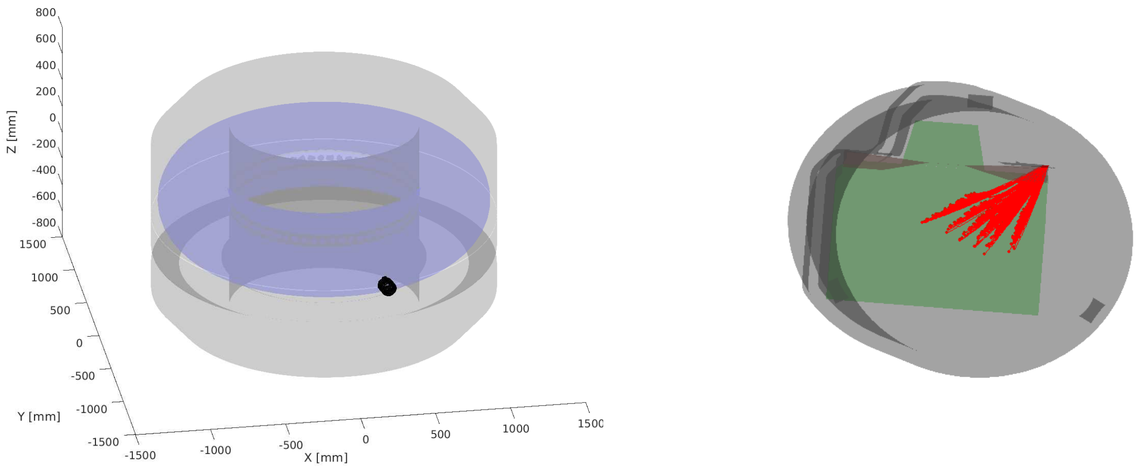

Figure B.1: Picures from the `plot` method. (left) the heatshield mesh (black) placed in the Tokamak (X,Y,Z) co-ordinates set. Also the vacuum vessel (grey) and the LCFS (blue) are depicted. (right) A close-up of the FILD detector with some helixes (red) plotted from the collimator slit (grey) to the scintillator plate (green).

Bibliography

[1] Stefano Alberti et al. "Recent progress in the upgrade of the TCV EC-system with two 1MW/2s dual-frequency (84/126GHz) gyrotrons". en. In: *EPJ Web of Conferences* 157 (2017). Publisher: EDP Sciences, p. 03001. ISSN: 2100-014X. DOI: 10.1051/epjconf/201715703001.

[2] T. P. Goodman and. "Experience in integrated control of the multi-megawatt electron cyclotron heating system on the TCV tokamak: the first decade". en. In: *Nuclear Fusion* 48.5 (Apr. 2008). Publisher: IOP Publishing, p. 054011. ISSN: 0029-5515. DOI: 10.1088/0029-5515/48/5/054011.

[3] J. Ayllon-Guerola et al. "Determination of the Fast-Ion Phase-Space Coverage for the FILD Spatial Array of the ASDEX Upgrade Tokamak". en. In: *Journal of Instrumentation* 14.10 (Oct. 2019). Publisher: IOP Publishing, p. C10032. ISSN: 1748-0221. DOI: 10.1088/1748-0221/14/10/C10032.

[4] S. Baeumel et al. "Scintillator probe for lost alpha measurements in JET". In: *Review of Scientific Instruments* 75.10 (Oct. 2004), pp. 3563–3565. ISSN: 0034-6748. DOI: 10.1063/1.1787916.

[5] J. B. Birks. "Scintillations from Organic Crystals: Specific Fluorescence and Relative Response to Different Radiations". en. In: *Proceedings of the Physical Society. Section A* 64.10 (Oct. 1951). Publisher: IOP Publishing, pp. 874–877. ISSN: 0370-1298. DOI: 10.1088/0370-1298/64/10/303.

[6] R. J. Buttery et al. "Neoclassical tearing modes". en. In: *Plasma Physics and Controlled Fusion* 42.12B (Dec. 2000). Publisher: IOP Publishing, B61. ISSN: 0741-3335. DOI: 10.1088/0741-3335/42/12B/306.

[7] E. M. Carolipio et al. "Simulations of beam ion transport during tearing modes in the DIII-D tokamak". en. In: *Nuclear Fusion* 42.7 (July 2002). Publisher: IOP Publishing, pp. 853–862. ISSN: 0029-5515. DOI: 10.1088/0029-5515/42/7/308.

[8] I. T. Chapman. "Controlling sawtooth oscillations in tokamak plasmas". en. In: *Plasma Physics and Controlled Fusion* 53.1 (Nov. 2010). Publisher: IOP Publishing, p. 013001. ISSN: 0741-3335. DOI: 10.1088/0741-3335/53/1/013001.

[9] Liu Chen, R. B. White, and M. N. Rosenbluth. "Excitation of Internal Kink Modes by Trapped Energetic Beam Ions". In: *Physical Review Letters* 52 (Mar. 1984), pp. 1122–1125. ISSN: 0031-9007. DOI: 10.1103/PhysRevLett.52.1122.

[10] S. Coda et al. "Physics research on the TCV tokamak facility: from conventional to alternative scenarios and beyond". en. In: *Nuclear Fusion* 59.11 (Aug. 2019). Publisher: IOP Publishing, p. 112023. ISSN: 0029-5515. DOI: 10.1088/1741-4326/ab25cb.

[11] Bruno Coppi and F. Porcelli. "Plasma Oscillation Bursts and Scattering of Intermediate Energy Alpha Particles". In: *Fusion Technology* 13.3 (Mar. 1988), pp. 447–452. ISSN: 0748-1896. DOI: 10.13182/FST88-A25122.

[12] D. S. Darrow. "Scintillator based energetic ion loss diagnostic for the National Spherical Torus Experiment". In: *Review of Scientific Instruments* 79.2 (Feb. 2008). Publisher: American Institute of Physics, p. 023502. ISSN: 0034-6748. DOI: 10.1063/1.2827514.

[13] A. Fasoli et al. "Chapter 5: Physics of energetic ions". en. In: *Nuclear Fusion* 47.6 (June 2007). Publisher: IOP Publishing, S264–S284. ISSN: 0029-5515. DOI: 10.1088/0029-5515/47/6/S05.

[14] F. Felici et al. "Real-time physics-model-based simulation of the current density profile in tokamak plasmas". en. In: *Nuclear Fusion* 51.8 (Aug. 2011). Publisher: IOP Publishing, p. 083052. ISSN: 0029-5515. DOI: 10.1088/0029-5515/51/8/083052.

[15] Federico Felici. *Real-Time Control of Tokamak Plasmas: from Control of Physics to Physics-Based Control*. en. Number: THESIS Publisher: EPFL. 2011. DOI: 10.5075/epfl-thesis-5203.

[16] R. K. Fisher et al. "Scintillator-based diagnostic for fast ion loss measurements on DIII-D". In: *Review of Scientific Instruments* 81.10 (Oct. 2010), p. 10D307. ISSN: 0034-6748. DOI: 10.1063/1.3490020.

[17] M. Fontana, L. Porte, and P. Molina Cabrera. "Correlation electron cyclotron emission diagnostic in TCV". In: *Review of Scientific Instruments* 88.8 (Aug. 2017), p. 083506. ISSN: 0034-6748. DOI: 10.1063/1.4997075.

[18] Ivo Furno et al. "Helicon wave-generated plasmas for negative ion beams for fusion". en. In: *EPJ Web of Conferences* 157 (2017). Publisher: EDP Sciences, p. 03014. ISSN: 2100-014X. DOI: 10.1051/epjconf/201715703014.

[19] J. Galdon-Quiroga et al. "Velocity space resolved absolute measurement of fast ion losses induced by a tearing mode in the ASDEX Upgrade tokamak". en. In: *Nuclear Fusion* 58.3 (Jan. 2018). Publisher: IOP Publishing, p. 036005. ISSN: 0029-5515. DOI: 10.1088/1741-4326/aaa33b.

[20] J. Galdon-Quiroga et al. "Velocity-space sensitivity and tomography of scintillator-based fast-ion loss detectors". en. In: *Plasma Physics and Controlled Fusion* 60.10 (2018), p. 105005. ISSN: 0741-3335. DOI: 10.1088/1361-6587/aad76e.

[21] M. García-Muñoz, H.-U. Fahrbach, and H. Zohm. "Scintillator based detector for fast-ion losses induced by magnetohydrodynamic instabilities in the ASDEX upgrade tokamak". In: *Review of Scientific Instruments* 80.5 (May 2009), p. 053503. ISSN: 0034-6748. DOI: 10.1063/1.3121543.

[22] M. García-Muñoz et al. "Characterization of scintillator screens for suprathermal ion detection in fusion devices". en. In: *Journal of Instrumentation* 6.04 (2011), P04002. ISSN: 1748-0221. DOI: 10.1088/1748-0221/6/04/P04002.

[23] M. García-Muñoz et al. "Fast-Ion Losses due to High-Frequency MHD Perturbations in the ASDEX Upgrade Tokamak". In: *Physical Review Letters* 100 (Feb. 2008), p. 055005. ISSN: 0031-9007. DOI: 10.1103/PhysRevLett.100.055005.

[24] M. García-Muñoz et al. "NTM induced fast ion losses in ASDEX Upgrade". en. In: *Nuclear Fusion* 47.7 (June 2007). Publisher: IOP Publishing, p. L10. ISSN: 0029-5515. DOI: 10.1088/0029-5515/47/7/L03.

[25] M. Garcia-Munoz et al. "Active control of Alfvén eigenmodes in magnetically confined toroidal plasmas". en. In: *Plasma Physics and Controlled Fusion* 61.5 (Mar. 2019). Publisher: IOP Publishing, p. 054007. ISSN: 0741-3335. DOI: 10.1088/1361-6587/aaef08.

[26] M. Garcia-Munoz et al. "Fast-ion losses induced by ELMs and externally applied magnetic perturbations in the ASDEX Upgrade tokamak". en. In: *Plasma Physics and Controlled Fusion* 55.12 (2013), p. 124014. ISSN: 0741-3335. DOI: 10.1088/0741-3335/55/12/124014.

[27] M. Garcia-Munoz et al. "Fast-ion transport induced by Alfvén eigenmodes in the ASDEX Upgrade tokamak". en. In: *Nuclear Fusion* 51.10 (2011), p. 103013. ISSN: 0029-5515. DOI: 10.1088/0029-5515/51/10/103013.

[28] B. Geiger et al. "Fast-ion transport in low density L-mode plasmas at TCV using FIDA spectroscopy and the TRANSP code". en. In: *Plasma Physics and Controlled Fusion* 59.11 (Sept. 2017). Publisher: IOP Publishing, p. 115002. ISSN: 0741-3335. DOI: 10.1088/1361-6587/aa8340.

[29] B. Geiger et al. "Observation of Alfvén Eigenmodes driven by off-axis neutral beam injection in the TCV tokamak". en. In: *Plasma Physics and Controlled Fusion* 62.9 (July 2020). Publisher: IOP Publishing, p. 095017. ISSN: 0741-3335. DOI: 10.1088/1361-6587/aba19e.

[30] M. Gobbin et al. "Numerical simulations of fast ion loss measurements induced by magnetic islands in the ASDEX Upgrade tokamak". en. In: *Nuclear Fusion* 49.9 (Sept. 2009). Publisher: IOP Publishing, p. 095021. ISSN: 0029-5515. DOI: 10.1088/0029-5515/49/9/095021.

[31] M. Gobbin et al. "Resonance between passing fast ions and MHD instabilities both in the tokamak and the RFP configurations". en. In: *Nuclear Fusion* 48.7 (May 2008). Publisher: IOP Publishing, p. 075002. ISSN: 0029-5515. DOI: 10.1088/0029-5515/48/7/075002.

[32] S. von Goeler, W. Stodiek, and N. Sauthoff. "Studies of Internal Disruptions and m=1 Oscillations in Tokamak Discharges with Soft—X-Ray Tecniques". In: *Physical Review Letters* 33.20 (Nov. 1974). Publisher: American Physical Society, pp. 1201–1203. DOI: 10.1103/PhysRevLett.33.1201.

[33] J. Gonzalez-Martin et al. "First measurements of a magnetically driven fast-ion loss detector on ASDEX Upgrade". en. In: *Journal of Instrumentation* 14.11 (Nov. 2019). Publisher: IOP Publishing, pp. C11005–C11005. ISSN: 1748-0221. DOI: 10.1088/1748-0221/14/11/C11005.

[34] J. Gonzalez-Martin et al. "First measurements of a scintillator based fast-ion loss detector near the ASDEX Upgrade divertor". In: *Review of Scientific Instruments* 89.10 (Aug. 2018), p. 10I106. ISSN: 0034-6748. DOI: 10.1063/1.5038968.

[35] Charles A. S. Hall and Kent Klitgaard. *Energy and the Wealth of Nations: Understanding the Biophysical Economy*. en. New York: Springer-Verlag, 2012. ISBN: 978-1-4419-9398-4. DOI: 10.1007/978-1-4419-9398-4.

[36] Yuval Noah Harari. *Sapiens: A Brief History of Humankind*. English. 1st edition. London: Vintage, Apr. 2015. ISBN: 978-0-09-959008-8.

[37] R. F. Heeter et al. "Fast magnetic fluctuation diagnostics for Alfvén eigenmode and magnetohydrodynamics studies at the Joint European Torus". In: *Review of Scientific Instruments* 71.11 (Nov. 2000). Publisher: American Institute of Physics, pp. 4092–4106. ISSN: 0034-6748. DOI: 10.1063/1.1313797.

[38] W. W. Heidbrink. "Basic physics of Alfvén instabilities driven by energetic particles in toroidally confined plasmas". In: *Physics of Plasmas* 15.5 (Feb. 2008), p. 055501. ISSN: 1070-664X. DOI: 10.1063/1.2838239.

[39] W. W. Heidbrink and G. J. Sadler. "The behaviour of fast ions in tokamak experiments". en. In: *Nuclear Fusion* 34.4 (1994), p. 535. ISSN: 0029-5515. DOI: 10.1088/0029-5515/34/4/I07.

[40] W. W. Heidbrink et al. "A Code that Simulates Fast-Ion D-alpha and Neutral Particle Measurements". en. In: *Communications in Computational Physics* 10.3 (Sept. 2011). Publisher: Cambridge University Press, pp. 716–741. ISSN: 1815-2406, 1991-7120. DOI: 10.4208/cicp.190810.080211a.

[41] W. W. Heidbrink et al. "Measurements of beam-ion confinement during tangential beam-driven instabilities in a bean tokamak experiment". In: *The Physics of Fluids* 30.6 (June 1987), pp. 1839–1852. ISSN: 0031-9171. DOI: 10.1063/1.866199.

[42] W. W. Heidbrink et al. "Tangential Neutral-Beam-Driven Instabilities in the Princeton Beta Experiment". In: *Physical Review Letters* 57.7 (Aug. 1986). Publisher: American Physical Society, pp. 835–838. DOI: 10.1103/PhysRevLett.57.835.

[43] E. Hirvijoki et al. "ASCOT: Solving the kinetic equation of minority particle species in tokamak plasmas". In: *Computer Physics Communications* 185.4 (Apr. 2014), pp. 1310–1321. ISSN: 0010-4655. DOI: 10.1016/j.cpc.2014.01.014.

[44] D. Iglesias et al. "An improved model for the accurate calculation of parallel heat fluxes at the JET bulk tungsten outer divertor". en. In: *Nuclear Fusion* 58.10 (Aug. 2018). Publisher: IOP Publishing, p. 106034. ISSN: 0029-5515. DOI: 10.1088/1741-4326/aad83e.

[45] L. B. Jackson. "A correction to impulse invariance". In: *IEEE Signal Processing Letters* 7.10 (Oct. 2000). Conference Name: IEEE Signal Processing Letters, pp. 273–275. ISSN: 1558-2361. DOI: 10.1109/97.870677.

[46] M. C. Jiménez-Ramos et al. "Characterization of scintillator materials for fast-ion loss detectors in nuclear fusion reactors". In: *Nuclear Instruments and Methods in Physics Research Section B: Beam Interactions with Materials and Atoms*. 21st International Conference on Ion Beam Analysis 332.Supplement C (Aug. 2014), pp. 216–219. ISSN: 0168-583X. DOI: 10.1016/j.nimb.2014.02.064.

[47] B. B. Kadomtsev. "Disruptive instability in Tokamaks". In: *Soviet Journal of Plasma Physics* 1 (Sept. 1975), pp. 710–715. ISSN: 0367-2921.

[48] Alexander N. Karpushov et al. "Neutral beam heating on the TCV tokamak". en. In: *Fusion Engineering and Design*. Proceedings of the 29th Symposium on Fusion Technology (SOFT-29) Prague, Czech Republic, September 5-9, 2016 123 (Nov. 2017), pp. 468–472. ISSN: 0920-3796. DOI: 10.1016/j.fusengdes.2017.02.076.

[49] Alexander N. Karpushov et al. "Neutral particle analyzer diagnostics on the TCV tokamak". In: *Review of Scientific Instruments* 77.3 (Mar. 2006), p. 033504. ISSN: 0034-6748. DOI: 10.1063/1.2185151.

[50] V. G. Kiptily et al. "Fusion product losses due to fishbone instabilities in deuterium JET plasmas". en. In: *Nuclear Fusion* 58.1 (2018), p. 014003. ISSN: 0029-5515. DOI: 10.1088/1741-4326/aa9340.

[51] Ya I. Kolesnichenko and Yu V. Yakovenko. "Theory of fast ion transport during sawtooth crashes in tokamaks". en. In: *Nuclear Fusion* 36.2 (Feb. 1996). Publisher: IOP Publishing, pp. 159–172. ISSN: 0029-5515. DOI: 10.1088/0029-5515/36/2/I04.

[52] Mengdi Kong. *Towards integrated control of tokamak plasmas: physics-based control of neoclassical tearing modes in the TCV tokamak*. en. Number: THESIS Publisher: EPFL. 2020. DOI: 10.5075/epfl-thesis-7510.

[53] E. Lazzaro and M. F. F. Nave. "Feedback control of rotating resistive modes". In: *The Physics of Fluids* 31.6 (June 1988). Publisher: American Institute of Physics, pp. 1623–1629. ISSN: 0031-9171. DOI: 10.1063/1.867004.

[54] M. Lennholm et al. "Demonstration of Effective Control of Fast-Ion-Stabilized Sawteeth by Electron-Cyclotron Current Drive". In: *Physical Review Letters* 102.11 (Mar. 2009), p. 115004. DOI: 10.1103/PhysRevLett.102.115004.

[55] E. C. Levy. "Complex-curve fitting". In: *IRE Transactions on Automatic Control* AC-4.1 (May 1959), pp. 37–43. ISSN: 0096-199X. DOI: 10.1109/TAC.1959.6429401.

[56] D. Liu et al. "Effect of sawtooth crashes on fast ion distribution in NSTX-U". en. In: *Nuclear Fusion* 58.8 (July 2018). Publisher: IOP Publishing, p. 082028. ISSN: 0029-5515. DOI: 10.1088/1741-4326/aac64f.

[57] Claudio Marini. *Poloidal CX visible light plasma rotation diagnostics in TCV*. en. Number: THESIS Publisher: EPFL. 2017. DOI: 10.5075/epfl-thesis-8031.

[58] K. McGuire et al. "Study of High-Beta Magnetohydrodynamic Modes and Fast-Ion Losses in PDX". In: *Physical Review Letters* 50.12 (Mar. 1983). Publisher: American Physical Society, pp. 891–895. DOI: 10.1103/PhysRevLett.50.891.

[59] Tomas Möller and Ben Trumbore. "Fast, Minimum Storage Ray-Triangle Intersection". In: *Journal of Graphics Tools* 2.1 (Jan. 1997), pp. 21–28. ISSN: 1086-7651. DOI: 10.1080/10867651.1997.10487468.

[60] J.-M. Moret et al. "Magnetic measurements on the TCV Tokamak". In: *Review of Scientific Instruments* 69.6 (June 1998), pp. 2333–2348. ISSN: 0034-6748. DOI: 10.1063/1.1148940.

[61] F. Nespoli et al. "Understanding and suppressing the near scrape-off layer heat flux feature in inboard-limited plasmas in TCV". en. In: *Nuclear Fusion* 57.12 (Sept. 2017). Publisher: IOP Publishing, p. 126029. ISSN: 0029-5515. DOI: 10.1088/1741-4326/aa84e0.

[62] Gustavo Paganini Canal. *Sawtooth Generated Magnetic Islands and the Properties of the Snowflake Divertor*. en. Number: THESIS Publisher: EPFL. 2014. DOI: 10.5075/epfl-thesis-6272.

[63] Alexei Pankin et al. "The tokamak Monte Carlo fast ion module NUBEAM in the National Transport Code Collaboration library". en. In: *Computer Physics Communications* 159.3 (June 2004), pp. 157–184. ISSN: 0010-4655. DOI: 10.1016/j.cpc.2003.11.002.

[64] Gregorij V. Pereverzev and P. N. Yushmanov. "ASTRA. Automated System for TRansport Analysis in a tokamak". In: (2002). Publisher: Max-Planck-Institut für Plasmaphysik.

[65] Steven Pinker. *Enlightenment Now: The Case for Reason, Science, Humanism, and Progress*. Inglese. New York, New York: Viking Pr, Feb. 2018. ISBN: 978-0-525-42757-5.

[66] R.A Pitts, R Chavan, and J.-M Moret. "The design of central column protection tiles for the TCV tokamak". en. In: *Nuclear Fusion* 39.10 (Oct. 1999), pp. 1433–1449. ISSN: 0029-5515. DOI: 10.1088/0029-5515/39/10/306.

[67] T. Ravensbergen et al. "Real-time feedback control of the impurity emission front in tokamak divertor plasmas". en. In: *Nature Communications* 12.1 (Feb. 2021). Number: 1 Publisher: Nature Publishing Group, p. 1105. ISSN: 2041-1723. DOI: 10.1038/s41467-021-21268-3.

[68] H. Reimerdes et al. "Initial TCV operation with a baffled divertor". en. In: *Nuclear Fusion* 61.2 (Jan. 2021). Publisher: IOP Publishing, p. 024002. ISSN: 0029-5515. DOI: 10.1088/1741-4326/abd196.

[69] Matt Ridley. *The Rational Optimist: How Prosperity Evolves*. English. Fourth Estate, May 2010.

[70] J. F. Rivero-Rodriguez et al. "A fast model to resolve the velocity-space of fast-ion losses detected in ASDEX Upgrade and MAST Upgrade". en. In: *Journal of Instrumentation* 14.09 (Sept. 2019). Publisher: IOP Publishing, pp. C09015–C09015. ISSN: 1748-0221. DOI: 10.1088/1748-0221/14/09/C09015.

[71] J. F. Rivero-Rodriguez et al. "A rotary and reciprocating scintillator based fast-ion loss detector for the MAST-U tokamak". In: *Review of Scientific Instruments* 89.10 (Sept. 2018). Publisher: American Institute of Physics, p. 10I112. ISSN: 0034-6748. DOI: 10.1063/1.5039311.

[72] M. Salewski et al. "High-definition velocity-space tomography of fast-ion dynamics". en. In: *Nuclear Fusion* 56.10 (2016), p. 106024. ISSN: 0029-5515. DOI: 10.1088/0029-5515/56/10/106024.

[73] O. Sauter et al. "Control of Neoclassical Tearing Modes by Sawtooth Control". In: *Physical Review Letters* 88.10 (Feb. 2002). Publisher: American Physical Society, p. 105001. DOI: 10.1103/PhysRevLett.88.105001.

[74] L. Spitzer. *Physics of Fully Ionized Gases*. en. Publication Title: Physics of Fully Ionized Gases. 1962.

[75] L. Tan and J. Jiang. *Digital Signal Processing*. en. Elsevier, 2019. ISBN: 978-0-12-815071-9. DOI: 10.1016/C2017-0-02319-4.

[76] D. Testa, A. Fasoli, and Contributors to the EFDA-JET 2000 Workprogramme. "The effect of plasma shaping on the damping of lownAlfvén eigenmodes in JET tokamak plasmas". en. In: *Nuclear Fusion* 41.7 (July 2001). Publisher: IOP Publishing, pp. 809–812. ISSN: 0029-5515. DOI: 10.1088/0029-5515/41/7/101.

[77] Duccio Testa et al. "3D, LTCC-type, high-frequency magnetic sensors for the TCV Tokamak". en. In: *Fusion Engineering and Design*. Proceedings of the 28th Symposium On Fusion Technology (SOFT-28) 96-97 (Oct. 2015), pp. 989–992. ISSN: 0920-3796. DOI: 10.1016/j.fusengdes.2015.05.065.

[78] C. K. Tsui et al. "Poloidal asymmetry in the narrow heat flux feature in the TCV scrape-off layer". In: *Physics of Plasmas* 24.6 (June 2017). Publisher: American Institute of Physics, p. 062508. ISSN: 1070-664X. DOI: 10.1063/1.4985075.

[79] M. Vallar. "APS -62nd Annual Meeting of the APS Division of Plasma Physics - Event - Modelling of fast ion diffusion with internal kink in TCV with positive and negative triangularity". In: *Bulletin of the American Physical Society*. American Physical Society.

[80] M. Vallar et al. “Status, scientific results and technical improvements of the NBH on TCV tokamak”. en. In: *Fusion Engineering and Design*. SI:SOFT-30 146 (Sept. 2019), pp. 773–777. ISSN: 0920-3796. DOI: 10.1016/j.fusengdes.2019.01.077.

[81] M. A. Van Zeeland et al. “Measurements and modeling of Alfvén eigenmode induced fast ion transport and loss in DIII-D and ASDEX Upgrade”. In: *Physics of Plasmas* 18.5 (May 2011). Publisher: American Institute of Physics, p. 056114. ISSN: 1070-664X. DOI: 10.1063/1.3574663.

[82] R. B. White et al. “Theory of mode-induced beam particle loss in tokamaks”. In: *The Physics of Fluids* 26.10 (Oct. 1983). Publisher: American Institute of Physics, pp. 2958–2965. ISSN: 0031-9171. DOI: 10.1063/1.864060.

Acknowledgements

If I may misquote: "*never in the history of a PhD was so much owed by only one to so many*".

I thank my supervisors, a three of a kind, with their different suits. Prof. A. Fasoli is the person you need when your brain overheats thinking to dozens of alleged mistakes or focuses on the cons rather than the pros. He has been a true source of self-confidence for me, always able to spot the silver lining of the clouds in my head.

Dr. D. Testa often paid attention to my mood and lent an ear so many times.

In the last year and half, Dr. B.P. Duval became an unofficial supervisor. He guided and supported me to take all the steps the thesis project required, and let me discover that I had more resources in myself than I thought.

I gratefully acknowledge the examiners Prof. J.P. Graves, Prof. M. Garcia-Muñoz and Prof. M. Salewski for their valuable comments to the thesis, the challenging questions at the oral exam and the interest they showed in my work during these years.

Ing. M. Toussaint and Ing. Y. Andrebe devoted significant efforts to design, install and commission the diagnostic. They gave me the possibility to learn many new things. Both have been helpful and constantly patient with me, and it has been a pleasure to work with them.

Special thanks go to the PSFT's people at the University of Sevilla with whom we collaborated for making TCV-FILD. In Fall 2018, they welcomed me to Sevilla in the best way possibile. I much appreciate their kindness in letting me feel quickly at ease among them and their availability in providing help in short time.

Dr. J.M. Ayllon-Guerola has been the collaborator anyone would enjoy to work with. I had so many moments of true fun with him, from the *Garlochi* to our traditional *peking duck*. He is an honest and trustworthy person who makes me feel understood when talking about serious things but always able to cheer me up. Thank you for being one of my dearest friends.

Dr. M. Vallar was an excellent colleague and friend. I learned so much from him, either in the office, on the mountains or while traversing the north of Italy by car.

The SPC is a great place to work, where it is hard to feel alone, especially in the throes of the hardest moments of a PhD life. *Les services*, students, scientists and the administration have been always generous to me.

I wish all the best to my past and present PhD and Post-doc colleagues. I had the chance to discuss, have good time and get stimulated by some of the smartest people I've ever met.

The support I received from Omar, Stefano, Severino, Ugo and Jean-Marc was precious. I am in debt with them for their help at work, in fixing my bike and for the time spent together during the coffee breaks. Severino deserves a special mention for the time I enjoyed talking with him about some of my preferred topics: books, bikes and life.

In October 2019, I lived the funniest and most intense weeks of this work. Assembling the FILD, from early in the morning to late hours, with the team of the *Cicciunazzi*, was an incredibly inspiring experience that boosted my commitment to pursue the goal of the PhD. My gratitude goes to Omar, Matthieu, Juanma and Nelson.

Thanks Nico, for the chats and the adventures, for camping without a tent the night of Marseilles, fighting with the Moby's crew, sailing to places where "*you have to tell me this to me*", for the lunch breaks talking about everything on this planet but work, the *orange juices*, the geo-guesser, the thousands of crazy projects and the insights about Milano's radical chic world. Thanks for having always shared your sincere opinions, for your *prese a male* and those *a bene* as well.

Thank you Federico for our strong, authentic friendship. I owe you so much for all the times you kept insisting that I was doing great, although I felt lost and hopeless. Your unique ability to take stock of the situation was so important to me. These years have been amazing: finding our way up and down the Alps, dancing on the crest, camping in the wind, being amused by the unavoidable force of the Nation, debating for hours about the fate of Europe or the borders of Russia. Do not forget to keep living the *Guido Anselmi* in yourself, *vecchio Snaporaz!*

I have found in Lausanne a second family of 30-year-old people. Marco and Anne-Charlotte have been funny flatmates and true friends. I enjoyed any dinner at home or exploring the restaurants in town, any *aperò* or exhausting party, any moment of joy with you. I had the best quarantine I could imagine with Anne-Charlotte and the most precious words from Marco. I look up to you, because you are wonderful people and you deserve all the best.

Many others I met in Switzerland and somewhere else. I thank all of them for what they gave me and for the occasions I had to give them. Thanks to my old friends Alessandro and Francesco from Oxford, Paolo, Dilo and Calo from Pisa, and Damiano, Tommaso, Michele and Ruben from the *Reign of Abruzzi.*

I have been always inspired and felt protected by my numerous cousins, aunts and uncles. A special mention for Marco who keeps looking after me.

As human beings, we are unique because we make ourselves pictures of the World and let other people know. I dedicate this work to Antonio Russo, who was killed for giving voice to those left behind, oppressed by injustices and wars.

"*I wanna thank my mother and father for having me, and my grandmothers and grandfathers for having them...*"

This thesis is dedicated to the memory of my father and my best friend Mattia. They have been always next to me, I talking to them, they living in my soul. They were with me when I was working until late, having a freezing walk in Ivalo or riding my bike in the Vaud.

I could not have succeeded without the love of my mother and my brother. They have been relentless taking care of me, always ready to comfort me and pushing me to embrace life.

Finally, thank you so much Giovanna, for your voice, your presence, for being my source of energy, for our love that is *mutual* and for the road we have ahead together.

Lorenzo Stipani

ADDRESS Rue de Genève 77, CH-1004, Lausanne

PHONE +41 (0)77 97 49 147

EMAIL lorenzo.stipani@gmail.com

NATIONALITY Italian

DATE OF BIRTH 28.03.1991

Experiences and education

2016-2021 PhD in Physics, Swiss Plasma Center, EPFL, Switzerland

Title of the thesis: *A Fast Ion Loss Detector for TCV*.

Experience in diagnostics for particle detection.
Maintenance of magnetic sensor acquisition systems.
Teaching assistant for general physics B.Sc. courses.

2013-2016 M.Sc. in Physics of Plasma, Università di Pisa, Italy

Erasmus+/Traineeship at "Rudolf Peierls" Center for Theoretical Physics, University of Oxford, UK.

2010-2013 B.Sc. in Physics, Università di Pisa, Italy

August 2009 Summer School in Physics, Princeton University, NJ, USA

Selected publications

- L. Stipani et al., "Sawtooth and magnetic precursor during NBH discharge on TCV", Poster for IAEA-TCM on energetic particles, Princeton, 5-8 September 2017

Skills

Languages Italian (native), English (fluent), French (professional)

Coding Matlab, Python, Linux, Git, LaTeX

Soft Team-working, cross-disciplinary approach, self-taught attitude.